

Republic of Iraq,  
Ministry of higher  
Education and  
Scientific research,  
University of Diyala,  
College of science,  
Department of physics



## **Synthesis and Characterization of (Polypyrrole-Ferrites) Nanocomposites for Multi-Applications**

A Thesis

Submitted to the Council of the College of Science, University of Diyala in a Partial  
Fulfillment of the Requirements for the Degree of Doctor of Philosophy of science in  
Physics

By

**Omar Ahmad Hussein Al-Jubouri**

**B. Sc. in Physics (2006)**

**M. Sc. in Physics (2012)**

Supervised By

**Prof. Dr.**

**Tahseen Hussein Mubarak**

**University of Diyala**

**2022 A.D.**

**Prof. Dr.**

**Isam Mohammed Ibrahim**

**University of Baghdad**

**1444 A.H.**

بِسْمِ اللَّهِ الرَّحْمَنِ الرَّحِيمِ

(قُلْ إِنَّ صَلَاتِي وَنُسُكِي وَمَحْيَايَ وَمَمَاتِي لِلَّهِ رَبِّ الْعَالَمِينَ (162) لَا  
شَرِيكَ لَهُ ۗ وَبِذَلِكَ أُمِرْتُ وَأَنَا أَوَّلُ الْمُسْلِمِينَ (163))

صدق الله العظيم

سورة الأنعام (162-163)

## *Dedication*

*Words are not enough to describe people who stand by me  
in better or worse, so I dedicate my Ph. D. to ...*

*My merciful parents*

*My supporters brothers and sister*

*My wonderful wife*

*My awesome children ..... Mohammed and Misk.*

*Omar*

## Acknowledgment

First of all, I would like to thank Almighty **Allah** for giving me the strength, knowledge, ability and opportunity to carry out this work.

It is high necessary to express my deep gratitude for people who support and encourage me during my study.

I would like to express my heartfelt thanks to my supervisors, **Prof. Dr. Tahseen H. Mubarak** and **Prof. Dr. Isam M. Ibrahim**, for their guidance, inspiration and encouragement.

I express my thanks to all members of Physics Department, especially postgraduate faculty members and staff of the college for their cooperation. I would also like to thank the staff of the thin-film laboratory in the Physics Dept. College of science, University of Baghdad for allowing me to finish my work.

I offer my special thanks to my research colleagues and friends, for their cooperation during the period of studies and thesis work.

My sincere thanks to my close friends (**Mr. Omar Yusuf, Dr. Rasheed Salih, Dr. Omar Al-Fahdawe, Dr. Hussein Sliman, Dr. Laith Ali & Dr. Mohammed Ihsan**) for their help and support.

Finally, I shall always be grateful to my father, mother, brothers (**Salih, Falih, Jassim, and Othman**), sister (**Wafaa**), and wife for their love (Noor), valuable advice, and support through the years of my study.

## Supervisors Certification

We certify that this thesis entitled “*Synthesis and characterization of (Polypyrrole-ferrites) Nanocomposites for Multi-applications*” for the student (**Omar Ahmad Hussein**), was prepared under our supervisions at the Department of Physics, College of Science, University of Diyala in partial fulfillment of requirements needed to award the degree of *Doctor of Philosophy (Ph.D.) of Science in Physics*.

Signature:

Name: **Dr. Tahseen H. Mubarak**

Title: Professor

Address: College of Science,

University of Diyala

Date: / / 2022

Signature:

Name: **Dr. Isam M. Ibrahim**

Title: Professor

Address: College of science,

University of Baghdad

Date: / / 2022

### **Head of the Physics Department**

In view of available recommendation, I forward this thesis for debate by the examining committee.

Signature:

Name: **Dr. Ammar Ayesb Habeeb**

Title: Assistant Professor

Head of the Physics Department

Address: College of Science, University of Diyala

Date: / / 2022

## Scientific Amendment

I certify that the thesis entitled "*Synthesis and characterization of (Polypyrrole-ferrites) Nanocomposites for Multi-applications*" presented by student (**Omar Ahmad Hussein**) has been evaluated scientifically, therefore, it is suitable for debate by examining committee.

Signature

Name: **Dr. Balqees M. Dheyaa**

Title: Professor

Address: University of Technology, Applied science department

Date:     /     / 2022

## Scientific Amendment

I certify that the thesis entitled "*Synthesis and characterization of (Polypyrrole-ferrites) Nanocomposites for Multi-applications*" presented by student (**Omar Ahmad Hussein**) has been evaluated scientifically, therefore, it is suitable for debate by examining committee.

Signature

Name: **Dr. Lamia Khudhair Abbas**

Title: Assistant Professor

Address: University of Baghdad, College of science, department of Physics

Date:     /     / 2022

## Linguistic Amendment

I certify that the thesis entitled "*Synthesis and characterization of (Polypyrrole-ferrites) Nanocomposites for Multi-applications*" presented by (**Omar Ahmad Hussein**) has been corrected linguistically; therefore, it is suitable for debate by examining committee.

Signature

Name: **Karim H. Hassan**

Title: Professor

Address: University of Diyala, College of science, department of chemistry

Date: / / 2022

## Examination Committee Certificate

We certify that we have read this thesis entitled "*Synthesis and characterization of (Polypyrrole-ferrites) Nanocomposites for Multi-applications*" and, as an examining committee, we examined the student (**Omar Ahmad Hussein**) on its content, and in what is related to it, and that in our opinion it meets the standard of a thesis for the degree of *Doctor of Philosophy of Science in Physics*.

**(Chairman)**

Signature

Name: **Dr. Sabah A. Salman**

Title: Professor

Address: College of Science, University of Diyala

Date:     /     / 2022

**(Member)**

Signature

Name: **Dr. Nadheer Jassim Mohammed**

Title: Professor

Address: College of Science,  
Al-Mustansiriyah University

Date:     /     / 2022

**(Member)**

Signature

Name: **Dr. Estabraq Talib Abdullah**

Title: Assistant Professor

Address: College of Science,  
University of Baghdad

Date:     /     / 2022

**(Member)**

Signature

Name: **Dr. Olfat A. Mahmood**

Title: Assistant Professor

Address: College of Science,  
University of Diyala

Date:     /     / 2022

**(Member)**

Signature

Name: **Dr. Muhammad Hameed Abdul-allah**

Title: Assistant Professor

Address: College of Science, University of  
Diyala

Date:     /     / 2022

**(Member / supervisor)**

Signature

Name: **Dr. Tahseen H. Mubarak**

Title: professor

Address:

Date:     /     / 2022

**(Member / supervisor)**

Signature

Name: **Dr. Isam M. Ibrahim**

Title: professor

Address:

Date:     /     / 2022

Approved by the Council of the College of Science

**(The dean)**                      Signature:

Name: **Dr. Tahseen H. Mubarak**

Date:     /     / 2022

Title: professor

## Abstract

This research concentrates on the preparation of polypyrrole nanofibers (PPy-NFs) polymer using chemical polymerization technique and the nanoparticles of  $(\text{Co}_{0.8-x}\text{Zn}_x\text{Mn}_{0.2}\text{Fe}_2\text{O}_4)$  by co-precipitation technique followed by thermal treatment in a hydrothermal autoclave reactor where the values of (x) were within range (0-0.8) with (0.2) increment in each sample. Then the polypyrrole nanofibers were decorated with different ferrite nanoparticles to obtain (PPy-NFs/Ferrite nanoparticles) nanocomposite.

The prepared materials were characterized via several techniques, including X-ray Diffraction (XRD), infrared spectroscopy (FTIR) and Field emission Scanning electron microscopy (FESEM). (XRD) results demonstrated the amorphous character of polypyrrole and the single phase cubic spinel for the ferrite nanoparticles. The Crystallite size ( $D_{311}$ ) of the ferrite particles was within the range (8.54-14.47) nm. Also, (FESEM) images revealed that polypyrrole has polymerized in form of a 1D nanofibers net. Also, ferrite nanoparticles are spherical with little change in particle size distribution. (FTIR) of ferrite nanoparticles revealed two distinct absorption bands belonging to the tetrahedral places and octahedral places, respectively. In addition to it exhibited fabulous coherence between polypyrrole (PPy-NFs) and Ferrite nanoparticles. This indicates for the infallible fabrication of nanocomposites. The optical characteristics of the samples had also examined, and it has been noted that the value of the energy gap and absorbance behavior change with the change in the addition ratios and ferrite content.

The magnetic measurements were made at room temperature showed that the prepared samples have definite magnetic properties. It was also observed that the values of the saturation magnetization altered through the cobalt

content change in the composition. It recorded highest value at (x=0) for (Co<sub>0.8-x</sub>Zn<sub>x</sub>Mn<sub>0.2</sub>Fe<sub>2</sub>O<sub>4</sub>), then it gradually decreases with the decrease in the cobalt content.

The prepared nanocomposite had been used to enhance the photodetector sensitivity. The highest photosensitivity for each of polypyrrole (PPy-NFs) was up to (43.42%) and ferrite nanoparticles was (81.47%) at (x=0.8). While Nanocomposite sample for (PPy-NFs/Zn<sub>0.8</sub>Mn<sub>0.2</sub>Fe<sub>2</sub>O<sub>4</sub>) was (103.74%) for light with power of (30 mW) and wavelength of (405 nm). The rise and fall time were about (0.5 sec).

The supercapacitors were prepared for polypyrrole, ferrite nanoparticles and nanocomposite samples in order to gain distinguish and periodically stable capacitances. The performance of samples had evaluated via CV, EIS as well GCD methods. The highest capacitance of the nanocomposite electrode for (PPy-NFs/Zn<sub>0.8</sub>Mn<sub>0.2</sub>Fe<sub>2</sub>O<sub>4</sub>) was equal (414.12 F/g) with scan rate (20mV/s).

Finally, the response of the prepared samples was studied for ammonia gas sensing. It was found that ammonia gas sensing increase gradually with the raise of the zinc content in the pure ferrite nanoparticles samples and the PPy-NFs nanocomposite samples. It was noted that the largest response of ammonia gas at a temperature of (50<sup>0</sup>C) for ferrite nanoparticles at (x=0.8) equals (679.01%) and the nanocomposite samples for (PPy-NFs/Zn<sub>0.8</sub>Mn<sub>0.2</sub>Fe<sub>2</sub>O<sub>4</sub>) was equal to (423.11%).

## Published and Accepted Research Articles

### List of Publications

- 1- Omar A. Hussein, T. H. Mubarak, Isam M. Ibrahim, **Enhancement the photosensitivity of PPy-NFs/Nanoferrite for Photodetector**, International Journal of Mechanical Engineering, ISSN: 0974-5823, Volume 7, No.3, PP. 274-284, 2022.
- 2- Omar A. Hussein, T. H. Mubarak, Isam M. Ibrahim, **Magnetic properties of Hybrid inorganic-organic flexible nanofibers**, NeuroQuantology, Volume 20, issue 4, PP. 64-72, 2022.
- 3- Omar A. Hussein, T. H. Mubarak, Isam M. Ibrahim, **Designing inorganic-organic nanofibers nanocomposite for Supercapacitor Applications**, NeuroQuantology, Volume 20, issue 5, PP. 1972-1983, 2022.

## Contents

| Subject                      | Page No. |
|------------------------------|----------|
| <b>Table of Contents</b>     | I        |
| <b>List of Figures</b>       | VI       |
| <b>List of Tables</b>        | X        |
| <b>List of Symbols</b>       | XI       |
| <b>List of Abbreviations</b> | XIII     |

## Table of Contents

| Item No.  | Subject                                   | P. No. |
|---|---|--------|
| Chapter One: Introduction and Literature Review |   | 1      |
| 1.1   | Introduction                              | 1      |
| 1.2   | Literature Review                         | 3      |
| 1.3   | Aims of the study                         | 11     |
| Chapter Two: Theoretical and Basic Concepts     |   | 12     |
| 2.1   | Introduction                              | 12     |
| 2.2   | Nanoscience and Nanotechnology Background | 12     |
| 2.3   | Nanomaterials Classification              | 13     |
| 2.4   | Conducting Polymers (CPs)                 | 14     |
| 2.5   | Classification of Conducting Polymers     | 15     |
| 2.5.1   | Intrinsically Conducting Polymers         | 15     |
| 2.5.1.1   | Conjugated Conducting Polymers            | 15     |
| 2.5.1.2   | Doped Conducting Polymers                 | 15     |
| 2.5.2   | Extrinsically Conducting Polymers         | 16     |
| 2.5.2.1   | Conductive Element Filled Polymers        | 16     |

|          |   |    |
|----------|---|----|
| 2.5.2.2  | Blended Conducting Polymers               | 16 |
| 2.6      | Synthesis of conducting polymers          | 16 |
| 2.6.1    | Chemical Polymerization                   | 17 |
| 2.6.2    | Electrochemical Polymerization            | 17 |
| 2.7      | Principles of Electrical Conduction       | 18 |
| 2.7.1    | Band Theory                               | 18 |
| 2.7.2    | Conduction by reinforcement               | 19 |
| 2.7.3    | Polaron and Bipolaron Model               | 20 |
| 2.8      | Conductive polymers activation            | 22 |
| 2.9      | Applications of conducting polymers       | 22 |
| 2.10     | Polypyrrole polymer (PPy)                 | 23 |
| 2.11     | Composites                                | 25 |
| 2.12     | Nanoparticle/Polymer Composite techniques | 26 |
| 2.12.1   | Solution Mixing                           | 27 |
| 2.12.2   | Melt blending                             | 27 |
| 2.12.3   | In-Situ Polymerization                    | 27 |
| 2.13     | Magneto Polymeric Materials               | 28 |
| 2.14     | Magnetic nanoparticles                    | 29 |
| 2.15     | Origin of Magnetism                       | 30 |
| 2.16     | Types of magnetic materials               | 32 |
| 2.17     | Ferrites                                  | 37 |
| 2.17.1   | Soft ferrite                              | 37 |
| 2.17.2   | Hard ferrite                              | 37 |
| 2.18     | Crystal structure of ferrites             | 38 |
| 2.18.1   | Spinel Ferrites                           | 38 |
| 2.18.1.1 | Normal spinel ferrites                    | 39 |

|          |   |    |
|----------|---|----|
| 2.18.1.2 | Mixed Spinel Ferrites   | 39 |
| 2.18.1.3 | Inverse Spinel Ferrites   | 40 |
| 2.18.2   | Garnet Ferrites   | 41 |
| 2.18.3   | Hexagonal ferrite   | 41 |
| 2.19     | Superparamagnetism  | 41 |
| 2.20     | Magnetic domains  | 44 |
| 2.21     | Properties of Magnetic Materials                                    | 47 |
| 2.21.1   | Magnetic Hysteresis   | 47 |
| 2.21.2   | Saturation Magnetisation  | 48 |
| 2.21.3   | Remanence (Retentivity)   | 49 |
| 2.21.4   | Coercivity  | 49 |
| 2.21.5   | Magnetic Anisotropy   | 49 |
| 2.22     | Synthesis of Ferrite Nanoparticles                                  | 51 |
| 2.22.1   | Co-precipitation technique  | 51 |
| 2.22.2   | Hydrothermal or solvothermal method                                 | 52 |
| 2.23     | Autoclave Requirements  | 53 |
| 2.24     | Conventional capacitors and supercapacitors                         | 53 |
| 2.25     | Types of supercapacitors  | 55 |
| 2.25.1   | Electrochemical Double Layer Supercapacitors                        | 55 |
| 2.25.2   | Pseudocapacitors  | 57 |
| 2.25.3   | Hybrid supercapacitors  | 57 |
| 2.26     | Supercapacitors applications  | 59 |
| 2.27     | Electrochemical Characterization Techniques for ECs<br>Applications | 60 |
| 2.27.1   | Cyclic Voltammetry (CV)   | 60 |
| 2.27.2   | Galvanostatic Charge-Discharge (GCD)                                | 63 |

|                                  |  |    |
|----------------------------------|--|----|
| 2.27.3                           | Electrochemical impedance spectroscopy   | 64 |
| 2.28                             | Photoconductivity  | 66 |
| 2.28.1                           | Current-time characteristics   | 67 |
| 2.28.2                           | Rise time and fall time upon a square-pulse signal   | 68 |
| 2.28.3                           | Sensitivity  | 69 |
| 2.29                             | The Term "Sensor"  | 69 |
| 2.29.1                           | Conducting polymer sensors   | 70 |
| 2.30                             | Characteristics used to study PPy, Ferrite and PPy nanocomposites  | 72 |
| 2.30.1                           | X-Ray Diffraction (XRD)  | 72 |
| 2.30.2                           | Field emission-scanning electron microscopes (FESEM)   | 75 |
| 2.30.3                           | Fourier Transform Infrared (FTIR) spectroscopy   | 76 |
| 2.31                             | Optical properties   | 77 |
| 2.31.1                           | Optical Properties of conducting Polymers  | 78 |
| 2.31.1.1                         | Optical Absorption: Formation of Excited States  | 78 |
| 2.31.1.2                         | Optical Emission: Relaxation of Excited States   | 78 |
| Chapter Three: Experimental Part |  | 80 |
| 3.1                              | Introduction   | 80 |
| 3.2                              | Materials and method   | 82 |
| 3.2.1                            | Materials and chemicals  | 82 |
| 3.2.2                            | Synthesis of Polypyrrole Nanofibers (PPy-NFs)  | 83 |
| 3.2.3                            | Synthesis of Ferrite Nanoparticles   | 84 |
| 3.2.4                            | Synthesis of Nanocomposite (PPy-NFs/Co <sub>0.8-x</sub> Zn <sub>x</sub> Mn <sub>0.2</sub> Fe <sub>2</sub> O <sub>4</sub> ) | 87 |
| 3.3                              | Substrate cleaning   | 87 |

|                                     |   |     |
|-------------------------------------|---|-----|
| 3.3.1                               | Substrate (glass) cleaning                              | 87  |
| 3.3.2                               | Wafer silicon cleaning                                  | 88  |
| 3.4                                 | Structural and morphological Characterization           | 89  |
| 3.4.1                               | X-ray Diffraction (XRD)                                 | 89  |
| 3.4.2                               | Field Emission Scanning Electron Microscopy (FESEM)     | 89  |
| 3.4.3                               | Fourier Transform Infrared Spectrometry (FTIR)          | 89  |
| 3.5                                 | Magnetic Properties                                     | 90  |
| 3.5.1                               | Vibrating Sample Magnetometer (VSM)                     | 90  |
| 3.6                                 | Optical Measurements                                    | 90  |
| 3.7                                 | Photodetector Fabrication                               | 91  |
| 3.7.1                               | Characteristic measurements of photoconductive detector | 91  |
| 3.8                                 | Electrochemical Characterization techniques             | 92  |
| 3.8.1                               | Cyclic voltammetry Measurement (CV)                     | 92  |
| 3.8.2                               | Galvanostatic charge-discharge Measurement (GCD)        | 93  |
| 3.8.3                               | Electro-chemical Impedance Measurement (EIS)            | 93  |
| 3.9                                 | Gas sensor  | 93  |
| 3.10                                | Samples Codes   | 95  |
| Chapter Four: Result and Discussion |   | 96  |
| 4.1                                 | Introduction  | 96  |
| 4.2                                 | The structural properties                               | 96  |
| 4.2.1                               | X-Ray Diffraction Analysis Results                      | 96  |
| 4.2.2                               | Fourier transform infrared (FTIR) spectroscopy analysis | 101 |
| 4.2.3                               | FESEM image analysis                                    | 105 |
| 4.3                                 | Magnetic properties                                     | 111 |

|            |   |     |
|------------|---|-----|
| 4.4        | optical properties                                    | 115 |
| 4.5        | Photoconductivity of Detector                         | 123 |
| 4.6        | Electrochemical application                           | 131 |
| 4.6.1      | Cyclic voltammetry measurements                       | 131 |
| 4.6.2      | Electrochemical impedance spectroscopy analysis (EIS) | 137 |
| 4.6.3      | Galvanostatic charge discharge measurements           | 141 |
| 4.7        | Ammonia gas sensing measurement                       | 146 |
| 4.8        | Suggestions for future work                           | 153 |
| 4.8.1      | Conclusions   | 153 |
| 4.8.2      | Future work suggestions                               | 155 |
| References |   | 156 |

### List of Figures

| Fig. No. | Figure Caption   | P. No. |
|----------|--|--------|
| 2.1      | Band theory.   | 19     |
| 2.2      | Conductivities of insulator, semi-conductors, metals and CPs.  | 20     |
| 2.3      | Structure of PPy in the neutral state.   | 25     |
| 2.4      | Demonstration of the magnetic moment associated with (a) an orbiting electron and (b) a spinning electron.                       | 31     |
| 2.5      | Different types of magnetic behavior.  | 36     |
| 2.6      | Unit cell of spinel structure $\text{MeFe}_2\text{O}_4$  | 39     |
| 2.7      | Cation distribution in normal spinel ferrites, mixed spinel ferrites and inverse spinel ferrites.                                | 40     |
| 2.8      | The energy density of a magnetic particle contains a term $K\sin^2\theta$ , the energy is minimized when $\theta = 0$ or $\pi$ . | 42     |
| 2.9      | The dependence of the relaxation time ( $\tau$ ) as a function of temperature T (scaled by $k_B/KV$ ) ....                       | 44     |

|      |  |    |
|------|--|----|
| 2.10 | Magnetic domains in a bulk material.   | 45 |
| 2.11 | (a) 180° and (b) 90° domain wall.  | 46 |
| 2.12 | Hysteresis loop.   | 48 |
| 2.13 | The magnetocrystalline anisotropy of cobalt.   | 50 |
| 2.14 | Schematic of a conventional capacitor.   | 54 |
| 2.15 | Schematic of an electrochemical double-layer capacitor.  | 54 |
| 2.16 | Schematic diagram of a typical charged EDLC.   | 56 |
| 2.17 | Equivalent circuit of three-electrode set-up.  | 60 |
| 2.18 | A typical electrochemical capacitor schematic exhibiting the differences between static (rectangular) and faradaic (curved) capacitance. | 62 |
| 2.19 | Plots of the Galvanostatic charge-discharge of (a) EDLC (b) pseudo-capacitive material.  | 64 |
| 2.20 | Schematic of typical Nyquist plots.  | 65 |
| 2.21 | Photoresponse graph that shows a quicker response time.  | 67 |
| 2.22 | Rise and decay time of signal for square-pulse signal.   | 68 |
| 2.23 | Schematic representation of x-ray diffraction.   | 73 |
| 2.24 | State energy diagram of some possible photophysical process in a typical fluorescent molecule.   | 79 |
| 3.1  | Diagram of the preparation materials.  | 81 |
| 3.2  | Diagram of the measurements and applications.  | 81 |
| 3.3  | Diagram of co-precipitation method pursued by heat treatment in an autoclave reactor.  | 86 |
| 3.4  | Diagram of the photocurrent measuring process in the photodetectors.   | 92 |
| 3.5  | Shows schematic of three-electrode system.   | 92 |
| 3.6  | Electrical circuit setup of gas sensor.  | 94 |
| 4.1  | XRD pattern of (PPy-NFs).  | 98 |

|      |   |     |
|------|---|-----|
| 4.2  | XRD patterns of the synthesized ( $\text{Co}_{0.8-x}\text{Zn}_x\text{Mn}_{0.2}\text{Fe}_2\text{O}_4$ ) nanoparticles.   | 99  |
| 4.3  | FTIR spectra for PPy-NFs and PPy-NFs nanocomposites include PF1, PF2, PF3, PF4 and PF5.   | 101 |
| 4.4  | FTIR spectrum of $\text{Co}_{0.8-x}\text{Zn}_x\text{Mn}_{0.2}\text{Fe}_2\text{O}_4$ samples.  | 104 |
| 4.5  | FESEM images of PPy-NFs at different magnification.   | 106 |
| 4.6  | FESEM images of ( $\text{Co}_{0.8-x}\text{Zn}_x\text{Mn}_{0.2}\text{Fe}_2\text{O}_4$ ) samples ( $x = 0, 0.2, 0.4, 0.6$ and $0.8$ ) at different magnification. | 108 |
| 4.7  | FESEM images of PPy-NFs nanocomposites samples at different magnification.  | 110 |
| 4.8  | Magnetization versus applied magnetic field of PPy-NFs, ferrite nanoparticles and PPy-NFs nanocomposites samples at 300K.                                       | 112 |
| 4.9  | Magnetization versus applied magnetic field of .....  | 113 |
| 4.10 | The absorption spectra for PPy-NFs and PPy-NFs nanocomposite samples.   | 116 |
| 4.11 | $(\alpha h\nu)^2$ vs. $(h\nu)$ plots for pure PPy-NFs.  | 117 |
| 4.12 | The absorption spectra for ferrite nanoparticles samples.   | 118 |
| 4.13 | Diagrams of $(\alpha h\nu)^2$ vs. $(h\nu)$ for F1, F2, F3, F4 and F5 samples.   | 120 |
| 4.14 | Diagrams of $(\alpha h\nu)^2$ vs. $(h\nu)$ for PF1, PF2, PF3, PF4 and PF5 samples.  | 122 |
| 4.15 | Variation of light sensitivity for PPy-NFs with various energy powers.  | 124 |
| 4.16 | Variation of light sensitivity for ferrite nanoparticles (F1, F2, F3, F4 and F5) with various light powers.   | 127 |

|      |   |     |
|------|---|-----|
| 4.17 | Variation of light sensitivity for PPy-NFs nanocomposites.....  | 129 |
| 4.18 | CV curves of the PPy-NFs.   | 133 |
| 4.19 | CV curves of the ferrite nanoparticles (F1, F2, F3, F4 and F5).   | 135 |
| 4.20 | CV curves of the PPy-NFs nanocomposite (PF1, PF2, PF3, PF4 and PFF) samples.                                    | 137 |
| 4.21 | Nyquist plots for a) PPy-NFs, b) F1, c) F2, d) F3, e) F4, f) F5, g) PF1, h) PF2, i) PF3, j) PF4 and k) PF5..... | 141 |
| 4.22 | Galvanostatic charge-discharge for PPy-NFs, ferrite nanoparticles and PPy-NFs electrodes for supercapacitors.   | 144 |
| 4.23 | Variation of resistance with time for PPy-NFs sensor.   | 147 |
| 4.24 | Variation of resistance with time for ferrite nanoparticles and PPy-NFs nanocomposite sensors.                  | 151 |
| 4.25 | Variation of resistance with time for ferrite nanoparticles sensors.  | 152 |
| 4.26 | Variation of resistance with time for PPy-NFs nanocomposite sensors.  | 152 |

## List of Tables

| Table No. | Table caption   | P. No. |
|-----------|---|--------|
| 3.1       | The raw materials of synthesise of (PPy-NFs) synthesis.   | 82     |
| 3.2       | The raw materials of synthesise of $(Co_{0.8-x}Zn_xMn_{0.2}Fe_2O_4)$ .  | 82     |
| 3.3       | (MO: Py: $FeCl_3$ ) molar ratio of (PPy-NFs) samples.   | 83     |
| 3.4       | Synthesis of $(Co_{0.8-x}Zn_xMn_{0.2}Fe_2O_4)$ from basic chemicals compounds and the weights that had been used.   | 85     |
| 3.5       | Prepared samples codes.   | 95     |
| 4.1       | XRD data of $Co_{0.8-x}Zn_xMn_{0.2}Fe_2O_4$ nanoparticles.  | 100    |
| 4.2       | FTIR absorption bands for PPy-NFs and PPy-NFs nanocomposites include PF1, PF2, PF3, PF4 and PF5.  | 102    |
| 4.3       | FTIR data for ferrite nanoparticles.  | 104    |
| 4.4       | The magnetic parameters for PPy-NFs, ferrite nanoparticles and PPy-NFs nanocomposite samples.   | 115    |
| 4.5       | Photosensitivity variation for prepared materials.  | 130    |
| 4.6       | $R_{ESR}$ and $R_{ct}$ for the PPy-NFs, ferrite nanoparticles and PPy-NFs nanocomposites samples.   | 139    |
| 4.7       | The responsivity, response time and recovery time for PPy-NFs, ferrite nanoparticles and PPy-NFs nanocomposite samples at $50^\circ C$ with 30 ppm of $NH_3$ gas concentration. | 153    |

## List of Symbols

| Symbol   | Meaning                         | Units                                    |
|----------|---------------------------------|--|
| f        | Frequency                       | Hz                                       |
| $\theta$ | Diffraction Angle               | Degree                                   |
| $T_c$    | Curie Temperature               | K or °C                                  |
| $T_N$    | Neel Temperature                | K or °C                                  |
| L        | Hopping Length                  | Å  |
| H        | Magnetic Field Strength         | A/m                                      |
| M        | Magnetization                   | emu/g                                    |
| $\mu$    | Magnetic Permeability of Medium | Hm <sup>-1</sup>                         |
| $\mu_0$  | Permeability of Free Space      | $4\pi \times 10^{-7}$ Hm <sup>-1</sup>   |
| $\mu_r$  | Relative Permeability           | Dimensionless                            |
| $M_s$    | Saturation Magnetization        | emu/g                                    |
| $B_s$    | Saturation Flux Density         | tesla (T)                                |
| $B_r$    | Remnant Induction               | tesla (T)                                |
| $H_c$    | Magnetic Coercivity             | A/m                                      |
| $\tau_0$ | Characteristic Relaxation Time  | s  |
| $\tau_N$ | Néel Relaxation Time            | s  |
| $\tau_B$ | Brown Relaxation Time           | s  |
| $\tau$   | Effective Relaxation Time       | s  |
| $T_B$    | Blocking Temperature            | K  |
| $\chi$   | Magnetic Susceptibility         | --                                       |
| $k_B$    | Boltzmann's Constant            | $1.38 \times 10^{-23}$ J·K <sup>-1</sup> |
| T        | Absolute Temperature            | K  |
| h, k, l  | Miller Indices                  | Integer                                  |

|                   |  |                           |
|-------------------|--|---------------------------|
| $\rho_x$          | X-ray density                            | $\text{g/cm}^3$           |
| D                 | Crystallite Size                         | nm                        |
| $E_g$             | Energy Gap                               | eV                        |
| $\lambda$         | Wavelength                               | nm                        |
| Q                 | Electron Charge                          | C                         |
| I                 | Electric Current                         | Ampere (A)                |
| V                 | Electric potential                       | Volt (V)                  |
| E                 | Electric Field                           | $\text{V.cm}^{-1}$        |
| $a_{\text{exp}}$  | Experimental Lattice Constant            | Å                         |
| $M_r$             | Remnant Magnetization                    | emu/g                     |
| $\alpha$          | Optical Absorption Coefficient           | -                         |
| R %               | Response of the Sensor                   | -                         |
| $R_{\text{air}}$  | Resistances of the Sensor in Air         | $\Omega$                  |
| $R_{\text{gas}}$  | Resistances of the Sensor in Gas         | $\Omega$                  |
| $\sigma$          | Conductivity                             | $(\Omega.\text{cm})^{-1}$ |
| $\sigma_e$        | Electrode Conductivity                   | $\text{S.cm}^{-1}$        |
| $Z_{\text{real}}$ | Real Parts of the Complex Impedance      | $\Omega$                  |
| $Z_{\text{imag}}$ | Imaginary Parts of the Complex Impedance | $\Omega$                  |
| C                 | Capacitance                              | F                         |
| Cs                | Specific Capacitances                    | $\text{F.g}^{-1}$         |
| m                 | Active Mass of the Electrode             | $\text{mg.cm}^2$          |

### List of Abbreviations

| <b>Abbreviation</b> | <b>Definition</b>                               |
|---------------------|---|
| CPs                 | Conducting Polymers                             |
| HCPs                | Hybrid Conducting Polymers                      |
| Py                  | Pyrrole   |
| PPy                 | Polypyrrole                                     |
| PPy-NFs             | Polypyrrole Nanofibers                          |
| MO                  | Methyl Orange                                   |
| SQUID               | Superconducting Quantum Interference Device     |
| HUMO                | Higher Unoccupied Molecular Orbitals            |
| LOMO                | Lower Occupied Molecular Orbitals               |
| ppm                 | Parts Per Million                               |
| CV                  | Cyclic Voltammetry                              |
| GCD                 | Galvanostatic Charge-Discharge                  |
| MNPs                | Magnetic Nanoparticles                          |
| VSM                 | Vibrating Sample Magnetometer                   |
| TEM                 | Transmission Electron Microscopy                |
| XRD                 | X-Ray Diffraction                               |
| FTIR                | Fourier Transform Infrared Spectroscopy         |
| FESEM               | Field Emission Scanning Electron Microscope     |
| VSM                 | Vibrating Sample Magnetometer                   |
| JCPDS               | Joint Committee on Powder Diffraction Standards |
| ESR                 | Equivalent Series Resistance                    |
| EMI                 | Electromagnetic Interference                    |
| SCE                 | Saturated calomel electrode                     |

## **Chapter one**

### **Introduction and Literature Review**

#### **1.1 Introduction**

This work addresses the characteristics of composite material consisting of polypyrrole nanofibers supported by ferrite nanoparticles. To begin with, polymers are an essential sort of chemical that living would've been more significantly harder without it. Polymer comes from the Greece words poly, which means many, plus mers, which incomes components as well as units with an in height molar mass. Every molecule is comprised of a large number of distinct composition units that are arranged in a logical order. Polymers, also known as macromolecules, are large molecules with a high molecular weight that are made via combining a great number of small molecules called monomers. Polymerization is process of joining monomers together to produce a polymer [1].

Synthesis polymers have been known and used as effective insulators for a long time. Billingham as well as Calvert contend that, “For most of the history of polymer technology, one of the most important characteristics of these polymers is their ability to work as an excellent electrical insulators.” Massive efforts have been made in the last two decades to develop innovative materials known as “conducting polymers” (CPs) [2]. Conducting polymers have been extensively studied for optical, electrochemical, and electronic applications due to their unique optical, electrical, and chemical features. When the right elements are doped into products, they can have conductivity ranging from semiconductors to metallic materials [3].

Due to their electric as well as electrochemical properties which are equivalent with those of traditional semiconductors as well as metals,

conducting polymers (CPs) have attracted a great attention across both basic plus applied investigation. CPs offer great features such as low manufacturing and treatment temperatures, adjustable conductivity, chemical and structural variety, and structural flexibility [4]. Impactful materials of CPs of good mechanical reliability, flexibility, as well as conductivities have been demonstrated to function as significant physical parts in light-emitting diodes[5], capacitors of electrochemical, actuators plus transistors [6], devices of electrochromic [7], cells of photovoltaic as well as sensors, battery, memories and electromagnetic induction (EMI) shielding [8].

Polyacetylene is the first conductive polymer that was discovered by Alan Heeger, Hideki Shirakawa, and Alan MacDiarmid in 1977. After this discovery, a variety of conductive polymers were investigated, including PANI, polypyrrole, polythiophene, PEDOT, besides PPV polymer [9].

Polyaniline (PANI), polypyrrole (PPy), and polythiophene (PTh) are the most appealing polymer groups [10]. Over the past decades, these conductive polymers have indeed been studied widely and described. Due to their low cost, great sensitivity, quick reaction, their ability to work at room temperature, those polymers but also its derivatives have frequently used in nanosensors [11]. Because of their exceptional electrical and magnetic properties, spinel ferrites are intriguing ceramic magnetic materials that have been the focus of extensive theoretical and experimental research. Spinel ferrite nanoparticles have remarkable physical and chemical features, including substantial anisotropy, high saturation magnetization, high magnetic permeability, good chemical stability [12], Superparamagnetism, and temperature-dependent hysteresis, among others. It is employed in a variety of applications, including soft magnetic powders, hyperthermia,

magnetic fluids, heat transfer systems, transformer cores, drug delivery orientation, data storage devices, and magnetic sensors [13]. Many ferrites could be classified as magnetism semiconductors due to its distinctive features plus good functional features. They have a wide range of uses in a variety of industries. The magnetic characteristics of ferrites are determined by phase purity and crystalline nature. Magnetorheology[14] and microwave absorption are two further applications of magnetic ferrites [15]. The different ferrites can be synthesized using a variety of processes. The magnetic behavior of ferrites is determined by the structure of ferrites, the cations Spread at the octahedral plus tetrahedral positions, models defects, the nanocrystallites size, and other factors [16].

## **1.2 Literature Review**

1. Hernandez et al. published a paper in 2007 about superior quality PPy-NWs made through template-directed chemical preparation. Temperature dependent electrical transport investigations revealed that the specimen was semiconducting with a minimal extent of disorder. For gaseous ammonia, sensors according to single nanowire demonstrated high sensitivity, detection limit, in addition to selectivity. At a concentration of approximately 40 ppm, the sensors provided reliable detection [17].
2. Yang et al. demonstrated in 2010 that using a  $\text{FeCl}_3$ -MO reactive template, they could make polypyrrole (PPy) nanofibers quickly and easily. Chemical sensors were built into the sensor device using the prepared PPy nanofibers to discover  $\text{NH}_3$  vapors. In comparison to bulk Polypyrrole, sensor in accordance with PPy-NFs outperformed bulk PPy when it comes to time response plus sensitivity [18].

3. Dubal et al. in 2011 Here, electrodeposition process for the production of PPy nanobricks have been tested. X-ray Diffraction, FTIR, TEM, plus SEM are used to characterize these PPy nanobricks. CV in addition GCD methods were used to assess the electrochemical performance of PPy material (electrode). Within the voltage range of  $4 \times 10^{-1}$  to  $-6 \times 10^{-1}$  Volt in  $5 \times 10^{-1}$  M sulfuric acid, a great Cs of  $47.6 \times 10$  F.g<sup>-1</sup> had attained. Furthermore, PPy electrode had an 89% discharge/charge efficiency [19].
4. Hosseini et al. in 2012 synthesized polypyrrole-MnFe<sub>2</sub>O<sub>4</sub> composites by core-shell construction using in situ-polymerization in the existence of surfactant plus doping. FeCl<sub>3</sub> also served as an oxidation factor. XRD, VSM, SEM, FTIR, and the four-wire technique were used to determine the structure and magnetic properties of manganese ferrite nanoparticles. Utilizing vector network analysers in the frequency region from eight to twelve GHz, the microwave-absorbing properties of nanocomposite powders were investigated. At 11.3GHz, A reflection loss of  $-1.2 \times 10$  dB measured as the minimal. The results of spectroanalysis show that Polypyrrole chains in addition to particles of ferrite have a mutual interaction [20].
5. Shinde et al. reported in 2013 a low-cost, innovative, in addition to easy chemical production of thin films PPy to supercapacitors applications. XRD, FTIR, and SEM are used to evaluate these PPy films. The electrochemical supercapacitors characteristics for PPy thin films were assessed via CV in a  $5 \times 10^{-1}$  M Sulfuric acid, with an extreme Cs of  $32.9 \times 10$  F/g with a scan rate about 5mV/s. Furthermore, electrochemical impedance measurements revealed that the (ESR) for thin films PPy are  $108 \times 10^{-2}$  ohm The charge transfer is attributable to both redox and non-redox reactions, as indicated by the Nyquist and Bode plots, which is supported by the findings of charge discharge experiments [21].

6. Geng et al. in 2013 synthesized polypyrrole/ $\gamma$ -Fe<sub>2</sub>O<sub>3</sub> hybrid materials in situ via sol-gel polymerization and studied them using FTIR, XRD, and HRTEM. At thirty, sixty, plus ninety Celsius, the sensitivities of gas in ammonia, CO, H<sub>2</sub>, acetone and ethanol atmospheres had measured. The gas sensitivities findings revealed which the polypyrrole/ $\gamma$ -Fe<sub>2</sub>O<sub>3</sub> had a great sensitivity for ammonia at a low working temp (<hundred Celsius), overcoming disadvantages of PPy's slow response time and  $\gamma$ -Fe<sub>2</sub>O<sub>3</sub> high operating temperature. As a result, the hybrids had crucial and practical properties for the production of gas sensors [22].
7. Eeu et al. in 2013 reinforced polypyrrole by reduced graphene oxide plus (Fe<sub>2</sub>O<sub>3</sub>) to obtain electrochemical stabilization and improvement, A simple one-pot chronoamperometry technique was used to create the ternary nanocomposite film. When comparing the nanocomposite to their individual (polypyrrole) as well as binary (polypyrrole/RGO) counterparts, cyclic voltammetry measurements revealed a two-fold and four-fold increase in current for the nanocomposite. Even after 200 charge/discharge cycles, the film of ternary composite retained its Cs quite well. The PPy/RGO/Fe<sub>2</sub>O<sub>3</sub> electrode has a specific capacitance of  $1257 \times 10^{-1} \text{ F.g}^{-1}$ , while the Polypyrrole/reduced graphene oxide plus polypyrrole materials (electrodes) have  $933 \times 10^{-1}$  and  $766 \times 10^{-1} \text{ F.g}^{-1}$ , respectively [23].
8. Ullah et al. In 2013 investigated the response mechanism of polypyrrole as a sensor to ammonia. The interaction of ammonia with the oligopyrrole lowers the impedance to electron transport across the oligomer backbone. Changes in electronic characteristics like as ionization potential, electron affinity, HOMO, LUMO, band gap, and  $\lambda_{\text{max}}$  are also used to assess resistance decrease. The capacity of nPy oligomers to detect ammonia is additionally aided by their electron affinity and band gap (HOMO to LUMO). When

- oligopyroles interact with  $\text{NH}_3$ , band gaps narrow and LUMO energies rise [24].
9. Navale et al. In 2014 used a spin coating method on a glass substrate to produce Polypyrrole-iron oxide hybrid nanocomposite sensor films, which were then analyzed for structural and morphological features using XRD, FTIR, and SEM. The hybrid nanocomposites' gas-sensing properties were investigated and compared to Polypyrrole plus  $\alpha$ -ferric oxide ( $\text{Fe}_2\text{O}_3$ ). This was discovered which polypyrrole/ $\alpha$ -ferric oxide ( $\text{Fe}_2\text{O}_3$ ) hybrid composites could somewhat compensate for limitations for pristine polypyrrole and ferric oxide. this was discovered that a polypyrrole/ $\alpha$ -ferric oxide ( $\text{Fe}_2\text{O}_3$ ) (fifty %) hybrid sensing working at room temp can discover Nitrogen dioxide ( $\text{NO}_2$ ) at small concentrations (ten ppm) and high selectivity compared to  $\text{C}_2\text{H}_5\text{OH}$  as well as sensitivity ( $5.6 \times 10\%$ ) and superior stabilization (85%) [25].
  10. Moloudi et al. In 2015 prepared a nanocomposite of hard ( $\text{BaFe}_{12}\text{O}_{19}$ )/soft ferrite, and then produced an in situ polymerisation method to create a PPy- $\text{BaFe}_{12}\text{O}_{19}/\text{Fe}_3\text{O}_4$  multicore-shell. VSM and the four-wire approach were used to characterize the nanocomposite's magnetic characteristics and electrical conductivity, respectively. Electrical conductivity of conducting ferromagnetic polymer nanocomposites is order of  $0.5 \times 10 \frac{\text{S}}{\text{cm}}$ , as well as  $M_s$  is  $0.3 \times 10 \frac{\text{emu}}{\text{g}}$  as prepared [26].
  11. Elahi et al. In a 2015 used sol-gel and in situ chemical polymerization to synthesize  $\text{Zn}_{0.5}\text{Ni}_{0.45}\text{Mn}_{0.05}\text{Fe}_2\text{O}_4$  and polypyrrole-ferrite nanocomposite structures. The formation of a two-phase system is revealed by XRD, FTIR, and FESEM experiments. When ferrite was added to PPy, the phase separation increased. Because of the bonding influence among the metals

cations with the polypyrrole, the electric density for the polypyrrole chain decreased, lowering conductivity. When ferrites are included into a conducting polypyrrole matrix, the dielectric constant and dielectric loss increase. When comparing pure samples to composite materials, the loss tangent was found to have large values. The magnetic characteristics of composites were also affected by the amount of ferrite [27].

12. Sun et al. in 2016 synthesized PPy/coated  $\text{ZnFe}_2\text{O}_4$  double-shelled hollow spheres in a study conducted. The  $\text{ZnFe}_2\text{O}_4$ /PPy composite that emerges combines the benefits of hollow structure and nanocompositing. The hollow interior reduces volume changes during charge and discharge, while the PPy coating improves structural stability and conductivity. The electrochemical performance of the  $\text{ZnFe}_2\text{O}_4$ /PPy composite is much better than that of pristine  $\text{ZnFe}_2\text{O}_4$  with a double-shelled hollow structure. This study found that combining hollow structure and nanocompositing to develop the electrochemical act of anode materials (Transition metal oxides or TMO) [28].
13. Mažeika et al. in 2018 synthesized  $\text{CoFe}_2\text{O}_4$ /polypyrrole composite nanoparticles using a high energy ball mill. For sample characterisation, Mössbauer and FTIR spectroscopies, VSM, and TEM were used. Nanoparticles were exposed to an alternating magnetic field to assess the specific loss power. When comparing  $\text{CoFe}_2\text{O}_4$  nanoparticles to  $\text{CoFe}_2\text{O}_4$ /polypyrrole composite nanoparticles, some differences in coercivity were detected and explained [29].
14. Zhang et al. in 2018 reported new  $\text{NH}_3$  gas sensing according to self-assembled Polypyrrole/ $\text{Zn}_2\text{SnO}_4$  composite. In-situ chemical oxidative polymerization was used to prepare the PPy nanospheres, and C element microspheres had used as a sacrificial model to synthesize the  $\text{Zn}_2\text{SnO}_4$

hollow nanospheres. The reported materials were characterized using XRD, FTIR, EDS, XPS, TEM, in addition to SEM techniques. When exposed for ammonia gas, gas sensor characteristics for Polypyrrole/ $Zn_2SnO_4$  nanofilm had studied. In terms of a reduction discovery limit, greater responsiveness, shorter response with recovery time, and exceptional repetition to ammonia gas, the PPy/ $Zn_2SnO_4$  Nanofilm sensor outperformed its pristine Polypyrrole and  $Zn_2SnO_4$ . The substantial improvement in gas sensor characteristics for PPy/ $Zn_2SnO_4$  Nanofilm is attributed to the deprotonation/protonation technique of  $NH_3$  adsorption/desorption on the Polypyrrole surface, unique relations at the p-n Hetero junction, as well as large surface area of the PPy/ $Zn_2SnO_4$  composite [30].

15. Assar et al. in 2019 prepared  $Co_{0.5}Ni_{0.2}Li_{0.15}Fe_{2.15}O_4$ /Polypyrrole using the mechano-synthetic technique. Their magnetic plus structural features were studied. The rise of the nonmagnetic Polypyrrole shell in comparison with nanoparticles magnetic in the core resulted in a linear drop in  $M_s$ ,  $M_r$ ,  $K_1$ , and an almost stable value of  $H_c$ , which was found and explained. This could also explain why the composite samples'  $\sigma_{dc}$  values were higher than the pure models'. The frequency dependency of the composite models  $\epsilon'$ ,  $\epsilon''$ ,  $\sigma'_{ac}$ , and  $\tan\delta$  has been studied. ( $Z'-Z''$ ) graphs of composite models revealed various overlapping semi-circles based on electrical variables. The semicircles relate to series parallel resistor-capacitor circuits. Depending on the electrical conditions, the composite models' ( $Z'-Z''$ ) charts revealed distinct overlapped semi-circles parts. These semi circles relate parallel series resistor-capacitor pairings [31].

16. Scindia et al. in 2019 prepared the composite electrode of  $NiFe_2O_4$ /PPy using easy with low cost in-situ chemical oxidation route in an aqueous medium by the presence of surfactant and described of the structural,

spectral, electrical, morphological and thermal investigations. The super capacitive behavior of NFO/Polypyrrole material (electrode) had studied in an aqueous  $10^{-1}$ N sulfuric acid (electrolyte sol). The NFO/polypyrrole electrode has the maximum  $C_s$  of  $72.166 \times 10 \text{ F.g}^{-1}$ . The specific power, specific energy, as well as coulomb efficiency, respectively, were found to be  $61.8 \times 10^{-1} \frac{\text{kW}}{\text{kg}}$ ,  $519.5 \times 10^{-1} \frac{\text{Wh}}{\text{kg}}$ , with  $990.8 \times 10^{-1} \%$ . This material electrode demonstrated electrochemical stabilization after  $(10^3)^{\text{th}}$  continuous CD cycles, and it was found to be an effective electrode substance for supercapacitors deices [32].

17. Chunping Xu et al. in 2019 used a one-step hydrothermal technique to synthesize polypyrrole-modified iron oxide nanomaterials. By performing the synthesis at various temperatures, the impact of the reaction temperature was examined. Nanohybrids manufactured were incorporated into electrodes to create supercapacitors devices. Controlling the (C+N)/Fe ratio on the surface, which is highly sensitive on reaction temperature, allowed for effective tailoring of the electrochemical characteristics. Ppy@Fe<sub>2</sub>O<sub>3</sub>-180°C nanohybrid had the highest electrochemical performance, with a noticeable capacitance amount of  $56 \times 10 \text{ F.g}^{-1}$  at a current density of  $5 \text{ A.g}^{-1}$  in addition to an extraordinary cycling stability of  $9.73 \times 10\%$  after  $2 \times 10^4$  cycles of CD at  $4 \times 10 \text{ A.g}^{-1}$  [33].

18. Yağan in 2019: Use aqueous solution comprising monomer and oxalic acid, polypyrrole was electropolymerized potentiodynamically on a prepassivated Fe electrode. PPy was electropolymerized between  $3 \times 10^{-1}$  and  $8 \times 10^{-1}$  Volt against saturated calomel electrode (SCE) at a scan rate about  $20 \frac{\text{mV}}{\text{s}}$ . CV, GCD cycling, plus EIS were utilized to investigate the electrochemical features of PPy coated Fe electrode. The greatest specific capacitance of a Fe

electrode covered with PPy is  $2280 \text{ F.g}^{-1}$  [34].

19. Liu et al. in 2019 used a simple and quick microwave approach to manufacture polypyrrole nanofiber (PPyNF)/NiO<sub>x</sub> composites. The samples were analyzed using differential scanning calorimetry and thermal gravimetric analysis, as well as X-ray photoelectron spectroscopy and SEM. PPyNF/NiO<sub>x</sub> nanocomposites were also electrochemically analyzed via GCD, CV, as well as EIS methods. They are the higher Cs ( $65.7 \times 10 \text{ F.g}^{-1}$  at  $0.05 \times 10 \text{ A/g}$ ), which means that it can be used in supercapacitors [35].
20. Wang et al. in 2020 synthesized polypyrrole/Fe<sub>2</sub>O<sub>3</sub> nanocomposites using a one-step hydrothermal method in order to improve polypyrrole's gas response to NO<sub>2</sub>. XPS, HRTEM, and TG studies have all shown the presence of ferric oxide in composites. At 50°C, the polypyrrole/Fe<sub>2</sub>O<sub>3</sub> sensor has a good selectivity for NO<sub>2</sub> and a fast response. The polypyrrole/Fe<sub>2</sub>O<sub>3</sub> materials are easier to manufacture in comparison to other polypyrrole/metal oxide materials, and the gas sensor has a greater response of 220.7%, a lower detection limit of 0.1 ppm, and a strong linear relationship when NO<sub>2</sub> concentrations vary from 0.1 ppm to 10 ppm. In comparison to pure polypyrrole and Fe<sub>2</sub>O<sub>3</sub>, the gas response is dramatically improved [36].

### 1.3 Aims of the study

- 1- By simple methods and effective cost, polypyrrole nanofibers (PPy-NFs) were synthesized by chemical oxidative polymerization technique. Nanoparticles of  $\text{Zn}_{0.8}\text{Mn}_{0.2}\text{Fe}_2\text{O}_4$  were prepared by the co-precipitation method and followed by heat treatment in an autoclave reactor As well as, (PPy-NFs/ $\text{Co}_{0.8-x}\text{Zn}_x\text{Mn}_{0.2}\text{Fe}_2\text{O}_4$ ) nanocomposites from PPy-NFs and ferrite nanoparticles.
- 2- Studying the influence of zinc replacement in magnetite structure on the structural properties, magnetic properties, optical properties, and performance efficiency of manufactured devices.
- 3- Selection of optimal conditions for the preparation of samples and their uses in electrochemical applications such as Supercapacitors, Optoelectronic Applications, and Gas Sensing.

## **Chapter Two**

### **Theoretical and Basic Concepts**

#### **2.1 Introduction**

This chapter delves into theoretical notions and nanotechnology, as well as the qualities, features, and applications of the materials studied. The methods used to prepare and measure them, as well as an explanation of the relationships and mathematical equations are also employed here.

#### **2.2 Nanoscience and Nanotechnology Background**

Progress in the field of material science can be used to chart the evolution of human civilization. Materials science is a convergence of physics, chemistry, biology, chemical engineering, mechanical, civil, and electrical engineering, among other science and engineering disciplines. One of the oldest branches of applied and engineering science is material science. With the advancement of materials science expertise, such as Nanotechnology, new branches are emerging. The introduction of nanoscience and nanotechnology as a leading technology of the twenty-first century has only accelerated material science's development. Nanoscience and nanotechnology are now synonymous with material science and technology. These nanostructure materials frequently have very strong electrical, optical, magnetic, and chemical capabilities that their bulk counterparts don't have, which could lead to new and intriguing applications.

The term "nano" should be defined as the beginning point for this presentation. The definition of this prefix is one-billionth ( $10^{-9}$ ) component, which originated in Greek and was used to denote anything extremely small.

As a result, at minimum 1 spatial dimension between one and hundred nanometer is described as Nanoscale. [37].

Nanoscience is the research of nanoscale materials that makes use of nanotechnology to characterize their unique chemical, physical, as well as biological features [38]. Nanotechnology is the advancement of miniaturization techniques that begins at the macroscopic level and leads to the nanoworld. It also encompasses the atomic, molecular plus supramolecular manipulation of functional systems to produce new nanoscale materials, structures, components, as well as systems. Nanomaterials are chemical compounds or materials with at minimum one external dimension on the nanoscale. Nanostructured materials are created to provide novel and distinctive qualities such as electrical, mechanical, and optical when comparing to the identical material without nanoscale properties [39].

### **2.3 Nanomaterials Classification**

Nanomaterials can be classified in a variety of ways, depending on their dimensions, for example (among others). They can be divided into four types based on their dimensions [40]:

1- 0D Nanomaterials: The essential feature of zero-dimensional nanomaterials is that they have all three dimensions compacted to nanoscale (are smaller than 100 nm). Nanoparticles are an example of this [41].

2- 1D Nanomaterials: Nanotubes, nanorods, and nanowires are all included in this category. One nanostructure dimension in these nanostructures would be larger than a nanometer [42].

3- 2D Nanomaterials: One of the three dimensions of thin films and surfaces has been compressed to the nanoscale. Metals, metallic oxides, and carbon-based materials can all be used to make them. Coatings and thin multilayer films, nanowalls, and nanosheets are among the nanofilms involved [43].

4- 3D Nanomaterials: These nanomaterials can be seen in structures and electronics, with all of these dimensions being outside the nanometer scale. Bulk materials made up of discrete blocks with dimensions ranging from 1 to 100 nanometers [44].

#### **2.4 Conducting Polymers (CPs)**

Polymer has long been thought of insulator, and their insulating qualities have led to applications. In fact, any electrical conduction in polymers caused by weakly coupled ions has previously been regarded as an unfavorable phenomenon. Polymers, on the other hand, have evolved from essentially passive substance as coat and vessel to effective matter with beneficial optic, electric, power storage, in addition to mechanical features [45]. Because of their conjugated  $\pi$ -bonds, conductive polymers are polyconjugated organic polymers that transmit electricity. Metallic conductivity or semiconductor properties are possible in such compounds. The ability to produce conductive polymers, primarily by dispersion, is their greatest benefit [46]. Conductive polymers are not thermoplastics, which means they cannot be thermoformed. They are organic compounds, like insulating polymers. They have good electrical conductivity, but mechanical qualities are not comparable to those of other commercially available polymers. Organic synthesis methods and advanced dispersion techniques can be used to fine-tune the electrical characteristics. Conducting polymers have limited electrical conductivity in their pure form (undoped or pristine state) and act like an insulator or a

semiconductor. By treating these polymers with proper oxidizing or reducing chemicals, they can be transformed to polymer salts with electrical conductivities comparable to metals. Synthetic metals are these types of doped polymers with high electrical conductivities [47].

## **2.5 Classification of Conducting Polymers**

Conducting polymers are classified into the following types:

### **2.5.1 Intrinsically Conducting Polymers**

#### **2.5.1.1 Conjugated Conducting Polymers**

They're conducting polymers with single and double bonds that alternate. The sigma ( $\sigma$ -bonds) is single bonds. One bond and one  $\pi$ -bond combine to form a double bond. The overlap of  $sp^2$  hybrid orbitals in conjugated polymers forms a sigma bond backbone. Carbon atoms' leftover orbitals overlap sideways with neighboring  $P_z$ -orbitals to create  $\pi$ -bonds. The electrons involved in the creation of  $\pi$ -bonds are delocalized throughout the polymer chain, resulting in the formation of valence and conduction bands. When the energy gap between the two bands is small, electrons being excited from the low-energy valence band to the high-energy conduction band, which results in higher conductivity [48].

#### **2.5.1.2 Doped Conducting Polymers**

Conjugation isn't enough to turn a polymer into a conductor. A technique known as 'Doping' can raise the conductivities of pristine polymers (pure conjugated polymers) from insulating. Dopants are introduced into polymer films or powders by exposing them to dopant vapors or solutions, or by

electrochemical oxidation and reduction. P-type dopants and n-type dopants are the two varieties of dopants [49].

## **2.5.2 Extrinsicly Conducting Polymers**

### **2.5.2.1 Conductive Element Filled Polymers**

To make the polymer conduct, an insulating type of polymer is mixed with appropriate conducting components such as carbon black, metallic fibers, metallic oxides, and so on. Percolation threshold refers to the smallest amount of conducting element necessary to make an insulating polymer conduct [50].

### **2.5.2.2 Blended Conducting Polymers**

It is produced by blending a regular polymer with a good conducting polymer. This approach produces polymers with improved physical, chemical, electrical, and mechanical properties, as well as the ability to be processed more readily [50].

## **2.6 Synthesis of Conducting Polymers**

Conducting polymer synthesis and characterisation has become a major focus of research in polymer and materials science [51]. New and unique architectures, good processibility, simplicity of synthesis, better defined three-dimensional structures, stability, solubility, and other factors will all play important roles in the synthesis of conducting polymers. Because conducting polymers are organic materials, their synthesis allows for some flexibility, allowing us to leverage device input and combine end-use needs to tune conducting polymer features. The flexibility of synthesis will be critical to the commercialization of conducting polymers. Chemical and electrochemical methods can be used to make conducting polymers.

### **2.6.1 Chemical Polymerization**

The reaction is carried out in this approach by mixing the monomer with various oxidants in an aqueous solution. The chemical reaction can be carried out for various lengths of time and at various temperatures. It is affordable, and the product yield is extremely high. The monomer is oxidized to a cation and then coupled to generate a coupled radical. The polymer chain is formed by the repeating of these radicals. Dispersion polymerization, interfacial polymerization, and vapor phase polymerization are examples of these processes. Interfacial polymerization is ex-situ, whereas dispersion is in-situ. This process uses a variety of oxidizing agents, including  $\text{FeCl}_3$ , ammonium persulphate, potassium paramagnet, and potassium dichromate, among others. In the case of vapor phase polymerization, the polymerization takes occur on an oxidizing agent-coated desirable surface. When the substrate is exposed to monomer vapour, a polymer film is formed on the necessary surface. Chemical polymerization can also be controlled by adjusting various factors like as concentration, reaction temperature, amount of doping, and so on [52]. In terms of acceptable conductivity qualities, for chemical polymerization of pyrrole monomer, ferric chloride and waters been discovered to have been the ideal oxidizing and solvents.

### **2.6.2 Electrochemical Polymerization**

The best films are made using the standard electrochemical process, which uses a divided cell with a working electrode, a counter electrode, and a reference electrode [53]. For the creation of electroactive/conductive films, the electrochemical polymerization process is commonly used. Conditions for electrolysis include current density, electrode potential, solvent, as well as electrolyte. can all be easily changed to influence the film properties. The

thickness of the polymers can also be controlled. The concentration and nature of the monomer/electrolyte, the solvent, cell parameters, electrode, temperature, applied voltage, and pH all affect the feature (quality) and yield of the film during electrochemical synthesis. As a result, it's difficult to optimize all of the parameters in a single experiment. Chemical polymerization, on the other hand, does not necessitate the use of any specific equipment and is a rather straightforward and quick procedure. The oxidant polymerization synthesizing pyrrole monomer using chemical oxidants in non-aqueous or aqueous solvents via chemical vapor deposition to generate PPy polymer as small particles, is the chemical polymerization approach [54].

## **2.7 Principles of Electrical Conduction**

### **2.7.1 Band Theory**

A material's electrical conductivity is determined in part by its electronic structure. The band theory provides the most reasonable explanation of a material's electrical structure. Atomic electrons can only have definite or quantized energy levels, according to quantum mechanics. The energy levels, on the other hand, form bands in the crystal lattice, where the atoms are closely spaced. The valence band is made up of the most occupied electronic levels, while the conduction band is made up of the least populated levels. The electrical characteristics of traditional materials are defined based on how the bands are filled. No conduction is noticed when the bands are totally filled or empty. When the band gap is narrow, thermal excitation of electrons from the valence band to the conduction band causes conductivity at room temperature, as it does in traditional semiconductors. Whenever the band gaps become broad, thermic energy being inadequate to drive electrons over the gaps at room temperature and the materials become insulators. Since the valence band

covers the conduction band in conductors, there is no band gap, resulting in strong conductivity (Figure 2.1) [55,56].

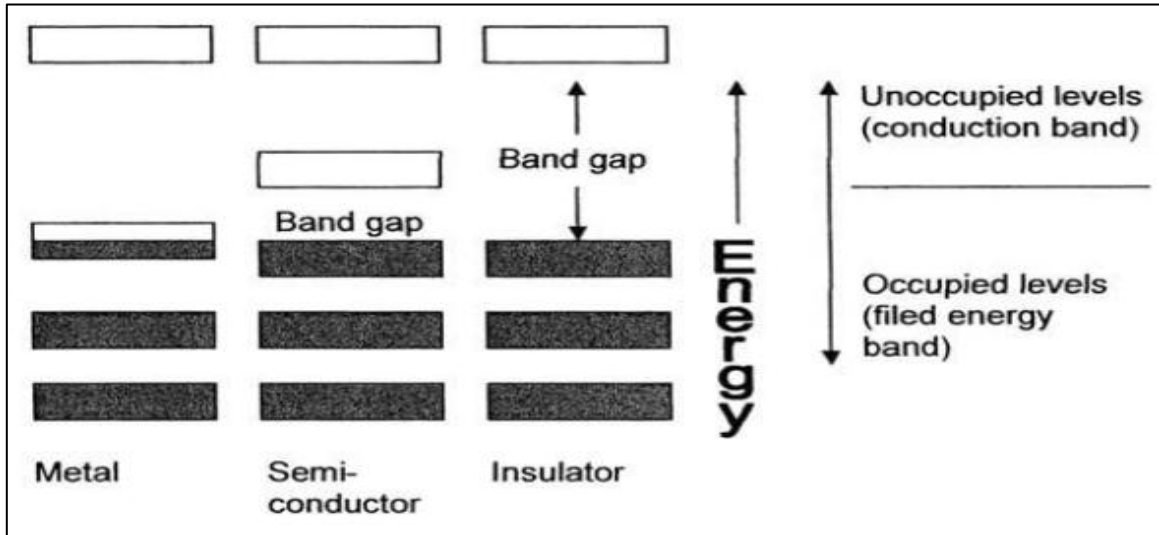


Figure 2.1: Band Theory.

### 2.7.2 Conduction by Reinforcement

Doping is the process of converting insulating polymers (for example, polyacetylene) into good conductors (Figure 2.2) [57]. Doping occurs when electron donors such as sodium or potassium (n doping, reduction) or electron acceptors such as  $I_2$ ,  $AsF_5$ , or  $FeCl_3$  (p doping, oxidation) create charge-transfer complexes. The doped polymer backbone becomes negatively or positively charged as a result of the process, with the dopant generating oppositely charged ions ( $Na^+$ ,  $K^+$ ,  $I^{3-}$ ,  $I^{5-}$ ,  $AsF_6^-$ ,  $FeCl_4^+$ ). An electric potential causes counterions to move in and out, allowing the polymer to transition between a conducting, doped state and an insulating, undoped state [58].

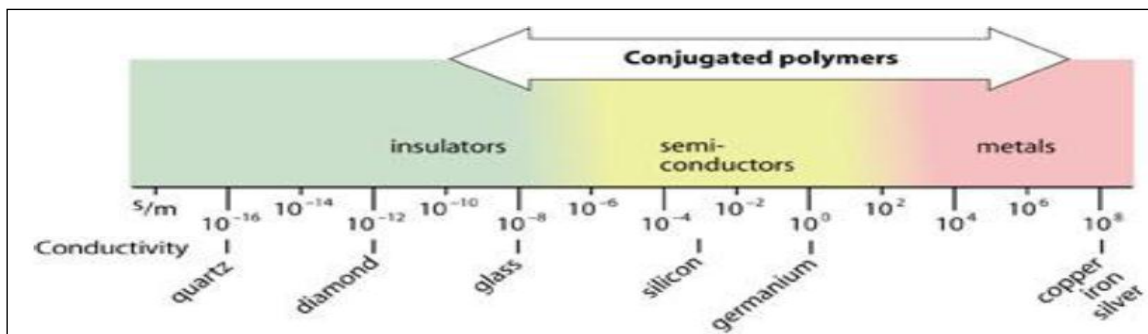


Figure 2.2: Conductivities of insulator, semi-conductors, metals and CPs.

### 2.7.3 Polaron and Bipolaron Model

When charge-carrying species (electrons or holes) are spinless, the band theory is insufficient to explain electrical conduction in electrically conducting organic materials like polypyrrole. Despite the fact that the mechanism is unknown, polaron and bipolaron conduction is now thought to be the most common mode of charge transfer in organic materials. This theory is also used to explain why doping causes color shifts to intensify dramatically. A bipolaron is a diradical dication, whereas a polaron is a radical cation which is somewhat delocalized across several monomer parts. The generation of polarons and bipolarons is determined by the doping level. Polarons are formed when doping levels are low, while bipolarons are formed when doping levels are high. Polarons and bipolarons can both migrate along polymer chains and are mobile [58].

The electrical conductivity of PPy conductive polymers is one of the most essential features of analytical applications. In the ground state, Polypyrrole polymer is a CPs with a non-created CB. (conduction band). Polarons and bipolarons are the major charge carriers in these polymeric conductors, as previously stated. The PPy conduction mechanism has yet to be clearly

identified due to the polymer's continual structural disruption [58]. Carrier hopping plus charge transport along polymer chains are the most frequently accepted views of conductivity in these systems [59]. With a complete valence band and an empty conduction band separated by an energy gap, electrically conducting polymers are known as semiconductors. Doping these polymers results in the formation of additional levels in band gap, allow electrons to traverse to these novel bands as well as boosting substance conductivity. Bipolarons have a significant influence on the electrical and transport properties of conductive polymers. The bipolaron concept was shown to provide an uniform and consistent picture of conductive doped polymer characteristics, and the potential of a narrow energy gap. The positive charges produced on the polymer's backbone serve as charge carriers for electrical conductivity (called polarons). It moves by travelling across sections of a conjugated polymer chain and hopping charges between chains [59].

Electrical conductivity is determined by the number among these charges in the substance and their relative transit. The charge on the polymer is stabilized by a counterion (in this instance, an anion, as well defined as a doped anion), while remains relatively immobile within the dry substance. As a result, instead of being ion conductors, these polymers are electrical conductors. As a result, the electrical conductivity of PPy is determined by the amount of carriers and their mobility. When the amount of doping is increased, the density of charge carriers increases. The nature and concentration of the electrolyte or counterion [60], plus the doping amount, current densities, and synthesis heat, all affect the conductivity of PPy films [61].

## **2.8 Conductive Polymers Activation**

To obtain high conductivities, CPs have been doped using several ways [62]. Undoped polymers have been known to be insulators, however their conductivity can shift from insulating to metallic when doped. However, because of their distinct chemical structures, [CPs] have a fundamentally different doping process than their inorganic counterparts. Charges are transported between dopants in the polymer during redox reactions, resulting in the creation of charge carriers [63]. The dopant has two functions: it removes electrons from the CP and adds electrons to the CP backbone. Doping causes electrons to be taken from the valence band's highest occupied molecular orbital (HOMO) (oxidation) or transferred to the conduction band's lowest unoccupied molecular orbital (LUMO) (reduction). Charge carriers being created inside the polymer including polarons, bipolarons, or solitons as a result of this oxidation/reduction process [64]. The electron passes directly from the polymer's HOMO to the dopant species in p-type doping, in the backbone, creating a hole. In negative category doping, in contrast, electrons from of dopant species migrate to a polymer's LUMO, growing electron density. Consequently, doping can be used to control the density and mobility of charge carriers [65].

## **2.9 Applications of Conducting Polymers**

Anti-static coatings, LED (light emitting diode), sensors, electromagnetic shielding, corrosion resistance, solid electrolytes for capacitors, and other applications have made conducting polymers one of the most widely investigated materials in recent decades [66]. Because conducting polymers have outstanding mechanical qualities and can be obtained in thin sheet form, a great number of gas sensors are made of them [67]. Because their electrical

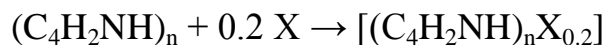
and optical properties may be controlled by doping-dedoping processes, CPs have been extensively studied as chemical sensors, optical sensors, and biosensors. Another application of conducting polymers that has recently emerged is conversion coatings for metals [68, 69]. The conducting polymer serves a dual purpose here, protecting the cathode while also resisting erosion. By shrinking the size of bulk devices, the development of nanometer-sized conducting polymers has increased their utility. In addition, combining these polymers with traditional polymers creates new classes of polymeric materials with improved electrical and optical properties. EMI shields, electronic packaging, display devices, and electrodes are all possible applications for these composites [70].

### 2.10 Polypyrrole Polymer (PPy)

Polypyrrole is a nitrogen-based ringed heterostructure with five members. The oxidation of pyrrole monomer results in the production of a conjugated chain with overlapping  $\pi$ -orbitals and positive charges, which is known as polypyrrole [71]. Chemical stability and electrical conductivity are provided by PPy's heteroatomic and  $\pi$ -conjugated backbone structure. Figure 2.3 depicts the structure of PPy. Some of the first examples of PPy were reported in 1919 by Angeli and Pieroni, who reported the formation of pyrrole blacks from pyrrole magnesium bromide.[72] Since then pyrrole oxidation reaction has been studied and reported in scientific literature. Different methods can be used to synthesize PPy, but the most common are electrochemical synthesis and chemical oxidation [73]. Chemical oxidation of pyrrole:



The process is thought to occur via the formation of the pi-radical cation  $C_4H_4NH^+$ . This electrophile attacks the C-2 carbon of an unoxidized molecule of pyrrole to give a dimeric cation  $[(C_4H_4NH)_2]^{++}$ . The process repeats itself many times. Conductive forms of PPy are prepared by oxidation ("p-doping") of the polymer:



The polymerization and p-doping can also be effected electrochemically. The resulting conductive polymers are peeled off of the anode. Cyclic voltammetry and chronocoulometry methods can be used for electrochemical synthesis of polypyrrole [74]. Because of its high electrical conductivity and outstanding environmental stability, polypyrrole has been researched extensively among conducting polymers [75]. Gas sensors, electrical devices, electrodes for rechargeable batteries and supercapacitors, electromagnetic shielding materials, corrosion-resistant materials, electrochromic devices, membranes, and other possible uses have all been investigated. Furthermore, the PPy nanostructure with a greater surface-to-volume ratio provides more efficient reactivity, which is critical in the development of highly efficient organic electronics [76]. Its ability to generate biologically suitable polymer matrix makes it a promising candidate in a variety of biomedical applications, including biosensors [77], tissue engineering [78], and implantable bio-devices. Its capacity to modify its redox activity has also increased its utility in solar cells, medication delivery systems, and other applications [79].

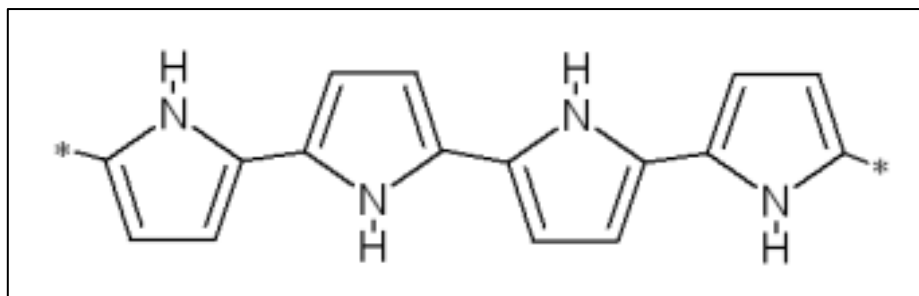


Figure 2.3: Structure of PPy in the neutral state.

## 2.11 Composites

A composite is a substance made up of two components or more, such as supporting (reinforcing) agent or filler as well as a matrix binder that works well together. When these components are combined, a new material with distinct traits and properties emerges. The components do not dissolve in the synthetic assemblage; rather, they merge into one another to function in harmony. The parts besides the interface between them could typically be physically identifiable, even though they operate as if they are one substance. The interface between the components, in general, controls the composite's behavior and properties. The qualities of the composite cannot be achieved by any of its components functioning alone because it is a completely new material with unique characteristics [80].

Nanocomposite is an important term that we must address. A nanocomposite is a composite material with at least one of its constituents' diameters on the nanoscale scale [81]. The chemical composition of each component and how the components interact determine the difference in optical, catalytic, or conductive capabilities between nanocomposites and their constituent components. This interaction is greatly influenced by the interface, size, form, and structure of each component. The qualities of the composites

should be equivalent to a simple sum of the attributes of the individual elements in extreme circumstances, where there is no or minimal interaction between the components. The features of the composite system can differ significantly from the simple sum of the attributes of the separate components when the interaction between the elements is strong. As a result of the high interaction, the individual components' properties are lost, and new features emerge [82].

The composites could be classified in several different methods. The structural components of composites can be classified as fibrous, laminar, or particulate. Fibrous composites are made up of fibers in a matrix, laminar composites are made up of layers in a matrix, and particulate composites are made up of particles in a matrix. Ceramic matrix composites, Polymer matrix composites, carbon-carbon matrix composites, metal matrix composites, as well as intermetallic composites, or hybrid composites can all be classified based on the type of matrix [83].

## **2.12 Nanoparticle/Polymer Composite Techniques**

Making good polymer matrix nanocomposites samples is a difficult task that requires a lot of time and effort. To make polymer matrix nanocomposites, researchers have used a variety of processing techniques. The physical and chemical differences between each system, as well as the various types of equipment available to researchers, make creating a universal technique for making polymer nanocomposites difficult. Depending on the processing efficiency and desired product properties, each polymer system requires a unique set of processing conditions to be formed. In general, the

various processing techniques do not produce comparable results. Several methods were used to create polymer nanocomposites. Nanofillers can be dispersed in polymers in three different ways. Solution mixing, melt blending, and in-situ polymerization are some of the techniques used.

### **2.12.1 Mixing of Solutions**

To get beyond the melt mixing method's limitations, both the polymer with the particles are dispersed or dissolved in sol. This method allows for surface modification without drying, which reduces particle agglomeration. The nanoparticle/polymer solution can be cast into a solid after dissolution, or the nanoparticle/polymer composite can be isolated using solvent evaporation or precipitation methods. For further processing, conventional techniques can be used [84].

### **2.12.2 Melt blending**

Nanofillers are incorporated into the polymer matrix while it is still molten in this method. Nanoparticles are dispersed inside the polymer matrix via extrusion and injection molding. This approach effectively prepares thermoplastic nanocomposites [85]. In between the voids of nanofillers, polymer chains are intercalated or exfoliated. Because no solvent is required for the manufacture of nanocomposites, the melt intercalation process is a preferred method in industry. The downside of the melt mixing method is that it causes tension and produces high temperatures [86].

### **2.12.3 In-Situ Polymerization**

Dispersing nanoparticles in a monomer solution or monomer, subsequently polymerizing the resultant mixture using traditional polymerization

procedures, is described as in-situ polymerization. The polymer can be grafted onto the particle surface using this approach. In-situ polymerization has been used to process several different forms of nanocomposites. PPy particle/amphiphilic elastomer nanocomposites [87], magnetite coated MWNTs/PPy composites [88], in addition to PPy/silver composites are just a few instances of in-situ polymerization. Optimum filler dispersion in the monomer is crucial for in-situ polymerization. The settling process is faster in a liquid than in a viscous melt because dispersion becomes simpler inside a liquid [89], this frequently necessitates modification of the particle surface. Polymer nanocomposites with molecular-level particle dispersion can be produced via in-situ polymerization. Finally, the functionalized nanoparticles become a chemically linked part of the polymer matrix, improving both mechanical and physical properties significantly. Other manufacturing procedures have been developed in addition to these three major processing methods. Solid intercalation, the sol-gel technique, and others are examples [90].

### **2.13 Magneto Polymeric Materials**

Composites made up of multiple materials can combine the qualities of their constituent materials into a single composite. Conducting polymers and ferrite materials can give unique or improved features for a variety of applications. Magneto polymeric materials are the name for these materials. Conducting polymerferrite composites with a well-organized structure offer a new functional combination of organic and inorganic materials [91]. The size scale of the component phases and the degree of mixing between the two phases have a significant impact on the characteristics of magneto polymeric nanocomposites [92]. These characterizations are critical for defining

properties such as electrical conductivity, magnetic behavior [93], catalytic effects, microwave absorption [94], drug delivery capacity and controllable release [95], and their applications in optoelectronics, rechargeable batteries, corrosion equipment, micro cavity resonance [96], biomedical markers, vibration damping media [97], wireless radio communication systems, and sensors in various technological applications [98]. Furthermore, in order to optimize their microwave absorption or electromagnetic shielding capabilities, these nanocomposites should have low dielectric loss. Conducting polymers are known to successfully shield electromagnetic waves created by an electric source, whereas only magnetic materials can effectively shield electromagnetic waves generated by a magnetic source, especially at low frequencies. As a result, the conducting polypyrrole–magnetic ferrite composites can be employed as microwave absorbers and EMI shielding from a variety of electromagnetic sources. Different polypyrrole (PPy) and ferrite nanocomposites have recently been produced, and each of these composites has shown to have highly intriguing features [99].

## **2.14 Magnetic Nanoparticles**

Nano magnetism is a branch of physics that studies the magnetic characteristics of objects with at least one dimension in the nanometer range. The study of the properties and uses of the magnetism of solitary nanoparticles, Nano dots, nanowires, thin films and multilayers, as well as macroscopic samples containing nanoscopic particles, is included in the scope of nano magnetism. Nanostructured materials are materials that contain particles, films, and other structures on the nanometric scale. Magnetic nanoparticles display a range of distinct magnetic phenomena that differ significantly from those seen in bulk. They have attracted a lot of attention

since these features can be useful in a range of applications [100], such as magnetic fluids, catalysis, bio-applications, magnetic resonance imaging, and data storage [101].

Many factors influence the magnetic characteristics of nanoparticles, the most important of which are chemical composition, crystal lattice type, particle size and shape, morphology, and particle interaction with the surrounding matrix and neighboring particles. The magnetic characteristics of materials can be altered by altering the size, shape, content, and structure of nanoparticles [102]. Magnetic nanoparticles have gotten a lot of attention in the last two decades. Magnetic nanoparticles for industrial and biomedical applications have been developed as a result of fundamental research into nanostructures, physical and magnetic properties, and toxicity (among other things).

### **2.15 Origin of Magnetism**

A magnetic field surrounds a source of potential and has a contoured sphere of influence or field, similar to gravitational and electrical fields. Magnetic dipoles are what cause the magnetic potential to exist. The orbital (L) and spin (S) motions of the electron are responsible for magnetism (as Figure 2.4). The motions of electrons, which are considered magnetic dipoles, produce very small currents. The atoms canceled each other out due to their random orientation. However, when apply magnetic field, the magnetic dipoles are net aligned, and the medium becomes magnetically polarized [103].

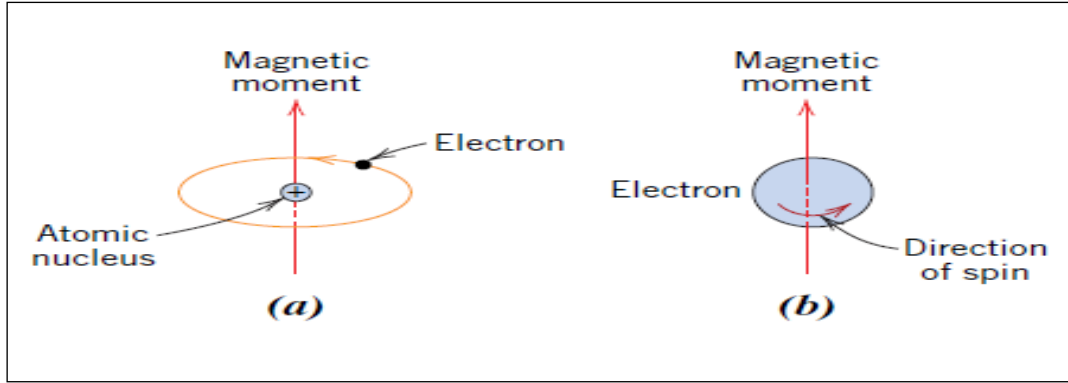


Figure 2.4: Demonstration of the magnetic moment associated with  
 (a) an orbiting electron and (b) a spinning electron.

Magnetic field  $H$  measures the intensity of the magnetic field (magnetic field strength) that magnetizes the substance. The magnetic induction or magnetic flux density inside the magnetized material that is subjected to a  $H$  field is known as  $B$ . The units of  $H$  are Amperes per meter or (A/m). Teslas [or webers per square meter or (Wb/m<sup>2</sup>)] are the units for  $B$ . The flux density ( $B$ ) and magnetic field strength ( $H$ ) are related by:

$$B = \mu H \dots\dots\dots (2.1)$$

The parameter  $\mu$  is called the permeability, which is a property of the specific medium through which the  $H$  field passes and in which  $B$  is measured. The permeability has dimensions of webers per ampere.meter (Wb/A.m) or henries per meter (H/m) [104].

Magnetization  $M$  refers to the magnetic moment for every unit of volume of a magnetic substance. (and has also units of A/m), The summation of the magnetic moments  $m_j$  for each volume of unit is the magnetization  $M$ .

$$M = \sum_{\text{volume}} m_j \dots\dots\dots (2.2)$$

The magnetic properties for magnetic materials are explained by the amount and sign of magnetization (M), as well as the manner M fluctuates with H. Magnetic susceptibility  $\chi$  is the ratio of these 2 variables.

$$\chi = M/H \dots\dots\dots (2.3)$$

The substance magnetization M is expressed via the formula:

$$B = \mu_0 (H + M) = \mu_r \mu_0 H = \mu H \dots\dots\dots (2.4)$$

The permeability of free space is  $\mu_0 = 4\pi \times 10^{-7}$  H/m, and B and H are denoted in Tesla (T) and A/m, respectively. The relative permeability of the substance is denoted by  $\mu_r$ , and it can be seen from the formulas (2.3) and (2.4) that:

$$\mu = \mu_0 (1 + \chi) \dots\dots\dots (2.5)$$

The values of  $\chi$  and  $\mu_r$  describe the magnetic features of a material [105].

## 2.16 Types of Magnetic Materials

**1. Diamagnetism:** Diamagnetic materials are those that lack elementary magnetic dipoles. A diamagnetic substance's magnetic susceptibility ( $\chi$ ) is negative, somewhat less than 1, and on the order of  $10^{-5}$ . There is no discernible diamagnetism fluctuation with temperature. Each atom has a net zero magnetic dipole moment in the absence of a magnetic field. The angular velocities of the electronic orbits are modified when a magnetic field is applied. These induced magnetic dipole moments align with the applied field in the opposite direction. In superconductors and artificial materials, diamagnetism can have a significant effect. Diamagnetic materials are repelled

by both magnet poles. Diamagnetic materials include water, gold, bismuth, copper, zinc, and mercury [106].

**2. Paramagnetism:** Every atom or molecule in some substances has its own permanent magnetic moment due to its orbital plus spin magnetic moments. In the absence of an exterior magnetic field, individual atomic magnetic moments are oriented arbitrarily. The net magnetic moment and magnetization of the material are both zero. However, when an exterior magnetic field is applied, the singular atomic magnetic moments tend to align in direction of the applied exterior magnetic field, resulting in a nonzero weak magnetization. The phenomenon is known as paramagnetism, and these materials are paramagnetic [107]. Materials possessing a permanent magnetic dipole moment, such as atomic or molecule structures with an odd number of atoms, or ions, or ions electrons in vacant orbitals, can exhibit paramagnetism. Because the overall spin of the system cannot be zero, paramagnetism is present in atoms, molecules, and lattice defects with an odd number of electrons. Paramagnetism can be found in metals, free atoms and ions with a partial fill inner shell, transition elements, plus a little compounds containing an even number of electrons, such as O element [108]. When a magnetic field is applied to paramagnetic materials, they attract each other. Diamagnetism can be found in paramagnetic materials, however the effect is usually minor. When these materials are exposed to an external magnetic field, they exhibit modest magnetism; however, once the field is removed, thermal motion disrupts the magnetic alignment. The magnetic susceptibility of these materials to an external magnetic field is extremely modest and positive. Thermal agitation (as temperature rises) disturbs the magnetic moments alignment, requiring larger fields to achieve the same magnetization. As a

result, as the temperature rises, the paramagnetic susceptibility falls. The temperature has an inverse relationship with paramagnetic susceptibility. It is as follows [107]:

$$\chi = C/T \dots\dots\dots (2.6)$$

It is referred to as the Curie Law of Paramagnetism. Hence,  $\chi$  denotes susceptibility of paramagnetic, T denotes absolute heat, as well as C denotes the Curie constant. Al, Ca, Mg, in addition to Na are instances of paramagnetic elements.

**3. Ferromagnetism:** The occurrence of spontaneous magnetization is called by Ferromagnetism. It is a significant number of molecule magnetic moments aligned in a proper orientation in the solid. Below only a certain temperature, referred to as the Curie temperature, does ferromagnetism appear. The moments have arbitrarily orientated above Curie temperature, resulting the net magnetization its value zero [108]. Ferromagnetism can occur whenever atoms were organized in a structure and their magnetic moments react with align them parallel to one another. Even in the absence of an external magnetic field, a ferromagnetic substance displays spontaneous magnetization because of align of their magnetic moments [107]. The transition metals Fe, Co, and Ni are examples of ferromagnetic materials, although additional elements and alloys containing transition or rare-earth elements are also ferromagnetic due to their unfilled 3d and 4f shells. To an external magnetic field, these materials had a positive as well as great magnetic susceptibility. They are attracted for magnetic fields and can keep their magnetic qualities after the exterior magnetic field has been eliminated. When heated ferromagnetic substances, the degree of alignment of the atomic magnetic moment diminishes due to thermal agitation of the atoms; finally, the thermal

agitation becomes so strong that the material becomes paramagnetic. The temperature of this transition is the Curie temperature,  $T_c$  (Fe:  $T_c = 770\text{ }^\circ\text{C}$ , Co:  $T_c = 1131\text{ }^\circ\text{C}$  and Ni:  $T_c = 358\text{ }^\circ\text{C}$ ). Above  $T_c$  the magnetic susceptibility varies according to the Curie-Weiss law [107].

**4. Antiferromagnetism:** In antiferromagnetic materials, the dipole moments remain equivalent, but neighboring dipoles are pointing in opposite directions. [109]. There are also materials having more than two sub lattices plus triangular, canted, and spiral spin arrangements. Antiferromagnetic matters have a non-zero modest magnetic moment as a result of these characteristics [110]. They exhibit a low positive susceptibility on the order of paramagnetic substance at all temperatures, whereas its susceptibilities fluctuate by a unusual way. Néel was the main developer of antiferromagnetism theory in 1932. At ambient temperature, chromium is the only element that exhibits antiferromagnetism [109]. Antiferromagnetic substances are comparable to ferromagnetic substances, however the anti-parallel arrangement or alignment for atomic moments is caused by the exchange contact between nearby atoms. As a result, the magnetic field cancels out, and the material behaves similarly to a paramagnetic material. The lower magnetic susceptibility of antiferromagnetic materials is due to the antiparallel arrangement of magnetic dipoles in these materials. These substances, as the ferromagnetic matters, turn paramagnetic at temperatures above the Néel temperature,  $T_N$  (Cr:  $T_N = 37\text{ }^\circ\text{C}$ ).

**5. Ferrimagnetism:** Ferrimagnetic materials have both spin-up and spin-down components in their spin structure, however one of those orientations have a net magnetic moment not equal zero [111]. In antiferromagnetism, the atoms magnetic moments on neighboring sub lattices remain opposed each other; nevertheless, the opposing moments are uneven in ferrimagnetic

materials. Over than two sub-lattices, as well as spiral or triangular arrangements for sub-lattices, could account for this magnetic moment [112]. Only compounds with more complicated crystal structures than pure elements exhibit ferrimagnetism. As ferromagnetic substances, these substances spontaneously magnetize below a certain temperature referred to the as Curie temperature ( $T_c$ ). Although the magnetic susceptibility of ferrimagnetic and ferromagnetic substances is identical, the arrangement or alignment of dipole moments is vastly various. Certain double oxides of iron and other metals, known as ferrites, are the most important ferrimagnetic compounds. Diamagnetism, paramagnetism, ferrimagnetism, antiferromagnetism, and ferromagnetism are all depicted in Figure. 2.5.

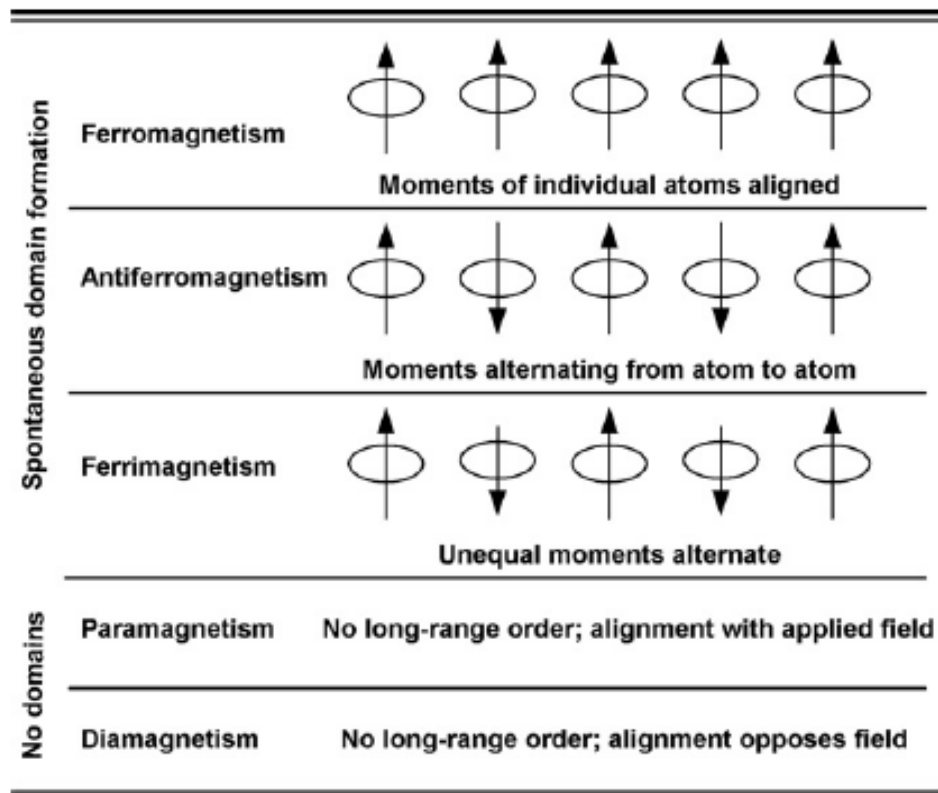


Figure 2.5: Different types of magnetic behavior [113].

## **2.17 Ferrites**

Engineers and scientists have long been fascinated by ferrites with unusual magnetic and electrical properties. Ferrites include non-conductive ferrimagnetic ceramic chemical substances made up of iron and oxygen or iron oxides such as  $\text{Fe}_3\text{O}_4$  (magnetite) and  $\text{Fe}_2\text{O}_3$  (hematite), in addition to metal oxides. Ferrites materials are hard, nonconductive, and brittle, just like most other ceramics. Ferrites are employed in magnetic recording medium as well as ferrite cores for transformers, permanent magnets, and microwave devices [114]. The ferrites are frequently classed as "soft" or "hard" depending on their magnetic characteristics.

### **2.17.1 Soft Ferrite**

Magnetic materials with a low coercivity field and a high resistance are known as soft ferrites. Through a modest magnitude of magnetic field, they are easily magnetizable and demagnetizable. The magnetization of these materials (soft ferrites) can quickly reverse due to their low coercivity and high resistivity, resulting in low hysteresis and eddy or foucault's currents losses. These substances are thus potential options for great frequency uses due to their little loss. Manganese-zinc, cobalt-zinc, nickel-zinc ferrite, as well as others are frequent models of soft ferrites. Due to its great saturation magnetization, great permeability, plus great resistivity, ferrites can be utilized in important applications like transformer cores, recording heads devices, inductors, as well as more other uses [115].

### **2.17.2 Hard ferrite**

Hard ferrites are permanent magnets with high coercivity and retentivity after being magnetized. The much more essential feature of these ferrites are

great coercivity, that is defined as a great values for magnetic crystallite anisotropy energy. They are difficult to magnetize or demagnetize with a modest amount of field. These materials are a great magnetic permeability and are composed of Fe and Sr or Ba oxides. This magnet can store a greater magnetic field than iron and they are frequently found in household products, particularly refrigerator magnets. Barium, Strontium, plus cobalt ferrite are models of hard ferrites which are utilized in a variety of applications such as permanent magnets, magnetic recording, and so on [116].

## 2.18 Crystal Structure of Ferrites

Ferrites are classified into three groups based on their crystal structure and chemical compositions: Spinel Ferrites, Garnets, and Hexagonal Ferrites are the three types of ferrites.

### 2.18.1 Spinel Ferrites

The standard formula for materials that crystallize in the spinel structure, or structures that are substantially related to it, is  $AB_2O_4$ , in which the oxygen atoms are packed closely together in a cubic structure, with the A and B cations occupying tetrahedral and octahedral lattice positions, respectively. Cubic ferrites belong to the  $Fd3m$  space group. The cubic unit cell has 56 atoms, with 24 cations occupying eight of the 64 tetrahedral sites (A sites) and sixteen of the 32 octahedral sites (B sites). 32 oxygen anions are compacted in a cubic close-packed arrangement. As a consequence, the cell has eight formula units ( $Z=8$ ), which correspond to  $(Me_8^{2+})_A[Me_{16}^{3+}]_B(O_{32}^{2-})_O$ . The divalent metal cations that inserted in ferrites structure were separated into those that preferred B-sites (Cobalt, Nickel, iron) and those that preferred A-sites (Manganese, Zinc) (figure 2.6) [117].

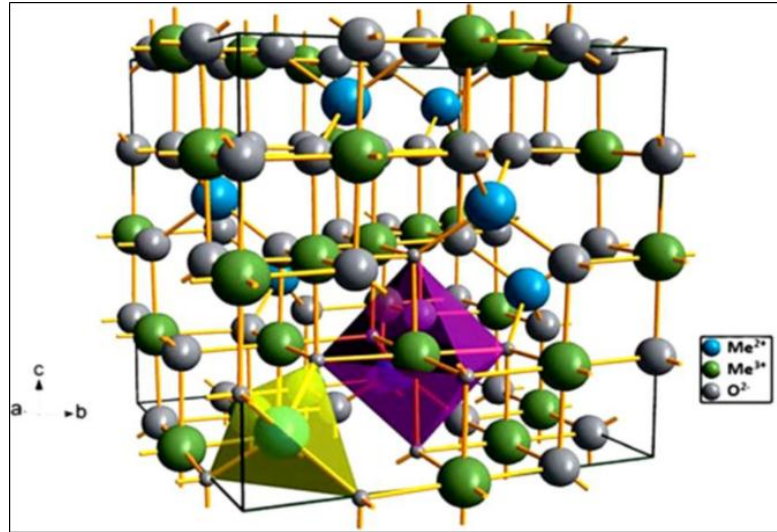


Figure 2.6: Unit cell of spinel structure  $\text{MeFe}_2\text{O}_4$  [117].

The general formula for spinel ferrites is  $M_{\delta}^{2+}Fe_{1-\delta}^{3+}[M_{1-\delta}^{2+}Fe_{1+\delta}^{3+}]O_4^{2-}$ . Square brackets denote octahedral sites, while tetrahedral sites are indicated by cations before the square brackets.  $\delta$  is the inversion degree that determines ferrite categorization. The spinel compounds can be categorized into three groups based on the cation distribution over distinct crystallographic locations [118]:

### 2.18.1.1 Normal Spinel Ferrites

Normal spinel structure, where all  $\text{Me}^{2+}$  ions occupy A sites; structural formula of such ferrites is  $\text{Me}^{2+}[\text{Fe}_2^{3+}]O_4^{2-}$ . This type of distribution takes place in zinc ferrites  $\text{Zn}^{2+}[\text{Fe}^{2+}\text{Fe}^{3+}]O_4^{2-}$ . This type of spinel ferrites is schematically illustrated in figure 2.7 [119].

### 2.18.1.2 Mixed Spinel Ferrites

When the cation  $\text{Me}^{2+}$  and  $\text{Fe}^{3+}$  occupied each A and B places, the ferrites has a mixed spinel configuration; the construction formula base of theses

ferrites are  $M_{1-\delta}^{2+}Fe_{\delta}^{3+}[Me_{\delta}^{2+}Fe_{2-\delta}^{3+}]O_4^{2-}$ , where  $\delta$  is the degree of inversion. This sort of structure is represented by  $MnFe_2O_4$ , which has an inversion degree of  $\delta=0.2$  and hence has the structural formula  $M_{0.8}^{2+}Fe_{0.2}^{3+}[Me_{0.2}^{2+}Fe_{1.8}^{3+}]O_4^{2-}$  [119,120]. Figure 2.7 shows a schematic representation of this form of spinel ferrite.

### 2.18.1.3 Inverse Spinel Ferrites

All  $Me^{2+}$  ions are in B-positions, and  $Fe^{3+}$  ions are evenly distributed across A and B-sites in this inversed spinel structure: structural formula of these ferrites are  $Fe^{3+}[M^{2+}Fe^{3+}]O_4^{2-}$ . Magnetite  $Fe_3O_4$ ,  $NiFe_2O_4$  and  $CoFe_2O_4$  have inversed spinel structure [119]. Half of the  $Fe^{3+}$  is put in A-sites and the other half in B-sites in inversed ferrites. The moments of magnetic for bivalent cation  $Me^{2+}$  in B-places are mutually reparation, plus the ferrite's resultant moment is attributable to these magnetic moments. Figure 2.7 shows a diagram of this form of spinel ferrite.

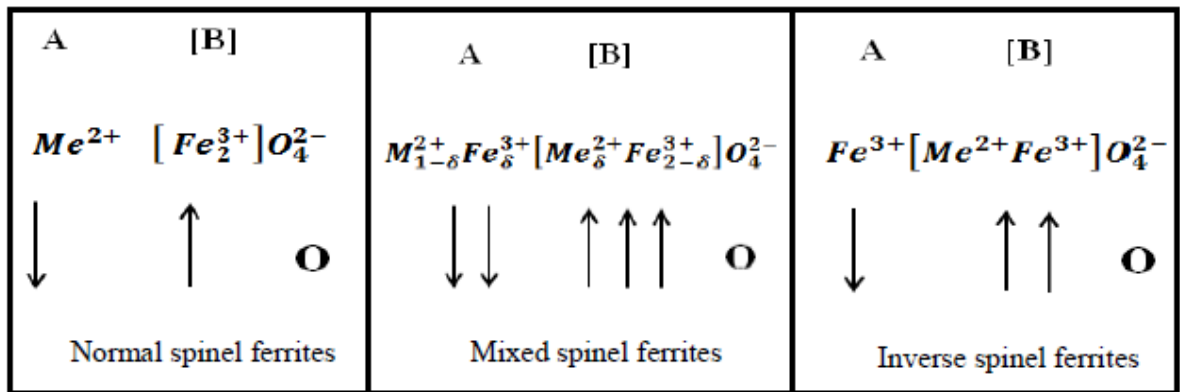


Figure 2.7: cation distribution in normal spinel ferrites, mixed spinel ferrites and inverse spinel ferrites [119].

### 2.18.2 Garnet Ferrites

Garnets have the typical formula  $\text{Me}_3\text{Fe}_5\text{O}_{12}$ , wherein Me is indeed a rare earth metals ion such as Gd, La, or Y. The unit cell of cubic consists of eight form units, or (160 atoms) and is characterized as a structure arrangement of about 96  $\text{O}^{2-}$  plus the cations of interstitial. The YIG (Yttrium iron garnet), also defined as  $\text{Y}_3\text{Fe}_5\text{O}_{12}$ , is well-known garnets [121].

### 2.18.3 Hexagonal Ferrite

Jonker and his colleagues investigated the hexagonal structures of ferrimagnetic oxides. Based on chemical formula and crystal structure, hexagonal ferrites are divided into numerous forms.  $\text{MFe}_{12}\text{O}_{19}$  is their typical formula, with M commonly being Ba, Sr, or Pb. Barium ferrite,  $\text{BaFe}_{12}\text{O}_{19}$ , is the most important hexagonal ferrite. Because of their great coercivity, hexagonal ferrites are often used like remaining (permanent) magnets. They're used on a regular basis. The oxygen ions in such ferrites have a closed packed hexagonal crystal structure. Its ferrite hexagonal lattices are similar the spinel having closely packed oxygens, but there are also metal ions with same atomic radius as oxygens (oxygen ions). Hexaferrites get more ions than ferrite of garnet and are generated through oxygen ion substitution. Barium, strontium, and lead make up the majority of these bigger ions [122].

### 2.19 Superparamagnetism

If the MNP's size falls below a crucial threshold, it may be constituted of a single magnetic domain. It may also exhibit superparamagnetic activity if the temperature is above a certain temperature known as the blocking temperature ( $T_B$ ) [123]. Small magnetic nanoparticles, in other words, show superparamagnetism, which has numerous essential features, including zero

(or minimal) coercivity. As the size of magnetic particles grows larger, the thermal energy available to allow free rotation of their spins becomes insufficient. As a result, nanoparticles over a particular size, known as the "superparamagnetic limit," begin to exhibit ferromagnetic properties [124]. Because the cost of forming a domain wall in a single-domain surpasses the reduction in magnetic energy, ferromagnetic particles must be downsized to be tiny enough to form monodomain. The magnetism of a small monodomain ferromagnetic particle is usually limited to lie either antiparallel or parallel to a specified direction. This could be attributable to a number of factors, such as magnetocrystalline anisotropy or shape anisotropy [125]. However, the assumed particle's energy density comprises  $K\sin^2\theta$ , where  $K$  is the anisotropy constant, which quantifies the energy density associated with this anisotropy, and is the angle formed by the magnetization and this specific axis.

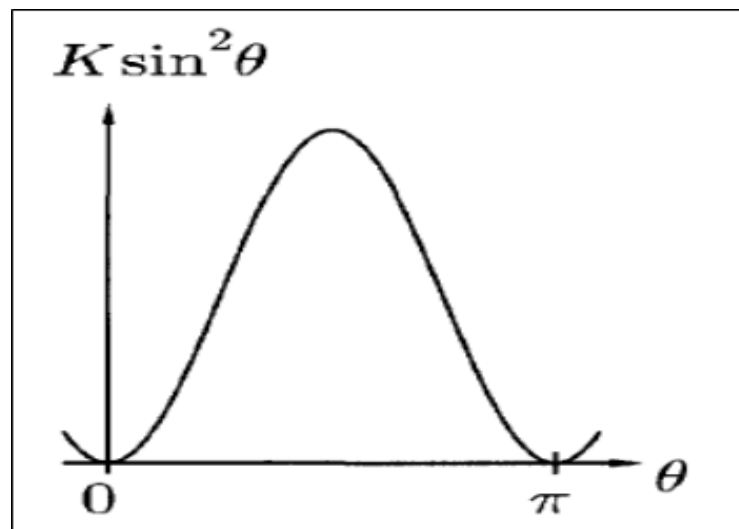


Figure 2.8: The energy density of a magnetic particle contains a term  $K\sin^2\theta$ , the energy is minimized when  $\theta = 0$  or  $\pi$  [126].

As a result, when  $\theta=0$  or  $\pi$ , the energy is minimized (Figure 2.8). To reverse a particle's magnetization from  $\theta = 0$  to  $\pi$  or from  $\pi$  to  $0$ , it needs an activation energy of  $E = K V$ . Thermal fluctuations can potentially turn the magnetization of very small particles, such as those with  $KV$  smaller than  $k_B T$  [127].

Assume that the distribution of these small ferromagnetic nanoparticles in a nonmagnetic medium is uniform, and that the particles are suitably spaced enough to avoid inter-particle interactions. For  $k_B T \gg K V$ , the system will behave like a paramagnet, but the individual moments will be huge in terms of the number of atomic moments in each given direction, each group enclosed within a ferromagnetic particle. As a result, such a system is known as a superparamagnet [128]. Moments within particles can fluctuate rapidly at high temperatures, the Néel relaxation time, which is exponentially dependent on the energy barrier and thermal energy, is given by the following equation [129]:

$$\tau_N = \tau_0 \exp\left(\frac{KV}{k_B T}\right) \dots\dots\dots (2.7)$$

Where  $\tau_0$  typically equal  $10^{-9}$ s is the characteristic relaxation time. The fluctuations slow down as the sample cools (Figure 2.9), the relaxation time grows, and the system tends to stop since it is significantly longer than the measuring time  $\tau$  of the provided laboratory instrument. Substituting the real time to monitor magnetic properties with a SQUID-magnetometer  $\tau = 100$ s into equation 2.7 yields the following equation [130]:

$$T_B = \frac{E_B}{25K_B} = \frac{KV}{25K_B} \dots\dots\dots (2.8)$$

The anisotropy prevents the spins from fluctuating below  $T_B$ , but the thermal energy overcomes the bonding of the total moment of the particles above  $T_B$ , causing the system to become superparamagnetic [130].

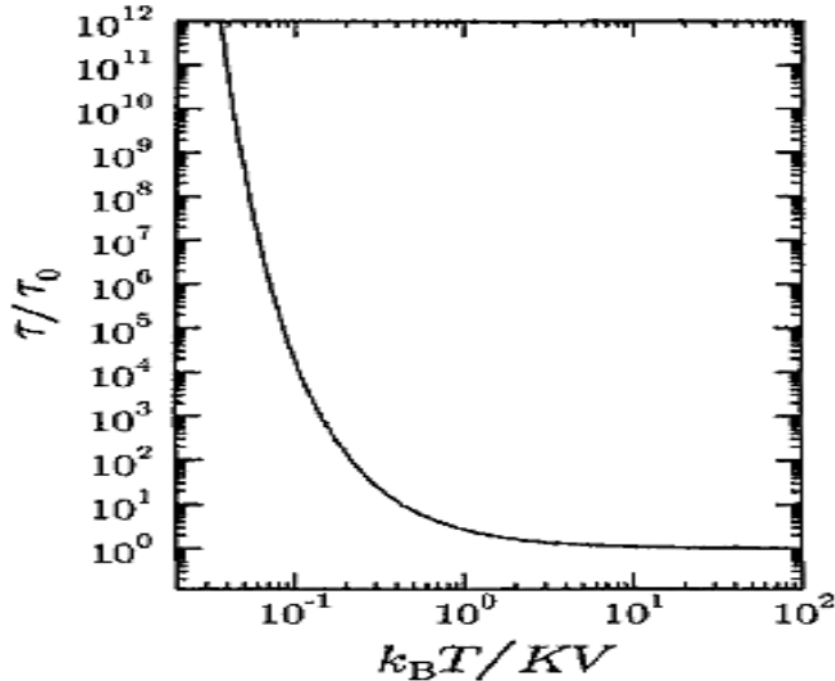


Figure 2.9: The dependence of the relaxation time ( $\tau$ ) as a function of temperature  $T$  (scaled by  $k_B/KV$ ) according to equation (2.7). As a result, as the temperature drops, the fluctuations slow down ( $\tau$  increase) [126].

## 2.20 Magnetic Domains

Under Curie temperature  $T_C$ , the bulk magnetic substances are separated into several tiny sections and domains, that are each totally magnetic. In other words, inside each domain, all moments are aligned in the same direction [131]. The domains are separated by domain walls, which have a specific width and energy connected with its production and presence. The mobility of domain walls is a common way to reverse magnetization [132]. Magnetization is defined as the vector sum including all magnet moments for atoms in a bulk

solid per unit volume for substance. Due to the solid bulk is made up of domains, are depicted in Fig. 2.10, the magnetization magnitude is generally lower than when aligned every atomic spin magnetic moments. Each domain has its own magnetization vector, which arises from the alignment of atomic magnetic moments within the domain. All of the material domains' magnetization vectors may not be aligned, resulting in a drop in overall magnetization. When the material's length scale is very small, however, the number of domains drops until there is only one domain when the material's characteristic size is below a critical size [133].

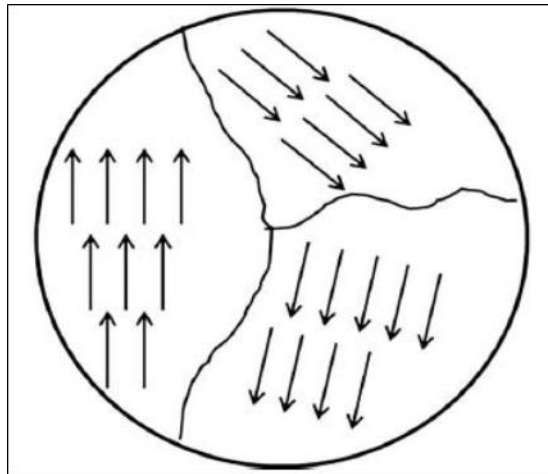


Figure 2.10: Magnetic domains in a bulk material [133].

A multi-domain structure can be found in massive magnetic particles, with domain walls separating regions of uniform magnetization. The balance between magnetostatic energy ( $\Delta E_{MS}$ ), which increases proportionately with material volume, and domain wall energy ( $E_{dw}$ ), which increases correspondingly with the interface area between domains, drives the formation of domain walls. If the sample size is reduced, a threshold volume is reached below which it takes more energy to construct a domain wall than to support the single-domain state's exterior magnetostatic energy. This crucial

dimension is usually a few tens of nanometers in size and is determined by the material parameters. The contribution of different anisotropy energy factors influences it.

The critical diameter ( $D_c$ ) of a spherical particle, below which it exists in a single-domain state, is reached when  $(\Delta E_{MS}) = (E_{dw})$  [134].

$$D_c \approx 18 \frac{\sqrt{AK_{eff}}}{M^2 \mu_0} \dots\dots\dots (2.9)$$

Where  $A$  is the exchange constant,  $K_{eff}$  is anisotropy constant,  $\mu_0$  is the vacuum permeability, and  $M$  is the saturation magnetization.

The angle of magnetization between two neighboring domains with the wall serving as a boundary can be used to classify domain walls.

- **180° wall:** A 180° domain wall represents the boundary between two domains with opposite magnetization (see Figure 2.11 (a)).
  - **90° wall :** A 90° domain wall represents the boundary between two domains with magnetization being perpendicular to each other (see Figure 2.11(b)).
- [135]

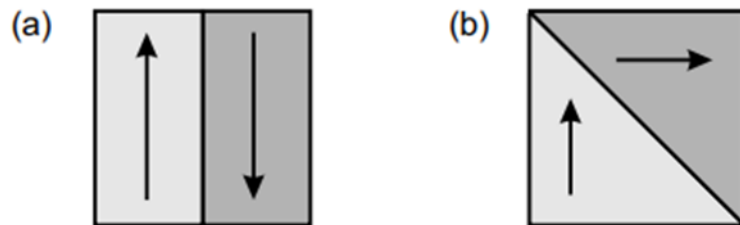


Figure 2.11 (a) 180° and (b) 90° domain wall.

## **2.21 Properties of Magnetic Materials**

### **2.21.1 Magnetic Hysteresis**

Hysteresis curves are well-known in ferromagnetic materials, as shown in figure 2.12. When a ferromagnetic material is exposed to an external magnetic field, the exterior field aligns the atomic dipoles. After the exterior field has been canceled, an alignment portion is retained, and the matter becomes magnetic. The connections among magnetic flux density  $B$  with magnetic field strength  $H$  in such materials are nonlinear. If the relation between the two is set as a function of increasing  $H$ , it shall pursue curves until furthermore rises in  $H$  result in no alteration in  $B$ . Magnetic saturation are the term for this condition. If the magnetic field is reduced linear, the plotted relation shall pursue an altered curve back the  $H$  to zero, where it shall be displaced of the initial curve via a magnitude known as the Retentivity or Remanence. When this connection are plotted for applied  $H$ , it forms an S-shaped loop. The amount of hysteresis, which is proportional to the material's coercivity, is described by the width of the center part of the S. When the applied electric current to the operating coil is removed, the leftover magnetic field continues to attract the armature, which may cause a relay to be slow to release [136].

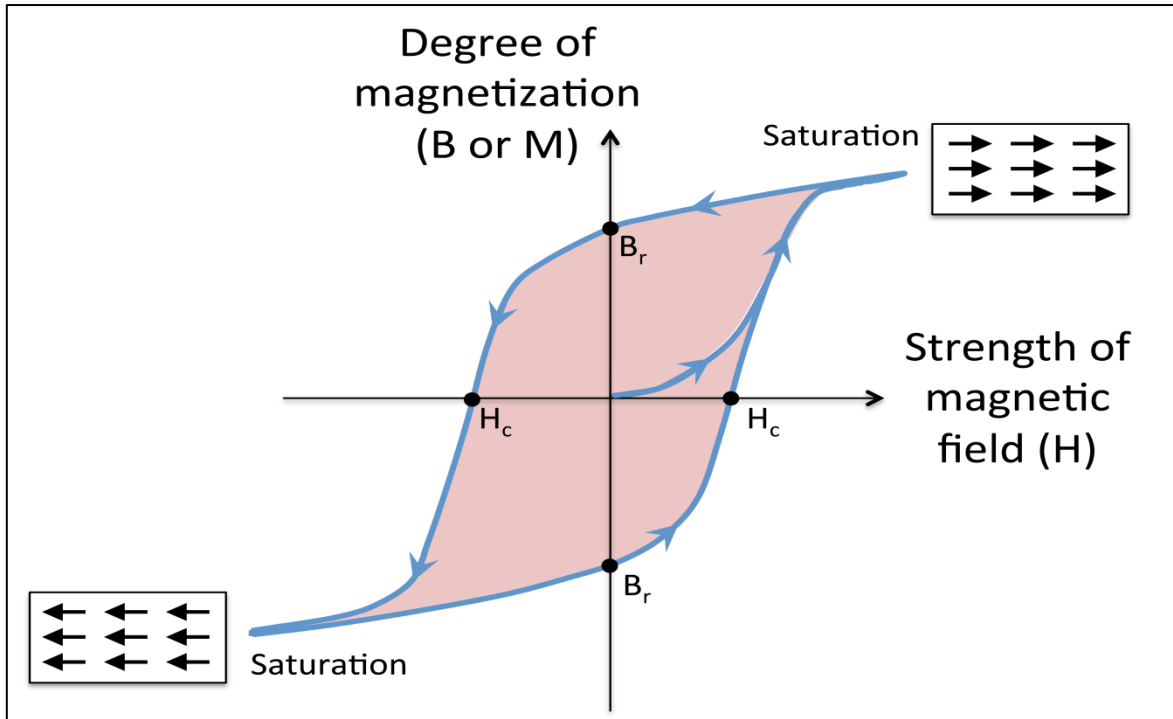


Figure 2.12: hysteresis loop [137].

### 2.21.2 Saturation Magnetization

The saturation magnetization ( $M_s$ ) is a measurement of a material's maximal field generation capacity. This is determined by the strength or intensity of the dipoles on the constituent atoms the substance, as well as how densely atoms get packed combined. The atomic dipole moment is influenced by the atom's nature and the compound's overall electronic composition. The packing density of the atomic moments is impacted by the crystalline phases and the existence of any impurities (non-magnetic elements) within the composition.  $M_s$  shall as well determined by how well those aligned moments in ferromagnetic materials at limited temperatures, as thermal vibration of the atoms causes misalignment of the moments and a decrease in  $M_s$ . Even at zero Kelvin, not all of the moments in ferrimagnetic materials align parallel, therefore  $M_s$  is dependent on both the relative alignment of the moments and

the temperature. Though that word is commonly utilized to denote magnetism inside a singular magnetic domain [138], Also known as spontaneous magnetisation, saturation magnetization ( $M_s$ ).

### **2.21.3 Remanence (Retentivity)**

It is the measurement of a magnetic material's remaining magnetic field  $M_r$  after the magnetizing force  $H$  is decreased to zero after saturation, or it may be stated as the magnetization left behind in a medium after an external magnetic field is eliminated.  $M_r$  is the symbol for it in equations. A hysteresis loop can be used to calculate the remanence magnitude at the loop's intersections with the vertical magnetization axis. It is dependent on the material's degree of magnetism before  $H$  is reduced to zero [139].

### **2.21.4 Coercivity**

The coercivity in ferromagnetic materials, also known as the coercive field, is the strength of the applied magnetic field required to reduce the magnetization to zero when the sample has been pushed to saturation in materials science. Coercivity is commonly expressed as ' $H_c$ ' and is measured in gauss, oersted, or ampere/meter units. A ferromagnetic substance is said to be a hard or permanent magnet when its coercive field is large [140].

### **2.21.5 Magnetic Anisotropy**

The dependence of the internal energy on the vector of spontaneous magnetization, which is represented by the term magnetic anisotropy, gives birth to hard and easy directions of magnetization. A system's overall magnetization will lean toward the easy-axis. The energy imbalance between the simple and hard axes is caused by spin-orbit interactions and long-range

dipolar coupling of magnetic moments. The spin-orbit coupling is responsible for intrinsic (magnetocrystalline) anisotropy, surface anisotropy, and magnetostriction, whereas dipolar contribution is responsible for shape anisotropy, which can be measured, for example, by assuming that the magnetic poles on the surfaces are distributed uniformly [141]. Anisotropy energies are typically in the range of  $10^2 - 10^7 \text{ Jm}^{-3}$ , which corresponds to per-atom energies of  $10^{-8} - 10^{-3} \text{ eV}$ . The anisotropy energy is bigger in low-symmetry lattices (of magnetic ions) and smaller in high-symmetry lattices. Magnetocrystalline and magnetostatic energies are the principal sources of anisotropy in bulk materials, but other types of anisotropies such as shape and surface anisotropy are important in tiny particles, thin films, and nanostructures [127,142]. This effect is seen in Figure 2.13 for a single cobalt crystal. Co's hexagonal crystal structure is easily magnetized in the direction of [0001] (Specifically, along on the c-axis.), However have difficult magnetization directions in the  $\langle 10\bar{1}0 \rangle$  type directions, that located on the primary plane ( $90^\circ$  from the simple direction). The anisotropy field,  $H_a$  (shown as figure 2.13), is a measure of magnetocrystalline anisotropy in the easy direction of magnetisation. It is the field necessary to spin all the moments in a saturated single crystal by  $90^\circ$  as one unit [136].

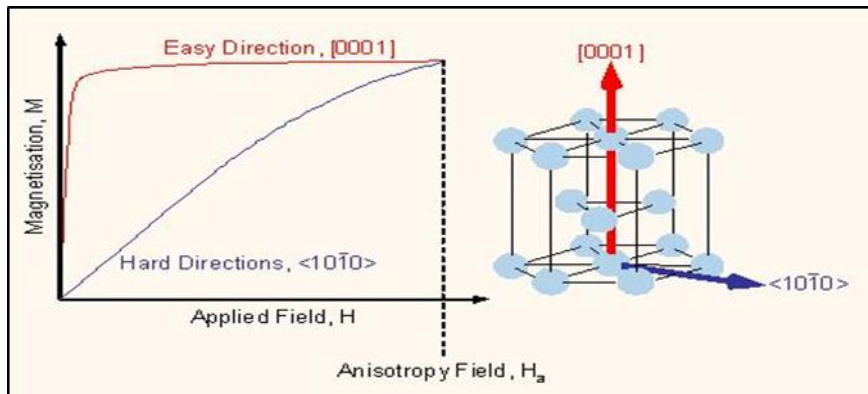


Figure 2.13: The magnetocrystalline anisotropy of cobalt.

## 2.22 Synthesis of Ferrite Nanoparticles

Magnetocrystalline, shape, and surface anisotropy energies all play a role in the magnetic characteristics of nanoparticles. It is consequently important to adjust the nature of the material, the form, and the size of nanoparticles in order to adapt magnetic characteristics of nanoparticles for numerous applications, such as magnetoelectric composites beneficial for sensor applications. Top-down (physical) or bottom-up (chemical or biological) approaches can be used to make magnetic ferrite nanoparticles. Many synthesis methods for ferrite nanoparticles are mentioned in the literature. Sol-Gel method [143], co-precipitation, hydrothermal synthesis [144], microfluidic [145], and thermal decomposition method [146] are the most prevalent approaches. Some of the methods employed in our project will be briefly discussed.

### 2.22.1 Co-precipitation Technique

This approach involves adding a base to aqueous  $\text{Fe}^{3+}$  salts and the matching divalent (binary) cation salts at either room temperature or increased temperature to produce ferrite nanoparticles. The  $\text{Fe}^{3+}/\text{M}^{2+}$  ratio, temperature, salt type, pH, plus surfactants presence are all parameters that affect the constitution, size, and nanoparticles shape. The below is indeed a typical reaction formula for the co-precipitation production of nanoferrite ( $\text{MFe}_2\text{O}_4$ ):



Where M can be  $\text{Fe}^{2+}$ ,  $\text{Mn}^{2+}$ ,  $\text{Co}^{2+}$ ,  $\text{Cu}^{2+}$ ,  $\text{Mg}^{2+}$ ,  $\text{Zn}^{2+}$  or  $\text{Ni}^{2+}$ . Highly alkaline media create goethite ( $\text{FeOOH}$ ) as an impurity alongside magnetite ( $\text{Fe}_3\text{O}_4$ ), [147], but high concentrations and temperatures favor the creation of spherical

nanoparticles because crystallographic growth direction is less selective [148]. This approach has been used to create a variety of ferrite nanoparticle morphologies, including spheres, [149] cubes, platelets [150], and rods [151]. Though the method can create nanoparticles on a large scale, one disadvantage has been that the particles had broad size distributions.

### **2.22.2 Hydrothermal or Solvothermal Method**

Because of its moderate operation conditions [152] and more adjustable particle size [153], the hydrothermal technique is commonly employed today. In addition to being hydrothermal, the synthesis is one-step, with no sintering or calcination required. This approach also has low cost, the ability to adjust the shape, size, and phase, and low energy usage [154]. This process provides a simple and environmentally benign way to make nanostructures including nanospheres, nanowires, and nanorods [155]. It's a phase in the co-precipitation synthesis process that involves an autoclave treatment within a Teflon container that can resist high temperatures [120]. A hydrothermal system uses high-pressure water at a temp above its boiling temperature (hundred Celsius) in a sealed autoclave vessel. Solvothermal method, as hydrothermal synthesis, employs the same approach but with a non-aqueous solvent. Higher temperature and pressure improve the solubility as well as reactive of the precursors, resulting in the creation of highly crystalline nanomaterials. This methods are utilized to make different nanoferrite, such as magnetite ( $\text{Fe}_3\text{O}_4$ ) [156], cobalt ferrite ( $\text{CoFe}_2\text{O}_4$ ), and nickel ferrite ( $\text{NiFe}_2\text{O}_4$ ) [157].

### 2.23 Autoclave Requirements

The closed system utilized in the hydrothermal process is called an autoclave. Because that includes a high-temperature hydrothermal solution, it must survive immense pressure and chemical attacks. As a result, the process's primary concerns are safety and upkeep. Many different kinds of autoclaves have indeed been developed, ranging from quartz tubes or pyrex for mild conditions to cold-cone seal types, flat-plate seal plus piston cylinder types, otherwise opposed anvil (diamond anvil) for drastic environments ( $>2 \times 10^3$  bar or more,  $10^3$  degrees Celsius). The general specifications for autoclaves are as follows

- 1-Acids, bases, as well as oxidizing agents do not react with it (Inert).
- 2-Simple to put together (or assemble) in addition to easy take apart (or disassemble).
- 3-Unlimited leak-proof capabilities at the specified pressure and temperature.
- 4-Durable enough to withstand extreme temperature and pressure experiments [158].

### 2.24 Conventional Capacitors and Supercapacitors

A traditional capacitor is a passive component that stores energy in the form of an electrostatic field rather than in chemical form. It is made up of two parallel electrodes (plates) that are separated by an insulating substance (dielectric). The capacitor is charged by passing voltage across the electrodes, causing positive and negative charges to migrate towards the opposite polarity electrodes' surfaces. When two plates are charged, a capacitor in a circuit acts as a voltage source, and current flows until the charge balance is complete

[159]. Supercapacitors and normal capacitors have similar underlying principles and schematics (see figures 2.14 and 2.15). An insulating dielectric material separates two conducting electrodes in a supercapacitor. The difference is that supercapacitor electrodes often have a substantially greater surface area than standard capacitor electrodes, and they are separated by an electrolyte solution in a separator. Because supercapacitors have a substantially larger surface area and a shorter distance between two electrodes, their capacitance and energy are dramatically higher than normal capacitors [160].

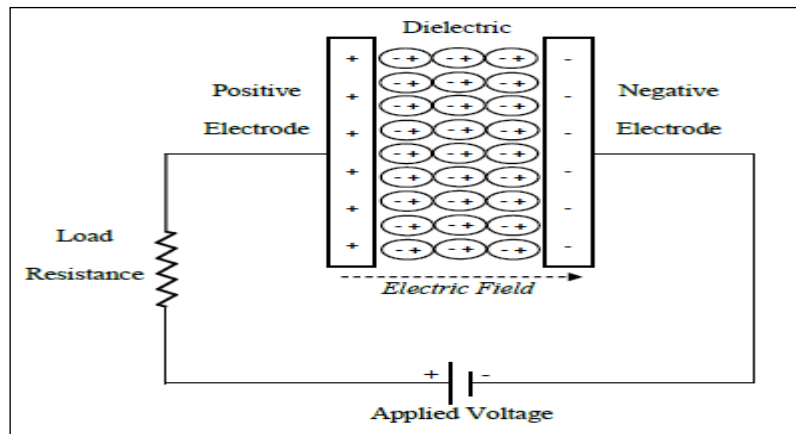


Figure 2.14: Schematic of a conventional capacitor [160].

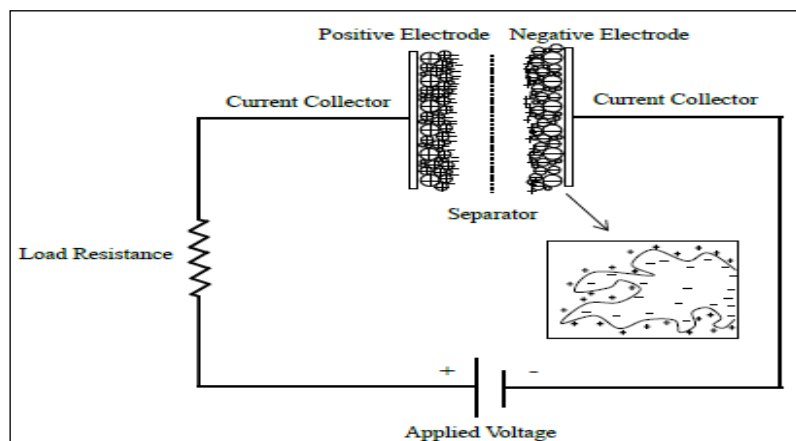


Figure 2.15: Schematic of an electrochemical double-layer capacitor [160].

## 2.25 Types of Supercapacitors

Supercapacitors are classified into different categories depend on their operation: electrochemical double-layer capacitors, pseudocapacitors, as well as hybrid capacitors. Most supercapacitors are distinguished by distinct charge-storage methods, which include electrostatic storage, reversible Faradaic redox, in addition to a connection between two [161].

### 2.25.1 Electrochemical Double Layer Supercapacitors (EDLCs)

Figure 2.16 depicts a schematic of typical charged EDLC. EDLC is electrochemical capacitor having a double layer that directly stores electrical energy, also known as the Helmholtz layer. In an EDLC, two electrodes are immersed in electrolyte and isolated by separator. Whenever a charging conductivity substance was placed inside an electrolyte sol to obtain a neutrality system, counter-charges of liquid phases collect nearer the charged surface [162]. Polarization of the (interfaces) contacts between the surface of the rigid electrode substance and the liquid electrolyte sol within the microscopic holes inside the electrode causes charges isolation. Surface dissociation, ion adsorption, as well as crystal lattice all contributes to surface charge [163]. EDLCs produce capacitance in the same way as a parallel plate capacitor does, which is referred to as double layer capacitance [164]:

$$C_{dl} = \frac{\epsilon_r \epsilon_0 A}{d} \dots\dots\dots (2.11)$$

Where  $\epsilon_r$  is the relative dielectric constant of the double layer.  $\epsilon_0$  is the permittivity of free space.  $d$  represents the effective thickness of the double layer with a surface area  $A$ .

When compared to traditional capacitors, the thickness of EDLC ranges is substantially less for the space between the platters for an dielectric capacitor [164]. At the electrolyte/electrode contact, an electro-chemical double-layer is employed to store charge electrically statically.

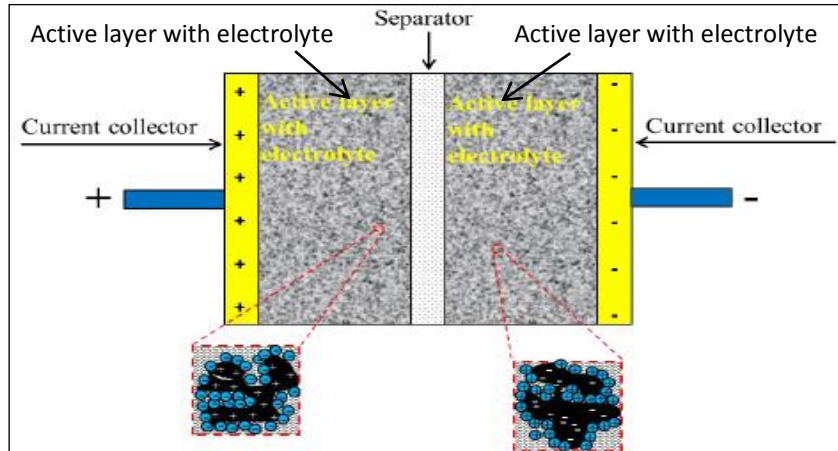


Figure 2.16: Schematic diagram of a typical charged EDLC.

Whenever voltage was apply across the electrodes, electrical charges are detached and joined to the oppositely charged sides. Furthermore, the oppositely charged ions in the electrolyte will permeate over the separator and into the porous electrode's surfaces. Every electrode side forms an electrolyte interface. However, there is no charge transfer due to the faraday process between the electrolyte and the electrode [162].

Since the beginning of the electrochemical capacitor's development, porous carbon has been used as an electrode material because of its high surface area, low cost, and excellent stability. Carbon materials like as carbon aerogels, ACs (activated carbons), graphene and carbon nanotubes have recently been employed extensively in EDLC electrodes to store charge. The overall capacitance of traditional capacitors is usually measured in  $\mu\text{F}$  or  $\text{pF}$ . In EDLCs, however, the combining of the huge available specific surface area

and atomic scale charge separation resulting in exceptionally great capacitance plus growing charge magnitude (electric energy) [165].

### 2.25.2 Pseudocapacitors

The second type of ES is the so-called pseudo capacitor. Unlike EDLCs, can electrostatically store charge, Charge is stored via pseudocapacitors faradically by transferring charge between the electrode and the electrolyte. Electrosorption, reduction-oxidation reactions, and intercalation processes are used to accomplish this. The existence of Faradaic processes may allow pseudocapacitors to reach higher capacitance characteristics and energy densities than EDLCs [166]. The most common pseudo-capacitive materials are transition metal oxides and metal nitrides ( $\text{RuO}_2$ ,  $\text{MnO}_2$  ...), hydroxydes and electroactive conductive polymers (PEDOT, PPy, PANi...) [167].

However, such capacitance arises as a result of certain applied thermodynamic circumstances, in which the electrode voltage (potential) is a continuous function of the charge passing thru the electrode, resulting inside a derivative  $dq/dV$ , that is equivalent to it and quantifiable as capacitance. The capacitance held by such devices is known as pseudocapacitance because it arises in a very difference manner than that of an EDLC, in which there is typically no charge transfer and capacitance arises electrostatically [168].

### 2.25.3 Hybrid Supercapacitors

Hybrid supercapacitors were created to combine the benefits of EDLCs and pseudocapacitors while resolving the majority of their drawbacks. Both of the preceding forms of supercapacitors had a symmetric design and used the same material for both electrodes. Without this symmetry, a new sort of supercapacitor termed "Hybrid capacitors" has been conceived, with two

different types of electrodes working in tandem. An interesting method for achieving intermediate performance between EDLCs and pseudo-capacitors is to combine an electrical double layer electrode with a pseudo-capacitive electrode. Due to faradaic exchanges on one of the electrodes, such capacitors can benefit from the excellent stability of a two layer system while obtaining larger capacitance values [169]. Via electrode construction, hybrid supercapacitors generally categorized into three categories:

i. **Asymmetric Hybrids** are formed by combining an EDLC electrode as well as a pseudocapacitor electrode [170]. In terms of cycling stability, asymmetric hybrid supercapacitors outperform identical pseudocapacitors. These offer greater power densities and energy than comparable size EDLCs.

ii. In contrast to asymmetric hybrids, **composite hybrid supercapacitors** utilize composite to integrate carbon substances with either MOs (metal oxides) or CPs (conductive polymer) as electrode matter [171]. Porous carbon compounds with such a large surface-area backbone can improve interaction with MOs (metal oxides) or CPs (conductive polymer) components as well as the electrolyte. Conductive polymer or Metal oxides could improve capacitance further through faradaic processes.

iii. **The Third Category Includes Battery-type Hybrid** that have two distinct electrodes: one for supercapacitors and one for batteries [172]. The energy density of batteries was higher than that of supercapacitors, whereas the power density of supercapacitors was higher than that of batteries. If battery-type hybrids could incorporate the greater energy density for batteries with the short charge time, specific power, reversibility, as well as cycle life for supercapacitors, they have a lot of promise to bridge the gap between standard supercapacitors and batteries. Hybrid capacitors are now being

studied in order to develop future breakthrough supercapacitors with high energy and power density while maintaining cycling stability.

## **2.26 Supercapacitors Applications**

Electrochemical capacitors, ultracapacitors, and electrochemical double-layer capacitors are some of the names given to supercapacitors. Supercapacitors can deliver a lot of power in a short amount of time, and they have a lot more charge/discharge cycles and a longer lifespan than batteries. Because of their adaptability, they've been used in a variety of applications [173]. It can be utilized to store energy in a range of applications, include tiny portable devices, transportation, or industrial machinery, and also hybrid electric (HEVs) plus electric vehicles (EVs) [174].

During engine start-up as well accelerating, supercapacitor may provide pulse energy to fuel cell or battery, as well as store energy for a brief amount of time during braking that could subsequently be re utilized when the vehicle resumed motion. Supercapacitor has also been used to replace or combine batteries as a source of electrical power for modern vehicles due to their high power delivery or absorption and comparatively high energy stored. [175].

The usage of supercapacitors have the apparent interest of decrease battery size as well as maintaining peak combustion motor performance, improving vehicle efficiency and greatly extending the life cycle of the primary source. Because of their tiny size, ability to have a longer cycle life, and capacity to swiftly charge and discharge.

Supercapacitors could be used in a variety of electrical microdevices due to their ease of downscaling. Important developments of such micro-systems could occur in the near future as a result of the generalization of Radio Frequency Identification, Micro Electro-Mechanical Systems, bio-sensors, and implanted medical devices. Maintenance-free energy storage devices that can be charged quickly and produce significant amounts of power would be extremely advantageous in light of these advances [176].

## 2.27 Electrochemical Characterization Techniques for ECs Applications

Cyclic voltammetry (CV), Galvanostatic charge-discharge (GCD), and impedance spectroscopy (EIS) are techniques for checking electrodes.

### 2.27.1 Cyclic Voltammetry (CV)

CV is a powerful and popular electrochemical technique used to obtain data about the thermodynamics of redox reactions, adsorption processes plus kinetics of heterogeneous electron transfer processes. [177].

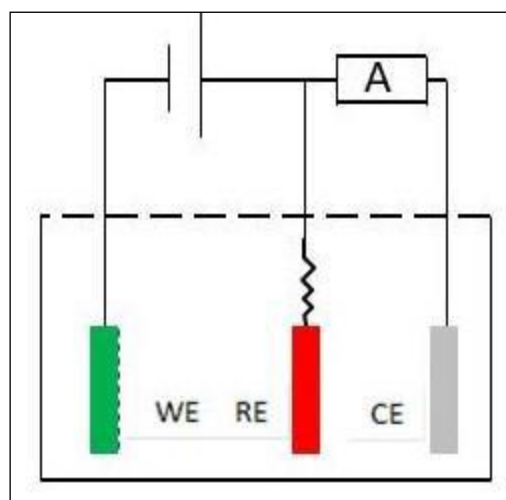


Figure 2.17: Equivalent circuit of three-electrode set-up [178]

As can be seen from (figure 2.17), The working electrode (WE), that is the electrode which has been measured and got in contacting with the electrolyte sol. , and a DC potential (direct current) apply to that circuit to promote charge transfer between both the electrodes and electrolyte sol., compose the CV cell. At a particular voltage, the reference electrode (RE) serves as the opposite half of the cell (cell half). To detect the voltage differential between the RE and WE layers, it is situated near the polarization's WE layer [178]. The CE (counter electrode) is in charge of supplying electrons so that current can pass between the WE and the CE. It's also in charge of supplying the current needed to balance the current flowing through the working electrode.

A cyclic voltammogram is produced by graphing the reported charge current of the counter electrode vs. the applying potential values. The cyclic voltammetry plot yields the following information:

- 1- The charge and discharge operation is reversible.
- 2-Indicators of any important phases in the electrode charge/discharge.
- 3-The average charge accumulated over a voltage window.
- 4-As the scan rates rise, so does the electrode's dynamic charge and discharge activity.

The behavior of the electrode material as either pseudocapacitive or electrochemical double layer capacitive systems is shown in Figure 2.18. The ideal EDLC cyclic voltammograms have a rectangular form [179]. This measurement reveals which charge storage is solely due to non-faradaic processes and is purely double layer capacitance. One striking feature of this type of behavior is which the applying current is unaffected by applied potential. The forward and backward scans of an ideal EDLC substance are

mirror images of each other [180]. Figure 2.18 shows the shape of a parallelogram, this denotes there is charge transfer resistance between an electrolyte and the electrode. Because the charges deposited on the electrode are dependent on the applied voltage, the electrode materials that demonstrate Faradaic processes produce a cyclic voltammogram that deviates from a rectangular form. The CVs of pseudocapacitors include redox peaks that show faradaic processes are involved [181].

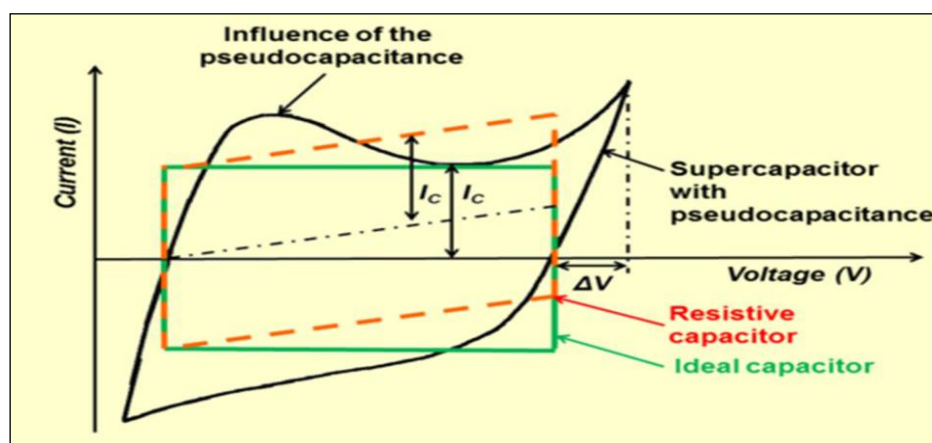


Figure 2.18: A typical electrochemical capacitor schematic exhibiting the differences between static (rectangular) and faradaic (curved) capacitance [182].

The most significant benefit of the CV is its simplicity, as capacitance is proportionate to area below the curve. Specific capacitance average is calculated using equation (2.12) [182] and the CV curves [182].

$$C = \frac{\int Idv}{2m\Delta V v} \dots\dots\dots (2.12)$$

Where  $C$  ( $F g^{-1}$ ) is specific capacitance,  $I$  (A) is voltammetric current,  $m$  (g) is mass of active materials in electrode,  $v$  (mV/s) is scan rate,  $\Delta V$  (V) is potential window in CV curves.

### 2.27.2 Galvanostatic Charge-Discharge (GCD)

The GCD technique is the most extensively used ECs application method and the most essential characterization instrument for determining the electrochemical performance of ECs electrode materials. Most of the key metrics of the ECs system, including as specific capacitance, power, and energy densities, may be retrieved using this characterisation technique [183].

A steady current pulse is applied to the cell and the voltage response is measured over time in the Galvanostatic procedure. The Cyclic Charge Discharge (CCD) is a widely used method for assessing battery and EDLC performance [184]. From GCD tests, the specific capacitance ( $C_s$ ) can be calculated using the following equation [185]:

$$C_s = \frac{I \times \Delta t}{m \times \Delta V} \dots\dots\dots (2.13)$$

Where  $C_s$  ( $F\ g^{-1}$ ) is specific capacitance,  $I$  is the discharge current (A),  $m$  is the mass (g) of the active materials,  $\Delta V$  represents the potential difference (V) and  $\Delta t$  is the discharge time (s).

The pattern of the GCD curve displays information on the nature and behavior of the manufactured electrode material. The relation between voltage (V) and time (sec) for EDLCs capacitors are linear, resulting in GCD curves that are mirror images of one another, as shown in Figure 2.19, whereas the relation between calculated potential (V) and time (sec) for pseudocapacitors isn't linear, resulting in GCD curves that are not mirror images of one another. Pseudocapacitive materials' GCD curves include at least one hump on their profile to represent the substance's redox activity. The GCD curves of EDLCs

materials, on the other hand, do not exhibit a hump since there is no redox activity on their surface, simply pure electrostatic charge separation [185].

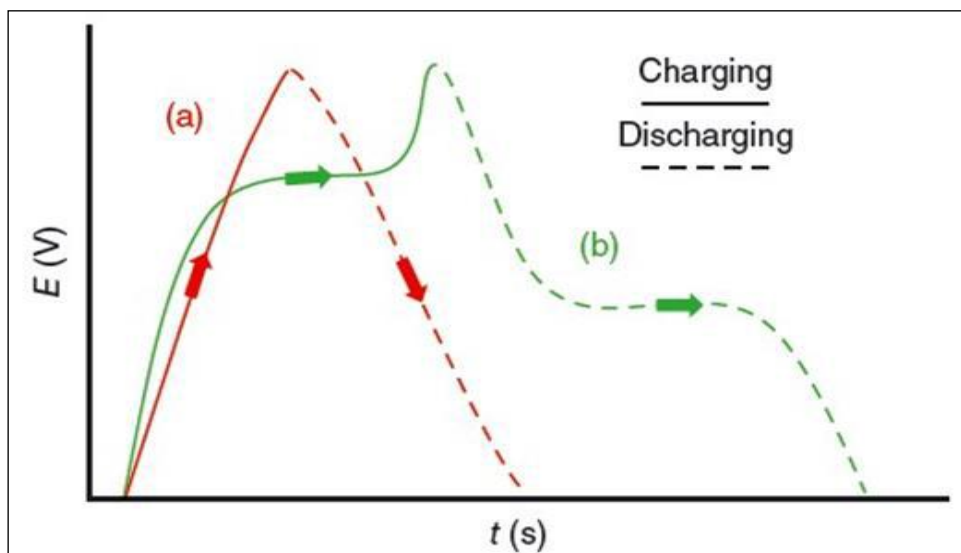


Figure 2.19: plots of the Galvanostatic charge-discharge of (a) EDLC (b) pseudo-capacitive material [185].

### 2.27.3 Electrochemical Impedance Spectroscopy (EIS)

EIS is a powerful technique for examining the electrochemical performance of supercapacitors in depth. EIS works by providing a modest alternating current (AC) potential to an electrochemical sample system over a wide range of frequencies and determining the subsequent variations in the current (A) produced from the sample's impedance as a function of frequency [186]. The results of this technique provide a wealth of information regarding the physiochemical process and electrochemical reaction kinetics. The advantages of this technique include the capacity to monitor frequency as well as time domain, as well as precise measurements made possible by recent advances in current electronic circuits and other factors. Derived from EIS, the capacitance is given by [187]:

$$C^{EIS} = \frac{1}{-2\pi f Z''} \dots\dots\dots (2.14)$$

Where  $f$  is the frequency of the applied potential harmonic and  $Z'$  and  $Z''$  are the real and imaginary impedance components, respectively. A "Nyquist Plot" is created by plotting the imaginary component for the graph just on Y-axis while plotting the real component on X-axis. Each Nyquist graph point represents impedance at a single frequency[188], and the Y-axis is negative. Figure 2.20 depicts a typical Nyquist plot in which the imaginary part,  $-Z_{imag}$ , is shown as a function of the real part,  $Z_{real}$ . It has a semicircle between points A and B at high frequencies, a non-vertical line between points B and C at intermediate frequencies, and a nearly vertical line beyond point C at low frequencies [189].

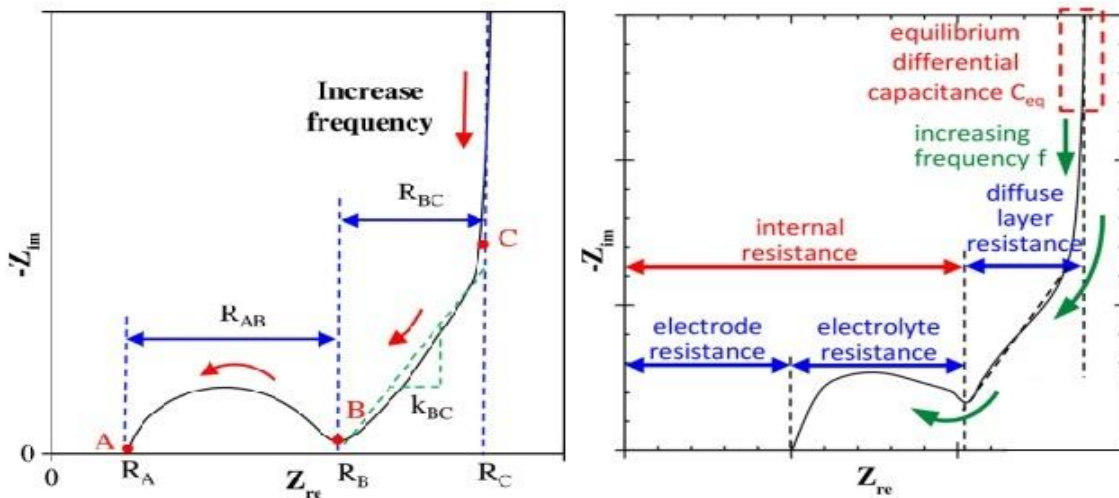


Figure 2.20: Schematic of typical Nyquist plots [189].

The resistances according to figure 2.20 are as follows:

- $R_A$  at point A is attributed to electrode resistance.

- The diameter of the semicircle  $R_{AB} = R_B - R_A$  is assigned to (a) the electrolyte resistance in the pores of the electrodes, (b) the resistance of contact between the current collector and the electrode.
- $R_B$  ( $R_B = R_A + R_{AB}$ ), is the internal resistance, and also called a charge transfer resistance [190].

## 2.28 Photoconductivity

Organic materials have an advantage over inorganic materials due to its mechanical characteristics, simple of processing, inexpensive, and range of energy gap substances with a wide absorption region as well as manipulation of the absorption edge employing organic chemicals. This suggests that polymer photodetectors with response across the full visible and near-IR spectra are achievable. Organic polymers and Organic small molecules had attracted much interest in latest years due to its potential uses in optoelectronics structures like photodetectors and photovoltaics that are commonly are using in optical scanners, remote control devices, wireless LAN, a color sensor for a digital camera, and automatic lighting controls [191].

Photoconductivity (PC) is the electrical conductivity that results from photo-induced electron excitations that absorb light.

Because photons interact with bound electrons of target atoms in semiconductors, electron-hole or e-h pairs are photo-produced, increasing carrier density and conductivity. [192]. the nature of photoexcitation and recombination processes, for example, can be studied using PC. The carriers densities, the lifetime of carriers, as well as dynamic carriers production, recombination mechanisms, and trapping all contribute to the material's

conductivity. Temperature, applying field, the intensity of light, and the energy of radiation are all variables [193]. the rise and decay curves of photocurrent are generally understood to be controlled with the recombination centers or trapping states in a photoconductor's forbidden energies region. As a result, these curves will be used to learn more about traps and recombination centers [194]. As shown in the linear equation for conductivity, the conductivity of a substance increases as the number of charge carriers increases due to excitations of electrons from the valance band to the conduction band, leaving holes behind [194,195].

$$\sigma = en [\mu_e + \mu_p] \dots\dots\dots (2.15)$$

Where n denotes the number of charge carriers, e denotes electron charge,  $\mu_e$  denotes electron mobility and  $\mu_p$  denotes hole mobility.

**2.28.1 Current-Time Characteristics**

When the light of a certain wavelength is incident directly onto a photodetector of an amount of time, then switched, and thereafter incident then. The results of these successive events are projected as follows as shown figure 2.21.

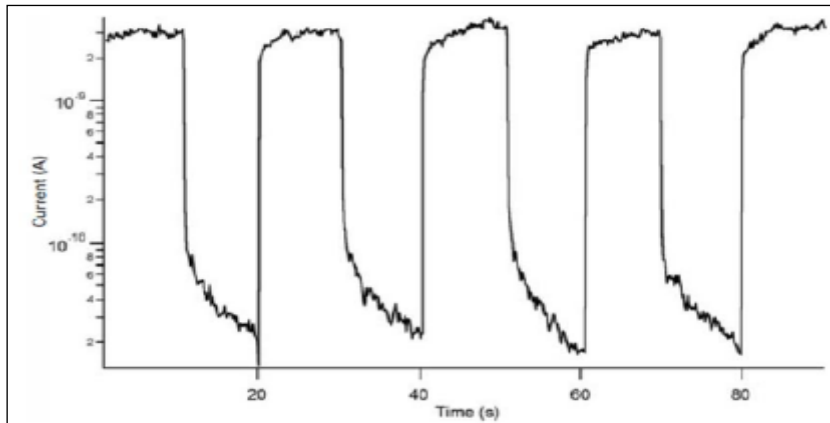


Figure 2.21: Photoresponse graph that shows a quicker response time [196].

### 2.28.2 Rise time and Fall Time upon a Square-Pulse Signal

The ( $\tau_r$ ) and ( $\tau_f$ ) responses of a detector to a "square-pulse signal" reveal their speed in the time domain. Figure 2.22 depicts the procedure for computing these time periods. [197,198].

. **Rise time ( $\tau_r$ ):** the amount of time required for the photodetector value to variance within specified percentages (10%–90%) of a peak level under abrupt lighting. This factor is commonly noted as a photodetector bandwidth  $\Delta f$ . [199,200]:

$$\tau_r = 2.2 / (2\pi\Delta f) = 0.35 / \Delta f \dots\dots\dots (2.16)$$

. **Fall time ( $\tau_f$ ):** when the light is turned off, the time it takes for the detector to reach its original current value before lighting ((i.e. in the dark) [201].

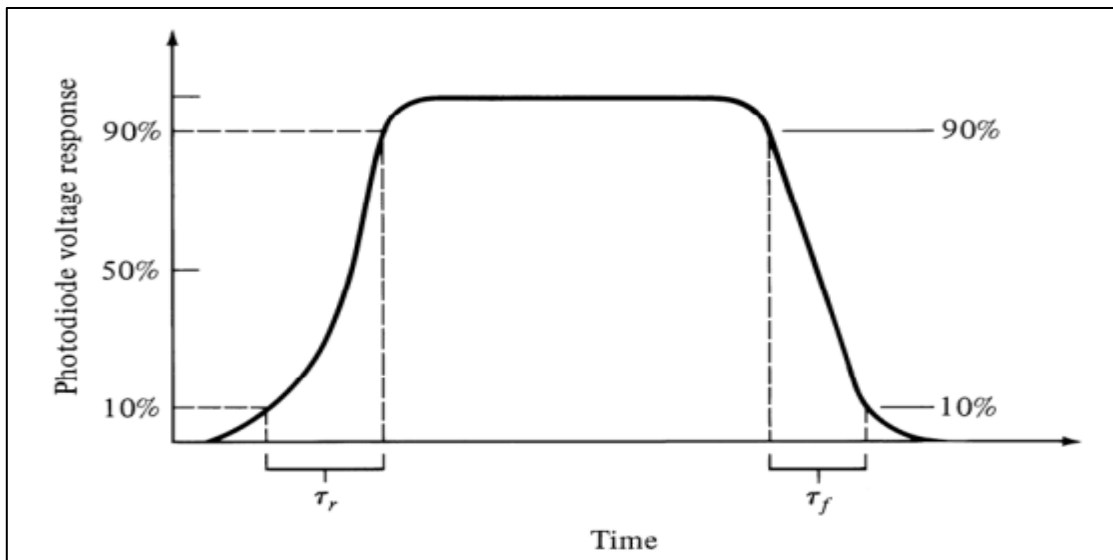


Figure 2.22: Rise and decay time of signal for square-pulse signal [198].

### 2.28.3 Sensitivity

One of the most crucial parameters that define a photodetector's efficiency is its sensitivity (S), which is determined by the formula below. [202,203]:

$$S(\%) = \frac{I_l - I_d}{I_d} \times 100 \dots\dots\dots (2.17)$$

The light current is  $I_l$ , while the dark current is  $I_d$ . Simply described, "sensitivity" refers to the amount of current that rises when a thin layer is exposed by light.

### 2.29 The Term "Sensor"

The electrical properties of thin films can be used for gas detection in so-called gas sensors because of their high sensitivity to ambient gases due to absorption effects. They're used in places where gas control and analysis are required [204]. A sensor is a device that can detect and transform physical parameters into electrical signals. Temperature, light, velocity, and biological and chemical concentrations are all physical factors. Because of the physical parameter, the sensor's electrical resistance can fluctuate, but this resistance change is usually transformed to a current or voltage. The accuracy, sensitivity, reproducibility, stability, and reaction time of sensors which compute physical variables are often described by their sensitivity, accuracy, reproducibility, response time, and stability [205]. Selectivity is another characteristic of sensors that monitor biological or chemical components. the cost, the Size, the lifetime, and the power consumption may be more or less relevant based on the sensor's intended uses [206].

Gas sensors are used in a variety of fields. For example, in cars and planes, they can be utilized as fire detectors, leak detectors, and ventilation

controllers. VOCs (volatile organic compounds) or odors produced by food or home goods are detected. Multi-sensor systems (Electronic noses are another name for them) are sophisticated gas sensor tools developed to assess such complex environmental mixes [207]. It was also becoming more important in the food sector and for air quality.

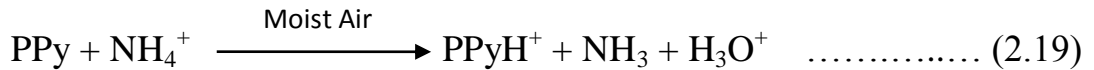
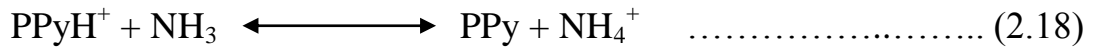
### **2.29.1 Conducting Polymer Sensors**

Conducting polymers have been more popular in gas/vapour sensors in recent years due to their high stability, ability to work at room temperature, remarkable processability, low power consumption, cost effectiveness, and other factors.

Polypyrrole polymers are conductive polymers with a conjugated  $\pi$ -electron system running through them. In their natural condition, these polymers are semiconductors, but when doped, they can conduct electricity with conductivities that are comparable to metals. PPy can generate selective layers in which the electrical characteristics are modulated by the physical and/or chemical interaction between the analyte gas and the conjugated polymer. Altering the functional group chemistry of the polymer, dopant engineering, microstructural alterations, and the addition of inorganic elements can all be used to customize the sensing capabilities [208].

As previously stated, the physical properties of conducting polymers are dependent on doping levels and doping method. Improving doping levels through chemical reactions at ambient temperature provides a simple method for detecting a variety of gases. When such a conducting polymer material comes into contact with gas, electron transfer causes a change in resistance and function of the sensor material. Electron-accepter gases such as  $\text{NO}_2$ ,  $\text{H}_2\text{S}$ ,

and  $I_2$  can remove PPy aromatic ring electrons, increasing the degree of doping and electrical conduction for p-type conductive polymers. On the other hand, electron donor gases can react with the PPy, causing electric conductance to change dramatically [209]. Polypyrrole, for example, has been used to study ammonia sensing in the laboratory. The interaction of PPy microwires with ammonia gas caused a change in resistance (conductivity), which was followed by the return to the original state when exposed to air. The following reasonable method can be used to depict the entire process of reversible reactions [210].



When a sensor is exposed to a specific gas concentration, its sensitivity is described by the change in resistance [210].

The sensor sensitivity can be calculated as:

$$S = \left| \frac{R_g - R_a}{R_a} \right| \times 100\% \dots\dots\dots (2.20)$$

Where  $S$  is the sensitivity,  $R_g$  and  $R_a$  are the film's electrical resistance in the existence of gas and the film's electrical resistance in the existence of air, respectively.

## 2.30 Characteristics used to study PPy, Ferrite and PPy nanocomposites

### 2.30.1 X-Ray Diffraction (XRD)

X-ray diffraction is a valuable tool for determining material characteristics. Chemical characterization, phase balance analysis, stress measurement, crystal direction identification, and determining the structure of solids, in addition to crystallite size determination, are all solved using this technique. Diffraction occurs only if the wave wavelength is also the same order of amount as the repeating spacing among the scattering centers [211].

X-rays are electromagnetic radiations with wavelengths ranging from 0.5 to 2.5 Å. The interatomic gap in solids is equivalent to the wavelength of X-rays. Longer wavelength radiations cannot resolve the structure on an atomic scale, whereas shorter wavelength radiations scatter unevenly via small angles. X-rays are created by the slowing of rapidly moving electrons in a metal target or the inelastic activation of core electrons in the target atoms. The first produces a broad continuous spectrum, whereas the second produces the distinctive X-rays [212].

X-ray diffractometers typically have three major components: the source of X-ray, a sample holder, and the detector of X-ray. The sample holding is in the middle of a circle, with the source and detector and their accompanying optics on the circumference. XRD analysis is based on Bragg's law. Bragg's angle ( $\theta$ ) is the angle formed by the plane of the sample and the X-ray source, while the angle formed by the X-ray projection and the detector is ( $2\theta$ ). Figure 2.23 shows the essential features of an X-ray diffractometer, where the angle between incident and diffracted X-rays is called the diffraction angle  $2\theta$  [213].

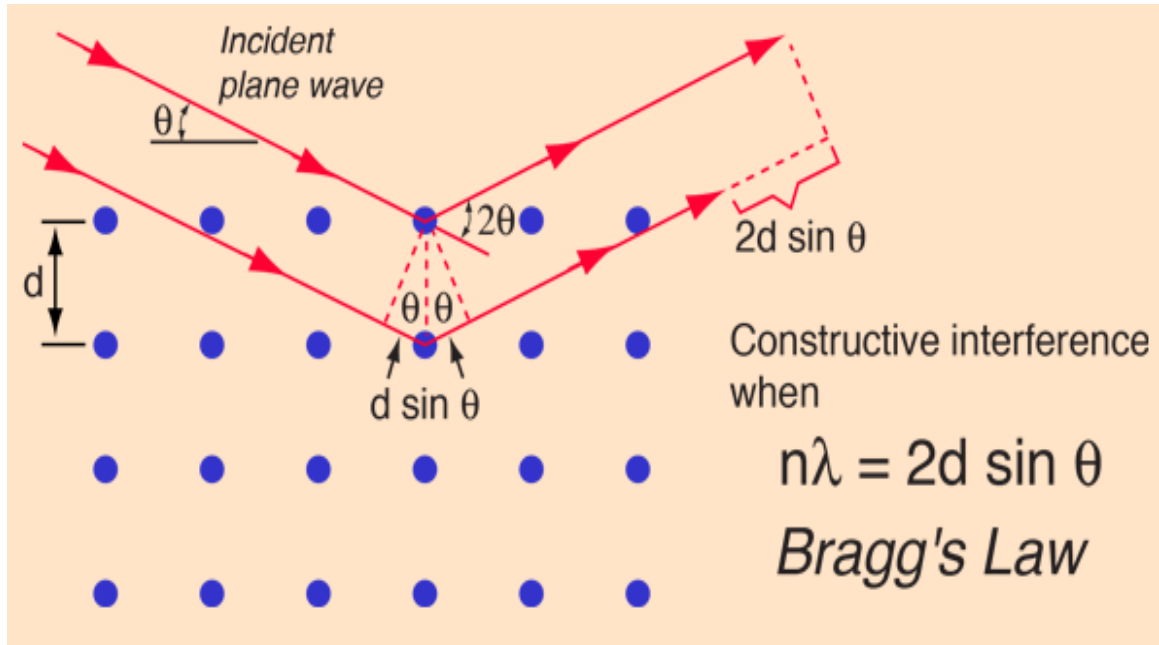


Figure 2.23: Schematic representation of x-ray diffraction [213].

Each crystalline substance has a unique atom arrangement that diffracts X-rays.

The X-rays must have wavelengths of the order of atomic distance in crystals to produce the diffraction phenomena. An incident X-ray beam is diffracted by a crystal plane aligned to fit Bragg's law. The following is how Bragg's law is written [213]:

$$n\lambda = 2d \sin\theta \dots\dots\dots (2.21)$$

Where The X-ray wavelength is denoted by  $\lambda$ , The atomic plane spacing is represented by  $d$ , and  $\theta$  is the diffraction angle half-value, then  $n$  is the reflection order. Therefore, when a detector scans the range angles of reflection, It results in a pattern of peaks with specified spacing & intensities.

Spinal ferrite has spinel structure crystallize in the cubic system. The cubic system's lattice constant ( $a$ ) is provided by the formula [213]:

$$a_{exp} = d_{hkl} \sqrt{h^2 + k^2 + l^2} \dots\dots\dots (2.22)$$

Where  $d_{hkl}$ : inter planer distance, h, k, l: Miller indices. Moreover, the x-ray density ( $\rho_x$ ), is influenced by the crystal's molar mass and lattice parameter, and is given by the following equation[213]:

$$\rho_x = \frac{z M}{N_A V} \dots\dots\dots (2.23)$$

The number of molecules in unit cell is denoted by Z ( $Z = 8$  for spinel ferrite), the sample's molecular mass expressed by M, the cubic structure's volume is  $V=a^3_{exp}$ , as well as  $N_A= 6.023 \times 10^{23}$  (atom/moleis) Avogadro's number. The crystallite size was calculated using Scherrer's equation based on the peak broadening on the XRD pattern [213]:

$$D = \frac{K\lambda}{\beta \cos \theta} \dots\dots\dots (2.24)$$

Where the crystallite size was denoted by the letter D, The wavelength of an X-ray is denoted by  $\lambda$ ,  $\theta$  to diffraction angle, The finite size broadening is represented by  $\beta$  plus The shape factor is denoted by the letter K( $K=94 \times 10^{-2}$ ) for cubic symmetry with spherical crystallites.

The letter L represents the hopping or jumping length, (The distance between magnetic cations is known as the jump length) for tetrahedral (A) and octahedral [B] site is calculated using the relations below [119]:

$$L_{A-A} = (a_{exp} \sqrt{3})/4 \dots\dots\dots (2.25a)$$

$$L_{B-B} = (a_{exp} \sqrt{2})/4 \dots\dots\dots (2.25b)$$

$$L_{A-B} = (a_{exp} \sqrt{11})/8 \dots\dots\dots (2.25c)$$

X-ray diffraction studies show that the PPy powder is amorphous in nature. The average chain separation can be calculated from these maxima using the relation[214]:

$$S = \frac{5\lambda}{8 \sin \theta} \dots\dots\dots (2.26)$$

Where S is the polymer chain separation,  $\lambda$  denotes the X-ray wavelength, and  $\theta$  represents the diffraction angle at the maximum intensity of the amorphous halo.

### 2.30.2 Field Emission-Scanning Electron Microscopes (FESEM)

SEMs are one of the most essential modern scientific tools, an instrument that allows researchers to examine the morphology of solid samples at better magnification, resolution, and depth of focus than an optical microscope. Nanotechnology has fueled the advancement of modern electron microscopy, with demands for higher resolution and more information from the sample. The field emission scanning electron microscope (FESEM) is a strong tool for studying the morphology of materials' surfaces by raster scanning over them with a high-energy electron beam with a resolution of a few nanometers [215].

By utilizing electrostatic or magnetic lenses, the electron beam can be focussed to a very small spot size. This is usually accomplished with electrostatic lenses. A scan generator is used to scan or raster the tiny beam onto the sample surface. The interaction of electrons with the atoms in the sample produces signals, which communicate information about the sample's surface shape, composition, and other features. These signals include secondary electrons, backscattered electrons, diffracted backscattered electrons, photons, visible light, and heat. Secondary electrons and

backscattered electrons are often employed to image samples: Secondary electrons will be best of displaying morphology and topography for specimens, while backscattered electrons will be optimal as exhibiting compositional variations in multiphase specimens [216]. The electron gun's job is to deliver a large, consistent current in a tiny beam. Thermionic emitter and field emitter are two different types of emission sources. The fundamental distinction between a scanning electron microscope (SEM) and a field emission scanning electron microscope (FESEM) is the type of emitter (FESEM). The images produced by FE-SEM are superior to those produced by thermionic emitter SEM. However, unlike hot cathode SEM, such FESEM is less prevalent [217].

### **2.30.3 Fourier Transform Infrared (FTIR) Spectroscopy**

(FTIR) are among the most essential analysis methods used to determine the chemical composition of geological samples like as shale, coals, liquids, silicate glass, melt impurities, microfossils, and minerals which can supply basal data on the molecular construction of inorganic or organic materials[218]. The core principle of FTIR technology is connected to transitions between quantized vibration energy states. In this study, infrared absorption occurs whenever the photons strike the molecules and excites it over to a high energy level. In the IR region of the light spectrum, excited states generate molecular bond vibrations with different wave numbers (or frequencies) (stretching, spinning, bending, wagging, rocking, plus out-of-plane e deformation) [219].The chemical bond's absorbed wavelength is one of its characteristics. The frequency of molecular bonding varies based on the type of bond and the components present [220].

The cation masses, cation oxygen bonding, and the lattice parameter all influence the vibration frequencies in IR spectra. The principal absorption bands  $\nu_1$  and  $\nu_2$  in the IR spectrum of spinel ferrites correspond to tetrahedral (A-O) and octahedral (B-O) sites, respectively. The equation was used to calculate the force constants at tetrahedral and octahedral sites ( $K_T$ ,  $K_O$ ) [221].

$$K\left(\frac{\text{dyne}}{\text{cm}}\right) = 58.98 \times 10^{-3} * (\nu (\text{cm}^{-1}))^2 * \mu(\text{amu}) \dots\dots\dots (2.27)$$

where the reduced mass is denoted by  $\mu_m$  and offered by  $\mu_m = (m_1 \times m_2) / (m_1 + m_2)$ , The atomic mass of the positive ions at the tetrahedral and octahedral sites is given by  $m_1$ , The atomic mass of anion is denoted by  $m_2$  (the atomic masses for the elements were taken from periodic table which are included in the appendix). The reduced masses ( $\mu_m$ ) of the bonds Co-O, Zn-O, Mn-O and Fe-O are respectively 12.58, 12.85, 12.39 and 12.43 (amu).

### 2.31 Optical Properties

The optical properties of semiconductors can be defined as those that include interactions between electro-magnetic radiations or light and the semiconductor, such as scattering effects, diffraction, absorption, reflection, and polarization [222]. Furthermore, optical characteristics of semiconductor films were important prerequisites for suitable uses in different of optoelectronics; these properties are dependent on the preparation method, annealing, substrate temperature, and deposition, as all changes in such conditions result in absorption edge deviations to low or high energies. As Polymer optical properties are determined by the main chain's molecular structure and shape. This relation among the optical band gap, absorption coefficient, and energy ( $h\nu$ ) of the incident-photon may be utilized to determine the optical band gap using Tauc's equation [223]:

$$\alpha h\nu = B (h\nu - E_{opt})^r \dots\dots\dots (2.28)$$

Where  $E_{opt}$  is the optical energy gap, B inversely proportional to amorphousity and r is an index which can be assumed to have values of 1/2, 3/2, 2 and 3, depending on the nature of the electronic transition responsible for the absorption.  $r = 1/2$  for allowed direct transition,  $r = 3/2$  for forbidden direct transition and  $r = 3$  for forbidden indirect transition, with  $r = 2$  refers to indirect allowed transitions. The optical energy band gaps ( $E_{opt}$ ) for direct transition can be found using equation 2.28 and plotting  $(\alpha h\nu)^2$  as a function of photon energy  $h\nu$ .

### 2.31.1 Optical Properties of Conducting Polymers

#### 2.31.1.1 Optical Absorption: Formation of Excited States

In a tiny molecule with an isolated double bond, the  $\pi$ -electron can be promoted from a lower energy state to a higher energy state by absorbing the photon with more energy from the energy gap ( $E_g$ ) between the two orbitals. On the other hand, a similar molecule with double conjugate bonds will have a HOMO (higher occupied molecular orbital ) as well a LUMO (lower unoccupied molecular orbital). Due to the decreased energy gap caused by orbital interactions, a low-energy photon may promote a  $\pi$ -electron from HOMO to LUMO; hence, the band energy gap in conjugated polymers may be even smaller [224].

#### 2.31.1.2 Optical Emission: Relaxation of Excited States

When a photon of sufficient energy ( $h\nu$ ) is absorbed by the conductive polymer, the electron can be promoted from HOMO to LUMO, resulting in an electrostatically bonded e-h pairs known as excitons [225]. This euphoric

condition might spread from one location to the next until it is deactivated. One of most important deactivations in conjugated polymers is luminescence (emission of light). Luminescence is divided into two groups according to the electronic spins participating in radiative transitions: fluorescence and phosphorescence [226], as shown in Figure 2.24 [227]. Phosphorescence occurs whenever the electrons in the excited levels had same spin as the electron in the corresponding ground level's orbital. Fluorescence occurs whenever an excited electron has same spin as an electron in the opposite ground orbital [228].

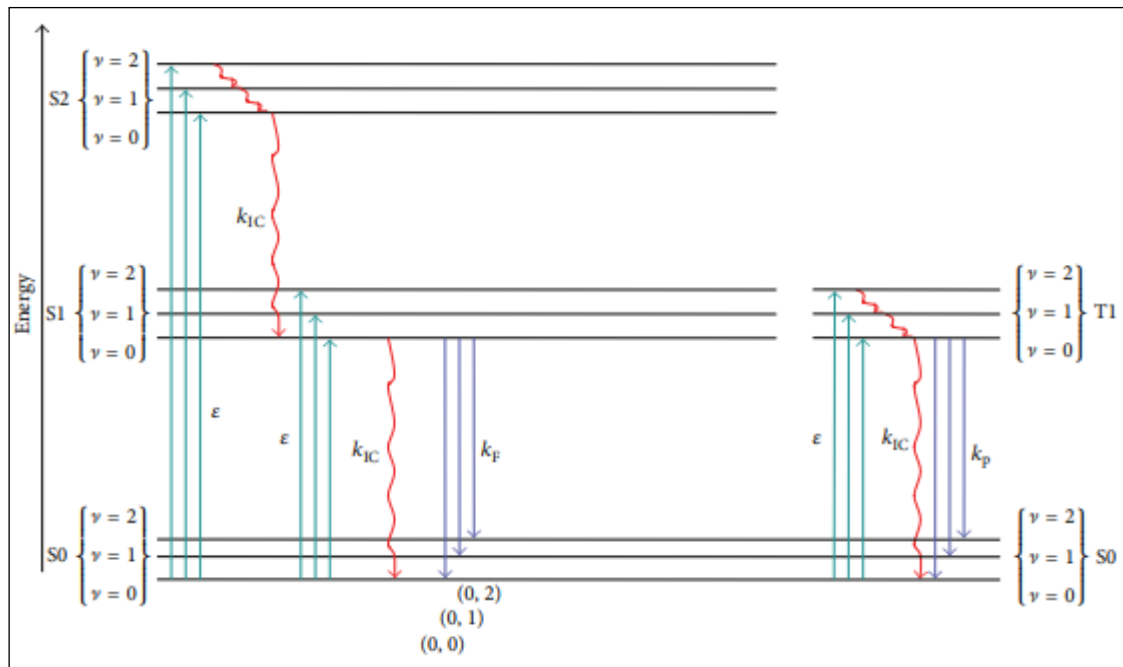


Figure 2.24: State energy diagram of some possible photophysical process in a typical fluorescent molecule.

## **Chapter Three**

### **Experimental Part**

#### **3.1 Introductions**

This chapter covers all practical experiments conducted under search conditions. It has several fundamental components: The first involves the production of ( $\text{Co}_{0.8-x}\text{Zn}_x\text{Mn}_{0.2}\text{Fe}_2\text{O}_4$ ) nanoparticles and the research of the influence of zinc replacement on the structural and magnetic characteristics, as well as the fabrication of polypyrrole nanofibers (PPy-NFs) and self-regulate magnetic nanoparticles. The second component concerns the creation of thin films built from nanocomposite samples (PPy-NFs/ $\text{Co}_{0.8-x}\text{Zn}_x\text{Mn}_{0.2}\text{Fe}_2\text{O}_4$ ) as well as their synthesis (figure 3.1). The following section offers a description of the sample preparation technique, the stages of the preparation process, and a list of the materials and instruments utilized in the process. On the other hand, it provides descriptions of characterization procedures utilized to demonstrate morphological, structural, magnetic, as well as optical characteristics of substances being manufactured for usage in supercapacitors, photodetector, in addition to gas sensor applications (figure 3.2).

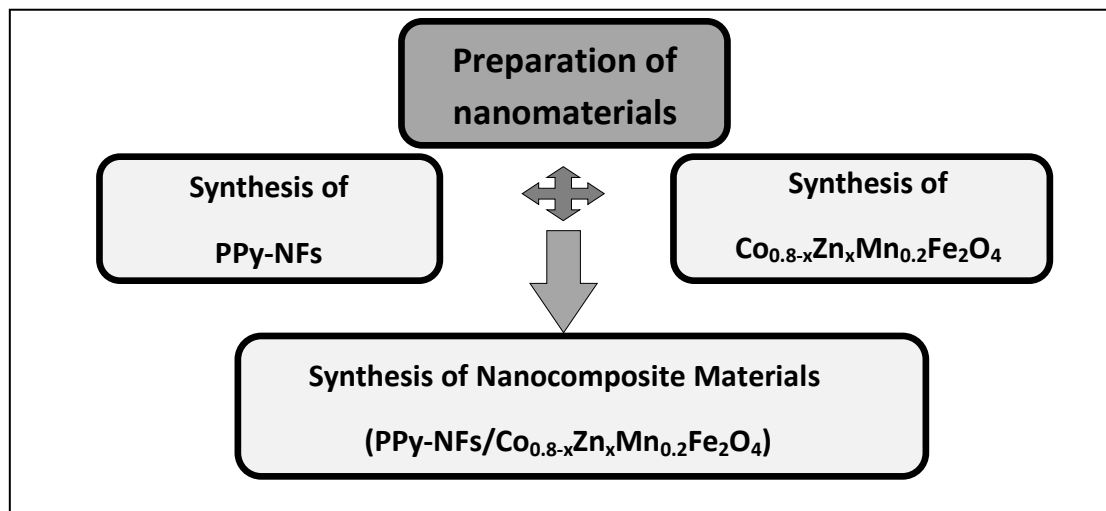


Figure 3.1: Diagram of the preparation materials.

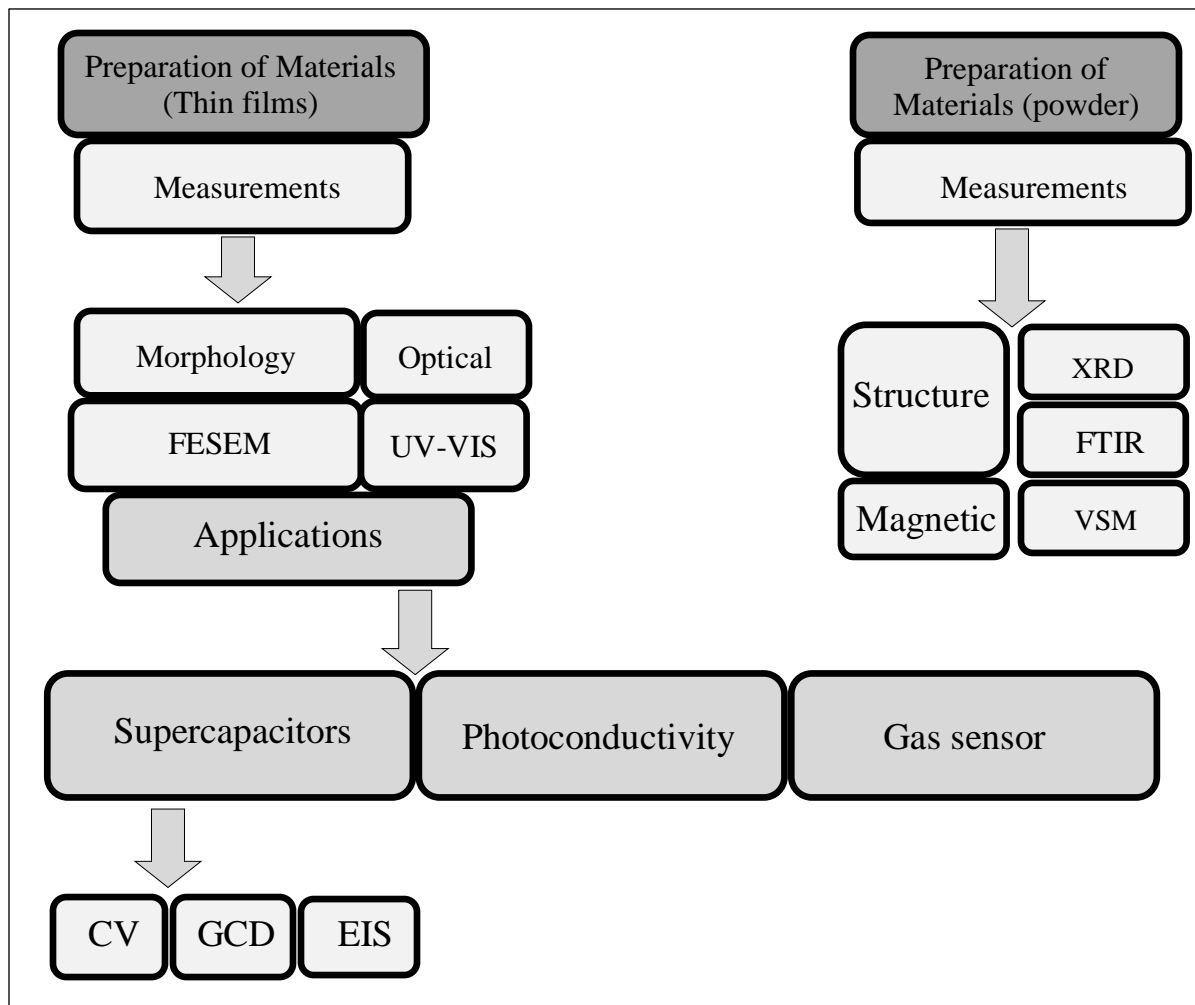


Figure 3.2: Diagram of materials checks and its applications.

## 3.2 Materials and Methods

### 3.2.1 Materials and Chemicals

The materials used in this work to synthesize polypyrrole nanofibers with ferrite nanoparticles are shown in tables 3.1 and 3.2.

Table 3.1: The raw materials of (PPy-NFs) synthesis.

| Materials           | Chemical formula  | Density (g/cm <sup>3</sup> ) | Mol. weight (g/mol) | Purity | Supplier                         |
|---------------------|---|------------------------------|---------------------|--------|----------------------------------|
| Pyrrole             | C <sub>4</sub> H <sub>5</sub> N                                   | 0.967                        | 67.091              | 98%    | Sigma Aldrich, China             |
| Iron (III) chloride | FeCl <sub>3</sub>   | 2.9                          | 162.21              | 98%    | AIPHA chemica                    |
| Methyl Orange       | C <sub>14</sub> H <sub>14</sub> N <sub>3</sub> NaO <sub>3</sub> S | 1.28                         | 327.33              | 99%    | LTD Rubilabor Chemical Co. Spain |

Table 3.2: The raw materials of (Co<sub>0.8-x</sub>Zn<sub>x</sub>Mn<sub>0.2</sub>Fe<sub>2</sub>O<sub>4</sub>) synthesis.

| Materials                            | Chemical formula                     | Mol. mass (g/mol) | Purity | Supplier             |
|--------------------------------------|--------------------------------------|-------------------|--------|----------------------|
| Iron (III) chloride                  | FeCl <sub>3</sub>                    | 162.21            | 98%    | AIPHA chemica        |
| Manganese (II) chloride tetrahydrate | MnCl <sub>2</sub> ·4H <sub>2</sub> O | 197.91            | 98%    | AIPHA chemical       |
| Zinc (II) chloride                   | ZnCl <sub>2</sub>                    | 136.286           | 98%    | ROMIL pure chemistry |
| Cobalt (II) chloride                 | CoCl <sub>2</sub>                    | 129.64            | 98%    | AIPHA chemical       |
| Sodium Hydroxide                     | NaOH                                 | 40                | 98%    | ROMIL pure chemistry |

### 3.2.2 Synthesis of Polypyrrole Nanofibers (PPy-NFs)

In the presence of methyl orange and Iron (III) chloride in distilled water, we used the following chemical method to synthesize PPy-NFs of the pyrrole monomer. 0.08185 g (2.5 mM) methyl orange (MO) was dissolved in distilled water (288 ml) and combined with (14 mM) pyrrole monomer to produce a (Py-MO) solution, which was then cooled to 3 °C using an ice bath. For 10 minutes, the mixture was vigorously agitated until the agglomerates vanished. 1.702 g (10mM) (FeCl<sub>3</sub>) is dissolved in thirty-three milliliters of distilled water (see table 3.3), then dropped in the manufactured (Py-MO) mixture during a 2-hour period. Following that, all of the aforesaid reactant mixtures simultaneously stirred in an ice-bath for 24 hours. To remove the remaining contaminants from PPy-NFs, the precipitated PPy-NFs were filtered and rinsed three times with acetone, alcohol, and distilled water. Lastly, the precursor product (powder) had dried for six hours at 75°C in an oven.

Table 3.3: (MO: Py: FeCl<sub>3</sub>) molar ratios of (PPy-NFs) samples.

| Sample code | MO        |              | Py        |              | FeCl <sub>3</sub> |              | MO: Py: FeCl <sub>3</sub> molar ratio |
|-------------|-----------|--------------|-----------|--------------|-------------------|--------------|---------------------------------------|
|             | Wight (g) | No. mol (mM) | Wight (g) | No. mol (mM) | Wight (g)         | No. mol (mM) |                                       |
| PPy-NFs     | 0.8185    | 2.5          | 0.9870    | 14           | 1.703             | 10           | 1 : 5.6 : 4                           |

### 3.2.3 Synthesis of Ferrite Nanoparticles

Magnetic nanoparticles (MNs) were prepared by co-precipitation method. The table 3.2 shows the chemical materials and their percentages purity utilized to make the samples. MNs samples with the structure ( $\text{Co}_{0.8-x}\text{Zn}_x\text{Mn}_{0.2}\text{Fe}_2\text{O}_4$ ), have been synthesized, with  $x = 0, 0.2, 0.4, 0.6,$  and  $0.8$ . To prepare each sample, stoichiometric molar quantities were weighed according to their molecular weights. The weights of the compounds and the appropriate number of moles necessary to prepare each sample are listed in Table 3.4. The weights of the reactant were calculated using the below equation:

$$\text{Mass (g)} = \text{No. of moles} \times \text{Molar Mass (g/mol)} \dots\dots\dots (3.1)$$

The co-precipitation approach was used with hydrothermal synthesis to produce ferrite nanoparticles ( $\text{Co}_{0.8-x}\text{Zn}_x\text{Mn}_{0.2}\text{Fe}_2\text{O}_4$ ). The stages are as follows: in separate beakers, we dissolve stoichiometric amounts of  $\text{FeCl}_3$  (Ferric chloride),  $\text{MnCl}_2 \cdot 4\text{H}_2\text{O}$  (Manganese (II) chloride tetrahydrate),  $\text{CoCl}_2$  (Cobalt (II) chloride) as well as  $\text{ZnCl}_2$  (Zinc (II) chloride) in de-ionized water. The mixture was then transferred to another heat-resistant beaker and stirred continuously to achieve a homogenous solution. In addition, sodium hydroxide ( $\text{NaOH}, 1.25 \text{ M L}^{-1}$ ) is dissolved in a hundred milliliters de-ionized water separately. Then it would be dropped in to metal salts sol at room temp. ( $\approx 27^\circ\text{C}$ ) until the pH reach  $\approx 12.5$ , ensuring that each of the metal ions in the sol was precipitated. After one hour of heating at  $90^\circ\text{C}$  with constant stirring, the solution was turned off as well allowed to cold at ambient heat. The magnetic decantation method was used to separate and collect magnetic nanoparticles. It was then rinsed many times with deionized water using a multi-funnels system to assure salt removal and expedite drying at  $27^\circ\text{C}$ . The wet product has re-dispersed in a  $\text{NaOH}$  solution ( $\text{pH} \approx 12.5$ ) after 60 minutes

of stirring. To avoid coalescence of neighboring nanoferrite particles, which occurs often during the high-temperature sintering process. When nanoparticles come into contact with one another. The heat treatment, which was done using the hydrothermal method, was the following phase in the fabrication process. The colloidal solution was moved to a 250 mL autoclave reactor lined with Teflon. After it has been sealed tightly, the autoclave is heated in a furnace at 250°C for 5 h. After that it was left to naturally cold outside at ambient temperature. The colloidal solution is then filtered and rinsed numerous times with ethanol and de-ionized water until the pH is even to 7. The final product is eventually place in the oven at 70 degrees Celsius for 1 h to form a stable phase of nanoferrite.

Table 3.4: Synthesis of ( $\text{Co}_{0.8-x}\text{Zn}_x\text{Mn}_{0.2}\text{Fe}_2\text{O}_4$ ) from basic chemicals compounds and the weights that had been used.

| x   | Structure  | FeCl <sub>3</sub> |              | MnCl <sub>2</sub> .4H <sub>2</sub> O |              | CoCl <sub>2</sub> |              | ZnCl <sub>2</sub> |              |
|-----|--|-------------------|--------------|--------------------------------------|--------------|-------------------|--------------|-------------------|--------------|
|     |  | Weight (g)        | No. mol (mM) | Weight (g)                           | No. mol (mM) | Weight (g)        | No. mol (mM) | Weight (g)        | No. mol (mM) |
| 0   | $\text{Co}_{0.8}\text{Mn}_{0.2}\text{Fe}_2\text{O}_4$                | 8.1105            | 50           | 0.9895                               | 5            | 2.5968            | 20           | 0                 | 0            |
| 0.2 | $\text{Co}_{0.6}\text{Zn}_{0.2}\text{Mn}_{0.2}\text{Fe}_2\text{O}_4$ | 8.1105            | 50           | 0.9895                               | 5            | 1.9476            | 15           | 0.6814            | 5            |
| 0.4 | $\text{Co}_{0.4}\text{Zn}_{0.4}\text{Mn}_{0.2}\text{Fe}_2\text{O}_4$ | 8.1105            | 50           | 0.9895                               | 5            | 1.2628            | 10           | 1.3628            | 10           |
| 0.6 | $\text{Co}_{0.2}\text{Zn}_{0.6}\text{Mn}_{0.2}\text{Fe}_2\text{O}_4$ | 8.1105            | 50           | 0.9895                               | 5            | 0.6492            | 5            | 2.0442            | 15           |
| 0.8 | $\text{Zn}_{0.8}\text{Mn}_{0.2}\text{Fe}_2\text{O}_4$                | 8.1105            | 50           | 0.9895                               | 5            | 0                 | 0            | 2.7257            | 20           |

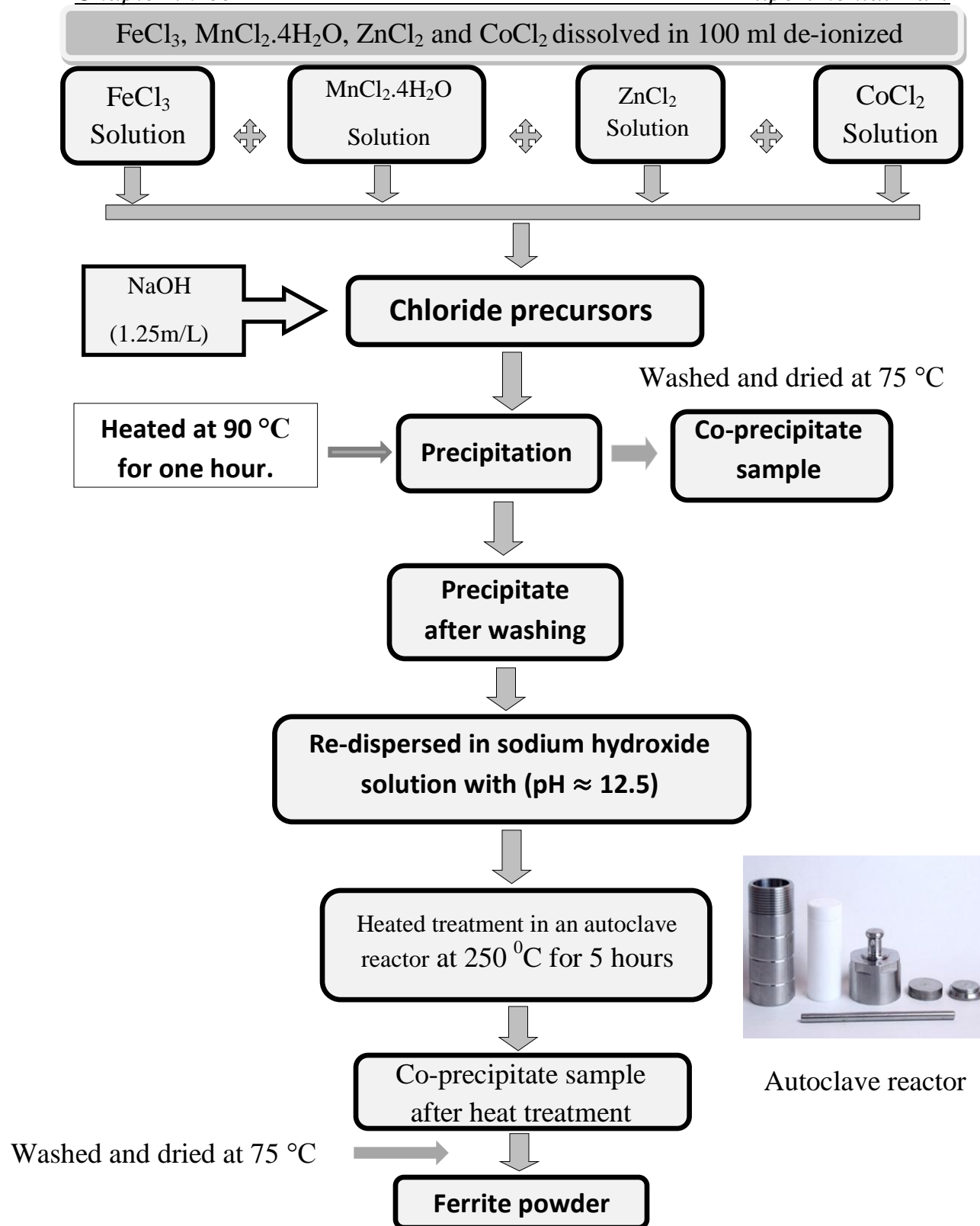


Figure 3.3: diagram of co-precipitation method pursued by heat treatment in an autoclave reactor.

### 3.2.4 Synthesis of Nanocomposite (PPy-NFs/ $\text{Co}_{0.8-x}\text{Zn}_x\text{Mn}_{0.2}\text{Fe}_2\text{O}_4$ )

0.03g of ( $\text{Co}_{0.8-x}\text{Zn}_x\text{Mn}_{0.2}\text{Fe}_2\text{O}_4$ ) samples were dissolved in thirty millimeters of pure (distilled) water then sonicated (stirred) for ten hours whereas 0.03g of PPy-NFs were dissolved in thirty millimeters of pure (distilled) water then sonicated (stirred) for two hours. Then,  $\text{Co}_{0.8-x}\text{Zn}_x\text{Mn}_{0.2}\text{Fe}_2\text{O}_4$  solution was added to PPy-NFs solution in volumetric proportions as follows (1:1). To obtain a homogenous dispersion, the resultant solution was sonicated for 10 hours.

### 3.3 Substrate Cleaning

The substrate is the most important part of the synthesis procedure. Various substrates, including glass, n- and p-type Silicon with crystal orientation, were used in the research (111). For each type of substrate, a specific technique is used. The basic goal of cleaning is to get rid of any dust, organic contamination, or other unknown particles (if present there). Cleaning the substrate before growth is critical for producing high-quality, dense, homogeneous, and aligned nanostructures.

#### 3.3.1 Substrate (Glass) Cleaning

The performance of final material applications is dependent on substrate cleaning to achieve a pollution-free surface. The following are the cleaning procedures for glass slide (plate) substrates:

- 1) The slides or plates are rinsed with pure water after being scrubbed with a soap solution to remove greasy particles from the surface.
- 2) The plates were immersed in an ultrasonic bath for Fifteen min after being put in a clear flask of pure water.

3) To exclude impurities like as oils or certain oxides, it is cleaned by combining pure water and ethanol solution.

4) Before usage, the plates are drying by blowing air on them.

### 3.3.2 Wafer Silicon Cleaning

For p- and n-type wafer silicon substrates, the Radio Corporation of America (RCA) cleaning method was applied [229]. Procedure performed as following:

1) Preparation of chemical solution mixture:

#### **Solution (A)**

H<sub>2</sub>O/NH<sub>4</sub>OH/H<sub>2</sub>O<sub>2</sub> (50ml: 10ml: 10ml) dissolved in glass beaker.

#### **Solution (B)**

HF/H<sub>2</sub>O (1ml: 50ml) dissolved in plastic beaker without heat.

#### **Solution (C)**

H<sub>2</sub>O/HCl /H<sub>2</sub>O<sub>2</sub> (60ml: 10ml: 10ml) dissolved in glass beaker.

2) The silicon slides were immersed in the solution for 10 minutes after the glass beaker with solution A was placed on a heater at (75<sup>0</sup>C).

3) silicon slides then immersed in the plastic beaker with Solution B for 20 second.

4) The glass beaker with solution C placed on the heater and its temperature raised to (75<sup>0</sup>C), then silicon slides immersed in this solution for 10 minutes.

5) Finally, silicon slides are dried by blowing air.

Note: The slides were soaked in distilled water for cleaning after each of the steps above.

### **3.4 Structural and morphological Characterization**

#### **3.4.1 X-ray diffraction (XRD)**

The phase composition and crystal construction of the samples are examined using XRD. The experiment was conducted using a powder X-Ray diffraction model XRD 6000 (Shimadzu-Japan) with high-intensity Cu K $\alpha$  radiations ( $15.406 \times 10^{-1}$  Angstrom), scan range of 10-80 degrees, and scan speed of 6 degrees per minute. By compared the XRD patterns of models to JCPDS standard information, crystalline substances and phases could be identified. Using the list of equations presented in the theoretical part, crystallite size, X-ray density, the lattice constants, and jumping length of nanoferrite powder, as well as polymer chain separation (S) for polypyrrole nanofibers were computed (chapter 2). (Note: Measured in Tehran, Iran).

#### **3.4.2 Field Emission Scanning Electron Microscopy (FESEM)**

Nanostructured surface morphology of thin films and powders had studied via a FESEM. MIRA3 model-TE-SCAN looks after this parameter (DeyPetronic, Tehran, Iran).

#### **3.4.3 Fourier Transform Infrared Spectrometry (FTIR)**

The scans of the FTIR measurements on spectrophotometer (Shimadzu-IRAffinity-1) in college of science (University of Baghdad) are utilized to analyze the spectrums of samples to use attenuated total reflectance modes at room temperature. FTIR data is acquired in the (400 to 4000)  $\text{cm}^{-1}$  wave number range.

### 3.5 Magnetic properties

At room temperature (27 °C), the magnetic features of all samples were examined using a Vibrating Sample Magnetometer (VSM). Most magnetic characteristics of samples can be determined by monitoring the hysteresis loop. (Note: Measured in Tehran, Iran).

#### 3.5.1 Vibrating Sample Magnetometer (VSM)

We used the VSM of model (EZ VSM Model 10) to get that M-H loop for measuring magnetization due to a change in applied field. In this type of B-H curve tracer, a prepared sample is put between the large magnetic coils. While current passes through the coils containing the magnetic sample, an extraordinarily strong magnetic field of around ten kilo Oersted is created. The specimen is vibrated at a specific frequency with the help of a sample holder. The magnitude of the electromotive force created in the coil in close proximity to the sample is used to determine the magnetization. The M-H curve was used to determine the magnetic parameters: saturation magnetization ( $M_s$ ), coercivity ( $H_c$ ), and remnant magnetization ( $M_r$ ).

### 3.6 Optical Measurements

UV/VIS measurements at room temperature were used to evaluate the optical characteristics of PPy-NFs,  $\text{Co}_{0.8-x}\text{Zn}_x\text{Mn}_{0.2}\text{Fe}_2\text{O}_4$ , and PPy-NFs nanocomposites. The SHIMADZU UV-1900i UV-Visible spectrophotometer has been utilized to examine optical parameters of thin films on glass substrates, like as absorbance and optical energy gap, over a wide wavelength region (190-1100 nm). The optical energy band gap is calculated using the wavelength absorbance output data in computer software ( $E_g$ ).

### 3.7 Photodetector Fabrication

Suitable masks were produced from aluminum metal and cleaned with distilled water and alcohol in order to determine the shape of the films that were utilized for sensor measurements. Figure 3.4 shows the schematic diagram of PPy-NFs,  $\text{Co}_{0.8-x}\text{Zn}_x\text{Mn}_{0.2}\text{Fe}_2\text{O}_4$  ferrite and PPy-NFs nanocomposite photodetector.

#### 3.7.1 Characteristic Measurements of Photoconductive Detector

Using an I-V Measurement device, Model: IVM-2.10.15, Iran, Company of Nano Pajouhan Raga, Photodetectors are tested for photoresponse in the dark then under lighting. A photodetector's spectral sensitivity is measured via a detector with a 405 nm laser diode as a source of light and a monochromator connected to a laptop running the Visual-Basic 5 program. Photodetectors' current–time characteristics are investigated in the dark then under lighting with power range of 10 mW to 30 mW. The photodetection device has been utilized to assess photodetector characteristics including rise time as well fall times plus sensitivity (S). The detector's on/off characteristics were evaluated at a wavelength that corresponded to maximal sensitivity, and formula 2.17 has been used to compute the sensitivity (S).

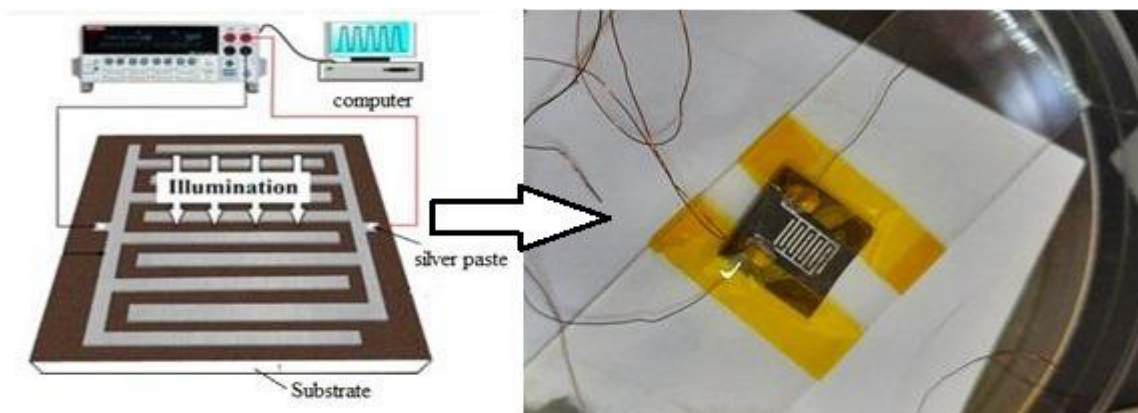


Figure 3.4: Diagram of the photocurrent measuring process in the photodetectors.

### 3.8 Electrochemical Characterization Techniques

The IVIUMSTAT. XR (Electrochemical Interface & Impedance Analyzer) was used to conduct CV, GCD, and EIS measurements to describe the electrochemical behavior of the electrodes. This was accomplished using a nickel foam ( $1 \times 1$ )  $\text{cm}^2$  substrate. To prepare it for supercapacitor testing, PPy-NFs,  $\text{Co}_{0.8-x}\text{Zn}_x\text{Mn}_{0.2}\text{Fe}_2\text{O}_4$  ferrite, and PPy-NFs nanocomposite were placed on it using the drop casting method. A portion of the aforesaid working electrode, Ag/AgCl as a reference electrode, and a platinum bar as a counter electrode were used in the three-electrode device.  $\text{H}_2\text{SO}_4$  (1.0 M) was used as the electrolyte. Figure 3.5 depicts a three-electrode design. (Note: Measured in Tehran, Iran).

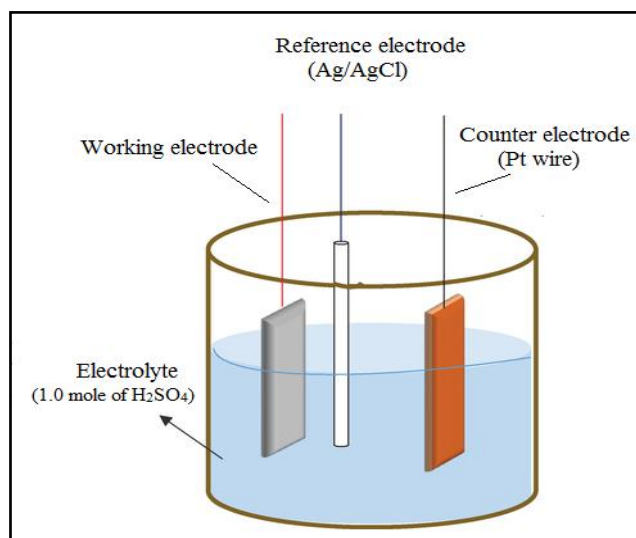


Figure 3.5: shows schematic of three-electrode system.

#### 3.8.1 Cyclic Voltammetry Measurement (CV)

The electrochemical characteristics of supercapacitor electrode materials can be determined using cyclic voltammetry (CV). The electrochemical characteristics of PPy-NFs, ferrite nanoparticles, as well as PPy-NFs

nanocomposites electrodes are examined via CV with a  $5 \frac{mV}{s}$  scan rate with a potential (voltage) domain -1V to 1V in 1M sulfuric acid electrolyte.

### 3.8.2 Galvanostatic Charge-Discharge Measurement (GCD)

A GCD check is another way to determine electrochemical capacitor capacitance efficiency. This testing examines the potential-reaction of electrode cell systems at a constant rate of CD (Charge-Discharge). All models are charged then discharged in a 1M sulfuric acid electrolyte at a constant current. The electrodes' specific capacitance is determined from discharge curves using equation 2.13.

### 3.8.3 Electro-Chemical Impedance Measurement (EIS)

The EIS examination is a valuable technique for identifying the basic behavior for supercapacitor electrode. The EIS experiments are carried out with a wide range of frequency values (10 Hz to 200 kHz).

## 3.9 Gas Sensor

Figure 3.6 shows the setup of the testing equipment, which includes a schematic design of the electrical circuit for gas sensing measurements. To make consistent solutions, specific amounts of the sample powder are dissolved in distilled water and ultrasoniced for 90 minutes. After choosing an appropriate mask to make the gold track to the electrode, these solutions were spin-coated on the silicon substrate, and molten gold was sprayed on the sample film by nozzle with a specific spraying time. The size of the gas sensor device was (1cm ×1cm).

In the gas sensing system, the gas sensor was placed inside a cylindrical steel chamber, with two pins of metal electrodes contacting the gas sensor's

gold electrodes to record the electrical resistance when the surface sample was exposed to air. The chamber is then sealed and the rotary pump is turned on to reduce the pressure inside the chamber to around 1 mbar. When a surface sample is exposed to ammonia gas with consistent periods of ON and OFF gas exposure, the electrometer records the change in electrical resistance as a function of time. (Note: Measured in Tehran, Iran).

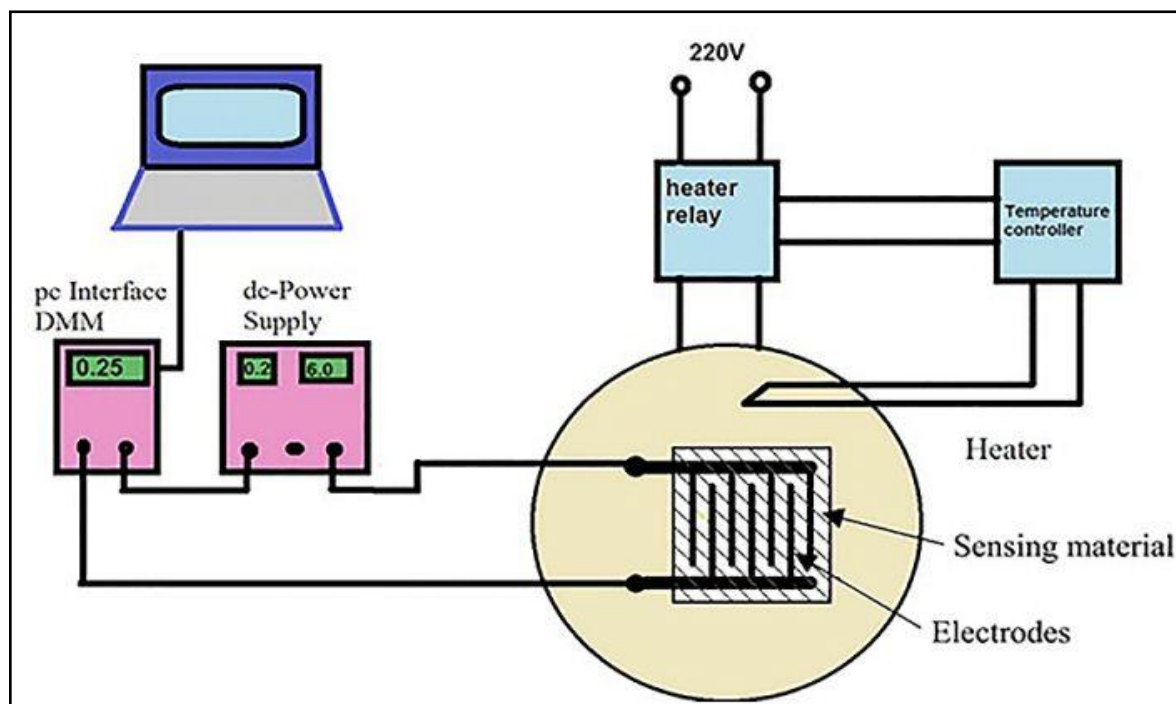


Figure 3.6: Electric circuit setup of gas sensor.

### 3.10 Samples Codes

The table below represents the codes of samples prepared in this work.

Table 3.5: Prepared samples codes.

| No. | The Sample   | The Sample code | No. | The sample  | The Sample code |
|-----|--|-----------------|-----|---|-----------------|
| 1   | Polypyrrole Nanofibers   | PPy-NFs         | 7   | PPy-NFs /Co <sub>0.8</sub> Mn <sub>0.2</sub> Fe <sub>2</sub> O <sub>4</sub>                   | PF1             |
| 2   | Co <sub>0.8</sub> Mn <sub>0.2</sub> Fe <sub>2</sub> O <sub>4</sub>                   | F1              | 8   | PPy-NFs /Co <sub>0.6</sub> Zn <sub>0.2</sub> Mn <sub>0.2</sub> Fe <sub>2</sub> O <sub>4</sub> | PF2             |
| 3   | Co <sub>0.6</sub> Zn <sub>0.2</sub> Mn <sub>0.2</sub> Fe <sub>2</sub> O <sub>4</sub> | F2              | 9   | PPy-NFs /Co <sub>0.4</sub> Zn <sub>0.4</sub> Mn <sub>0.2</sub> Fe <sub>2</sub> O <sub>4</sub> | PF3             |
| 4   | Co <sub>0.4</sub> Zn <sub>0.4</sub> Mn <sub>0.2</sub> Fe <sub>2</sub> O <sub>4</sub> | F3              | 10  | PPy-NFs /Co <sub>0.2</sub> Zn <sub>0.6</sub> Mn <sub>0.2</sub> Fe <sub>2</sub> O <sub>4</sub> | PF4             |
| 5   | Co <sub>0.2</sub> Zn <sub>0.6</sub> Mn <sub>0.2</sub> Fe <sub>2</sub> O <sub>4</sub> | F4              | 11  | PPy-NFs /Zn <sub>0.8</sub> Mn <sub>0.2</sub> Fe <sub>2</sub> O <sub>4</sub>                   | PF5             |
| 6   | Zn <sub>0.8</sub> Mn <sub>0.2</sub> Fe <sub>2</sub> O <sub>4</sub>                   | F5              |     |   |                 |

## Chapter Four

### Results and Discussion

#### 4.1 Introduction

This chapter covers the findings, including the structural, morphological, and optical properties of PPy-NFs, ferrite nanoparticles, and PPy-NFs nanocomposites samples. This chapter also covers photosensitivity, supercapacitor, and gas sensor applications for PPy-NFs, as well as ferrite and Polypyrrole-NFs deposited on Si, glass, in addition to Ni-foam substrates.

#### 4.2 The structural properties

##### 4.2.1 X-Ray diffraction Analysis results

XRD was used to investigate crystal structures and characterize phase contents in PPy-NFs, ferrite nanoparticles, and PPy-NFs nanocomposites samples, with  $2\theta$  values in the range of 10-80 degrees. Fig. 4.1 depicts Spectra of PPy-NFs. The PPy-NFs powder is amorphous in form, meaning it is a non-crystalline solid with atom distribution that does not follow any crystalline structure, according to X-ray diffraction tests. The wide peak was caused by X-rays diffusing from the PPy-NFs chain. Figure 4.1 shows a broad peak at roughly  $2\theta = 24.5^\circ$ , which corresponds to the (102) directions [230]. Amorphous PPy is distinguished by its broad apex. A broad halo pattern in the ranges  $2\theta = 10^\circ - 35^\circ$  is connected to PPy-NFs formed by oxidative polymerization and is typical of polypyrrole doped structures. The average chain separation (S) for polypyrrole nanofibers (PPy-NFs) is computed using equation 2.26, which comes out to  $4.53\text{\AA}$ .

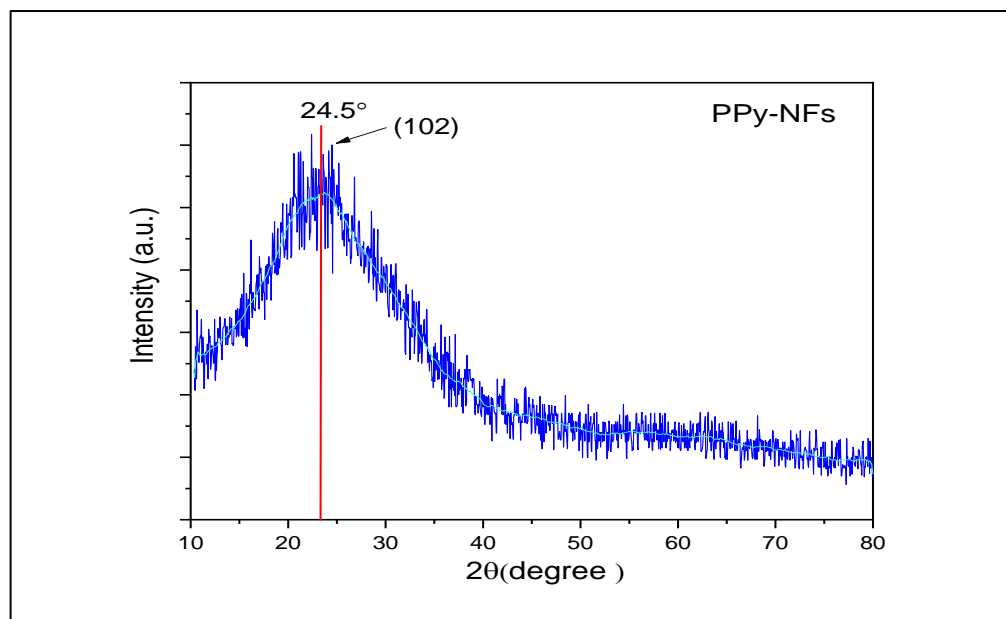


Figure 4.1: XRD pattern of (PPy-NFs) powder.

A detailed evaluation of all cell parameters had been undertaken for XRD analysis on the chemical ( $\text{Co}_{0.8}\text{Mn}_{0.2}\text{Fe}_2\text{O}_4$ ) in figure 4.2. The samples reveal single phase cubic spinel with the  $Fd3m$  space group and favorable orientations along the (111), (220), (311), (400), (422), (511), (440) and (533). They are cataloged with (JCPDs card no. 22-1086). The nanocrystalline structure of these ferrites is reflected in the broadening of the peaks. As for the compound ( $\text{Zn}_{0.8}\text{Mn}_{0.2}\text{Fe}_2\text{O}_4$ ) in figure 4.2, the major peaks obtained were (111), (220), (311), (222), (400), (422), (511), (440) and (533). They used JCPDS (74-2402), ICSD (01-074-2399), and  $\text{Mn}_3\text{O}_4$  card no. to index successfully (024-0734). Expected cubic spinel peaks (Space group:  $Fd3m$ ) are present in the sample, as well as a single-phase structure ( $\text{Zn}_{0.8}\text{Mn}_{0.2}\text{Fe}_2\text{O}_4$ ). It can also be concluded that the ions  $\text{Mn}^{2+}$  and  $\text{Zn}^{2+}$  were replaced in the nanoferrite construction. Despite this, phase analyses verified the existence of ( $\text{Mn}_3\text{O}_4$ ) in the structure, and the width of the peaks confirmed the presence of nanosize particles. When compared to the XRD cards for the above generated materials, cubic spinel phase development was

confirmed in all samples of compound  $\text{Co}_{0.8-x}\text{Zn}_x\text{Mn}_{0.2}\text{Fe}_2\text{O}_4$  ( $x= 0.2, 0.4$  and  $0.6$ ). The diffraction peaks of the cubic spinel phase are associated to the (111), (220), (311), (222), (400), (422), (511), (440) and (533) crystal planes, which corresponds to face centered cubic crystal structure with  $\text{Fd}3\text{m}$  space group.

The cubic spinel phase is clearly represented by the XRD peaks of the as-prepared sample. Without any impurity phase, the cubic spinel phase is kept in the sample at ( $x=0.2$ ). One peak occurs in the XRD pattern after the zinc is added to the samples ( $x=0.4, 0.6$  and  $0.8$ ). The development of the ( $\text{Mn}_3\text{O}_4$ ) phase is thought to have caused this peak. Because Mn cations are unstable/metastable at any of the interstitial locations of the cubic spinel structure, this process of sample alteration may be understood. Mn cations were transferred to the spinel structure's interstitial locations as a result of the reaction route, resulting in the creation of ( $\text{Mn}_3\text{O}_4$ ). The samples had a structural formula of spinel ferrite, with bivalent cations dispersed both on tetrahedral and octahedral positions. Because  $\text{Zn}^{2+}$  ions preferentially use the A-sites and  $\text{Co}^{2+}$  ions favorably occupy the B-sites, while  $\text{Fe}^{3+}$  and  $\text{Mn}^{2+}$  ions are dispersed between the A and B-sites. The synthesis process and annealing temperature have a significant impact on the distribution of cations and structural parameters [231]. Using equation 2.22, the experimental lattice constant ( $a_{\text{exp}}$ ) for the greatest intensity peak (311) from X-ray diffraction data was calculated and inserted into table 4.1. Because  $\text{Zn}^{2+}$  ions have a lesser ion radii than  $\text{Co}^{2+}$  cations, the decreased lattice parameter are clearly related to the substitution of Zn cations with Co ions in the A-position (tetrahedral position). Where the ion radii of replaced ions in A-position;  $r(\text{Co}_A^{2+} = 0.58\text{\AA})$ ,  $r(\text{Mn}_A^{2+} = 0.66\text{\AA})$ ,  $r(\text{Zn}_A^{2+} = 0.6\text{\AA})$  and  $r(\text{Fe}_A^{3+} = 0.49\text{\AA})$  Moreover,

the ion radius of the cations in B-position;  $r(\text{Co}_B^{2+} = 0.745\text{\AA})$ ,  $r(\text{Mn}_B^{2+} = 0.83\text{\AA})$ ,  $r(\text{Zn}_B^{2+} = 0.74\text{\AA})$  and  $r(\text{Fe}_B^{3+} = 0.645\text{\AA})$ .

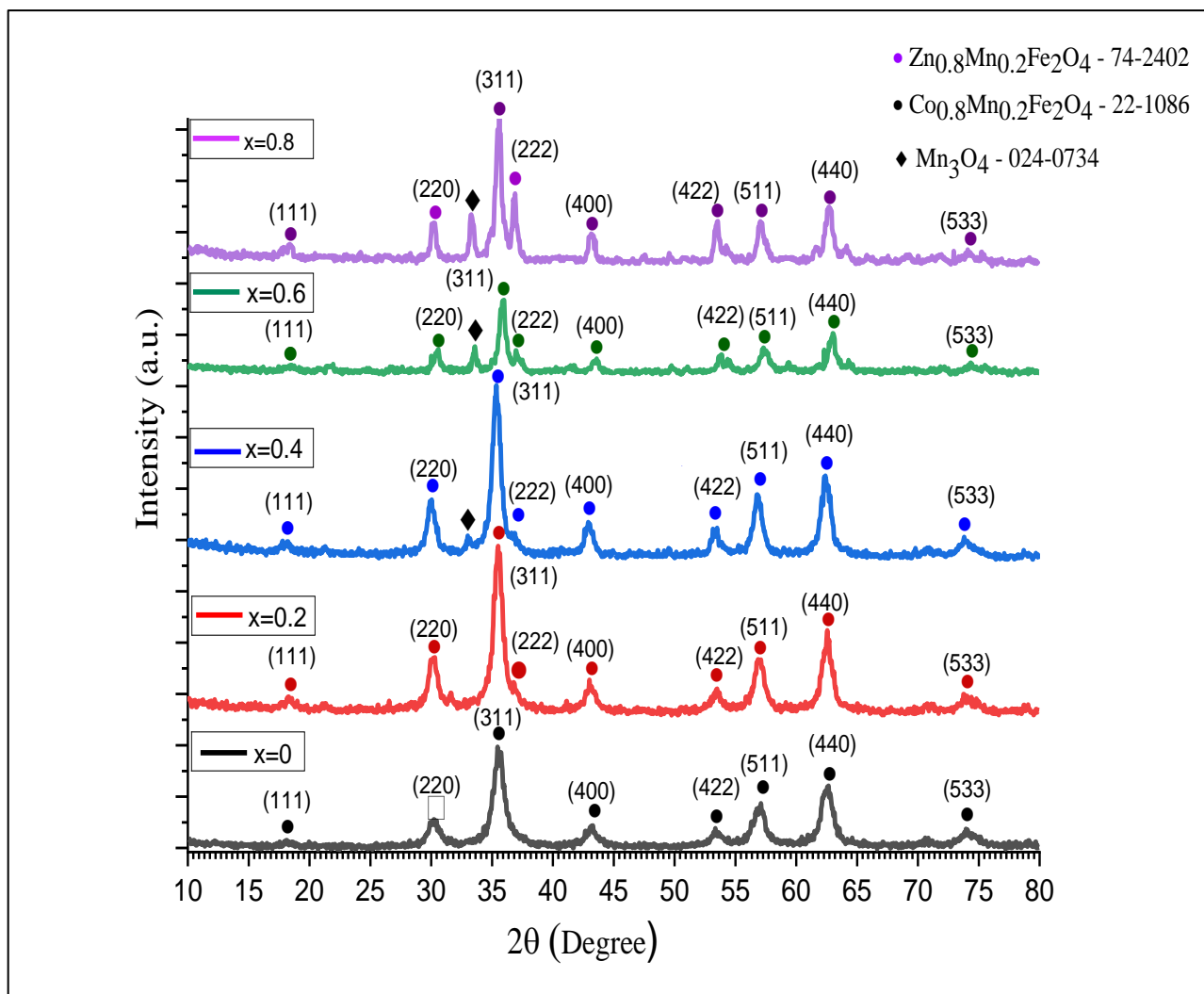


Figure 4.2: XRD patterns of  $(\text{Co}_{0.8-x}\text{Zn}_x\text{Mn}_{0.2}\text{Fe}_2\text{O}_4)$  nanoparticles.

The molecular weight (M W) and a unit cell's volume (V) are proportional to the X-Ray density  $\rho_x$  ( $\text{g cm}^{-3}$ ). It has an inverse relationship with the cubic unit cell. Using equation 2.23, X-Ray density is estimated from X-ray data and entered into the table 4.1. The molecular mass of substituted ion zinc ( $65.384 \text{ g mol}^{-1}$ ) is higher than that of cobalt ( $58.9332 \text{ g mol}^{-1}$ ) and zinc addition lowers the lattice constant. As a result, a rise in zinc causes an increase in density.

Table 4.1 shows the crystallite size (D) calculated using Scherer's equation 2.24. The strongest reflection was calculated in the (311) plane. X-ray diffraction from cations located at A and B sites causes the highest intensity at the plane (311) [232]. Because of the substitution of  $Zn^{2+}$  with  $Co^{2+}$  in the ferrite structure, the crystallite size has increased with increasing ionic radius. Similarly, it can be seen from table 4.1 that zinc substitution has an effect on crystallite size because crystallite sizes are highly influenced by electronic configuration, cation distribution, binding energies, and ionic radius [233]. Finally, the equations (2.25a, 2.25b, and 2.25c) were used to compute the hopping length (L). Table 4.1 shows that as the zinc concentration rises, the spaces among cations (B-B), (A-B), plus (A-A) of the nanoferrite system reduction. The fact that a component with larger ion radii,  $Co^{2+}$ , was substituted with an ion with smaller ion radii,  $Zn^{2+}$ , explains it.

Table 4.1: XRD data of  $Co_{0.8-x}Zn_xMn_{0.2}Fe_2O_4$  nanoparticles.

| (x) | Lattice constant | X-ray density            | Molecular mass | crystallite size ( $D_{311}$ ) | Hopping length (Å) |           |           |
|-----|------------------|--------------------------|----------------|--------------------------------|--------------------|-----------|-----------|
|     | $a_{exp}(Å)$     | $\rho_x(\frac{g}{cm^3})$ | $g\ mol^{-1}$  | $D_{ave}(nm)$                  | $L_{A-A}$          | $L_{B-B}$ | $L_{A-B}$ |
| 0.0 | 8.45             | 5.147                    | 233.82         | 14.47                          | 3.658              | 2.987     | 3.503     |
| 0.2 | 8.43             | 5.212                    | 235.11         | 13.5                           | 3.650              | 2.980     | 3.494     |
| 0.4 | 8.40             | 5.297                    | 236.4          | 12.62                          | 3.637              | 2.9698    | 3.482     |
| 0.6 | 8.39             | 5.345                    | 237.69         | 11.87                          | 3.632              | 2.966     | 3.478     |
| 0.8 | 8.38             | 5.393                    | 238.98         | 8.54                           | 3.628              | 2.962     | 3.474     |

### 4.2.2 Fourier transform infrared (FTIR) Spectroscopic Analysis

Pyrrole oxidative polymerization in nanofibers was confirmed using FTIR spectroscopy. Figure 4.3 shows FTIR bands that are quite similar to those found in the literature for polypyrrole [234,235]. The bands at 1558 and 1415  $\text{cm}^{-1}$  correspond with the basic vibration for the polypyrrole ring, while the band at 1026  $\text{cm}^{-1}$  corresponds to the =C–H in-plane vibrations. The C–N stretching vibrations corresponded to the band at 1173  $\text{cm}^{-1}$ , whereas the C=O and N–H wagging were responsible for the bands at 1703 and 1640  $\text{cm}^{-1}$ . In the domain between 4000 and 2500  $\text{cm}^{-1}$ , all of the spectra have a large adsorption band, which is typically assigned to the adsorption band of O–H, C–H, and N–H groups [236]. Table 4.2 shows all FTIR peaks of PPy-NFs.

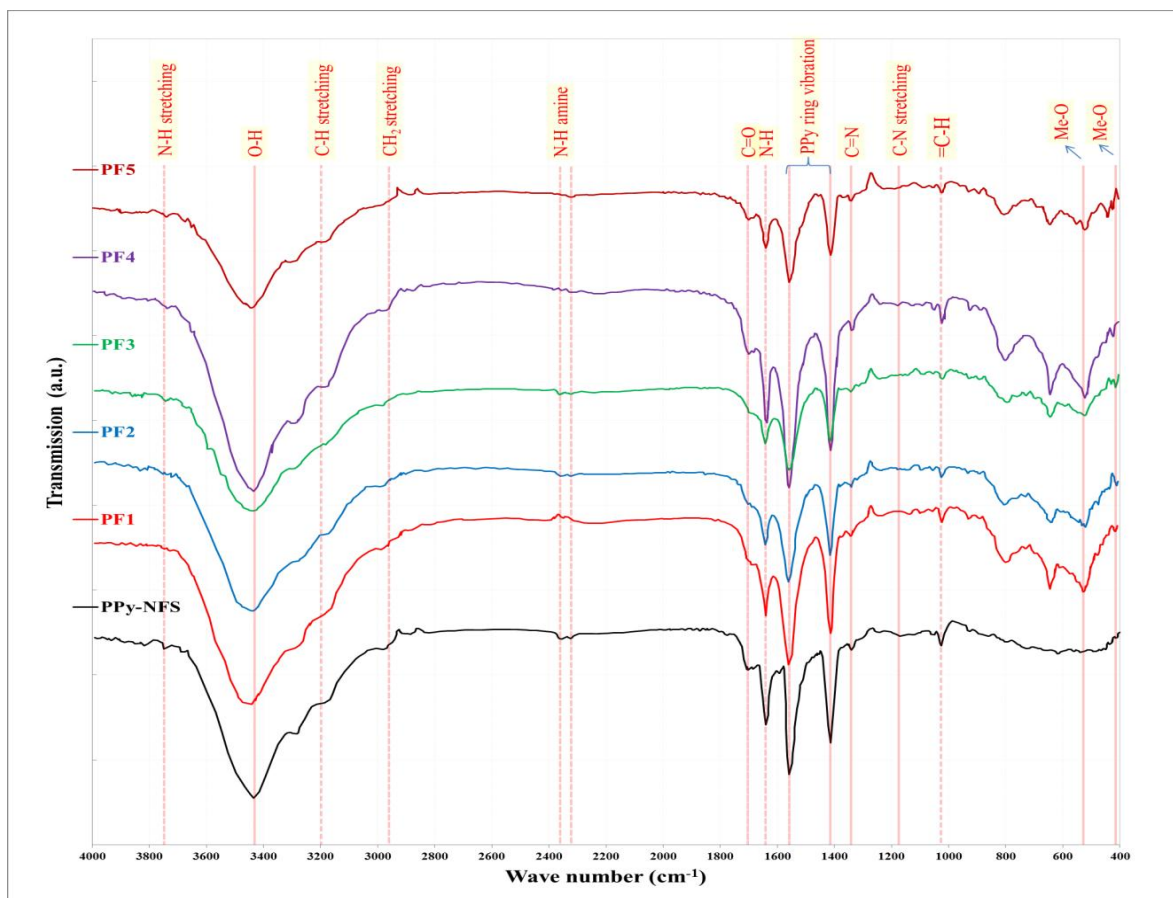


Figure 4.3: FTIR spectra for PPy-NFs and PPy-NFs nanocomposites include PF1, PF2, PF3, PF4 and PF5.

Table 4.2: FTIR absorption bands for PPy-NFs and PPy-NFs nanocomposites include PF1, PF2, PF3, PF4 and PF5.

| Band Type                  | PPy-NFs | PF1     | PF2     | PF3     | PF4     | PF5     |
|----------------------------|---------|---------|---------|---------|---------|---------|
| N-H stretching             | 3747.33 | 3756.27 | -       | -       | -       | -       |
| O-H                        | 3432.05 | 3454.41 | 3440.99 | 3443.23 | 3436.52 | 3443.23 |
| C-H stretching             | 3197.27 | 3208.45 | 3183.85 | -       | 3203.98 | 3199.50 |
| CH <sub>2</sub> stretching | 2960.25 | 2951.30 | 2987.08 | -       | 2973.66 | -       |
| N-H amine                  | 2360.99 | -       | -       | -       | -       | -       |
|                            | 2322.98 | -       | -       | -       | -       | -       |
| C=O                        | 1703.60 | 1696.89 | 1697.50 | 1696.89 | 1703.60 | 1705.84 |
| N-H                        | 1640.99 | 1640.99 | 1645.47 | 1640.99 | 1638.76 | 1640.99 |
| PPY-ring vibration         | 1558.26 | 1562.73 | 1560.50 | 1556.02 | 1558.26 | 1558.26 |
|                            | 1415.16 | 1417.39 | 1417.39 | 1419.63 | 1412.92 | 1412.92 |
| C=N                        | 1341.37 | 1343.60 | 1341.37 | 1314.53 | 1339.13 | 1341.37 |
| C-N stretching             | 1173.66 | 1198.26 | -       | -       | -       | -       |
| =C-H                       | 1026.09 | 1023.85 | 1030.56 | 1021.61 | 1023.85 | 1023.85 |

In figure 4.4, the FTIR spectra of ferrite nanoparticles in the (4000-300)  $\text{cm}^{-1}$  region is shown as transmittance versus wavenumber. The characteristic peaks at about  $\approx 625 \text{ cm}^{-1}$  and  $\approx 350 \text{ cm}^{-1}$  which correlates to M-O (metal-oxygen) intrinsic stretching vibrations at octahedral and tetrahedral positions, respectively [237].

In the domain between 4000 and 1250  $\text{cm}^{-1}$ , A large adsorption band can be found in all the spectra which are typically attributed to the O-H, N-H, in addition to C-H adsorption bands. Based on the ion radius at octahedral and tetrahedral positions, the peak site for the (Fe-O) iron-oxygen bond between

split-bands is given at figure 4.4. Furthermore, the bonds lengths are inversely proportional with a wavenumber. Because the ion radii of positioned cations at A-places are lesser than that of B-places, the length of bond in A-places will be smaller. As a result, the bonds at A-places vibrating more quickly. The substantial variation in vibrational frequency reflects changes in the lengths of bond of metal ion complexes present in ferrite's spinel construction. With rising  $Zn^{2+}$  ion concentration, the higher vibrational frequency ( $\nu_1$ ) appears to be growing while the lower vibrational frequency ( $\nu_2$ ) appears to be dropping. It can be deduced based on the position of a certain metal ion in the spinel structure between A and B-sites, as well as the ionic radius at the A-site where  $Zn^{2+}$  is substituted by  $Co^{2+}$ . When the amount of zinc added to the compound is increased, the bond length shortens.

The peak site of Fe-O (iron-oxygen) bond at the B-place specific among the split-band in absorption bands according to Waldron-supposed i.e.  $\nu_1/\nu_2 \approx 1.41421$  [238]. That is, it corresponds to the calculated values in the table 4.3.

The force constants of the octahedral positions ( $k_O$ ) as well tetrahedral positions ( $k_T$ ) were computed via formula 2.27 listed in table 4.3.

With increased  $Zn^{2+}$  level,  $k_T$  increases while  $k_O$  drops. Furthermore, the computed values of  $k_T$  are bigger than those of  $k_O$ , implying that the band frequency associated with tetrahedral sites is higher than that associated with octahedral position. The length of bond values of A-position, on the other hand, are less than those of B- position. This is because the bond length and the force constants are inversely proportional [239]. Also, the influence of the lower mass ( $\mu$ ) on the force constants results.

Table 4.3: FTIR data for ferrite nanoparticles.

| The samples   | $\nu_1$<br>( $\text{cm}^{-1}$ ) | $\nu_2$<br>( $\text{cm}^{-1}$ ) | $k_T \times 10^5$<br>dynes $\text{cm}^{-1}$ | $k_O \times 10^5$<br>dynes $\text{cm}^{-1}$ | $\nu_1/\nu_2$ |
|---|---------------------------------|---------------------------------|---|---|---------------|
| $\text{Co}_{0.8} \text{Mn}_{0.2} \text{Fe}_2\text{O}_4$                 | 561.2                           | 417                             | 2.310                                       | 1.266                                       | 1.34          |
| $\text{Co}_{0.6} \text{Zn}_{0.2} \text{Mn}_{0.2} \text{Fe}_2\text{O}_4$ | 557                             | 424.3                           | 2.275                                       | 1.320                                       | 1.31          |
| $\text{Co}_{0.4} \text{Zn}_{0.4} \text{Mn}_{0.2} \text{Fe}_2\text{O}_4$ | 569                             | 422.4                           | 2.374                                       | 1.308                                       | 1.34          |
| $\text{Co}_{0.2} \text{Zn}_{0.6} \text{Mn}_{0.2} \text{Fe}_2\text{O}_4$ | 582.5                           | 408.9                           | 2.488                                       | 1.226                                       | 1.42          |
| $\text{Zn}_{0.8} \text{Mn}_{0.2} \text{Fe}_2\text{O}_4$                 | 592.1                           | 407.9                           | 2.571                                       | 1.219                                       | 1.45          |

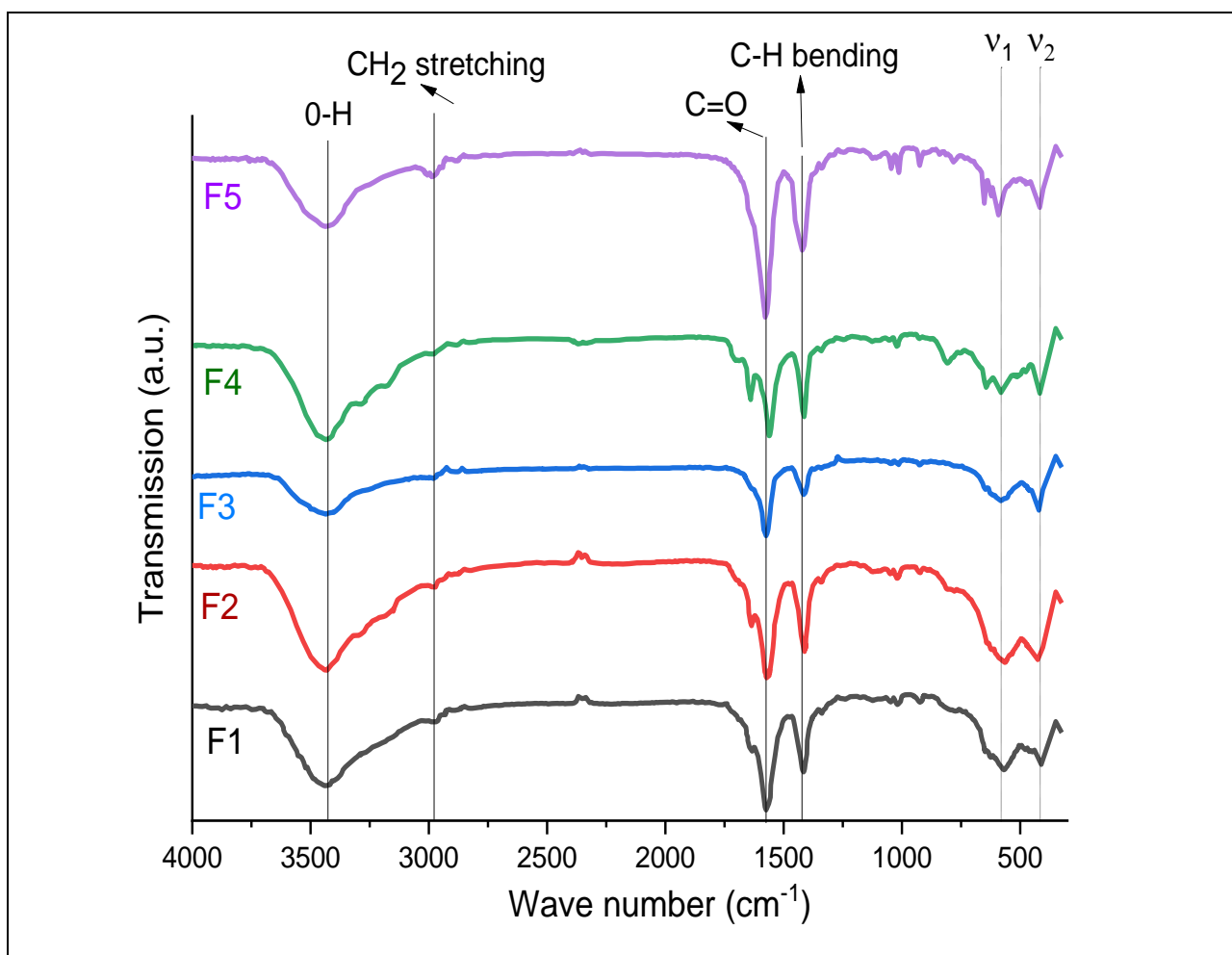
Figure 4.4: FTIR spectrum of  $\text{Co}_{0.8-x}\text{Zn}_x\text{Mn}_{0.2}\text{Fe}_2\text{O}_4$  samples.

Fig. 4.3 displays the FTIR spectra attained of polypyrrole-nanofibers as well as polypyrrole-nanofibers nanocomposites. The distinguishing peaks of polypyrrole-nanofibers at  $1560\text{ cm}^{-1}$   $1417\text{ cm}^{-1}$  and etc. were detected in the polypyrrole-nanofibers nanocomposites FTIR spectra.

It's worth noting that in practically all nanocomposite samples, the PPy-NFs peak broadens somewhat at bands, and the ferrite peaks are scarcely visible. Each of the peaks detected in the finger print area of polypyrrole-nanofibers were also visible in the FTIR spectra of polypyrrole-nanofibers nanocomposites, representing that the main components for polypyrrole-nanofibers as well as their nanocomposite with ferrite had the similar chemical construction.

Incorporation of ferrite and development of Hybrid organic-inorganic resulted in a minor alter of the FTIR bands from its pristine site. Physical interactions between active sites in PPy-NFs and ferrite nanoparticles are responsible for this modest shift in peak location, indicating that PPy-NFs chains are well mixed or enclosed by ferrite nanoparticles [240,241]. (Also confirmed by FESEM images). Table 4.2 summarizes the assignments of the bands that characterize PPy-NFs nanocomposites at different ferrite volume ratios.

### 4.2.3 FESEM image analysis

The topographical and morphological features of composites and pure materials are revealed via FE-SEM. Figure 4.5 shows FESEM images of (PPy-NFs) samples generated utilizing the oxidative polymerization technique. All of the samples contain (1D) nanofibers, which have a rough surface and vary in diameter, with tens of microns in length and diameters ranging from  $\sim 50$  to  $\sim 130$  nm. The micrograph clearly demonstrates a typical

FESEM image of doped PPy-NFs, as well as the fact that nanostructures are formed by a network of densely entangled twisted and coarse nanofibers.

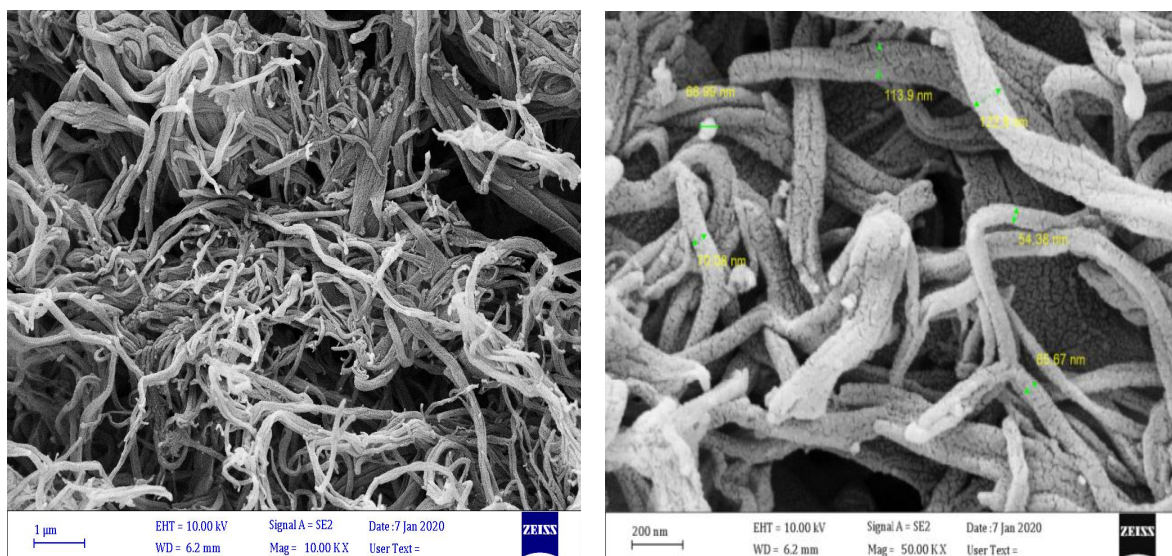
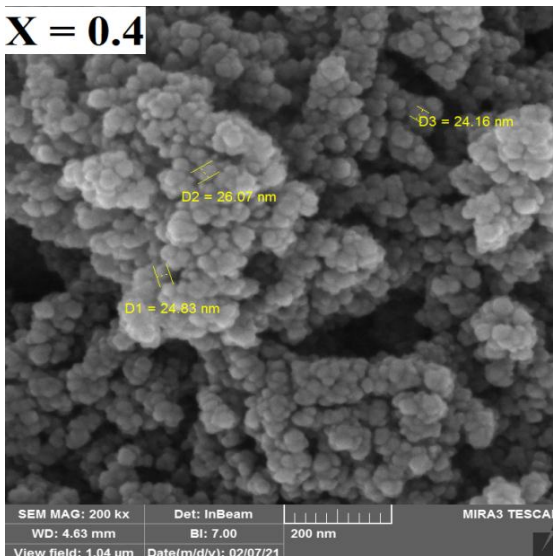
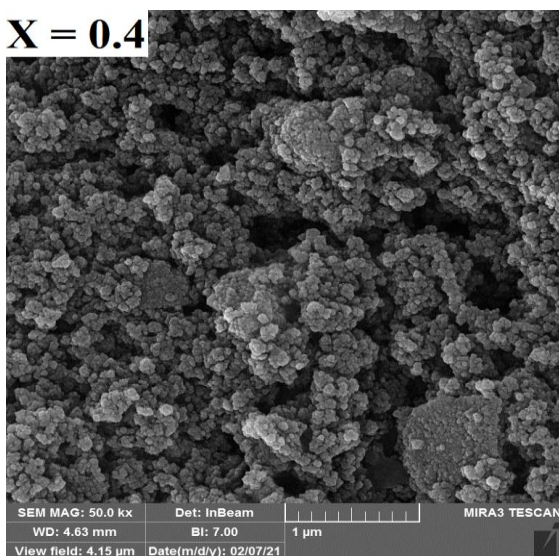
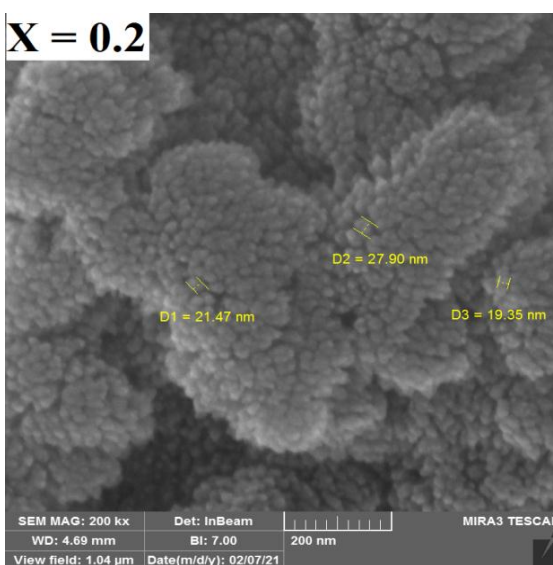
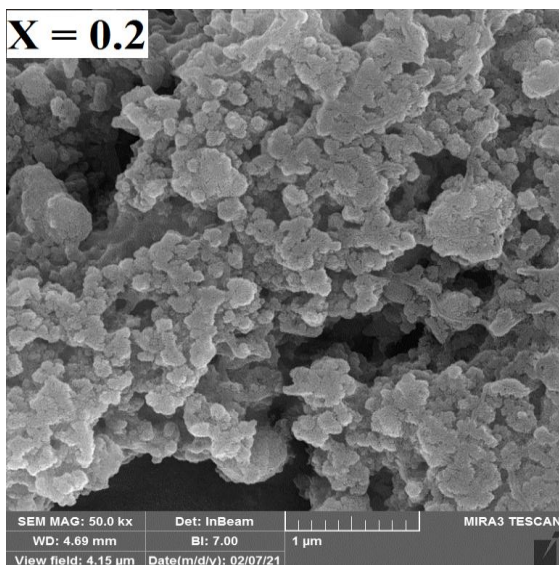
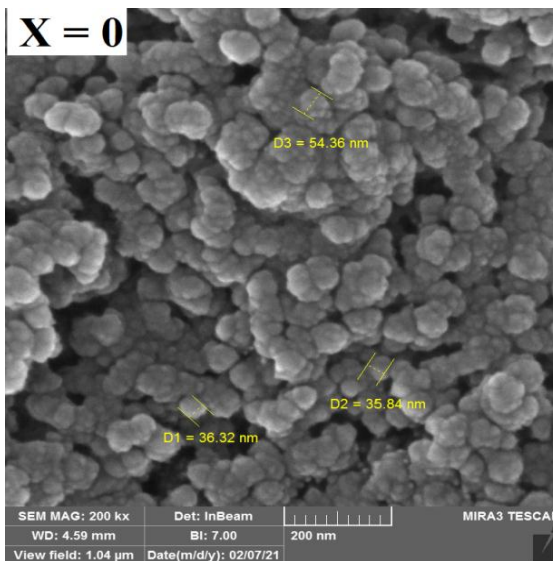
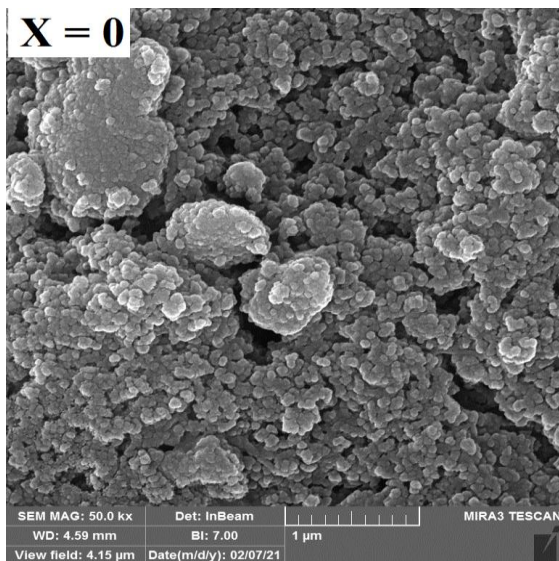


Figure 4.5: FESEM images of PPy-NFs at different magnification.

Figure 4.6 shows a FESEM image of ferrite nanoparticles with a denser view of the powder sample and relatively homogenous grain distribution. In addition, the magnetic particles in the arrangement were closely packed and harmonic. These micrographs show nearly spherical particles with the size distributed in a range of  $\sim(55-35)$ ,  $\sim(28-20)$ ,  $\sim(26-24)$ ,  $\sim(26-21)$  and  $\sim(20-13)$  nm for  $(\text{Co}_{0.8}\text{Mn}_{0.2}\text{Fe}_2\text{O}_4)$ ,  $(\text{Co}_{0.6}\text{Zn}_{0.2}\text{Mn}_{0.2}\text{Fe}_2\text{O}_4)$ ,  $(\text{Co}_{0.4}\text{Zn}_{0.4}\text{Mn}_{0.2}\text{Fe}_2\text{O}_4)$ ,  $(\text{Co}_{0.2}\text{Zn}_{0.6}\text{Mn}_{0.2}\text{Fe}_2\text{O}_4)$  and  $(\text{Zn}_{0.8}\text{Mn}_{0.2}\text{Fe}_2\text{O}_4)$  samples respectively. As a result, the surface morphological and microstructure images match the XRD data quite well. There were only a few pores among the particles in the samples. The magnetic nanoparticles tended to clump together because of their magnetic properties. Furthermore, developing forces such as capillary, electrostatic, and Van-der-Waal forces generate mutual interactions between nanoparticles, causing agglomeration.



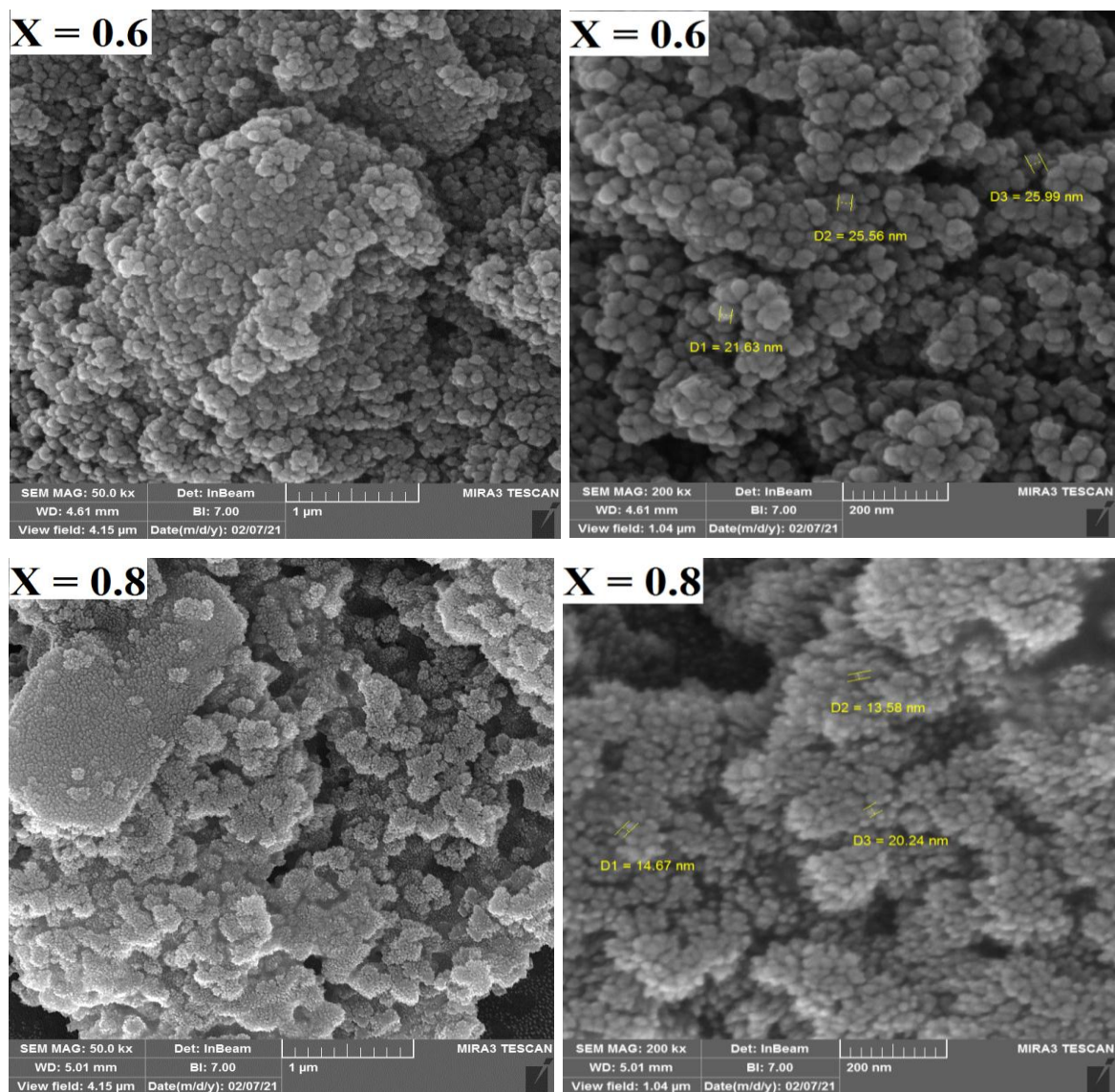
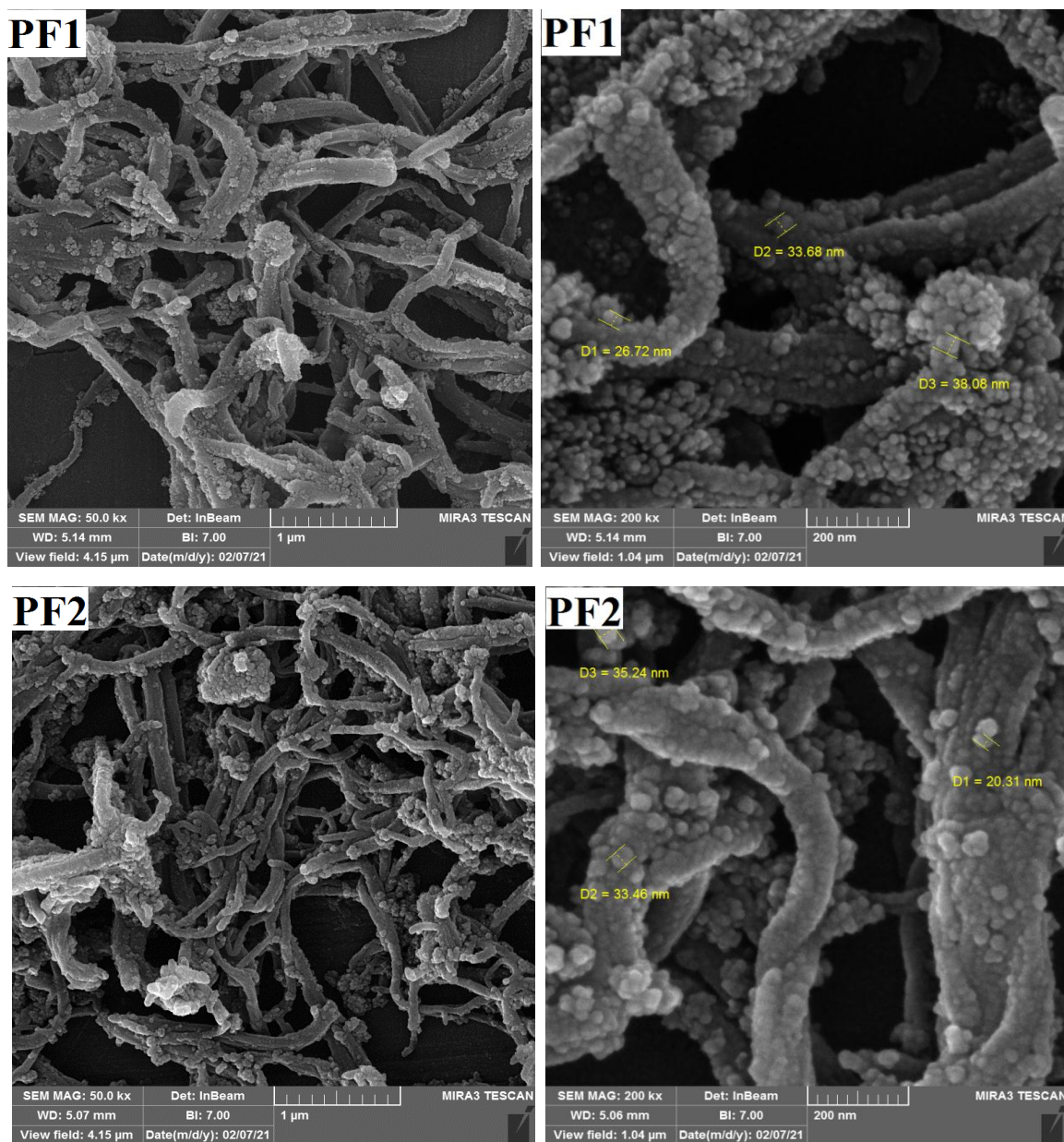


Figure 4.6: FESEM images of  $(\text{Co}_{0.8-x}\text{Zn}_x\text{Mn}_{0.2}\text{Fe}_2\text{O}_4)$  samples ( $x = 0, 0.2, 0.4, 0.6$  and  $0.8$ ) at different magnification.

The PPy-NFs nanocomposites were decorated in the form of a grainy surface structure. FESEM had detected it. The FESEM pictures in figure (4.7) demonstrate that the samples had both ferrite nanoparticles piled on the surface of the PPy-nanofibers. As a result, the figures show a progressive increase in ferrite on polymer fibers and an improvement in ferrite particle attachment. On the conductive polymer matrix, the magnetic particles are evenly distributed. This signified that the composites had been thoroughly

combined and blended. The ferrite concentration appears to be beneficial in occupying polymer porous sites and increasing interaction surface area and surface energy. All of these factors contribute to improvements in structural and electrical properties. As a result, the physical attributes of the material, such as shape, size, appearance, and condition, would alter without changing the internal structure. Because the roughness of the fiber has a considerable impact on the particle-fiber adhesion strength.



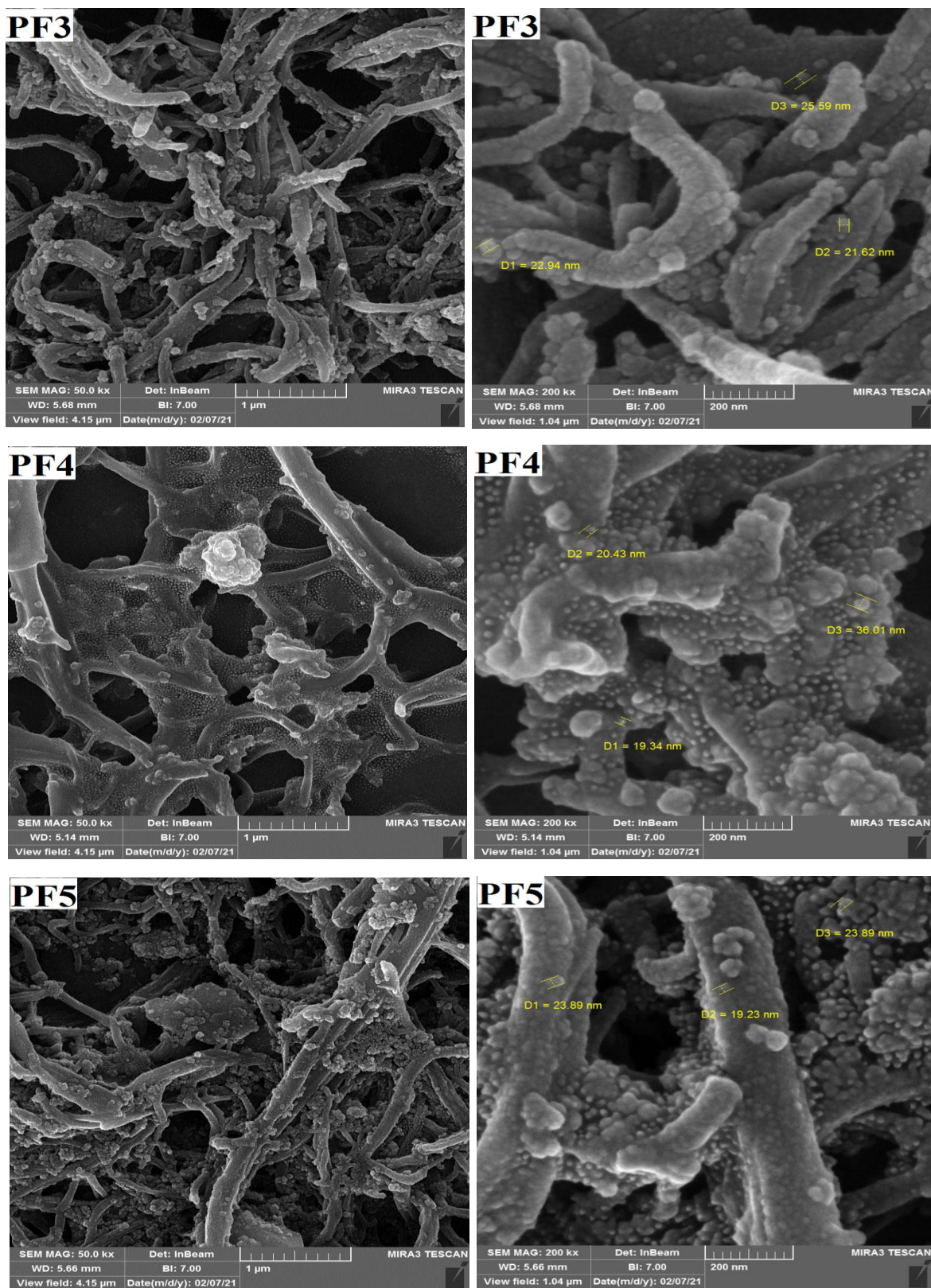


Figure 4.7: FESEM images of PPy-NFs nanocomposites samples at different magnification.

### 4.3 Magnetic Properties

Figure 4.8 depicts the magnetization of polypyrrole nanofibers (PPy-NFs), Ferrite nanoparticles, and PPy-NFs nanocomposites samples at 27 degrees Celsius with an applied magnetic field (H) ranging from -10 to +10 kOe. The magnetic characteristics of PPy-NFs are observed to be dependent on the amount of oxidant (Iron (III) chloride). At 10 KOe, the maximum magnetization ( $M_s$ ) of PPy-NFs is 14.95 emu/g, with a retentivity ( $M_r$ ) of 0.58 emu/g and a coercivity ( $H_c$ ) of 74.54 Oe. There is no question that during the polymerization process in the presence of impurity material, there is a link between the magnetization of materials and their internal atomic structure ( $FeCl_3$ ). As a result, interactions between non-magnetic PPy-NFs chains and  $Fe^{+3}$  ions are responsible for magnetization in the (PPy-NFs) polymer [242].

It may be possible to explain the interactions the  $Fe^{+3}$  ions with non-magnetic Polypyrrole chains. The interaction of the PPy polarons with iron species such as  $Fe^{+3}$  ions derived from the Iron(III) chloride oxidant could change the intrinsic local orientation of the polarons, causing the localization of these polarons to act on the magnetic impurities surrounding them, resulting in an effective magnetic field. In other words, the orientation of PPy polarons is determined by the interaction of magnetic impurities and PPy chains. If magnetic impurities are discovered, the interaction between magnetic polarons may be ferromagnetic; the greatest of this effective magnetic field was observed when the spins of the localized charge carriers were parallel [243].

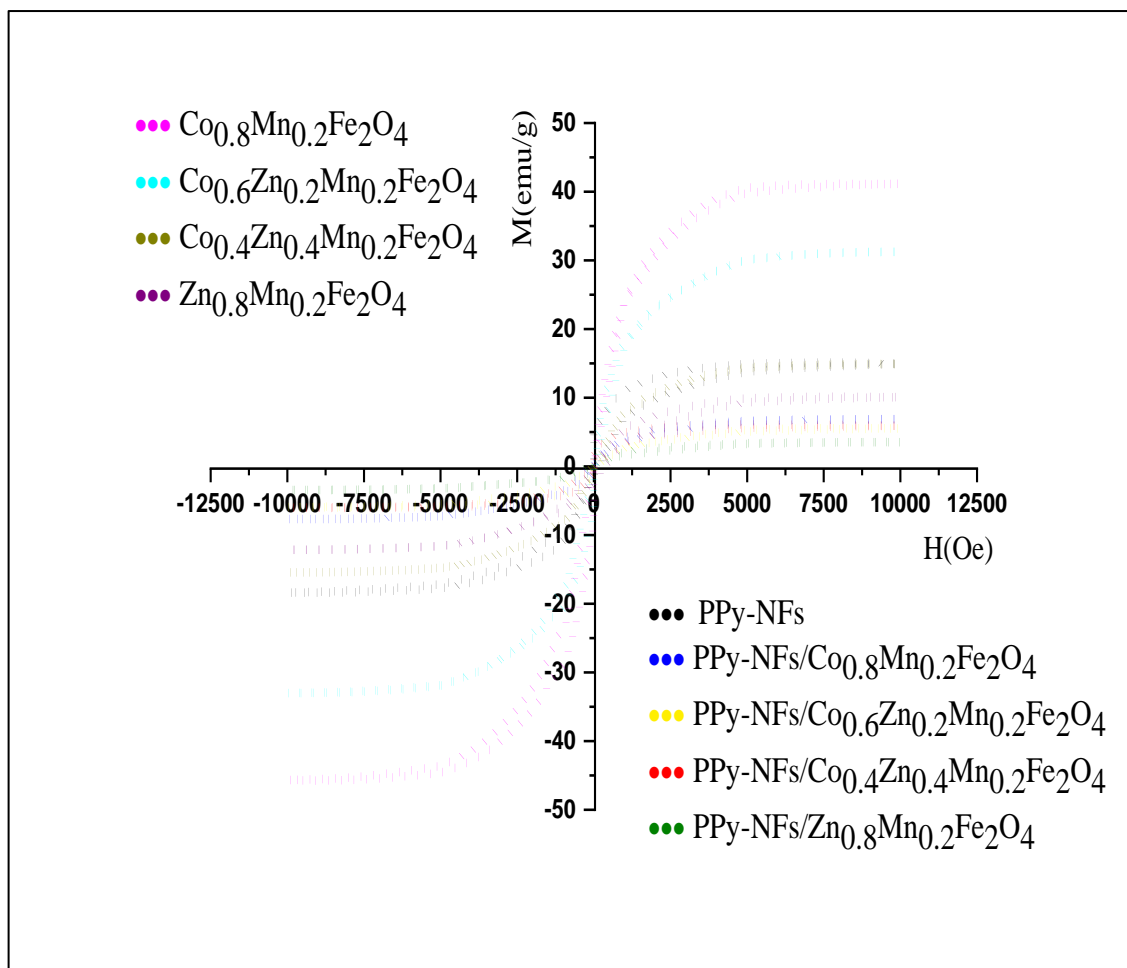


Figure 4.8: Magnetization versus applied magnetic field of PPy-NFs, ferrite nanoparticles and PPy-NFs nanocomposites samples at 300K.

The saturation magnetization ( $M_s$ ), coercivity ( $H_c$ ), and retentivity ( $M_r$ ) of ferrite nanoparticles were shown by the M-H curves ( $M_r$ ). Total magnetic moments in spinel ferrite are determined by the distribution of cations between tetrahedral and octahedral sites, according to Neel [244].

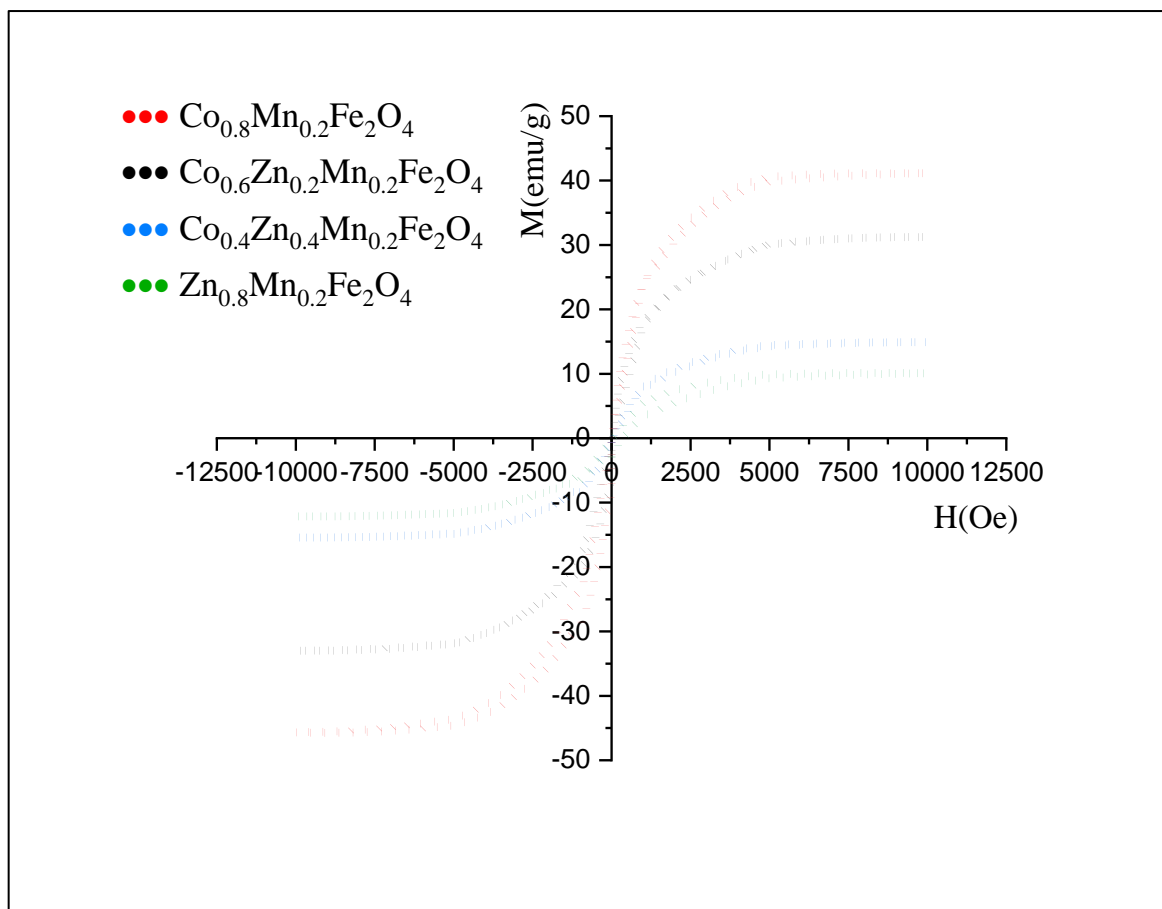


Figure 4.9: Magnetization versus applied magnetic field of  $\text{Co}_{0.8-x}\text{Zn}_x\text{Mn}_{0.2}\text{Fe}_2\text{O}_4$  ( $x=0.0, 0.2, 0.4$  and  $0.8$ ) samples at 300K.

From the Magnetization-magnetic field curves, ( $M_s$ ), ( $M_r$ ) and ( $H_c$ ) values for ferrite nanoparticles were determined and inserted in table (4.4).

There was a noticeable impact of chemical structure on magnetic conduct on Magnetization-magnetic field curves as well as its derivative curves. The value of ( $M_s$ ) decreases as Zinc substitution increases in this study. The decrease in  $M_s$  value with additional nonmagnetic  $\text{Zn}^{2+}$  ions could be attributed to a difference in cation distribution between A-positions and B-positions, which diminishes the spinel-structure's net magnetic moment. Saturation magnetization rises from 10.13 to 41.15 emu/g as Cobalt ions

content rises. This could be due to the fact that  $\text{Co}^{2+}$  ions are doped at interstitial sites rather than  $\text{Fe}^{3+}$  sites in the structural lattice, leading the A-B site's super exchange interaction to be strengthened, resulting in a rise in overall magnetic moment. The magnetic  $\text{Co}^{2+}$  ions replace in the spinel structure, and the magnetic moment's net value rises as the quantity of magnetic ions grows. Whenever  $\text{Fe}^{3+}$  ions at B-positions were substituted by magnetic  $\text{Co}^{2+}$  ions, the magnetic moment of the A-position sublattice ( $M_A$ ) drops while that of the B-position sublattice ( $M_B$ ) increases due to the difference in magnetic moments of  $\text{Fe}^{3+}$  ( $5\mu_B$ ) and  $\text{Co}^{2+}$  ( $3\mu_B$ ). As a result, the value of  $M$ , which equals  $M_B - M_A$  [245], the net magnetic moment, will increase.

The magnetic properties of ferrite systems are known to be influenced by magnetocrystalline anisotropy, lattice defects, dislocations, internal stresses, grain size and shape, porosity, and secondary phases. The observed change in coercivity in the current study could be attributable to a decrease in particle size and the distribution of  $\text{Fe}^{3+}$  ions [246].

The magnetic effect in the PPy-NFs nanocomposite samples was noticeable. The composite samples' saturation magnetization and retentivity were lower than pure ferrite particles.  $M_s$ ,  $M_r$ , and  $H_c$  all decreased as the number of magnetic nanoparticles in the samples decreased, which is mostly determined by the magnetic ferrite volume fraction. Furthermore, PPy-NFs contributed to the isolation of magnetic particles and the noncollinearization of ferrite's collinear ferromagnetic order, causing ferromagnetic order disruption. Furthermore, surface spin-pinning for magnetic moments at the ferrite/support interface may occur, resulting in a drop in ferrite particle magnetic-surface anisotropies [247]. As a result, the coercivity of PPy-

NFs/ferrite nanocomposites is generally lower than that of pure ferrite samples [27]. As a result of the above, we may deduce that doping type volume fraction, grain growth, amount of oxidant, bulk density, anisotropy, and surface are all factors that can affect magnetic properties. Based on the M-H curves, the variables of ( $M_s$ ), ( $M_r$ ) and ( $H_c$ ) for PPy-NFs nanocomposite samples were determined and inserted in table (4.4).

Table 4.4: The magnetic parameters for PPy-NFs, ferrite nanoparticles and PPy-NFs nanocomposite samples.

| The Samples                                | $M_s$<br>(emu/g) | $M_r$<br>(emu/g) | $H_c$<br>(Oe) |
|--|------------------|------------------|---------------|
| PPy-NFs                                    | 14.95            | 0.58             | 74.54         |
| $Co_{0.8}Mn_{0.2}Fe_2O_4$                  | 41.15            | 0.45             | 13.25         |
| $Co_{0.6}Zn_{0.2}Mn_{0.2}Fe_2O_4$          | 31.24            | 0.73             | 35.7          |
| $Co_{0.4}Zn_{0.4}Mn_{0.2}Fe_2O_4$          | 14.91            | 0.197            | 22.72         |
| $Zn_{0.8}Mn_{0.2}Fe_2O_4$                  | 10.13            | 0.22             | 35.07         |
| PPy-NFs/ $Co_{0.8}Mn_{0.2}Fe_2O_4$         | 6.87             | 0.2              | 27.5          |
| PPy-NFs/ $Co_{0.6}Zn_{0.2}Mn_{0.2}Fe_2O_4$ | 5.55             | 0.045            | 9.65          |
| PPy-NFs/ $Co_{0.4}Zn_{0.4}Mn_{0.2}Fe_2O_4$ | 6.08             | 0.084            | 13.10         |
| PPy-NFs/ $Zn_{0.8}Mn_{0.2}Fe_2O_4$         | 3.54             | 0.163            | 13.15         |

#### 4.4 Optical properties

Optical spectroscopy is a useful technique for studying the behavior of nanocomposites and the conducting states that correspond to the absorbance bands of conducting polymers' inter and intra gap states (CPs). The

absorption spectra for PPy-NFs acquired across the range (200-1100) nm are shown in figure 4.10.

The spectra of PPy-NFs has a peak at 315 nm and a broad absorption band between 450 and 550 nm. The first peak played a role in the  $\pi - \pi^*$  interband shift. Transition from the VB to the neutral state CB of PPy-NFs, which is indicative of PPy production. The presence of polymerization is revealed by the broad absorption band. It could be attributed to polaron band transitions that match. The free carrier tail of oxidized polypyrrole is shown by a high absorption after  $\sim 600$  nm. Depending on the chain length, the absorption peak varies as the number of accessible delocalized electrons increases. This UV-Vis spectrum confirms that the substance generated is polypyrrole. The ratio of the two absorbance maxima indicates the polymer's doping level, which is determined by the oxidation degree and conjugation length [248].

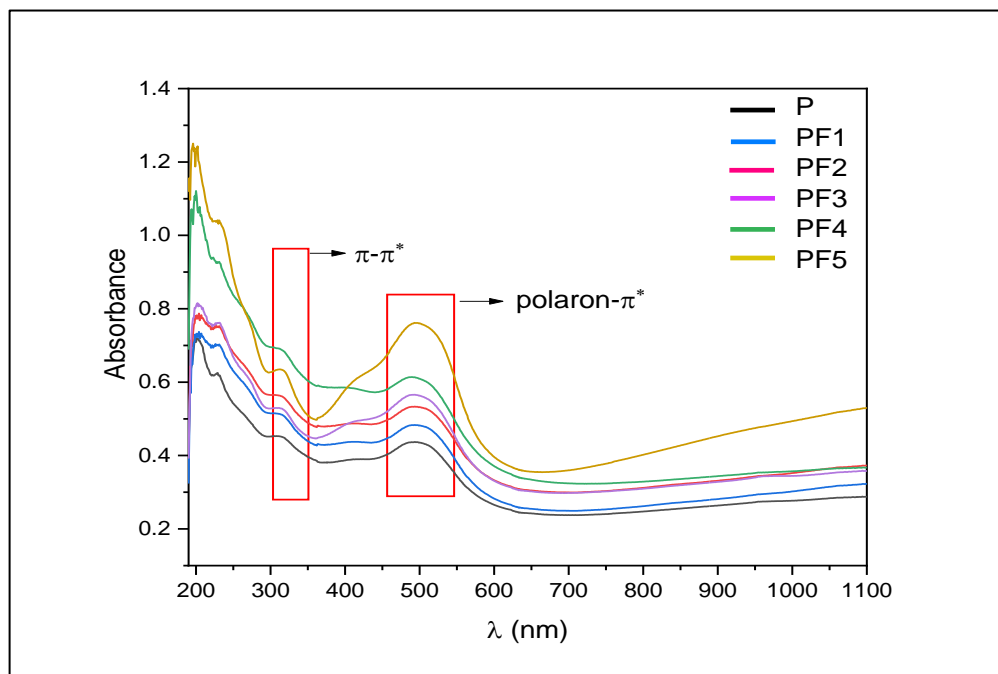


Figure 4.10: The absorption spectra for PPy-NFs and PPy-NFs nanocomposites.

Figure 4.11 represents the plot between  $(\alpha h\nu)^2$  and  $h\nu$  for PPy-NFs model. The optical energy band gap of the PPy-NFs sample was measured to be about 3.90 eV.

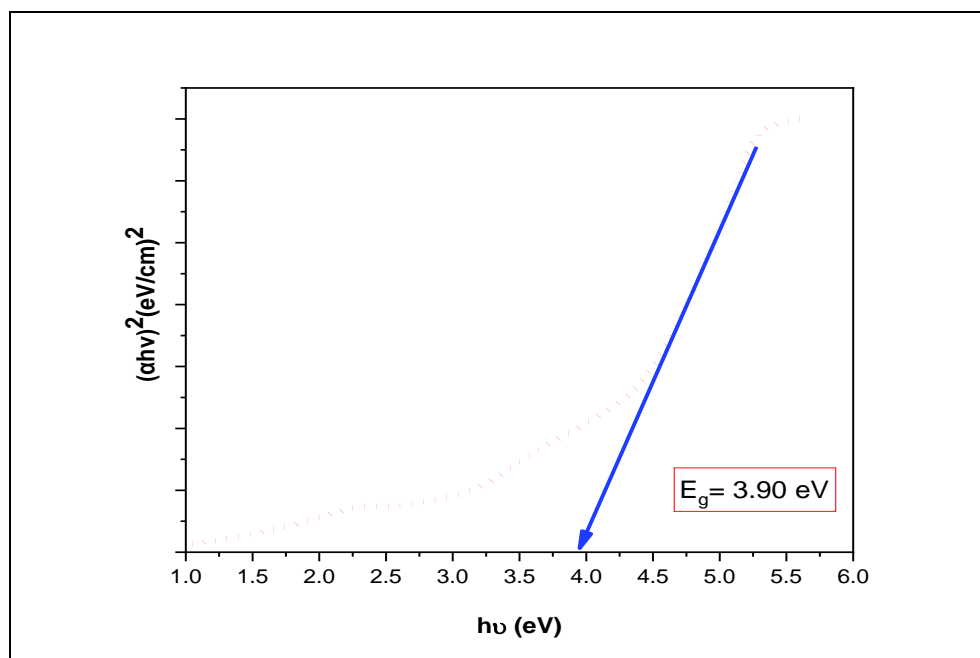


Figure 4.11:  $(\alpha h\nu)^2$  vs.  $(h\nu)$  plots for pure PPy-NFs.

After creating a properly sonicated colloidal solution of ferrite with distilled water as the solvent, the absorption spectra of the obtained samples for ferrite nanoparticles were also investigated. Anywhere within the electromagnetic spectrum, molecules, atoms, and ions can conduct an electronic transition from of the ground state towards the excited state.

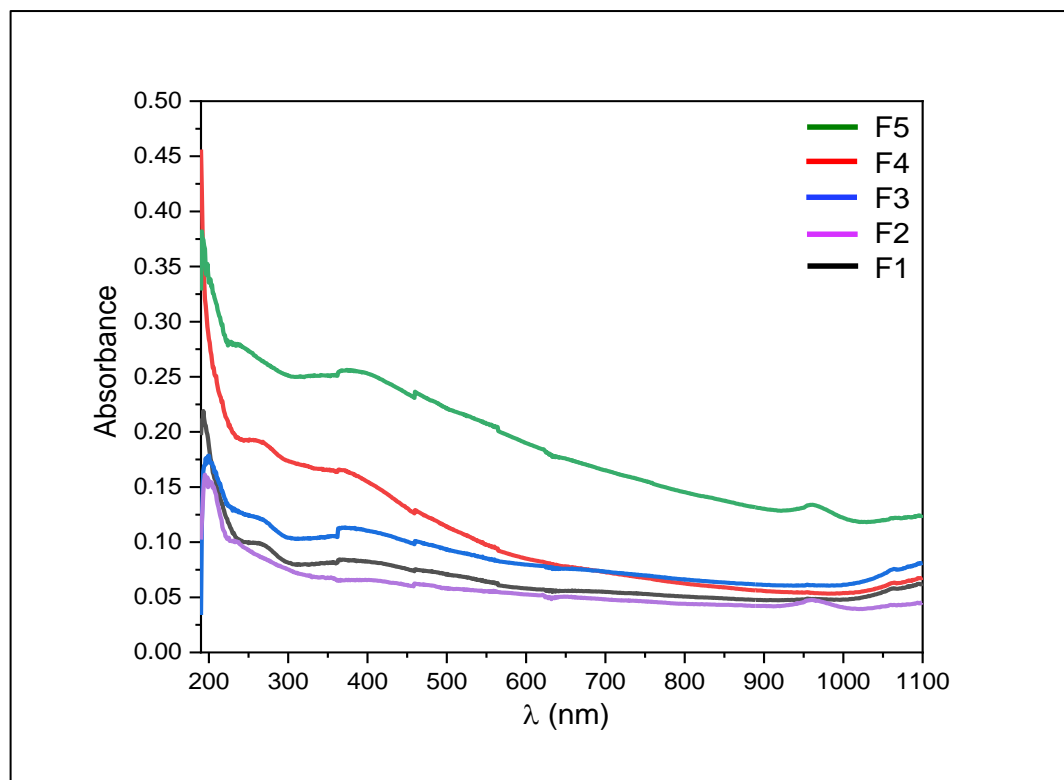


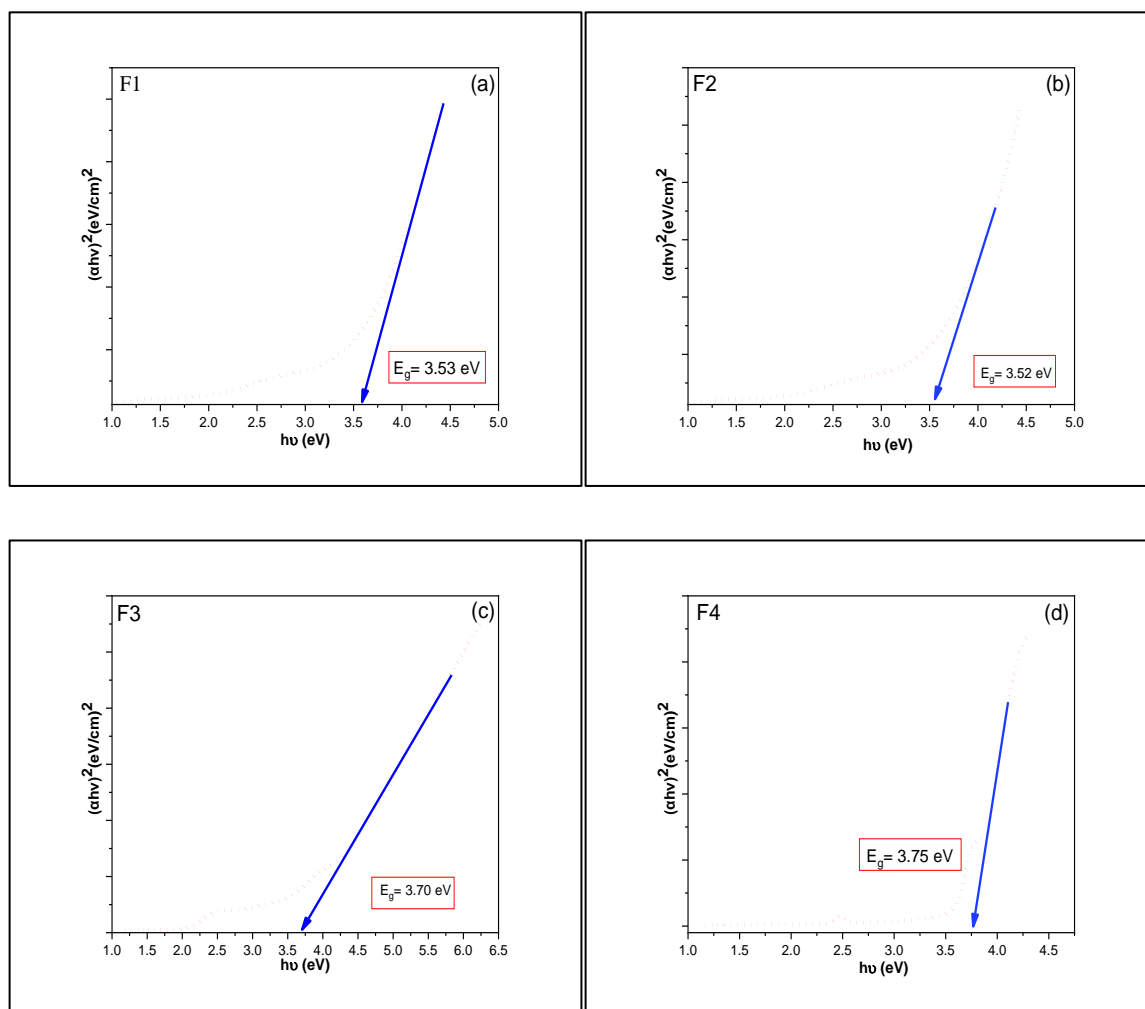
Figure 4.12: The absorption spectra for ferrite nanoparticles samples.

Figure 4.12 shows that when the concentration of Zinc increases, the absorbance increases, indicating structural changes caused by variations in doping percentage, which can be attributed to the localized conductivity levels introduced by  $Zn^{2+}$  cations. Short wavelengths (high energies) increase absorption, which corresponds to the material's energy gap (when the incident photon has an energy equal or more than the energy gap value). This is due to the interaction of material electrons with incoming photons that have sufficient energy to cause electron transitions.

Figure 4.12, represents the absorbance spectra for nanoferrit samples recorded over the range (200–1100) nm. Figure 4.13 represents the plot between  $(\alpha h\nu)^2$  and  $h\nu$  for F1, F2, F3, F4 and F5 samples. The optical energy

bandgap value of their samples are about 3.53eV, 3.52eV, 03.70eV, 3.750eV and 03.80eV respectively.

It's worth noting that replacing Co with Zn results in a rise in  $E_g$ . As is well known, many factors such as the presence of impurities, crystalline size, and structural characteristics influence the band gap value. In the above scenario, the rise in energy band gap value can be explained by a decrease in lattice parameter due to an increase in Zn concentration [249]. Similarly, the addition of a Co ion, which shifted Fe's octahedral configuration, increased the electron state in the outer orbital area, lowering the band gap energy [250].



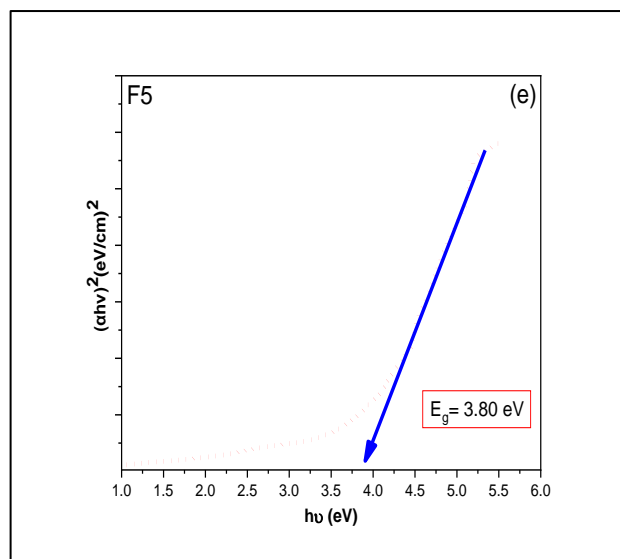


Figure 4.13: Diagrams of  $(\alpha h\nu)^2$  vs.  $(h\nu)$  for F1, F2, F3, F4 and F5 samples.

Figure 4.10 displays the UV-visible absorption spectra for the polypyrrole nanofibers nanocomposites. Understanding the behavior of nanocomposites and the conduction states that correspond to the absorption bands of inter- and intra-gap states of conductive polymers requires the use of optical spectroscopy. Samples of nanocomposites exhibit optical absorbance spectra with peaks in the 300-600 nanometer wavelength regions.

There are two absorption bands at (300,345) nanometer and (455,545) nanometer appear in the UV-Vis absorption spectra of PF1, PF2, PF3, PF4, and PF5. The wavelength band peak (300,345) nm is caused by the  $\pi-\pi^*$  transition of the benzenoid ring. Polaron- $\pi^*$  transitions are responsible for the second peak of the wavelength absorption band (455, 545) nm. In this scenario, the absorption peak positions of PF1, PF2, PF3, PF4, and PF5 nanocomposites were found to be at (308 nm, 488 nm), (307 nm, 489 nm), (312 nm, 491 nm), (310 nm, 494 nm), and (313 nm, 496 nm), respectively. In comparison to the pure PPy NFs, the absorption peaks of the PF1, PF2, PF3,

PF4, and PF5 are quite intriguing to study, albeit with some shift in their positions. The observed shift in the typical peak positions could be attributed to surface alterations or to the interaction between ferrite nanoparticles and polypyrrole. Figure 4.14 represents the plot between  $(\alpha h\nu)^2$  and  $h\nu$  for PF1, PF2, PF3, PF4 and PF5 samples. The optical energy band gap values of their samples are about 4.18eV, 4.20eV, 4.270eV, 04.62eV and 4.95eV respectively.

These optical band gap energy levels can be explained by the distribution of cations at ferrite structure lattice locations. Cobalt ions prefer the octahedral position, while Zn cations favor the tetrahedral position. Fe cations inhabit both the tetrahedral positions and octahedral positions. In a spinel ferrite unit cell, the electrical conduction process is mostly based on electron jumping among ferrous ( $\text{Fe}^{2+}$ ) and ferric ( $\text{Fe}^{3+}$ ) ions at B-position (octahedral symmetry position). this is generally recognized which during the depositing process,  $\text{Co}^{2+}$  and  $\text{Zn}^{2+}$  are oxidized to  $\text{Co}^{3+}$  and  $\text{Zn}^{3+}$ , resulting in the holes. The mechanism of conductivity in ferrites was based on electron jumping among ferrous ( $\text{Fe}^{2+}$ ) and ferric ( $\text{Fe}^{3+}$ ) cations at the B-position, in addition to positive hole jumping. Because the energy of ionization for cobalt ( $3232 \frac{\text{kJ}}{\text{mol}}$ ) is lesser than that of Zn ( $3833 \frac{\text{kJ}}{\text{mol}}$ ), the conversion of  $\text{Co}^{2+}$  to  $\text{Co}^{3+}$  is significantly easier than that of  $\text{Zn}^{2+}$  to  $\text{Zn}^{3+}$ . Furthermore, holes are easily formed in cobalt-rich samples, and the amount of 'concentrations of carrier ' holes rises proportionally as the concentration of cobalt ions increases. the positive holes and the electrons jumping can be caused by a decrease in the resistance of synthesized materials, As a result, the optical band gap energy amounts for composite film models have dropped [251].

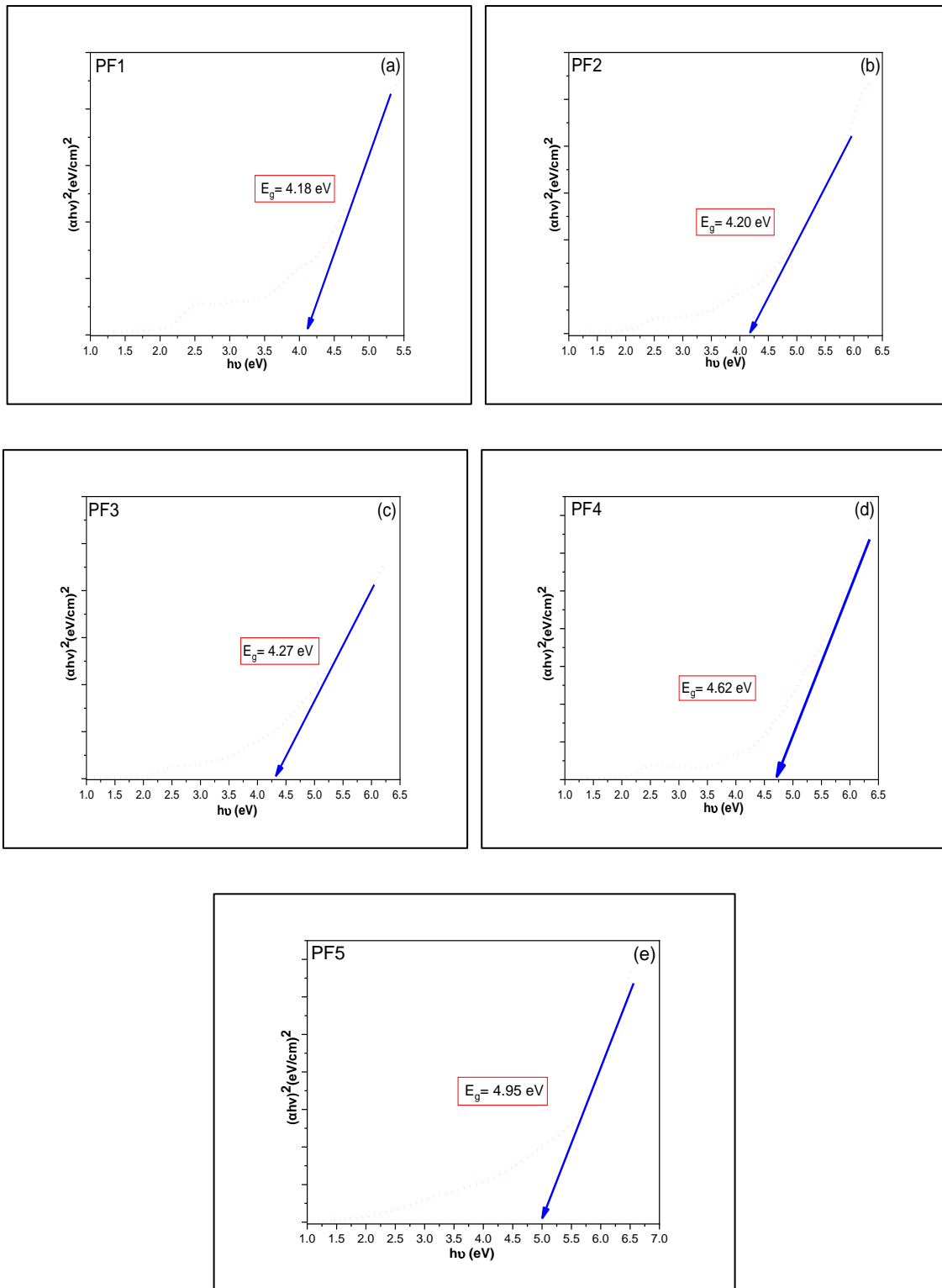


Figure 4.14: Diagrams of  $(\alpha h\nu)^2$  vs.  $(h\nu)$  for PF1, PF2, PF3, PF4 and PF5 samples.

#### 4.5 Photoconductivity of Detectors

PPy-NFs and ferrite nanoparticles, as well as PPy-NFs nanocomposites, were studied with and without light. Doped samples showed increased photocurrents. As a result of these changes in photoconductive characteristics, PPy-NFs nanocomposites of samples are a viable contender for photoconductive applications.

When a sample is illuminated, the sensitivities (S) are used to calculate how much current rises in it. While lighted, conductive polymers improve the conductivity of electrical by converting a light into potential or current, and they might be employed in photoconductive devices [252]. The chemical structures of the (CPs) dictate the effective excitons dissociation to free electrons, thus governs general photoresponse sensitivity [253]. The conductivity rises when the illumination is turned on, and while the illumination is turned off, the current backs to its original rate. As seen in the accompanying figures, this process is repeated multiple times, with the rise and fall times for each condition being around  $\approx 5 \times 10^{-1}$  sec (turn off, turn on). The current time characteristics (I-t) for photoexcitation-induced current in samples were measured at (405 nm) wavelengths with changed illumination powers (ten mW, fifteen mW, twenty mW, plus thirty mW).

The photocurrent responses of pristine polypyrrole-nanofibers (PPy-NFs) in addition to polypyrrole-nanofibers with differ doping levels of differ nanomaterials had examined in the Figures below of PF1, PF2, PF3, PF4, and PF5 to identify the best doped material to generate the greatest detector performance. The photocurrent response achieved its maximum value at a

particular amount of doping, representing that the polypyrrole nanofibers/materials had the highest photosensitivity efficiency.

As seen in the figures below, the dark current value is continuous and nearly constant even after many cycles for each illumination intensity, indicating a functional, repeatable, stable, and active device. The repeatability and optical response speed of photodetectors in applications define their capacity.

Figures 4.15, 4.16, and 4.17, which illustrate the light sensitivity conduct of the pristine CPs (polypyrrole nanofibers) and when polypyrrole nanofibers (PPy-NFs) are doped with variable concentrations of differ particles, indicate the changes in photocurrent responses across diverse samples. As shown in in the figures, the weak photocurrent response of pristine polypyrrole nanofibers was related to its low light absorption (the restriction on incident photons' depth of penetration), particularly the high proportion of recombination of photogenerated charges[254] and maybe to the compositional disorder feature in the pristine PPy-NFs specimen, which is apparent from the FESEM images and XRD data [255].

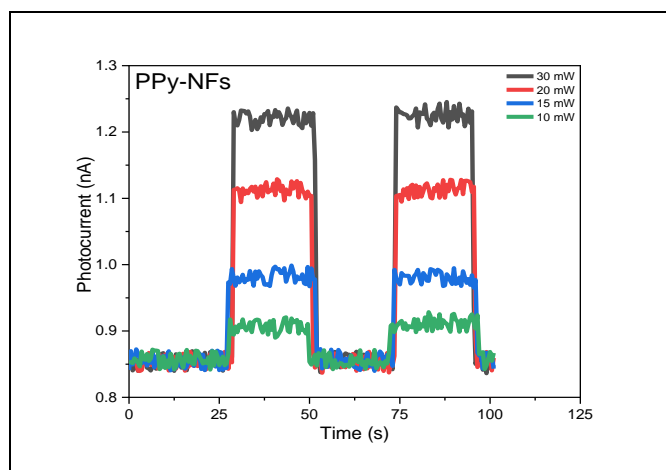


Figure 4.15: Light sensitivity of PPy-NFs with varying energy powers.

Several solutions have been investigated to address these challenges, including the decorating of photoactive molecules to lengthen and enhance photon adsorption, and the creation of homogeneous composite structures to promote charge transfer and wavelength selectivity.

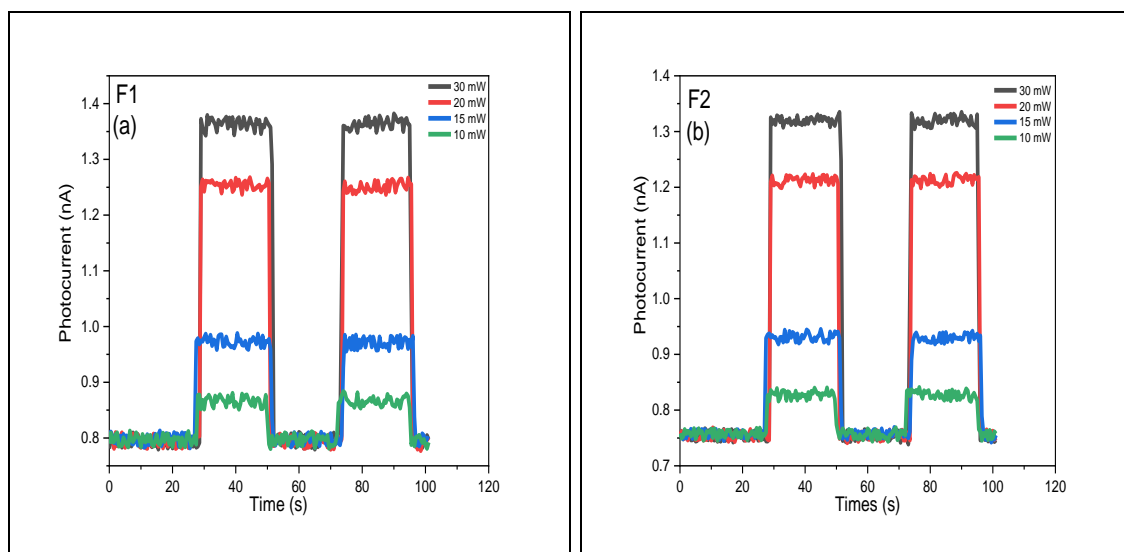
It's worth noting that, while ferrite nanoparticles exhibit specific optical absorpance in the vis-light areas, ferrite-based photodetectors have received little attention. In comparison to other ferrites, the photocurrents of ferrite nanoparticles are quite low. However, numerous test parameters, such as illumination wavelength, light intensity, the device configuration, the external applied bias, and other, have a significant impact on the intensity of the photocurrent [256].

The measured photocurrents versus time of the ferrite nanoparticles samples under laser irradiation (405 nm) with (10 mW, 15 mW, 20 mW, and 30 mW) varied energy powers at room temperature are shown in Figure 4.16. The photocurrents attain a steady state as soon as the laser is switched on, pursued by a swift fall once the laser is switched off. The photosensitivities by the laser powers (ten, fifteen, twenty, and thirty mW) are given in the table 4.5, as are the rise and fall times of the photocurrents generated.

When the incident laser power is increased from 10 mW to 30 mW, the photocurrent magnitudes grow linearly. When the ferrite-based photodetector had affected by illumination (405 nm), the photons were absorbed by the ferrite nanoparticles. Electron-hole pairs are produced when light is exposed the ferrite-based photodetector, and these charge carriers flow in the direction of the opposite electrode under the influence of the applied bias to participate to the exterior photocurrent.

The detector sensitivity is computed utilizing formula 2.17. The photodetector's maximum sensitivity amounts obtained for F1, F2, F3, F4 and F5 are 76.07, 79.34, 88.74, 84.04 and 89.82 respectively.

The photosensitivity of ferrite samples increases to a limit point as the quantity of free electrons as well as electron–hole pairs grows, resulting in increased electrical conductivity and low dark current values. While it was discovered that when photogenerated electrons are held due to positive oxygen vacancies in the thinfilm, the photocurrent reduces dramatically, resulting in severe recombination with photogenerated holes [257]. Surface roughness, oxygen vacancies, and donor density are the primary operators controlling the photoconductive effect and may account for some of the variation in photosensitivity values of the ferrite samples [258].



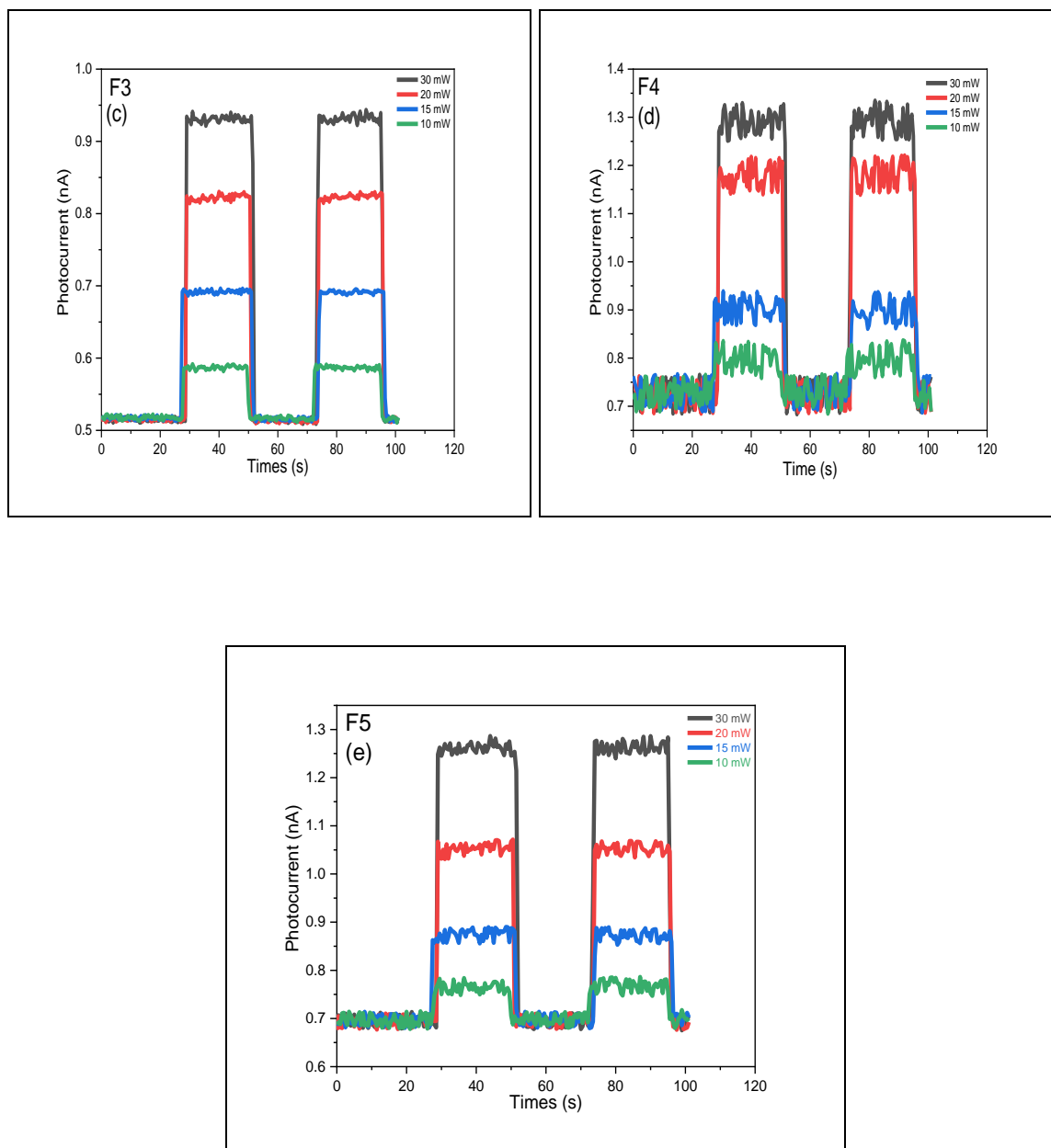


Figure 4.16: Variation of light sensitivity of ferrite nanoparticles (F1, F2, F3, F4 and F5) with various light powers.

The sensitivity rate of the PPy-NFs nanocomposite has clearly improved due to polymer doping, as shown in Figure 4.17. PPy-NFs with ferrite nanoparticles, on the other hand, demonstrated a significantly higher photocurrent response when compared to pure PPy-NFs. the photon

absorption from Polypyrrole transported the electron from (HOMO) to the (LUMO) and to the above-mentioned reasons which led to an improvement in photosensitivity values in pure ferrite thin films enhanced the sensitivity for PPy-NFs nanocomposites. The excited electrons are readily inserted in to polypyrrole conduction band (CB), and then through the doped material's conduction band (CB). Because the electrons obtained their excitation energy from the light source, it is possible to control the current-responses in a semiconductor detector appears clear. The aforementioned phenomena could lead to efficient separation of photo-created charges, leading to higher efficiency in convert illumination photon to current.

The photocurrent then decreased as the doping concentration rate decreased. This is because such modified compounds on the material electrodes impede intermediary electron transmit and partially prohibit the electron donor of the surface interface and the light-formed holes [259]. All of the foregoing data demonstrated that the sensing interface was manufactured effectively.

Finally, this research shows how conducting polymer doping considerably improves the sensitivity of the photodetector. The table 4.5 summarizes the changes in the rise times and fall times, as well as detector sensitivities, when the polypyrrole-nanofibers are doping with differ nanoferrite material and at varied illumination powers.

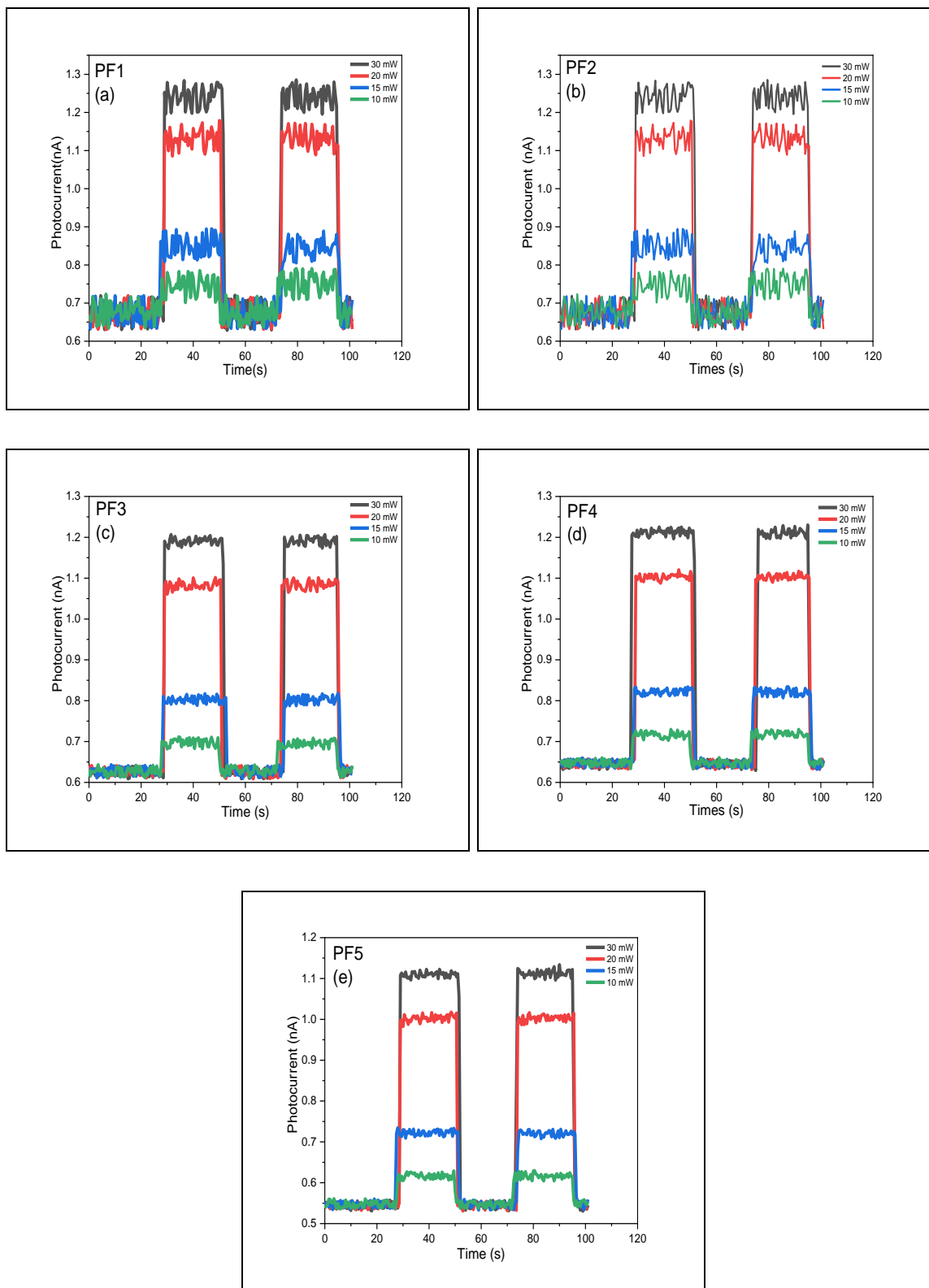


Figure 4.17: Variation of light sensitivity of PPy-NFs nanocomposites include (PF1, PF2, PF3, PF4 and PF5) with various light powers.

Table 4.5: photosensitivity variation with power for prepared materials.

| Sample code | Sensitivity (30 mW) | Sensitivity (20 mW) | Sensitivity (15 mW) | Sensitivity (10 mW) | Rise Time(s)       | Fall Time(s)       |
|-------------|---------------------|---------------------|---------------------|---------------------|--------------------|--------------------|
| F1          | 72.54%              | 58.94%              | 22.92%              | 9.57%               | $5 \times 10^{-1}$ | $5 \times 10^{-1}$ |
| F2          | 75.72%              | 61.53%              | 24.27%              | 10.74%              | $5 \times 10^{-1}$ | $5 \times 10^{-1}$ |
| F3          | 81%                 | 64.88%              | 34.49%              | 14.53%              | $5 \times 10^{-1}$ | $5 \times 10^{-1}$ |
| F4          | 80.22%              | 63.14%              | 26.69%              | 11.85%              | $5 \times 10^{-1}$ | $5 \times 10^{-1}$ |
| F5          | 81.47%              | 66.99%              | 35.01%              | 16.75%              | $5 \times 10^{-1}$ | $5 \times 10^{-1}$ |
| P           | 43.42%              | 31.10%              | 14.78%              | 7.15%               | $5 \times 10^{-1}$ | $5 \times 10^{-1}$ |
| PF1         | 85.58%              | 70.04%              | 26.15%              | 11.73%              | $5 \times 10^{-1}$ | $5 \times 10^{-1}$ |
| PF2         | 86.03%              | 70.87%              | 28.06%              | 12.03%              | $5 \times 10^{-1}$ | $5 \times 10^{-1}$ |
| PF3         | 88.81%              | 72.2%               | 28.41%              | 13.57%              | $5 \times 10^{-1}$ | $5 \times 10^{-1}$ |
| PF4         | 90.95%              | 73.48%              | 32.08%              | 16.98%              | $5 \times 10^{-1}$ | $5 \times 10^{-1}$ |
| PF5         | 103.74%             | 84.27%              | 36.81%              | 17.25%              | $5 \times 10^{-1}$ | $5 \times 10^{-1}$ |

## 4.6 Electrochemical application

Drop casting is used to deposit PPy-NFs, Nanoferrite, and PPy-NFs nanocomposite on the Ni-foam (its area is  $1\text{cm}^2$ ) substrate, which will then be submerged in 1ml of sulfuric acid ( $\text{H}_2\text{SO}_4$ ). After that it's evaluated utilizing CV, GCD, as well as EIS testing curves to determine capacity and electrochemical supercapacitors categorization.

The experiments are achieved in a 3-electrode glass cell containing a Platinum electrode (counter electrode), Ag/AgCl electrode (reference electrode), in addition to deposited materials as a working electrode in 1.0 M  $\text{H}_2\text{SO}_4$  aqueous electrolyte on Ni-foam substrate. Identical electrodes with an average thickness of  $0.2\text{ mg/cm}^2$  are used in supercapacitor testing.

### 4.6.1 Cyclic Voltammetry Measurements

All internal and exterior parameters should be considered when analyzing a sample's electrochemical behavior. Because material properties, cell topologies, and experimental conditions may differ, some of these factors will have a direct impact on device performance. The particle size of active materials, electrolyte content, electrode thickness, scan rate, and working temperature all have a role in CV measurements [260]. The crystal structure and cation distribution among tetrahedral sites as well as octahedral sites influence the electrochemical features of metal oxides [261].

CV curves had utilized to describe the electrochemical act. CV curves for PPy-NFs, ferrite nanoparticles and PPy-NFs Nanocomposites supercapacitors in sulfuric acid at  $20\frac{\text{mV}}{\text{s}}$  scan rate. The influence of doping on polypyrrole

with different ferrite nanoparticle ratios on CV findings was explored for obtain the optimum electrochemical efficiency for manufactured.

Ferrite nanoparticles (Zinc and Manganese ferrites) exhibit large specific capacitances, necessitating further research. Conductive polymers, such as polypyrrole (PPy-NFs) and its derivatives, on the other hand, are appealing as supercapacitor electrode materials because of the enhanced pseudo-capacitance potential they may create [262]. As a result, in order to improve electrochemical performance, the benefits of ferrite nanoparticles and polypyrrole nanofibers are merged in the PPy-NFs/ferrite nanoparticles composite film.

Figure 4.18 depicts cyclic voltammetry for PPy-NFs samples at a scan rate of 20mv/s. A variety of potential windows can be seen. The potential window for PPy-NFs is between 1 and -1 V. Equation 2.12 can be used to compute specific capacitances ( $C_s$ ) based on the loop area (shown by the appropriate figure for each CV curve) and the active mass ( $0.2 \text{ mg/cm}^2$ ) for the electrode. For the first cycle, PPy-NFs have a specific capacitance of 305 F/g. The anodic peak position in the PPy-NFs sample is less than 0.9 V, which may be due to the oxidative reaction of the PPy NFs electrode with the electrolyte, and the cathodic peak position is -0.9V, which might be due to the electrode's reductive response with the electrolyte.

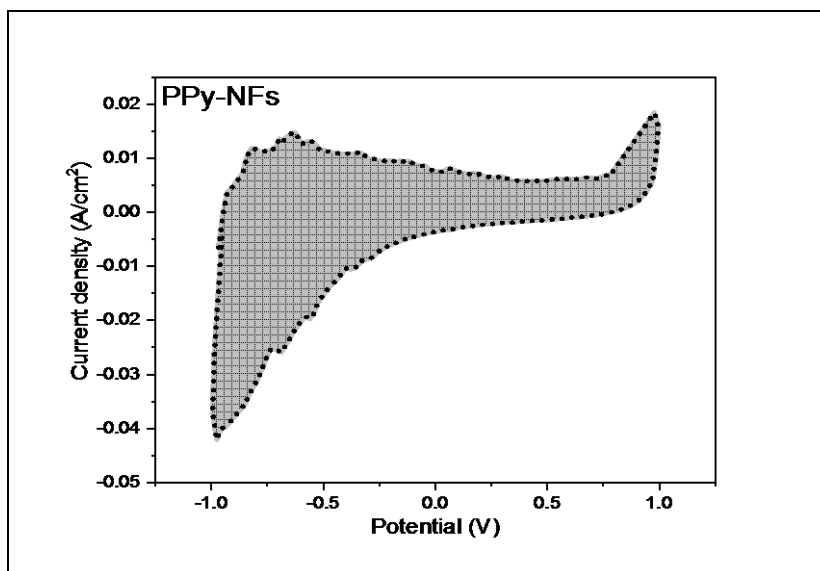


Figure 4.18: CV curves of the PPy-NFs.

Figure 4.19 illustrates cyclic voltammetry with a scan rate of 20mV/s for ferrite nanoparticles samples. The specific capacitances of the ferrite nanoparticles samples can be estimated using the circumstances listed above (active mass, scan rate, potential window, and loop area). The specific capacitances of the F1, F2, F3, F4 and F5 equal 218.24 F/g, 206 F/g, 239.75F/g, 230.01F/g and 263.74 F/g respectively.

According to published studies on spinel ferrites, the majority of these materials have a low cost of preparation, a changeable oxidation state, a large specific surface area, low resistance, and exciting electrochemical activity.

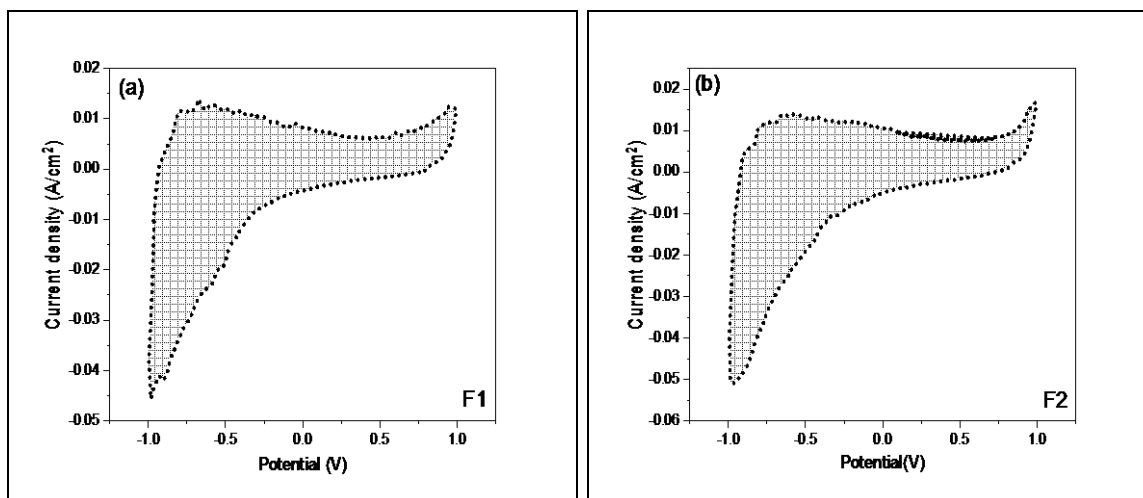
The periodic voltammograms of various samples have a crescent form, as seen in figure 4.19. Through a redox process at the electrode surface, transition metal oxides in all ferrite samples demonstrate pseudocapacitive behavior. Where the electrochemical behavior is caused by a complex chemical composition and the synergistic action of several metal cation valences. In addition, Fe-based spinel mixed transition metal oxides undergo

redox reactions and improve electronic conductivity, which is advantageous in electrochemical applications.

This is consistent with studies into mixed transition metal oxides as a supercapacitor electrode material to improve energy density and overall performance. The pseudocapacitive mechanism is the primary source of charge storage in it [263].

The electrode of ferrite in electrolyte revealed a redox hump (figure 4.19) which indicated an occurrence of faradaic processes.

We also detected a shift in redox peaks with changes in cation type and volume fraction in the material that participate in the production of spinel ferrite structure, confirming the material's outstanding pseudocapacitive nature.



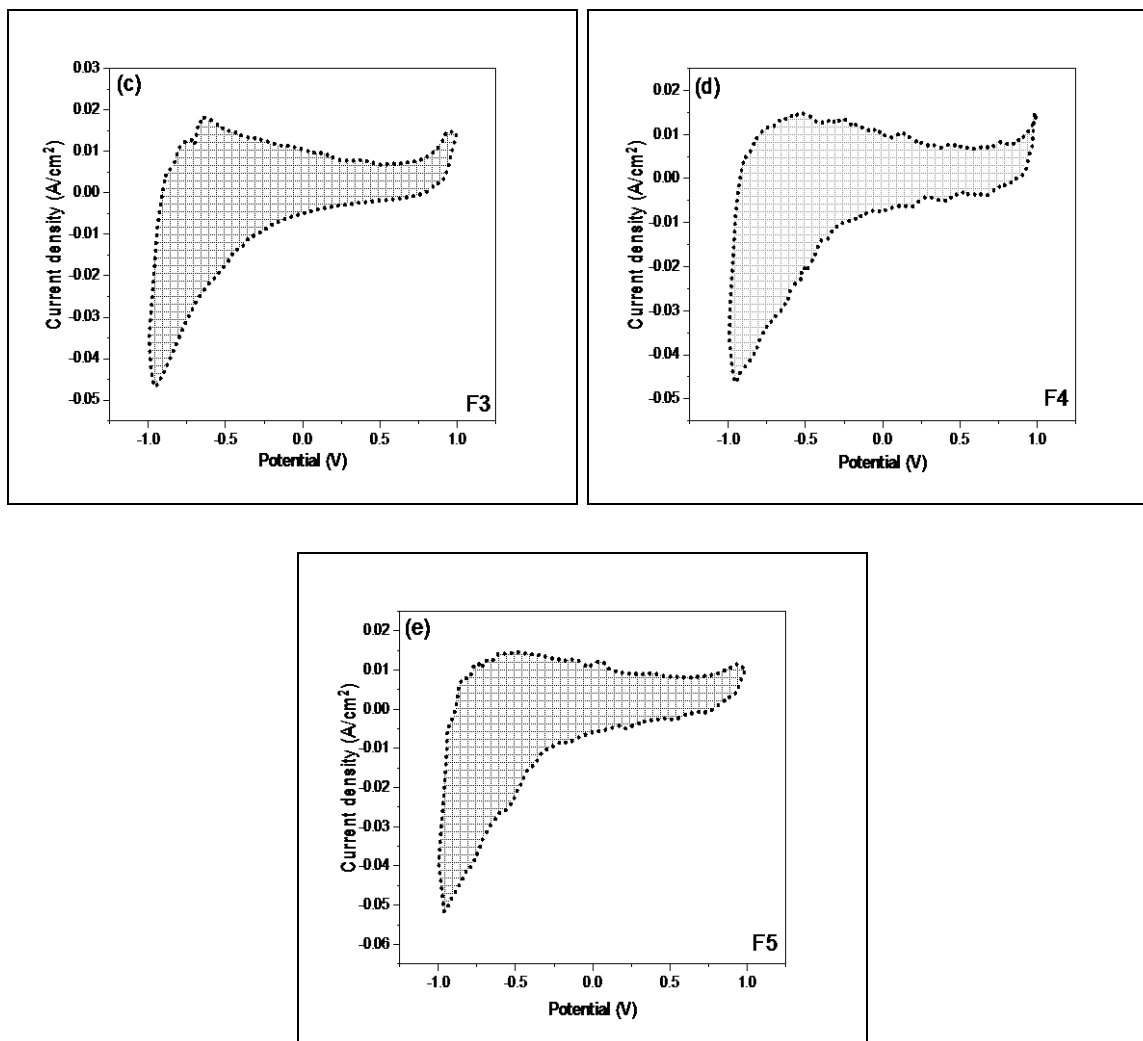


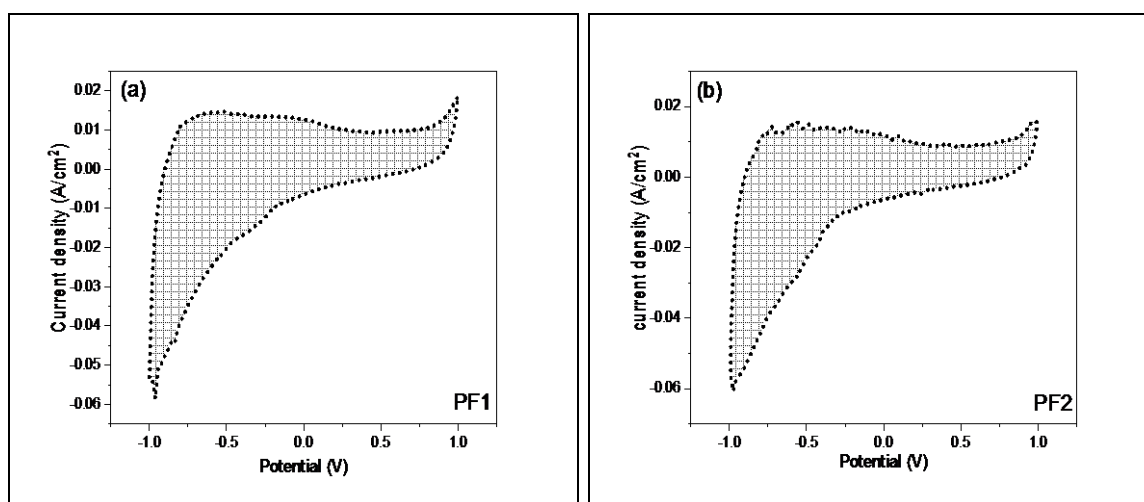
Figure 4.19: CV curves of the ferrite nanoparticles (F1, F2, F3, F4 and F5).

The current study focused on an unique cost-effective PPy-NFs nanocomposite synthesis using spinel ferrite material. The electrochemical conducts of the nanocomposites were investigated using CV checks, which validated the composite electrode's supercapacitive capability (figure 4.20). The specific capacitances of PF1, PF2, PF3, PF4, and PF5 are 338.98 F/g, 326.27 F/g, 346.01 F/g, 370.39 and 414.12 F/g respectively.

PPy-NFs nanocomposite electrodes have a higher specific capacitance than other electrodes. As a result, the PPy-NFs nanocomposite electrode

outperforms both pure PPy-NFs and ferrite electrodes in terms of supercapacitive performance. This is because the composite components have a greater synergistic effect. Because of its conductive character, the inclusion of PPy-NFs leads in increased ion transport into the electroactive electrode material as well as a component harmony effect [264].

Ferrite is a magnetic substance with strong chemical stability and good catalytic properties, however it is electrically resistive. Although PPy-NFs are a conducting polymer, its nanocomposites are both magnetic and electrically conducting. Because of its reversible redox activity, the PPy-NFs nanocomposite is being explored as a viable electrode material.



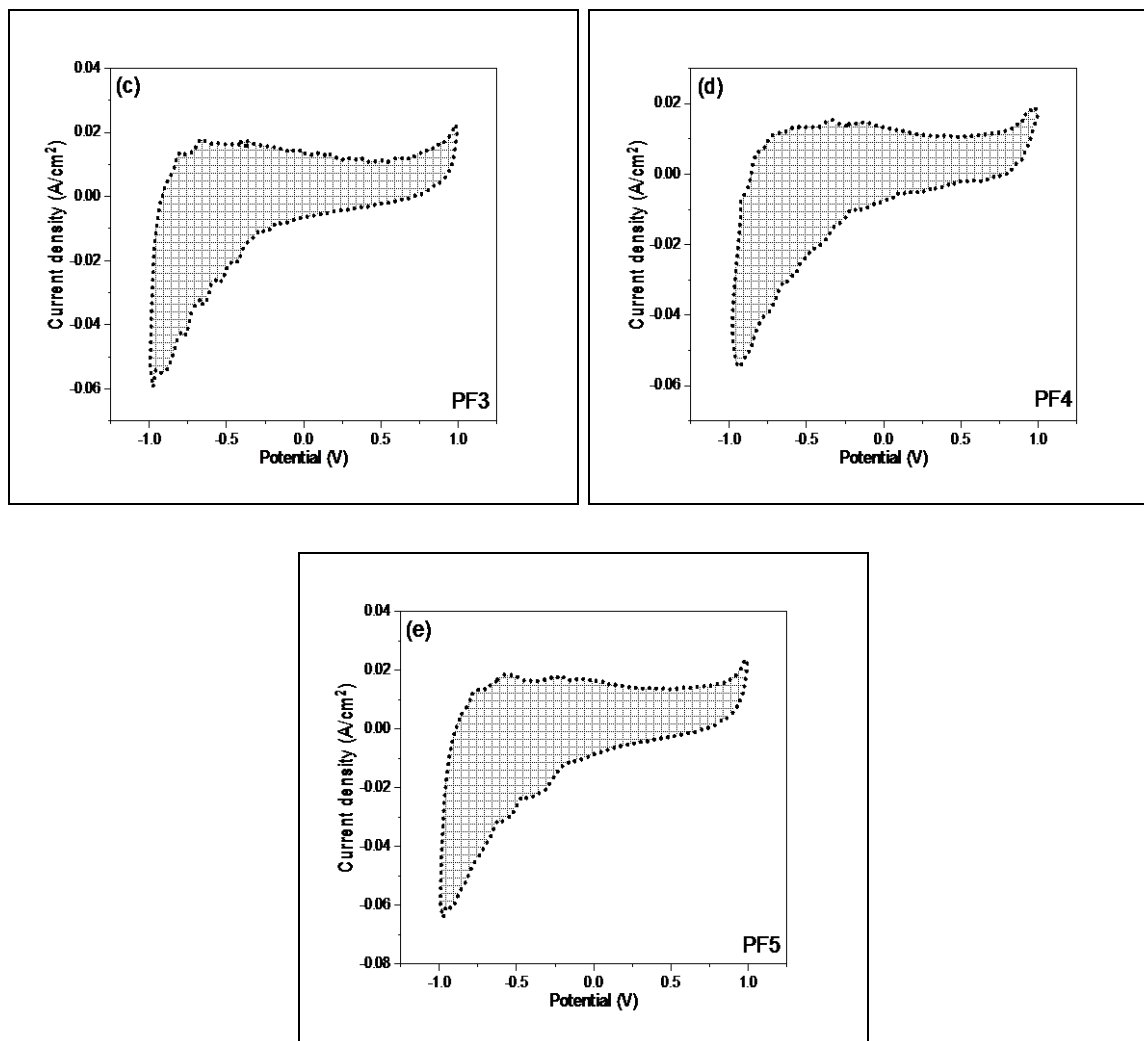


Figure 4.20: CV curves of the PPy-NFs nanocomposite (PF1, PF2, PF3, PF4 and PF5) samples.

#### 4.6.2 Electrochemical impedance spectroscopy analysis (EIS)

EIS uses Nyquist plots to display the negative of the imaginary against the real sections of the complicated impedance of electrochemical cells (EIS). The plots of EIS spectra for PPy nanofibers, ferrite nanoparticles, and PPy-NFs nanocomposite cathodes with a frequency domain of ( $10^{-1}$  Hz - 200 kHz) are shown in Figure 4.21. Electrochemical impedance spectroscopy provides a material resistance that can be used to determine the material's conductive performance. In the high and low frequency areas, the Nyquist plot contains

semicircles and inclined straight lines, respectively. The charge transfer process at the electrode–electrolyte contact is represented by semicircles. As a result, a semicircle intercepting at the x-axis ( $Z'$ ) indicates the ( $R_{\text{ESR}}$ ), which includes the electrolyte's ionic resistance, the electrode material's electronic resistance, and the contact resistance at various phase interfaces. The ( $R_{\text{ct}}$ ) is represented by the semicircle in the high-frequency zone.

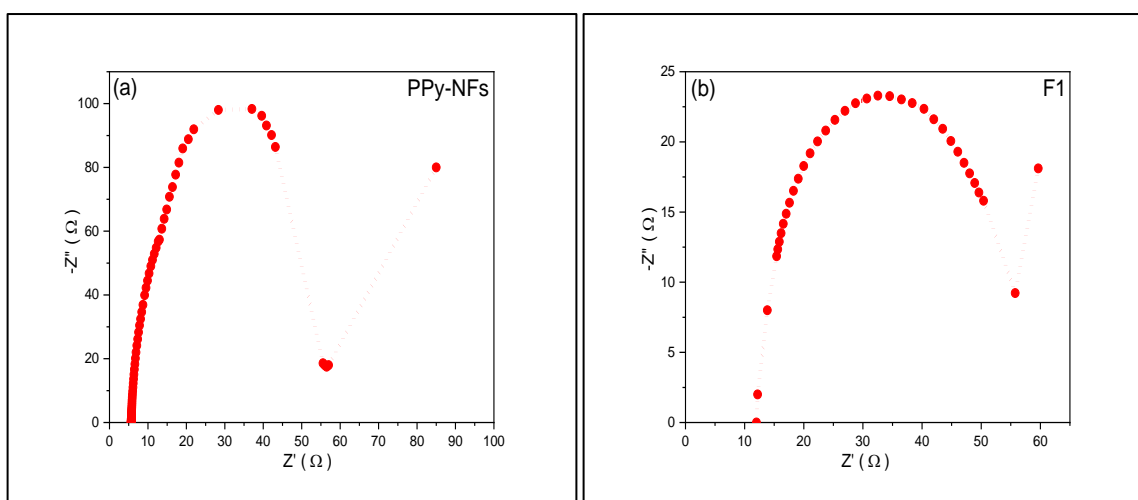
The Nyquist plots of the samples are provided in Figure (4.21) to quantify the better electrode. Table (4.6) shows the measured  $R_{\text{ESR}}$  and  $R_{\text{ct}}$  values for the synthesised materials. The Nyquist data displays which electrode has the lowest  $R_{\text{ESR}}$  and charge transfer resistance ( $R_{\text{ct}}$ ) compared to the others. It makes improved charge transfer techniques possible. As a result, higher surface area and tiny particles promote electrolyte penetration and ions diffusion. Furthermore, the low frequency region for all samples exhibits an inclined plane above  $45^{\circ}$ , which is connected to the material's pseudocapacitive characteristic [265].

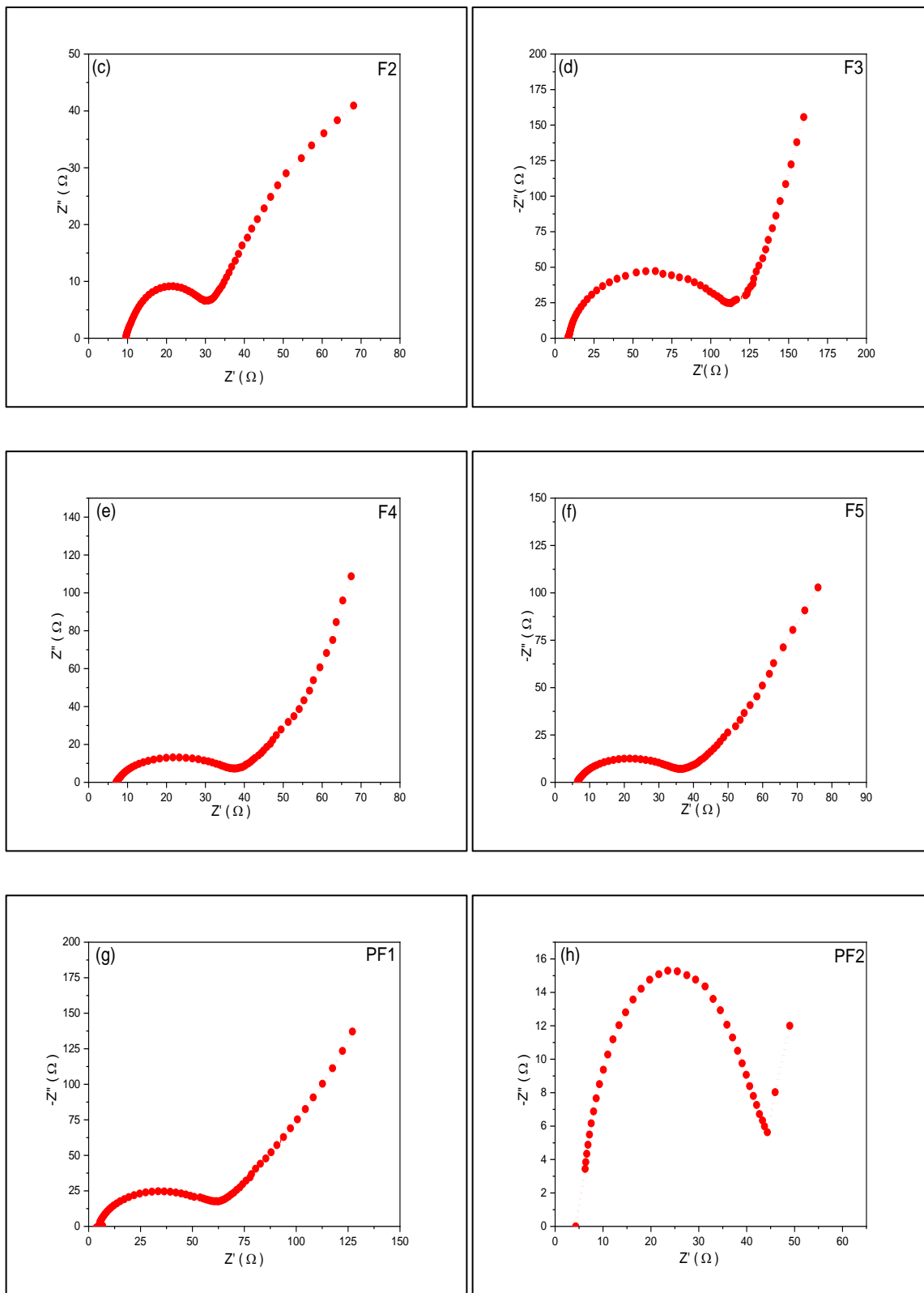
These findings further reveal that the PPy-NFs, ferrite nanoparticles, and PPy nanocomposites have outstanding electrochemical cycle stability due to the synergistic effect of sample components, indicating that they could be used as electrode materials for electrochemical supercapacitors.

It is clear that the ( $R_{\text{ct}}$ ) of some samples is greater than that of others. This could be due to ion condensation on the electrode's outer surface, the existence of contaminants during the active material preparation, and difficult-to-control laboratory conditions.

Table 4.6:  $R_{\text{ESR}}$  and  $R_{\text{ct}}$  for the PPy-NFs, ferrite nanoparticles and PPy-NFs nanocomposites samples.

| Sample code | Equivalent series resistance, $R_{\text{ESR}}$ ( $\Omega$ ) | Charge transfer resistance, $R_{\text{ct}}$ ( $\Omega$ ) |
|-------------|---|--|
| p           | 5.66  | 50.34  |
| F1          | 11.99   | 43.76  |
| F2          | 9.39  | 20.07  |
| F3          | 9.66  | 103.54   |
| F4          | 7.13  | 30.49  |
| F5          | 6.45  | 29.68  |
| PF1         | 4.86  | 56.78  |
| PF2         | 4.30  | 40.05  |
| PF3         | 3.01  | 51.11  |
| PF4         | 4.12  | 40.01  |
| PF5         | 2.2   | 41.11  |





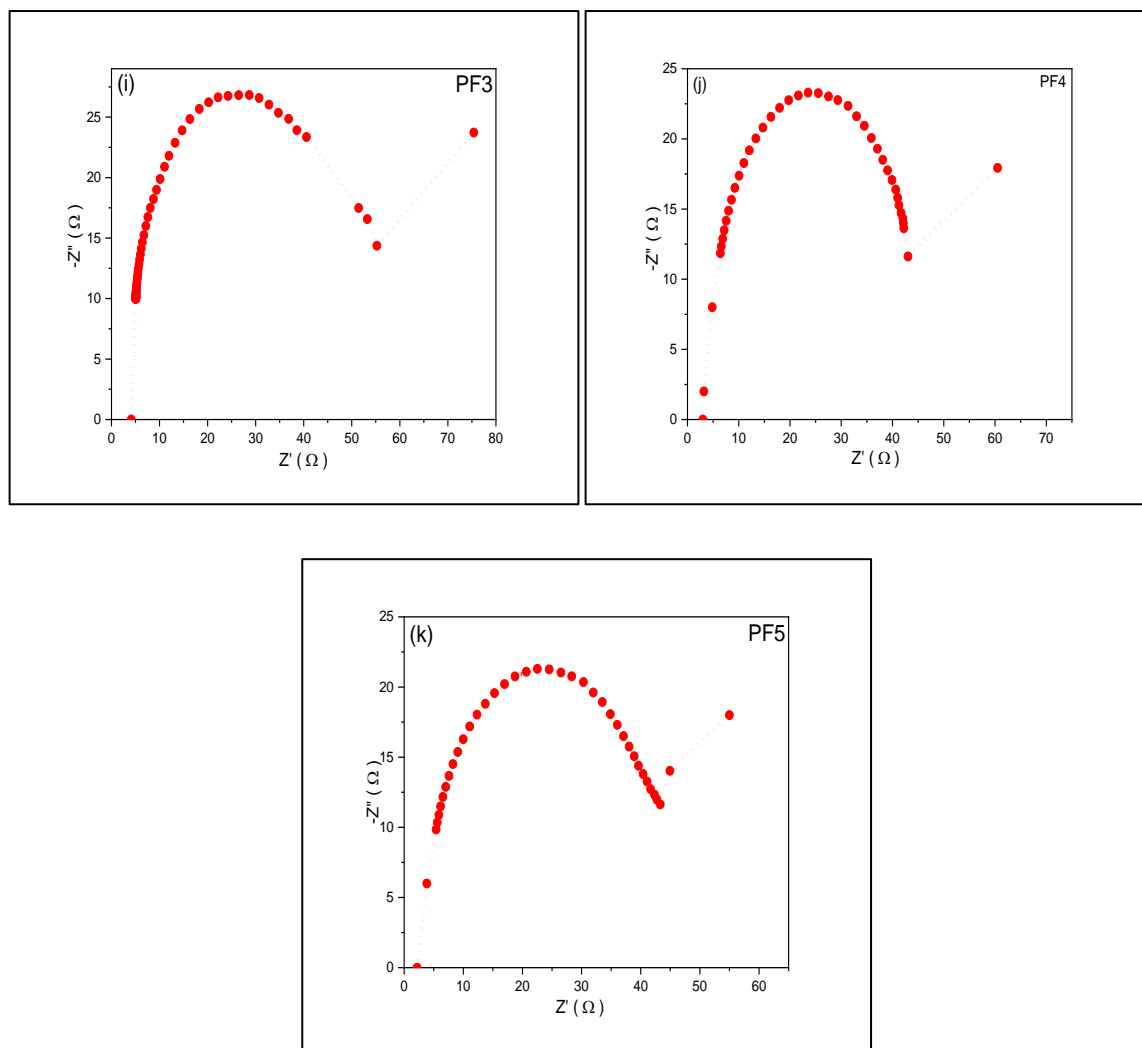


Figure 4.21: Nyquist plots for a) PPy-NFs, b) F1, c) F2, d) F3, e) F4, f) F5, g) PF1, h) PF2, i) PF3, j) PF4 and k) PF5 samples at (0.1 Hz- 200 KHz).

#### 4.6.3 Galvanostatic Charge Discharge Measurements (GCD)

Electrochemical efficiency was evaluated using a galvanostatic charge/discharge analysis. Figure 4.22 shows the charge/discharge curves of PPy-NFs, ferrite nanoparticles, and PPy-NFs nanocomposite electrodes.

At a specific current density, Galvanostatic charge-discharge tests of electrodes were performed. Figure 4.22 shows the CD curves of electrodes in sulfuric acid as electrolyte. Most of the prepared electrode's discharge curves

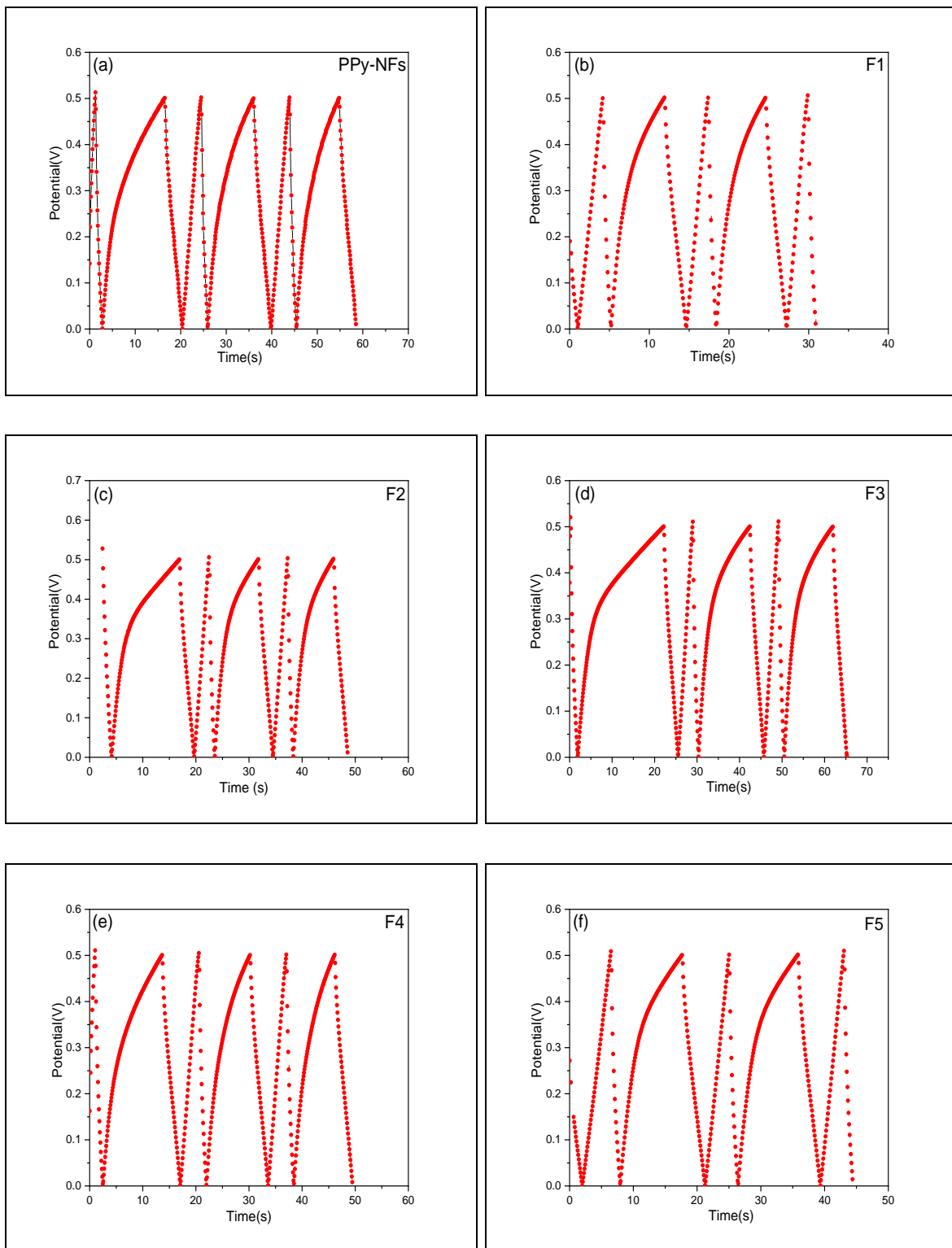
are not perfectly straight. As a result, the Faradaic reaction takes place. As a result, it has supercapacitive properties. Internal resistance is the most critical factor, because it is what causes the initial decline in potential. Internal resistance is caused by interfacial contact resistance between sulfuric acid electrolyte and electrodes, which is affected by surface morphology of electrode and other characteristics. Due to active material loading, the interaction between polypyrrole and nanoferrites in the matrix of polymer has a significant impact changes in the morphology of composite electrodes. However, because of the varied morphologies of electrode, the resistance of the supercapacitor is reduced due to the formation of a high electrolyte/electrode contact surface area. In order of ferrite nanoparticles < PPy-NFs < PPy-NFs nanocomposites, the discharge time of electrodes rises. This property is due to the rises conductivity of the synthesis electrodes, that allows for faster charge transfer in the composite electrode [32].

As shown above, the discharge time increases as the number of PPy-NFs increases. Furthermore, the CD curve for PPy-NFs nanocomposite is less symmetrical than that of pure ferrite nanoparticles, indicating that the material's pseudocapacitance is increased with the addition of PPy-NFs. The synergistic effect of nanocomposite components is responsible for the increase in electrochemical performance of samples as shown by cyclic voltammetry and charge discharge studies.

Galvanostatic charge discharge figures can show the curves stability in the fundamental media generally. This shows that the electrode is stable in base conditions as well suitable with H<sub>2</sub>SO<sub>4</sub>.

The curves of GCD with reduced current densities show enhanced faradic contribution (redox reactions) to the charge accumulation approach, and

charge/discharge timings show superior electro chemical reversibility, indicating that these samples can be used in supercapacitors [266].



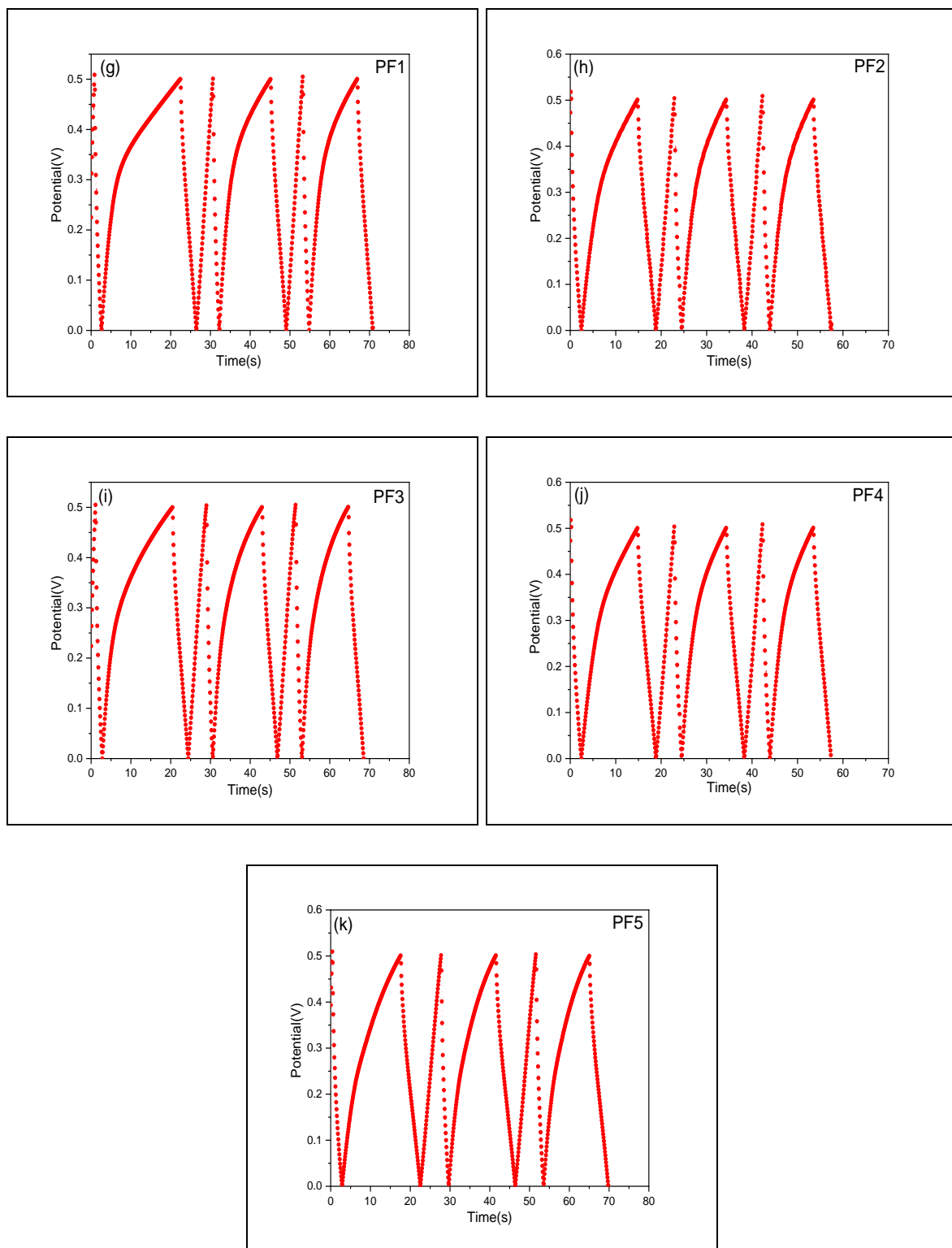


Figure 4.22: Galvanostatic charge-discharge for PPy-NFs, ferrite nanoparticles and PPy-NFs electrodes for supercapacitors.

Overall, the results of CV, GCD, and EIS clearly reveal that among the generated samples, F5 (pure ferrite nanoparticles) and PF5 (PPy-NFs nanocomposites) exhibit superior electrode performance in 1M H<sub>2</sub>SO<sub>4</sub>. This is due to the nanocomposite components' synergistic and compatible effect, as well as their reduced particle size, appropriate surface area, and low charge transfer resistance compared to other samples.

## 4.7 Ammonia Gas Sensing Measurement

Ammonia is colorless gas or compressed liquid with a strong odor. It is one of the most harmful and toxic gases, damaging the lungs, skin, and eyes. Ammonia concentrations in the human body of up to 500 parts per million (ppm) can be exceedingly hazardous. It can cause pulmonary oedema, or the collection of fluid in the lungs, at 1000 parts per million. At low ppm concentrations, the human nose has a hard difficulty detecting ammonia. VOC gases such as liquid ammonia have piqued the interest of researchers since they not only pollute the environment but also have a direct influence on human health. Regardless, these gases are used in the production of other products that are strongly tied to human life [267]. The presence of such hazardous VOCs is very likely, necessitating the development of sensors to identify poisonous and combustible chemicals early on. Nanomaterials with the right size, dimension, and shape show a lot of promise for sensing applications. Gas sensor performance is influenced by humidity, working temperature, plus gas concentration. Features connected with ferrites morphologies, like the contact area, the specific surface area, the grain size, the porosity, the grain stacking order, as well as aggregation, are influencing factors in addition to external influences.

The reactions of PPy-NFs to  $\text{NH}_3$  exposure at  $50^\circ\text{C}$  with 30 ppm are shown in Figure 4.23. It is commonly known that PPy is a p-type conducting semiconductor. When PPy is exposed to an electron donor gas, such as  $\text{NH}_3$ , it undergoes a redox process. When  $\text{NH}_3$  is added to PPy, the charge-carrier concentration of the polymer drops, and neutral polymer backbones form. When PPy-NFs were exposed to  $\text{NH}_3$  vapor for 34.2 seconds, the resistance increased dramatically. As a result, PPy-NFs made this way have a

characteristic nanofiber morphology and perform better in terms of sensitivity and response time [268].

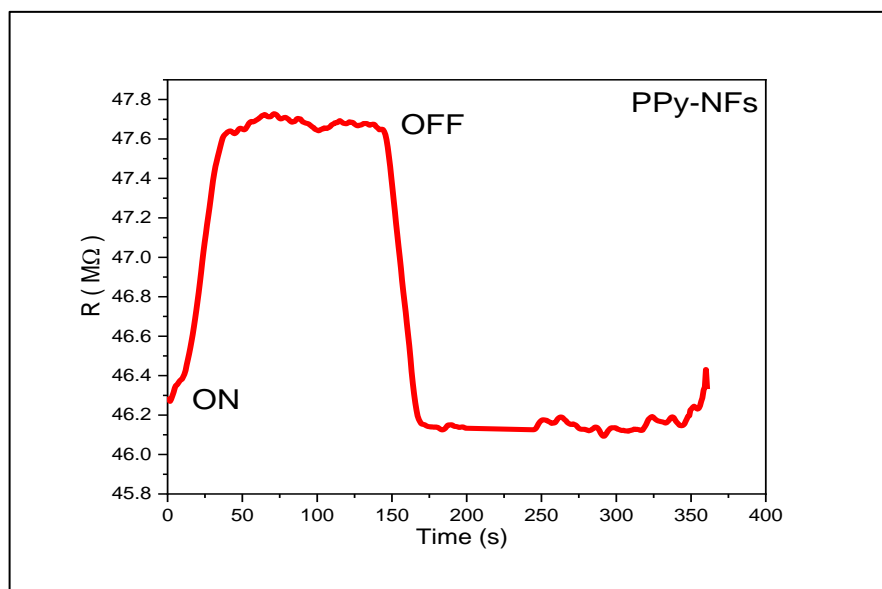


Figure 4.23: Variation of resistance with time for PPy-NFs sensor.

Surface area and active sites that allow the adsorption and diffusion of gas molecules, which are dependent on the interaction for complex of the gas-solid interface, can be used to explain the gas sensor technique as well response of ferrite nanoparticles sensing [267]. Due to its spinel crystal structure, ferrite nanoparticles offer great capabilities as a novel sensing material, and defects such as oxygen vacancies are easily formed inside or on the surface. Furthermore, the unusual crystal composition for transition metal cations inserted in the  $\text{Fe}^{2+}\text{Fe}^{3+}\text{O}^4$  construction performs fine in reducing gas discovery (detection) [269].

Pure ferrite nanoparticles have a distinctive microstructure and a large specific surface area, which provides ample sites for gas adsorption and so improves sensing capability. Also, metal doping (ion substitution) may rise the diffusion or transfer rate of carrier as well as smaller the potential barrier

height of the grain boundary; the hybrid structure could control electron depletion region in addition to potential barrier at its interface via Fermi energy level interaction and energy band to enhance gas sensor effectiveness [269].

The sensitivity at 50°C with 30 ppm increases when the Zn ratio increases, as seen in figure 4.24. For all prepared samples, the sensitivity value of ammonia NH<sub>3</sub> was estimated using equation 2.20. At 50 degrees Celsius, all specimens demonstrated a great sensitivity to NH<sub>3</sub> gas, as shown in Figure 4.24. The existence of vacuoles in addition to the nanoparticles' small size increases sensitivity for ferrite nanoparticles samples because they have the highest roughness as seen in FESEM images (this is consistent with what researchers indicated [270]). In general, Zn doping increases sensitivity since a reduce oxygen causes oxygen voids to form. The sensitivity will rise because the sensitivity machinery in metal oxides happens via the oxygen ions adsorption on the surface (because to vacancies or voids, the oxygen concentration of the (Co<sub>0.8-x</sub>Zn<sub>x</sub> Mn<sub>0.2</sub>Fe<sub>2</sub>O<sub>4</sub>) lattice increases oxygen ion adsorption on the sensor's surface). By adsorbing oxygen gas from air on the sample's surface, the chemisorption process captures electrons from of the material's C B. This increases the vacancies concentration in the air, lowering its resistance. Whenever the analyser gas (ammonia) comes into contact with the sensor surface of the material, the chemisorbed O<sub>2</sub> molecules interact with Ammonia, delivering electrons towards the sensor material's C B. Therefore, charge carriers concentration (holes) falls whereas resistance increases. Lastly, the creation of extra imperfection positions with a wide surface area promotes enhanced NH<sub>3</sub> diffusion in the substance, leading to improved sensor performance. As a consequence, conductivity, surface accessibility,

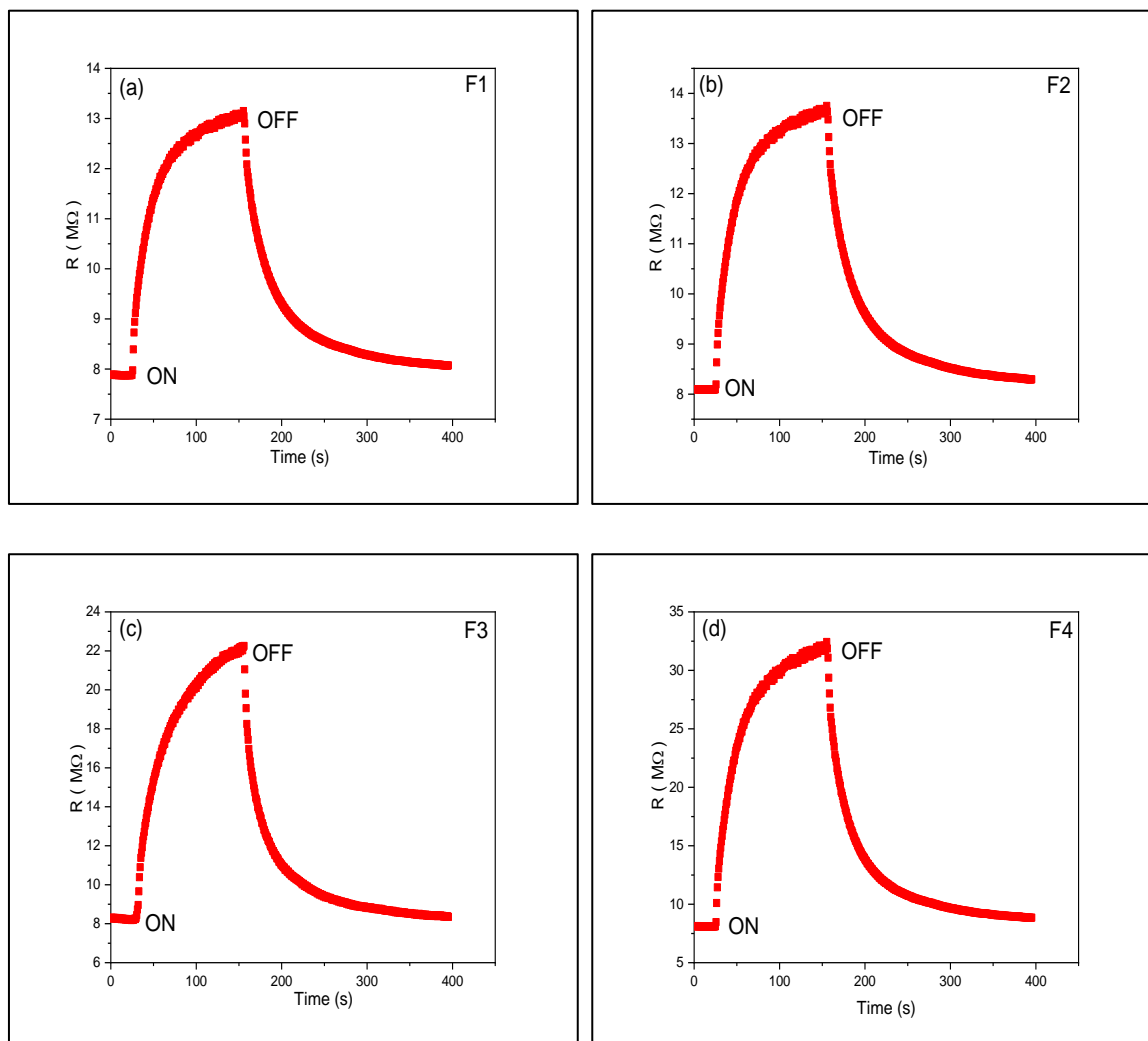
and  $\text{NH}_3$  adsorption all improve. Because analytic gas adsorption and desorption are reliant on surface area, surface area is critical in gas sensing behavior [271,272].

It can be said, that the sensor have acceptable and standard sensing properties because of the ferrite nanoparticles ( $\text{Co}_{0.8-x}\text{Zn}_x\text{Mn}_{0.2}\text{Fe}_2\text{O}_4$ ) have a good sensitivity as well as a mild response time and recovery time ranging from 50.4-79.2s and 71.6-89.6 s respectively. This sensor response could be owing to the sensor's small crystalline size and correct grain size, which causes the grain boundaries to grow, as well as the other factors described above. It contributed to the enhancement of the gas sensor's properties.

According to the findings in table 4.7, the responses obtained with PPy-NFs nanocomposites were higher than with pure polypyrrole nanofibers (see figure 4.24). The improved sensing conduct can be attributed to the synergistic behavior of PPy-NFs chains and nanoferrite components. Furthermore, in the nanocomposite, the surface area of ferrite nanoparticles plays a critical function. This improves gas adsorption and diffusion on the surface. In addition, the nanocomposite revealed three-dimensional nanostructures in FESEM pictures. Since the composite has a great specific surface area and a nanostructure that is intersectionly orientated,  $\text{NH}_3$  molecules should be able to move freely and diffuse while also having more reaction sites available, which will increase the response's amplitude [273].

The fact that PPy-NFs and ferrite metal oxides behave as p-type semiconductors could be another explanation (The majority of the carriers are holes). As a result, hetero-junctions are likely to occur in conductive polymers/metal oxide hybrids, potentially creating a unique system accountable for this behavior. This disrupts the charge carrying process across

the polymer, resulting in a higher electrical resistance and, as a result, improved gas sensing qualities when compared to the pristine polymer [274]. Figures 4.25 and 4.26 show variation of resistance with time for ferrite nanoparticles and PPy-NFs nanocomposite sensors of  $\text{NH}_3$  gas at  $50^\circ\text{C}$ , respectively.



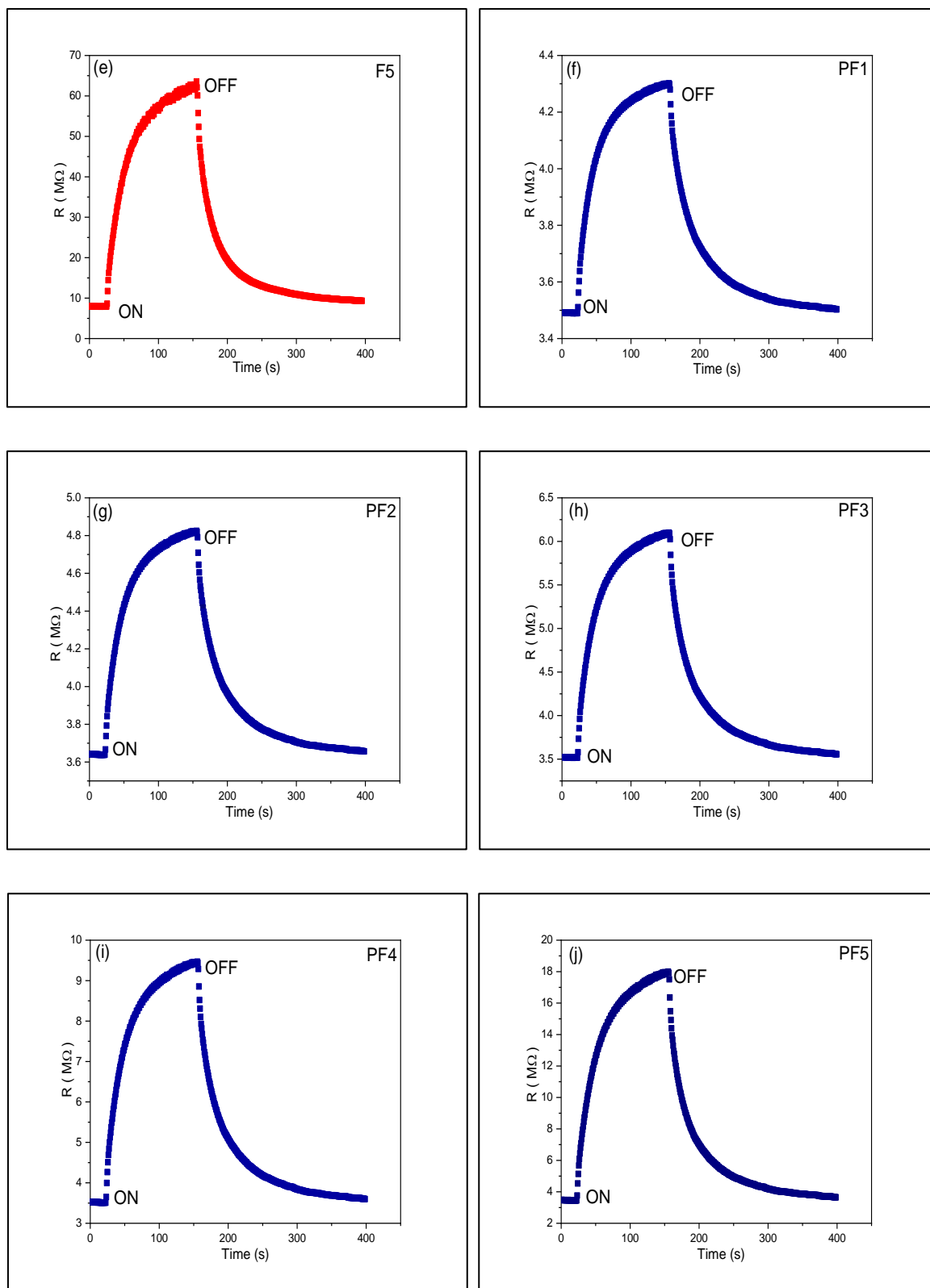


Figure 4.24: Variation of resistance with time for ferrite nanoparticles and PPy-NFs nanocomposite sensors, ( $NH_3$  gas at  $50^\circ C$  with 30 ppm).

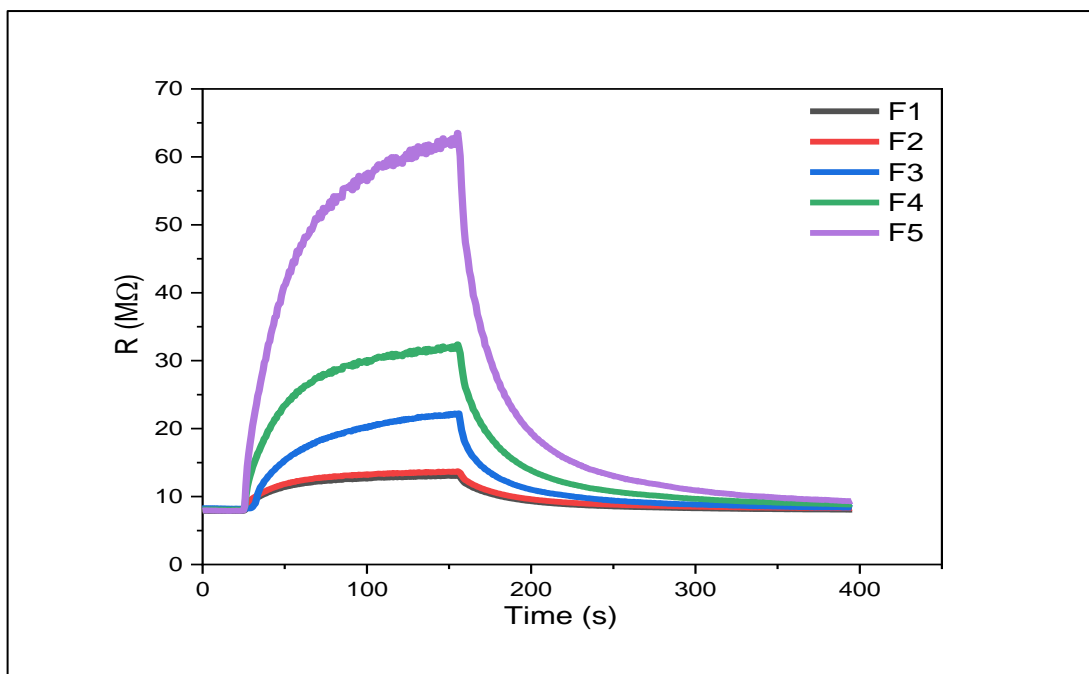


Figure 4.25: Variation of resistance with time for ferrite nanoparticles sensors, ( $\text{NH}_3$  gas at  $50^\circ\text{C}$  with 30 ppm).

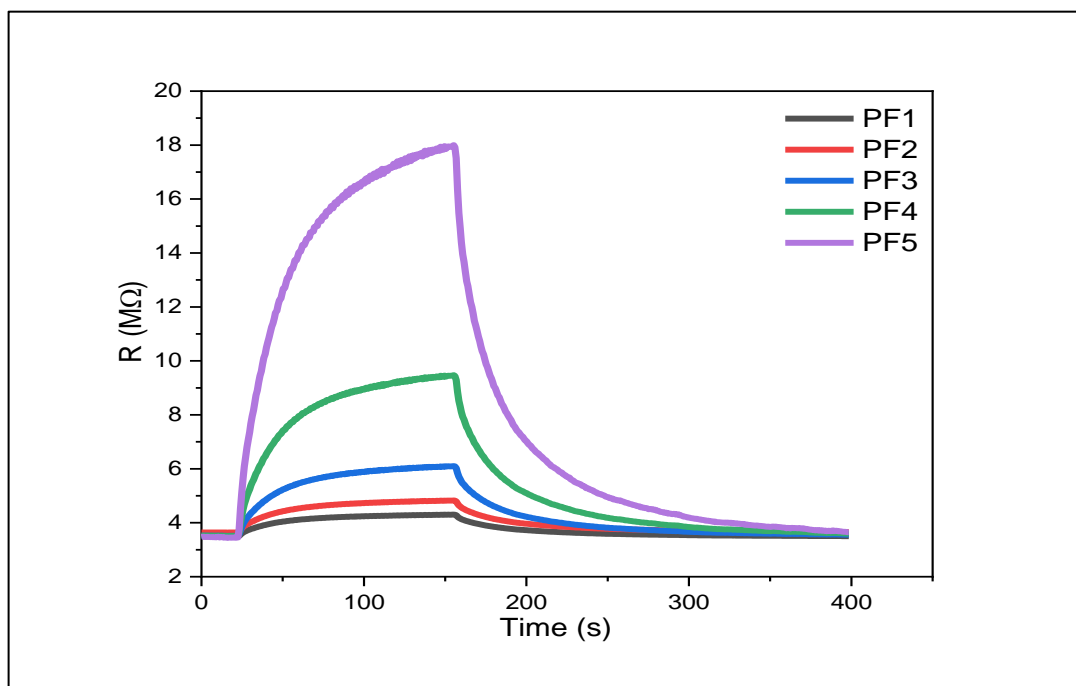


Figure 4.26: Variation of resistance with time for PPy-NFs nanocomposite sensors, ( $\text{NH}_3$  gas at  $50^\circ\text{C}$  with 30ppm).

Table 4.7: The responsivity, response time and recovery time for PPy-NFs, ferrite nanoparticles and PPy-NFs nanocomposite samples at 50°C with 30 ppm of NH<sub>3</sub> gas concentration.

| Sample code | Responsivity % | Response time (s) | Recovery time (s) |
|-------------|----------------|-------------------|-------------------|
| PPy-NFs     | 3.01           | 34.2              | 25.6              |
| F1          | 66.26          | 45.4              | 73                |
| F2          | 69.23          | 54.2              | 68.8              |
| F3          | 170.5          | 75.2              | 71.6              |
| F4          | 297.43         | 63.8              | 67.6              |
| F5          | 679.01         | 61.6              | 71.3              |
| PF1         | 23.24          | 51.2              | 83.6              |
| PF2         | 32.49          | 46.4              | 74.4              |
| PF3         | 73.30          | 47.8              | 72.8              |
| PF4         | 168.06         | 59.8              | 78                |
| PF5         | 423.11         | 65.2              | 79.1              |

## 4.8 Conclusions and Future work suggestions

### 4.8.1 Conclusions

Chemical oxidative polymerization was used to create polypyrrole nanofibers (PPy-NFs), which is a simple and feasible process. In addition, using the hydrothermal autoclave reactor and the co-precipitation approach, Co<sub>0.8-x</sub>Zn<sub>x</sub>Mn<sub>0.2</sub>Fe<sub>2</sub>O<sub>4</sub> (x=0, 0.2, 0.4, 0.6, and 0.8) was synthesized. Later, Co<sub>0.8-x</sub>Zn<sub>x</sub>Mn<sub>0.2</sub>Fe<sub>2</sub>O<sub>4</sub> nanoparticles were added to PPy-NFs to create the PPy-

NFs nanocomposite. We will concentrate on a few key conclusions from the research process that are listed below.

1-Polypyrrole nanofibers (PPy-NFs) are amorphous and  $\text{Co}_{0.8-x}\text{Zn}_x\text{Mn}_{0.2}\text{Fe}_2\text{O}_4$  is a single phase cubic spinel according to XRD spectra.

2-The FTIR spectra revealed two main absorption bands in the  $600\text{-}400\text{ cm}^{-1}$  region, indicating to a cubic spinel creation. In addition, the formation of PPy-NFs and PPy-NFs nanocomposites was validated by its studies.

3-FESEM images demonstrated that the Polypyrrole was polymerized in one dimension nanofibers materials. The ferrite nanoparticles are spherical with light alteration in the nanoparticle size distributions. Dopant materials (ferrite nanoparticles) are loaded onto the PPy nanofibers net successfully.

4-The samples' optical characteristics were examined. The energy gap of samples varies with doping ratio and ferrite nanoparticles content.

5-At room temperature, magnetic measurements revealed that the samples exhibited different magnetic characteristics. The maximum magnetization, coercivity, and remanence at 10 KOe were all different in the nanocomposites samples as the cobalt content in the structure changed.

5-By doping PPy-NFs with ferrite nanoparticles, the sensitivity of photosensors in prepared samples can be improved.

6-The supercapacitor electrodes were prepared from polypyrrole nanofibers, ferrite nanoparticles and nanocomposites samples in order to get samples with characteristic and stable capacitances. The nanocomposite samples had higher capacitances than pure samples (PPy-NFs and ferrite nanoparticles). As a result, supercapacitor capacitances are dependent on doping.

7-NH<sub>3</sub> gas responsivity of ferrite nanoparticles samples was higher than PPy-NFs polymer samples and nanocomposites samples. With increased zinc concentration, its value rises in ferrite samples. Furthermore, after doping with ferrite nanoparticles, the responsiveness of the PPy-NFs polymer improved.

#### **4.8.2 Future work suggestions**

- 1- Using PPy-NFs and PPy-NFs nanocomposites in radiation absorption and shielding application as well in biomedical applications.
- 2- Using other ferrites (Cobalt and Zinc ferrite) as dopant materials with pure PPy-NFs in electrochemical capacitors application.
- 3- Studying PPy-NFs and PPy-NFs nanocomposites as a gas sensor for NO<sub>2</sub>, CO<sub>2</sub> and H<sub>2</sub>S gases.

## References

- [1] Ravve, Abraham, "Principles of Polymer Chemistry", Springer Science & Business Media, (2013).
- [2] A. Talaie, "Electronic Properties of Novel Polypyrrole and Polyaniline Materials: A resistometric Approach", Ph. D. Thesis, University of Wollongong, (1994).
- [3] A. G. MacDiarmid, "Synthetic Metals: A novel role for Organic Polymers (Nobel lecture)", *Angewandte Chemie International Edition*, vol. 40, no. 14, pp. 2581-2590, (2001).
- [4] Gribkova, O. L., Omelchenko, O. D., Tameev, A. R., Lypenko, D. A., Nekrasov, A. A., Posudievskii, O. Y. and Vannikov, A. V., "The specific Effect of Graphene Additives in Polyaniline-based Nanocomposite Layers on Performance Characteristics of Electroluminescent and Photovoltaic Devices", *High Energy Chemistry*, vol. 50, no. 2, pp. 134-138, (2016).
- [5] B. Philip, J. Xie, J. K. Abraham, and V. K. Varadan, "A new Synthetic Route to Enhance Polyaniline Assembly on Carbon Nanotubes in Tubular Composites", *smart materials and structures*, vol. 13, no. 6, p. N105, (2004).
- [6] Jiang X., Setodoi S., Fukumoto S., Imae I., Komaguchi K., Yano J. and, Harima Y, "An easy One-step Electrosynthesis of Graphene/Polyaniline Composites and Electrochemical Capacitor", *Carbon N. Y.*, vol. 67, pp. 662–672, (2014).
- [7] K.-Y. Shen, C. W. Hu, L. C. Chang, and K.-C. Ho, "A complementary Electrochromic Device based on Carbon Nanotubes/Conducting Polymers", *Solar energy materials and solar cells*, vol. 98, pp. 294-299, (2012).
- [8] W. S. Huang, B.D. Humphrey and A.G. MacDiarmid, "Polyaniline, a Novel Conducting Polymer. Morphology and Chemistry of its Oxidation and Reduction in Aqueous Electrolytes", *Journal of the Chemical Society, Faraday Transactions 1: Physical Chemistry in Condensed Phases*, vol. 82, pp. 2385-2400, (1986).

## References

- [9] Shirakawa, Hideki, Alan McDiarmid, and Alan Heeger, "Twenty-Five years of Conducting Polymers", *Chemical communications*, vol. 7, pp. 1-4, (2003).
- [10] Grancarić A. M., Jerković I., Koncar V., Cochrane C., Kelly F. M., Soulat D., and, Legrand X., "Conductive Polymers for Smart Textile Applications", *Journal of Industrial Textiles*, vol. 48, no. 3, pp. 612-642, (2018).
- [11] S. B. Kondawar, P. T. Patil, and S. P. Agrawal, "Chemical Vapour Sensing Properties of Electrospun Nanofibers of Polyaniline/ZnO Nanocomposites", *Adv. Mater. Lett.*, vol. 5, no. 7, pp. 389-395, (2014).
- [12] Joseph J., Tangsali R. B., Pillai V. M., Choudhary R. J., Phase D. M., and Ganeshan V., "Structure and Magnetic Properties of Highly Textured Nanocrystalline Mn–Zn Ferrite Thin film", *Physica B: Condensed Matter*, vol. 456, pp. 293-297, (2015).
- [13] Z. Jia and R. D. K. Misra, "Magnetic Sensors for Data Storage: Perspective and Future Outlook", *Materials Technology*, vol. 26, no. 4, pp. 191-199, (2011).
- [14] A.V. Anupama, V. Kumaran and B. Sahoo, "Synthesis of Highly Magnetic Mn-Zn Ferrite ( $Mn_{0.7}Zn_{0.3}Fe_2O_4$ ) Ceramic Powder and its use in Smart Magnetorheological Fluid", *Rheologica Acta*, vol.58, no. 5, pp. 273-280, (2019).
- [15] H.K. Choudhary, S.P. Pawar, R. Kumar, A.V. Anupama, S. Bose and B. Sahoo, "Mechanistic Insight into the Critical Concentration of Barium Hexaferrite and the Conductive Polymeric Phase with Respect to Synergistically Electromagnetic Interference (EMI) Shielding", *Chemistry Select* vol. 2, no.2, pp. 830-841, (2017).

## References

- [16] A. Manikandan, J.J. Vijaya, L.J. Kennedy and M. Bououdina, "Microwave Combustion Synthesis , Structural , Optical and Magnetic properties of  $Zn_{1-x}Sr_xFe_2O_4$  Nanoparticles", *Ceramics International*, vol. 39, no. 5, pp. 5909-5917, (2013).
- [17] Hernandez, S. C., Chaudhuri, D., Chen, W., Myung, N. V., and Mulchandani, A., "Single polypyrrole Nanowire Ammonia Gas Sensor", *Electroanalysis: An International Journal Devoted to Fundamental and Practical Aspects of Electroanalysis*, vol. 19, no. (19-20), pp. 2125-2130, (2007).
- [18] Xiaoming Yang, Liang Li and Ye Zhao, "Ag/AgCl-decorated Polypyrrole Nanotubes and their Sensory Properties", *Synthetic Metals*, vol. 160, no. 17-18, pp.1822-1825, (2010).
- [19] D.P. Dubal, S.V. Patil, W.B. Kim and C.D. Lokhande, "Supercapacitors based on Electrochemically Deposited Polypyrrole Nanobricks", *Materials Letters*, vol. 65, pp. 2628-2631, (2011).
- [20] S. H. Hosseini and A. Asadnia, "Synthesis, Characterization, and Microwave-Absorbing Properties of Polypyrrole/ $MnFe_2O_4$  Nanocomposite", *Journal of Nanomaterials*, vol. 2012, Article ID 198973, pp. 6, (2012).
- [21] Sujata S. Shinde, Girish S. Gund, Vijay S. Kumbhar, Bebi H. Patil and Chandrakant D.Lokhande, "Novel Chemical Synthesis of Polypyrrole Thin Film Electrodes for Supercapacitor Application", *European Polymer Journal*, vol. 49, Issue 11, pp. 3734-3739, (2013).
- [22] Lina Geng and Shihua Wu, "Preparation, Characterization and Gas Sensitivity of Polypyrrole/  $\gamma$ - $Fe_2O_3$  Hybrid Materials", *Materials Research Bulletin*, vol. 48, no. 10, pp. 4339-4343, (2013).
- [23] Y. C. Eeu, H. N. Lim, Y. S. Lim, S. A. Zakarya, and N.M. Huang, "Electrodeposition of Polypyrrole/Reduced Graphene Oxide/Iron Oxide

## References

Nanocomposite as Supercapacitor Electrode Material", Journal of Nanomaterials, Article ID 653890, pp. 6, (2013).

[24] Habib Ullah, Khurshid Ayubb, Zakir Ullah, Muhammad Hanif, Raziq Nawaz, Anwar-ul-Haq Ali Shah and Salma Bilal, "Theoretical insight of Polypyrrole Ammonia Gas Sensor", Synthetic Metals, vol. 172, pp.14-20, (2013).

[25] S.T. Navale, G.D. Khuspe M.A. Chougule and V.B. Patil,"Room Temperature NO<sub>2</sub> Gas Sensor based on PPy/ $\alpha$ -Fe<sub>2</sub>O<sub>3</sub> Hybrid Nanocomposites", Ceramics International, vol.40, no. 6, pp. 8013-8020, (2014).

[26] S. H. Hosseini, A. Asadnia and M. Moloudi, "Preparation and Electromagnetic Wave absorption hard–soft Ba Ferrite/Polypyrrole Core-Shell Nanocomposites", Materials Research Innovations,vol. 19, no. 2, pp.107-112, (2015).

[27] Asmat Elahi, N. A. Niaz, M. S. Awan, Abdul Shakoor, Khalid Mahmood and Yaqoob Khan, "Structural, Electrical, and Magnetic Properties of Polypyrrole-Zn<sub>0.5</sub>Ni<sub>0.45</sub>Mn<sub>0.05</sub>Fe<sub>2</sub>O<sub>4</sub> Nanocomposites Prepared by In Situ Chemical Polymerization", Polymer Science Series B, vol. 57, No. 6, pp. 738-749, (2015).

[28] Xiaoran Sun, Hongwei Zhang , Liang Zhou, Xiaodan Huang, and Chengzhong yu, "Polypyrrole-Coated Zinc Ferrite Hollow Spheres with Improved Cycling Stability for Lithium-Ion Batteries", Wiley online library, vol. 12, no. 27, pp. 3732-3737, (2016).

[29] K. Mažeika, V. Bėčytė, Yu.O. Tykhonenko-Polishchuk, M.M. Kulyk, O.V. Yelenich and A.I. Tovstolytkin,"Comparison between Magnetic Properties of CoFe<sub>2</sub>O<sub>4</sub> and CoFe<sub>2</sub>O<sub>4</sub>/Polypyrrole Nanoparticles", Lithuanian Journal of Physics, vol. 58, no. 3, pp. 267-276, (2018).

## References

- [30] Dongzhi Zhang, Zhenling Wu, Xiaoqi Zong and Yong Zhang, "Fabrication of Polypyrrole/ $Zn_2SnO_4$  Nanofilm for Ultra-highly Sensitive Ammonia Sensing Application", *Sensors and Actuators B: Chemical*, vol. 274, no. 20, pp.575-586, (2018).
- [31] S.T. Assar, H.F. Abosheisha and E. H. El-Ghazzawy , "Preparation and Study of some Physical Properties of Co-Ni-Li Ferrite/Polypyrrole Nanocomposites ", *Journal of Alloys and Compounds*, vol. 802, pp. 553-561, (2019).
- [32] Sacchidanand S. Scindia, Ramesh B. Kamble and Jayant A. Kher," Nickel Ferrite/Polypyrrole core-shell Composite as an efficient Electrode Material for High-Performance Supercapacitor", *AIP Advances*, vol. 9, no. 5, pp. 055218, (2019).
- [33] Chunping Xu, Alain R. Puente-Santiago, Daily Rodríguez-Padrón, Alvaro Caballero, Alina M. Balu, Antonio A. Romero, Mario J. Muñoz-Batista and Rafael Luque, "Controllable Design of Polypyrrole-Iron Oxide Nanocoral Architectures for Supercapacitors with Ultrahigh Cycling Stability", *ACS Appl. Energy Mater.* , vol. 2, no. 3, pp. 2161-2168, (2019).
- [34] Aziz Yağan,"Investigation of Polypyrrole-Based Iron Electrodes as Supercapacitors", *Int. J. Electrochem. Sci.*, vol. 14, pp.3978-3985, (2019).
- [35] Huijun Liu, Qiang Zhao, Kewei Wang, Zhen Lu, Feng Feng and Yong Guo, " Facile Synthesis of Polypyrrole Nanofiber (PPyNF)/NiOx Composites by a Microwave Method and Application in Supercapacitors", *RSC Adv.*, vol. 9, no. 12, pp. 6890-6897, (2019).
- [36] Chao Wang, Ming Yang , Lihong Liu, Yingming Xu, Xianfa Zhang , Xiaoli Cheng, Shan Gao,Yuan Gao and Lihua Huo," One-step Synthesis of Polypyrrole/ $Fe_2O_3$  Nanocomposite and the a enhanced Response of  $NO_2$  at Low Temperature", *Journal of Colloid and Interface Science*, vol. 560, pp. 312-320, (2020).

## References

- [37] Schwartz, Mel. , "New Materials, Processes, and Methods Technology", Crc Press, (2005).
- [38] Trotta F., and Mele A., "Nanomaterials: Classification and Properties. Nanosponges: Synthesis and Applications", First Edition, Wiley, London, (2019).
- [39] Ozin, Geoffrey A. and Cademartiri L., "Nanochemistry: What Is Next?", *Small*, vol. 5, no. 1, pp. 1240-1244 , (2009).
- [40] Jeevanandam J., Barhoum A., Chan Y. S., Dufresne A., and Danquah M. K. , "Review on Nanoparticles and Nanostructured Materials: History, Sources, Toxicity and Regulations", *Beilstein Journal of Nanotechnology*, vol. 9, no. 1, pp. 1050-1074, (2018).
- [41] Pang, S., Zhou, Z., and Wang, Q. , "Smart 0D Nanomaterials Assembled by Green Luminescent Terbium Hybrids for The Detection of Tryptophan", *Journal of Nanoparticle Research*, vol. 15, no. 3, pp. 1-9, (2013).
- [42] Han, J. T., Choi, S., Jang, J. I., Seol, S. K., Woo, J. S., Jeong, H. J., and Lee, G. W. , "Rearrangement of 1d Conducting Nanomaterials Towards Highly Electrically Conducting Nanocomposite Fibres for Electronic Textiles", *Scientific Reports*, vol. 5, no. 1, pp. 1-7, (2015).
- [43] Luo, B., Liu, G., and Wang, L., "Recent Advances in 2d Materials for Photocatalysis", *Nanoscale*, vol. 8, no. 13, pp. 6904-6920, (2016).
- [44] Liu P., Hao Q., Xia X., Lu L., Lei W., and Wang X. , "3D Hierarchical Mesoporous Flowerlike Cobalt oxide Nanomaterials: Controllable Synthesis and Electrochemical Properties", *The Journal of Physical Chemistry C*, vol. 119, no. 16, pp. 8537-8546, (2015).
- [45] Inzelt György, "Conducting Polymers: A new Era in Electrochemistry", Springer Science & Business Media, (2012).

## References

- [46] Prasanna Chandrasekhar," Conducting Polymers, Fundamentals and Applications a Practical Approach", Ashwin-Ushas Corp., Inc., Kluwer Academic Publishers In (1999).
- [47] Le, Thanh Hai, Yukyung Kim, and Hyeonseok Yoon., "Electrical and Electrochemical Properties of Conducting Polymers", *Polymers*, vol. 9, no. 4, pp. 150, (2017).
- [48] Bredas J.L., R.R. Chance, and R. Silbey, "Comparative Theoretical Study of The Doping Conjugated Polymers; Polarons In Polyacetylene and Polyparaphenylene", *Physical Review B*, vol. 26, no. 10, pp. 5843-5854, (1982).
- [49] Michael S. Freund and Bhavana A. Deore," Self-Doped Conducting Polymers", John Wiley & Sons Ltd, (2007).
- [50] Dr. B. S. Chauhan, "Engineering Chemistry", University Science Press, First Edition, (2013).
- [51] Hari Singh Nalwa, "Handbook of organic Conductive Molecules and Polymers", John Wiley and Sons Ltd., (1997).
- [52] Skotheim Terje A., "Handbook of Conducting Polymers", Crc Press, (Ed.), (1997).
- [53] Cheng Q., Pavlinek V., Li C., Lengalova A., He Y., and Saha P. ,"Synthesis and Characterization of New Mesoporous Material With Conducting Polypyrrole Confined In Mesoporous Silica", *Materials Chemistry and Physics*, vol. 98, no. (2-3), pp. 504-508, (2006).
- [54] Ansari R., "Polypyrrole Conducting Electroactive Polymers: Synthesis and Stability Studies", *E-Journal of Chemistry*, vol.3, no.13, pp. 186-201, (2006).
- [55] J. L. Bredas and G. B. Street, "Polarons, Bipolarons, and Solitons in Conducting Polymers", *Accounts of Chemical Research*, vol. 18, no. 10, pp. 309-315, (1985).

## References

- [56] Charles Kittel, "Introduction to Solid State Physics", John Wiley & Sons, Inc, Eight Edition, (2005).
- [57] A. K. Bhargava, "Engineering Materials: Polymers Ceramics and Composites", Second Edition, Phi Learning Private Limited, (2012).
- [58] Kricheldorf, H.R., Nuyken, O. and Swift, G., "Handbook of Polymer Synthesis", Marcel Dekker., Ch. 12, pp. 1-4, (2005).
- [59] J. L. Bredas, "Bipolarons in Doped Conjugated Polymers: A Critical Comparison between Theoretical Results and Experimental Data", Molecular Crystals and Liquid Crystals, vol. 118, no. 1, pp. 49-56, (1985).
- [60] R. A. Khalkhali, "Effect of Thermal Treatment on Electrical Conductivities of Polypyrrole Conducting Polymers", Iranian Polymer Journal, vol. 13, no. 1, pp. 53-60, (2004).
- [61] D. S. Maddison and J. Unsworth, "Optimization of Synthesis Conditions of Polypyrrole from Aqueous Solutions," Synthetic Metals, vol. 30, no. 1, pp. 47-55, (1989).
- [62] Macdiarmid A. G., Mammone R. J., Kaner R. B., and Porter L. , "The Concept of Doping of Conducting Polymers: The Role of reduction Potentials", Philosophical Transactions of The Royal Society of London. Series A, Mathematical and Physical Sciences, vol. 314, no. 1528, pp. 3-15, (1985).
- [63] Cuuran S., Hauser A.S. and Roth S., "Conductive Polymers: Synthesis and Electrical Properties. In Handbook of organic Conductive Molecules and Polymers", Hari, S.N., Ed.; John Wiley & Sons: New York, Ny, USA, vol. 2, pp. 1-60, (1997).
- [64] Wan M. "Conducting Polymers with Micro or Nanometer Structure", Beijing: Tsinghua University Press, (2008).
- [65] Zhang Y., B. De Boer, and Paul W. B., "Controllable Molecular Doping and Charge Transport In Solution-Processed Polymer Semiconducting Layers", Advanced Functional Materials, vol. 19, no.12, pp. 1901-1905, (2009).

## References

- [66] Guo X., and A. Facchetti, "The Journey of Conducting Polymers from Discovery to Application", *Nature Materials*, vol. 19, no. 9, pp. 922-928, (2020).
- [67] Mcquade D. Tyler, Anthony E. Pullen, and Timothy M. Swager, "Conjugated Polymer-Based Chemical Sensors." *Chemical Reviews*, vol. 100, no.7, pp. 2537-2574, (2000).
- [68] Ahuja T. and D. Kumar, "Recent Progress in The Development of Nano-Structured Conducting Polymers/Nanocomposites for Sensor Applications", *Sensors and Actuators B: Chemical*, vol. 136, no.1, pp. 275-286, (2009).
- [69] Reut J., A. Öpik, and K. Idla, "Corrosion Behavior of Polypyrrole Coated Mild Steel", *Synthetic Metals*, vol. 102, no.1-3, pp. 1392-1393, (1999).
- [70] De Oliveira, H. P., C. A. S. Andrade, and C. P. De Melo. "Optical and Dielectric Properties of Polypyrrole Nanoparticles in A Polyvinylalcohol Matrix", *Synthetic Metals*, vol. 155, no. 3, pp. 631-634, (2005).
- [71] Heeger Alan J, "Semiconducting and Metallic Polymers: The Fourth Generation of Polymeric Materials", *The Journal of Physical Chemistry B*, vol. 105, no. 36, pp. 8475-8491, (2001).
- [72] A. Angeli and A. pieroni, *Qazz. Chim. Ital.* 49 (I), 164 (1919).
- [73] Sadki S., Schottland P., Brodie N., and Sabouraud G., "The mechanisms of pyrrole electropolymerization. *Chemical Society Reviews*, 29(5), 283-293, (2000).
- [74] Sharifi-Viand, A. Mahjani, M. G., and Jafarian M., "Determination of fractal rough surface of polypyrrole film: AFM and electrochemical analysis", *Synthetic metals*, 191, 104-112, (2014).
- [75] Liu Ran, Jonathon Duay and Sang Bok Lee. "Redox Exchange Induced MnO<sub>2</sub> Nanoparticle Enrichment in Poly (3, 4-Ethylenedioxythiophene) Nanowires for Electrochemical Energy Storage", *Acs Nano*, vol. 4, no. 7, pp. 4299-4307, (2010).

## References

- [76] Wang J. and Mustafa M., "Carbon-Nanotubes Doped Polypyrrole Glucose Biosensor", *Analytica Chimica Acta*, vol. 539, no. 1-2, pp. 209-213, (2005).
- [77] Ghanbari K. H., S. Z. Bathaie, and M. F. Mousavi, "Electrochemically Fabricated Polypyrrole Nanofiber-Modified Electrode as a New Electrochemical DNA Biosensor", *Biosensors and Bioelectronics*, vol. 23, no. 12, pp. 1825-1831, (2008).
- [78] Martina, Monique, and Dietmar W. Hutmacher, "Biodegradable polymers applied in tissue engineering research: a review", *Polymer International*, vol. 56, no. 2, pp. 145-157, (2007).
- [79] Harley C., "The Formation of an Electrochemical Sensor for The Selective Detection of Dopamine", Doctoral dissertation, National University of Ireland Maynooth, (2009).
- [80] Clyne T. W. and Hull D., "An Introduction to Composite Materials", Cambridge University Press, (2019).
- [81] S.G. Advani, "Processing and Properties of nanocomposites, World Scientific, (Ed.), (2006).
- [82] Li Jinghong, and Jin Z. Zhang. "Optical Properties and Applications of Hybrid Semiconductor Nanomaterials", *Coordination Chemistry Reviews*, vol. 253, no. 23-24, pp. 3015-3041, (2009).
- [83] Schwartz M.M., "Composite Materials, Volume I: Properties, Nondestructive Testing and Repair", Prentice-Hall Inc., New Jersey, (1997).
- [84] Rane A. V., Kanny K., Abitha V. K., and Thomas S. , "Methods For Synthesis of Nanoparticles and Fabrication of Nanocomposites", In *Synthesis of Inorganic Nanomaterials*-Woodhead Publishing, pp. 121-139, (2018).
- [85] Kornmann X., H. Lindberg, and L. A. Berglund, "Synthesis of Epoxy-Clay Nanocomposites. Influence of the nature of the Curing Agent on Structure", *Polymer*, vol. 42, no. 10, pp. 4493-4499, (2001).

## References

- [86] Filippi S., Marazzato C., Magagnini P., Famulari A., Arosio P., and Meille S. V., "Structure and Morphology of HDPE-g-MA/organoclay nanocomposites: Effects of the preparation procedures", *European Polymer Journal*, vol. 44, no. 4, pp. 987-1002, (2008).
- [87] Lee E. S., Park J. H., Wallace G. G., and Bae Y. H., "In Situ Formed Processable Polypyrrole Nanoparticle/Amphiphilic Elastomer Composites and their Properties", *Polymer International*, vol. 53, no. 4, pp. 400-405, (2004).
- [88] Dallas P., Niarchos D., Vrbanic D., Boukos N., Pejovnik S., Trapalis C. and Petridis D.," Interfacial Polymerization of Pyrrole and In Situ Synthesis of Polypyrrole/Silver Nanocomposites", *Polymer*, vol. 48, no. 7, (2007).
- [89] Souza V. C., and M. G. N. Quadri, "Organic-Inorganic Hybrid Membranes in Separation Processes: A 10-Year Review", *Brazilian Journal of Chemical Engineering*, vol. 30, pp. 683-700, (2013).
- [90] Pellegrino Musto, Giuseppe Ragosta, Gennaro Scarinzi and Leno Mascia, "polyimide-silica Nanocomposites: spectroscopic, morphological and mechanical investigations", *Polymer*, vol. 45, no. 5, pp.1697-1706, (2004).
- [91] M. Q. Zhang, M. Z. Rong, and K. Friedrich, "In Hand-Book of Organic-Inorganic Hybrid Materials and Nano-Composites", Ed. By H. S. Nalwa, (American Science Publishers, California), vol. 2, pp. 113, (2003).
- [92] Ding S. J., Zhang C. L., Yang M., Qu X. Z., Lu Y. F., and Yang Z. Z., "Template Synthesis of composite hollow spheres using Sulfonated Polystyrene Hollow Spheres", *Polymer*, vol. 47, pp. 25, pp. 8360-8366, (2006).
- [93] Xiaofeng Lu, Youhai Yu, Liang Chen, Huaping Mao, Han Gao, Jue Wang, Wanjin Zhang and Yen Wei, "Aniline Dimer-COOH Assisted Preparation of Well-Dispersed Polyaniline-Fe<sub>3</sub>O<sub>4</sub> Nanoparticles", *Nanotechnology*, vol. 16, no. 9, pp. 1660, (2005).

## References

- [94] Nunes J., Herlihy K. P., Mair L., Superfine R., and Desimone, J. M., "Multifunctional Shape and Size Specific Magneto-Polymer Composite Particles", *Nano Letters*, vol. 10, no. 4, pp. 1113-1119, (2010).
- [95] Xiao Yinghong, and Chang Ming Li, "Nanocomposites: From Fabrications to Electrochemical Bioapplications", *Electroanalysis: An International Journal Devoted to Fundamental and Practical Aspects of Electroanalysis*, vol. 20, no. 6, pp. 648-662, (2008).
- [96] Caruso Frank, "Nanoengineering of Particle Surfaces", *Advanced Materials*, vol.13, no. 1, pp.11-22, (2001).
- [97] Rafique, M. M. A., E. Kandare, and Stephan S., "Fiber-Reinforced Magneto-Polymer Matrix Composites (FR-MPMCs)-A review", *Journal of Materials Research*, vol. 32, no. 6, pp.1020-1046, (2017).
- [98] C. Zhang, Q. Li, and Y. Ye, "Preparation and Characterization of Polypyrrole/Nano-SrFe<sub>12</sub>O<sub>19</sub> Composites by In situ polymerization method", *Synthetic Metals*, vol. 159, no. 11, pp. 1008-1013, (2009).
- [99] Ding H., Liu X. M., Wan M., and Fu, S. Y., "Electromagnetic Functionalized Cage-Like Polyaniline Composite Nanostructures", *The Journal of Physical Chemistry B*, vol. 112, no. 31, pp. 9289-9294, (2008).
- [100] Jun Y. w., Seo J. w., and Cheon J., "Nanoscaling laws of Magnetic Nanoparticles and their applicabilities in Biomedical Sciences", *Accounts of chemical research*, vol. 41, no.2, pp. 179-189, (2008).
- [101] Lu A.-H., Salabas E., and Schüth F., "Magnetic Nanoparticles: Synthesis, Protection, Functionalization, and Application", *Angewandte Chemie International Edition*, vol. 46, no. 8, pp. 1222-1244, (2007).
- [102] Gubin S., Koksharov Y. A., Khomutov G., and Yu. Y. G., "Magnetic Nanoparticles: Preparation, Structure and Properties", *Russ. Chem. Rev.*, vol. 74, no. 6, pp. 489-520, (2005).
- [103] B. D. Cullity and C. D. Graham, "Introduction to Magnetic Materials", A John Wiley & Sons. Inc., Hoboken, New Jersey, (2009).

## References

- [104] William D. Callister, Jr., "Materials Science and Engineering: An Introduction", 7th Ed, John Wiley & Sons, Inc, (2007).
- [105] McHenry, M. E., and Laughlin, "Magnetic moment and magnetization", Characterization of materials, (2012).
- [106] Khan H. M., "Effect of Divalent and Trivalent Cations on the Electrical and Magnetic Properties of Hexa-ferrites", (Doctoral dissertation, Bahauddin Zakariya University Multan, Pakistan), (2016).
- [107] Vijaya and Rangarajan, "Materials Science" , Mcgraw-Hill Publishing Company Limited, New Delhi, (2000).
- [108] Kittel, "Introduction to Solid State Physics", 7th Ed. John Wiley and Sons, Newyork, (1996).
- [109] Omar M. A., "Elementary Solid State Physics: Principles and Applications", Addison-Wesley Publishing Company, Amsterdam, (1962).
- [110] Allan H. M., "The Physical Principles of Magnetism", John Wiley and Sons, (1965).
- [111] Reitz, Milford and Chrisly, "Foundations of electromagnetic Theory", 3rd Ed. Addison-Wesley Publishing Company, London (1979).
- [112] Veena Gopalan E., and Anantharaman, M. R., "On the Synthesis and Multifunctional Properties of some Nanocrystalline Spinel Ferrites and Magnetic Nanocomposites", (Doctoral dissertation, Cochin University of Science & Technology), (2009).
- [113] Mathew D. S., and Juang R. S., "An overview of the Structure and Magnetism of Spinel Ferrite Nanoparticles and their Synthesis in Microemulsions", Chemical engineering journal, vol. 129, no. 1-3, pp. 51-65, (2007).

## References

- [114] Goldman A., "Modern Ferrite Technology", Springer Science & Business Media, (2006).
- [115] Y. Yafet, and C. Kittle, "X-ray Diffraction and Magnetic Measurements of the Fe-Cr Spinel," *Phy. Rev*, vol. 87, pp. 290, (1952).
- [116] B. D. Cullity, and C. D. Graham, "Introduction to Magnetic Materials", John Wiley & Sons, (2011).
- [117] Tetiana Tatarchuk, Mohamed Bououdina, J. Judith Vijaya, and L. John Kennedy, "Spinel Ferrite Nanoparticles: Synthesis, Crystal Structure, Properties, and Perspective Applications", In International conference on nanotechnology and nanomaterials, vol.195, pp.305-325, (2016).
- [118] Mastai, Y., "Advances in crystallization processes", BoD-Books on Demand., (2012).
- [119] M. G. Naseri and E. B. Saion, "Crystallization in Spinel Ferrite Nanoparticles", *Advances in Crystallization Processes*, pp.349-380, (2012).
- [120] Mahhouti Z., "Synthesis and Characterization of Functional monodispersed cobalt ferrite nanoparticles", (Doctoral Dissertation, Amiens), (2019).
- [121] Winkler G., "Crystallography, chemistry and technology of ferrites; In: *Magnetic properties of materials*", Ed. J Smit, New York, McGraw-Hill, (1971).
- [122] R. Valenzuela, "Magnetic Ceramics", Cambridge University Press, Cambridge, (1994).
- [123] Issa B., Obaidat I. M., Albiss B. A., and Haik Y., "Magnetic Nanoparticles: Surface Effects and Properties Related to Biomedicine Applications", *International Journal of Molecular Sciences*, vol. 14, no. 11, pp. 21266-21305, (2013).

## References

- [124] Mehrmohammadi M., Yoon K. Y., Qu M., Johnston K. P., and Emelianov S. Y., "Enhanced pulsed magneto-motive ultrasound imaging using superparamagnetic nanoclusters", *Nanotechnology*, vol. 22, no.4, pp.1-8, (2010).
- [125] J. Frenkel, and J. Doefman, "Spontaneous and Induced Magnetisation in Ferromagnetic Bodies", *Nature*, vol.126, no.3173, pp.274-275, (1930).
- [126] Stephen Blundell, "Magnetism in condensed matter", Oxford University Press, (2001).
- [127] Subhankar Bedanta and Wolfgang Kleemann, "Supermagnetism" , *Journal of Physics D: Applied Physics*, vol.42, no.1, (2009).
- [128] Chao Liu, Bingsuo Zou, Adam J. Rondinone, and Z. John Zhang, "Chemical Control of Superparamagnetic Properties of Magnesium and Cobalt Spinel Ferrite Nanoparticles Through Atomic Level Magnetic Couplings" , *Journal of the American Chemical Society*, vol.122, no.26, pp. 6263-6267, (2000).
- [129] U. Nowak, O. N. Mryasov, R. Wieser, K. Guslienko and R. W.Chantrell, "Spin Dynamics of Magnetic Nanoparticles: Beyond Brown's Theory" , *Physical Review B*, vol.72, no.17, pp. 172410, (2005).
- [130] Elena-Lorena Salabas, "Structural and Magnetic Investigations of Magnetic Nanoparticles and Core-Shell Colloids", University of Duisburg-Essen, Doctoral dissertation, (2004).
- [131] W. D. Kingery, H. K. Bowen, and D. R. Uhlmann, "Introduction to Ceramics", Wiley New York, (1976).
- [132] D. L. Leslie-Pelecky, and R. D. Rieke, "Magnetic Properties of Nanostructured Materials", *Chemistry of Materials*, vol. 8, no. 8, pp. 1770-1783, (1996).

## References

- [133] Teja A. S., and Koh P. Y., "Synthesis, properties, and applications of magnetic iron oxide nanoparticles", *Progress in crystal growth and characterization of materials*, vol. 55, no. 1-2, pp. 22-45, (2009).
- [134] N. Kumar, and S. Kumbhat, "Essentials in nanoscience and nanotechnology", John Wiley & Sons, Inc., Hoboken, New Jersey, USA, (2016).
- [135] Getzlaff M., "Fundamentals of Magnetism", Springer Science & Business Media, (2007).
- [136] S. Tapdiya, "Synthesis and Characterization of Some mixed Ferrites", Jiwaji University, Gwalior, (2017).
- [137] Sirdeshmukh, D. B., Sirdeshmukh, L., Subhadra, K. G., and Sunandana, C. S., "Physics of Semiconductors. In Electrical, Electronic and Magnetic Properties of Solids", Springer International Publishing ,(2014).
- [138] Bradford P., "The aggregation of Iron oxide nanoparticles in Magnetic fields", (Doctoral Dissertation, University of Birmingham), (2012).
- [139] Morton J. J. "Magnetic Properties of Materials". JJLM Trinity, (2012).
- [140] Sgobba S., "Physics and Measurements of Magnetic Materials", Arxiv Preprint Arxiv, pp.1103-1069, (2011).
- [141] E. C. Stoner, F.R.S. and E. P. Wohlfarth, "A mechanism of Magnetic Hysteresis In Heterogeneous Alloys", *Philosophical Transactions of The Royal Society of London. Series A, Mathematical and Physical Sciences*, vol. 240, no. 826, pp. 599-642, (1948).
- [142] J. L. Dormann, D. Fiorani, and E. Tronic, "Magnetic Relaxation In Fine-Particle Systems" , *Advances In Chemical Physics*, vol.98, pp. 283-493, (1997).

## References

- [143] Mahhouti Z., Ben Ali, M. El Moussaoui, H. Hamedoun, M. El Marssi, M. El Kenz, A. and Benyoussef A., "Structural and magnetic properties of  $\text{Co}_{0.7}\text{Ni}_{0.3}\text{Fe}_2\text{O}_4$  Nanoparticles Synthesized by sol-gel Method", *Applied Physics A*, vol. 122, no. 7, pp. 1-6, (2016).
- [144] Daou T. J., Pourroy G., Bégin-Colin S., Greneche J. M., Ulhaq-Bouillet C., Legaré P., and Rogez G., "Hydrothermal Synthesis of Monodisperse Magnetite Nanoparticles," *Chemistry of Materials*, vol. 18, no. 18, pp. 4399-4404, (2006).
- [145] A. Abou-Hassan, S. Neveu, V. Dupuis, and V. Cabuil, "Synthesis of cobalt ferrite nanoparticles in Continuous-Flow Microreactors", *RSC advances*, vol. 2, no. 30, pp. 11263-11266, (2012).
- [146] Pérez-Mirabet, L. Solano, E. Martínez-Julián, F. Guzmán, R. Arbiol, J. Puig T., and Ricart S., "One-pot synthesis of stable colloidal solutions of  $\text{MFe}_2\text{O}_4$  nanoparticles using oleylamine as solvent and stabilizer", *Materials Research Bulletin*, vol. 48, no. 3, pp. 966-972, (2013).
- [147] T. Sugimoto and E. Matijevic, "Formation of uniform spherical magnetite particles by crystallization from ferrous hydroxide gels", *Journal of Colloid and Interface Science*, vol. 74, no. 1, pp. 227-243, (1980).
- [148] Olsson R. T., Salazar-Alvarez G., Hedenqvist M. S., Gedde U. W., Lindberg F., and Savage S. J., "Controlled synthesis of near-stoichiometric cobalt ferrite nanoparticles", *Chemistry of materials*, vol. 17, no. 20, pp. 5109-5118, (2005).
- [149] Maaz K., Mumtaz A., Hasanain S. K., and Ceylan A., "Synthesis and magnetic properties of cobalt ferrite ( $\text{CoFe}_2\text{O}_4$ ) nanoparticles prepared by wet chemical route", *Journal of magnetism and magnetic materials*, vol. 308, no. 2, pp. 289-295, (2007).

## References

- [150] Qi Y., Yang Y., Zhao X., Liu X., Wu P., Zhang F., and Xu S., "Controllable magnetic properties of cobalt ferrite particles derived from layered double hydroxide precursors", *Particuology*, vol. 8, no.3, pp.207-211, (2010).
- [151] Yang C., and Yan H., "A green and facile approach for synthesis of magnetite nanoparticles with tunable sizes and morphologies", *Materials Letters*, vol.73, pp. 129-132, (2012).
- [152] Byrappa K., and Adschiri T., "Hydrothermal technology for nanotechnology", *Progress in crystal growth and characterization of materials*, vol. 53, no. 2, pp. 117-166, (2007).
- [153] Yao C., Shin Y., Wang L. Q., Windisch C. F., Samuels W. D., Arey B. W., and Exarhos G. J. , "Hydrothermal dehydration of aqueous fructose solutions in a closed system", *The Journal of Physical Chemistry C*, vol. 111, no. 42, pp. 15141-15145, (2007).
- [154] Köseoğlu Y, Alan F, Tan M, Yilgin R and Öztürk M.," Low Temperature Hydrothermal synthesis and characterization of Mn doped cobalt ferrite nanoparticles", *Ceramics International*, vol. 38, no. 5, pp. 3625-3634, (2012).
- [155] Ahmadian-Fard-Fini S, Salavati-Niasari M and Ghanbari D., "Hydrothermal green synthesis of Magnetic Fe<sub>3</sub>O<sub>4</sub>-carbon dots by Lemon and grape fruit extracts and as a photoluminescence sensor for detecting of E. Coli Bacteria", *Spectrochimica Acta Part A: molecular and biomolecular spectroscopy*, vol. 203, pp. 481-93, (2018).
- [156] Tian Y., Yu B., Li X., and Li K., "Facile solvothermal synthesis of monodisperse Fe<sub>3</sub>O<sub>4</sub> nanocrystals with precise size control of one nanometre as potential MRI contrast agents", *Journal of Materials Chemistry*, vol. 21, no. 8, pp. 2476-2481, (2011).

## References

- [157] Zabihi R., and Nejati K., "Preparation and magnetic properties of nanosize nickel ferrite particles using hydrothermal method", *Chemistry Central Journal*, vol. 6, no. 23, (2012).
- [158] Park J., "Nanostructured semiconducting metal oxide for Use in Gas sensor", PhD. Thesis, University of Wollongong, (2010).
- [159] M. Lu, F. Beguin, and E. Frackowak, "Supercapacitors materials, systems, and applications", John Wiley and Sons, Weinheim, Germany, (2013).
- [160] Zhang R., "A study of flexible supercapacitors: design, manufacture and testing", (Doctoral dissertation, Brunel University London), (2016).
- [161] S.M. Chen, R. Ramachandran, V. Mani and R. Saraswathi, "Recent Advancements In Electrode Materials For The High-Performance Electrochemical Supercapacitors: A Review", *Int. J. Electrochem. Sci.*, vol. 9, no. 8, pp. 4072-4085, (2014).
- [162] B. E. Conway, "Electrochemical Supercapacitors: Scientific Fundamentals and Technological Applications", Springer Science & Business Media, (2013).
- [163] Zhang Y., Feng H., Wu X., Wang L., Zhang A., Xia T. and Zhang L., "Progress of Electrochemical Capacitor Electrode Materials: A Review", *Int. J. Hydrogen Energy*, vol. 34, no. 11, pp. 4889-4899, (2009).
- [164] M. V Fedorov and A. A. Kornyshev, "Towards Understanding The Structure and Capacitance of Electrical Double Layer In Ionic Liquids", *Electrochimica Acta*, vol. 53, no. 23, pp. 6835-6840, (2008).
- [165] A. K. Shukla, S. Sampath, and K. Vijayamohanan, "Electrochemical Supercapacitors: Energy Storage Beyond Batteries," *Current Science*, vol. 79, no. 12, pp. 1656-1661, (2000).

## References

[166] Bakheet Awad Alresheedi, "Supercapacitors Based on Carbon Nanotube Fuzzy Fabric Structural Composites", The degree of Doctor of Philosophy In Materials Engineering, University of Dayton, Dayton, Ohio, (2012).

[167] Lassegues J. C., "Super-capacitors; Supercondensateurs", Techniques de l'Ingenieur. Genie Electrique , 5, (2001).

[168] Y. Wang, "Manganese Dioxide Based Composite Electrodes For Electrochemical Supercapacitors", Doctoral dissertation, McMaster University, (2012).

[169] A. Burke, "Ultracapacitors: Why, How, and Where is the Technology", J. Power Sources, vol. 91, no. 1, pp. 37-50, (2000).

[170] C. Arbizzani, M. Mastragostino and F. Soavi, "New Trends In Electrochemical Supercapacitors", Journal of Power Sources. vol. 100, no.1-2, pp. 164-170, (2001).

[171] C. Peng, S. Zhang, D. Jewell and G.Z. Chen, "Carbon Nanotube and Conducting Polymer Composites for Supercapacitors", Progress in Natural science, vo. 18, no. 7, pp. 777-788, (2008).

[172] W.G. Pell, and B.E. Conway, "Peculiarities and Requirements of Asymmetric Capacitor devices based on Combination of Capacitor and Battery-Type Electrodes", Journal of power Sources. vol. 136, no. 2, pp. 334-345, (2004).

[173] Lé T., "Fundamental insights into dynamic ionic exchange in vertically-oriented nanostructured materials via fast electrogravimetric methods. Applications to energy storage mechanisms", (Doctoral dissertation, Sorbonne university), (2018).

[174] L. T. Lam and R. Louey, "Development of ultra-Battery for Hybrid-Electric vehicle Applications," Journal of Power Sources, vol. 158, no. 2, pp. 1140-1148, (2006).

## References

- [175] P. Thounthong, V. Chunkag, P. Sethakul, B. Davat, and M. Hinaje, "Comparative study of fuel-cell vehicle Hybridization with Battery or supercapacitor Storage Device", *IEEE transactions on vehicular technology*, vol. 58, no. 8, pp. 3892–3904, (2009).
- [176] S. Pan, J. Ren, X. Fang, and H. Peng, "Integration: an effective strategy to develop multifunctional energy storage devices", *Advanced Energy Materials*, vol. 6, no. 4, pp. 1501867, (2016).
- [177] W. Plieth, "Electrochemistry for Materials Science", 1st Ed. Elsevier B.V, (2008).
- [178] X. Yuan and N. Xu, "Determination of hydrogen diffusion coefficient in metal hydride electrode by cyclic voltammetry", *Journal of alloys and compounds*, vol. 316, no. 1-2, pp. 113-117, (2001).
- [179] D. Weingarth, M. Zeiger, N. Jäckel, M. Aslan, G. Feng, and V. Presser, "Graphitization as A universal tool to tailor the potential-Dependent capacitance of carbon supercapacitors", *Advanced Energy Materials*, vol. 4, no. 13, pp. 1-13, (2014).
- [180] R. Signorelli, D. C. Ku, J. G. Kassakian, and J. E. Schindall, "electrochemical double-layer capacitors using carbon nanotube electrode structures", *Proceedings of the IEEE*, vol. 97, no. 11, pp. 1837-1847, (2009).
- [181] B. E. Conway and W. G. Pell, "Double-layer and pseudocapacitance types of electrochemical capacitors and their applications to the development of hybrid devices", *Journal of Solid State Electrochemistry*, vol. 7, no. 9, pp. 637-644, (2003).
- [182] E. Frackowiak and F. Beguin, "Carbon Materials for The Electrochemical Storage of Energy In Capacitors", *Carbon N. Y.*, vol. 39, no. 6, pp. 937-950, (2001).
- [183] Y. Gao, S. Chen, D. Cao, G. Wang, and J. Yin, "Electrochemical Capacitance of  $\text{Co}_3\text{O}_4$  Nanowire Arrays supported on Nickel Foam," *Journal of Power Sources*, vol. 195, no. 6, pp. 1757-1760, (2010).

## References

- [184] Raza W., Ali, F., Raza N., Luo Y., Kim K. H., Yang J., and Kwon E. E., "Recent advancements in supercapacitor technology", *Nano Energy*, vol. 52, pp. 441-473, (2018).
- [185] B. K. Kim, S. Sy, A. Yu, and J. Zhang, "Electrochemical Supercapacitors for Energy Storage and Conversion", *Handbook of clean energy systems*, pp. 1-25, (2015).
- [186] F. Lufrano and P. Staiti, "Performance Improvement of Nafion based solid state electrochemical supercapacitor", *Electrochimica Acta*. vol. 49, no. 16, pp. 2683-2689, (2004).
- [187] Kampouris, D. K., Ji, X., Randviir, E. P., and Banks, C. E. "A new approach for the improved interpretation of capacitance measurements for materials utilized in energy Storage", *Rsc Advances*, vol. 5, no. 17, pp. 12782-12791, (2015).
- [188] Q. Cheng, J. Tang, J. Ma, H. Zhang, N. Shinya, and L.-C. Qin, "Graphene and carbon nanotube composite electrodes for supercapacitors with ultra-high energy density", *Physical Chemistry Chemical Physics*, vol. 13, no. 39, pp. 17615-17624, (2011).
- [189] Mei B. A., Munteshari O., Lau J., Dunn B., and Pilon L., "Physical interpretations of Nyquist plots of EDLC electrodes and devices", *The Journal of Physical Chemistry C*, vol. 122, no. 1, pp. 194-206, (2018).
- [190] Z. He, and F. Mansfeld, "Exploring the use of electrochemical impedance Spectroscopy (EIS) in microbial fuel cell studies", *Energy & Environmental Science*, vol. 2, pp. 215-219, (2009).
- [191] j. Wang g. Yu, g. Srdanov, and a. J. Heeger, "Color characterization of large area polymer image sensors," *Organic Electronics*, vol. 1, no. 1, pp. 33-40, (2000).
- [192] Al-Haddad, R. M., Ali, I. M., Ibrahim, I. M., and Ahmed, N. M., "Photoconductivity and Performance of Mn<sup>2+</sup> and Ce<sup>3+</sup> Doped ZnS Quantum Dot Detectors", *Engineering and Technology Journal*, vol. 33, no. 9, pp. 1608-1618.

## References

- [193] Joshi N. V., "photoconductivity: art: science & technology", vol. 25. Crc press, (1990).
- [194] S. Srivastava, s. K. Mishra, r. S. Yadav, r. K. Srivastava, a. C. Panday, and s. G. Prakash, "Photoconductivity and darkconductivity studies of Mn-doped ZnS nanoparticles", Digest Journal of Nanomaterials and Biostructures, vol. 5, no. 1, pp. 161-167, (2010).
- [195] R. Shankar, R. Srivastava, and S. Prakash, " Photoconductivity and Darkconductivity in ZnO: Cu, Br," journal of international academy of physical sciences, vol. 16, no. 3, pp. 283-288, (2012).
- [196]Taffelli A., Dirè S., Quaranta a., and Pancheri L., "Mos2 based photodetectors: a review", Sensors, vol. 21, no. 8, pp. 2758.
- [197] Hou Y., Mei Z., and Du X., "Semiconductor ultraviolet photodetectors based on ZnO and  $Mg_xZn_{1-x}O$ ", Journal of physics D: Applied physics, vol. 47, no. 28, pp. 283001, (2014).
- [198] Jia-ming Liu, "Photonic Devices", cambridge university press: cambridge, (2005).
- [199] Ahmed M. S., I.M. Ali, and N. A.Bakr. "Photodetector Properties of Polyaniline/CuO Nanostructures Synthesized by Hydrothermal Technique." (2019).
- [200] Monroy E., Omnès F., and Calle, F. J. S. S., "Wide-Bandgap Semiconductor Ultraviolet Photodetectors", Semiconductor science and technology, vol. 18, no. 4,(2003).
- [201] Vandervalk C. J., Wenckebach T., and Planken P. C., "Full mathematical description of electro-optic detection in optically Isotropic Crystals", JOSA B, vol. 21, no. 3, pp. 622-631, (2004).
- [202] Kumar P., Saxena N., Dewan S., Singh F., and Gupta V., "Giant UV-Sensitivity of Ion Beam Irradiated Nanocrystalline CdS Thin films", RSC advances, vol. 6, no. 5, pp. 3642-3649, (2016).

## References

- [203] Mohammed F. K., Beh K. P., Ramizy A., Ahmed N. M., Yam F. K., and Hassan Z., "Improvement of Porous GaN-Based UV Photodetector with Graphene Cladding", *Applied Sciences*, vol.11, no. 22, pp. 10833, (2021).
- [204] Kasturi Lal Chopra and Inderjeet Kaur, "Thin film Device Applications", Indian Institute Of technology New Delhi, India, Plenum Press, New York, (1983).
- [205] Fraden J., and Fraden J., "Handbook of modern sensors: physics, designs, and applications", New York: Springer, (2004).
- [206] Gründler P., "Chemical Sensors: An introduction for Scientists and Engineers", Springer Science & Business Media, (2007).
- [207] Licznarski B. "Thick-film Gas Microsensors based on Tin Dioxide", *Bulletin of the Polish Academy of Sciences: Technical Sciences*, vol.52, no. 1, (2004).
- [208] Albert K. J., Lewis N. S., Schauer C. L., Sotzing G. A., Stitzel S. E., Vaid T. P., and Walt D. R., "Cross-Reactive Chemical Sensor Arrays", *Chemical reviews*, vol.100, no. 7, pp. 2595-2626, (2000).
- [209] Sa V., Choudhury S., Gadkari S. C. Gupta S. K., and Yakhmi J. V., "Room Temperature Operated Ammonia Gas Sensor using Polycarbazole Langmuir-Blodgett film", *Sensors and Actuators B: Chemical*, vol. 107, no. 1, pp. 277-282, (2005).
- [210] Garg R., Kumar V., Kumar D., and Chakarvarti S. K., "Polypyrrole Microwires as Toxic Gas Sensors for Ammonia and Hydrogen Sulphide", *J. Sensors Instrum.*, vol. 3, no. 1, pp. 1-13, (2015).
- [211] Thakurdesai M., Kulkarni N. Chalke, B., and Mahadkar A., "Synthesis of CdSe Films by Annealing of Cd/Se Bilayer", *Chalcogenide Letters*, vol.8, no. 3, pp. 223-229, (2011).

## References

- [212] Lark-Horovitz, Karl, and Vivian Annabelle Johnson, "Solid State Physics: Preparation, Structure, Mechanical and Thermal Properties", vol. 6. Academic Press, (1959).
- [213] Sharma R., Bisen D. P., Shukla U., and Sharma B. G., "X-ray Diffraction: A powerful Method of Characterizing Nanomaterials", Recent research in science and technology, vol. 4, no. 8, (2012).
- [214] MA C., SG P., PR G., Shashwati S., and VB. P., "Synthesis and Characterization of Polypyrrole (PPy) thin films", Soft nanoscience letters, (2011).
- [215] Makhlof A. S. H., and Barhoum A., "Emerging Applications of Nanoparticles and Architectural Nanostructures: current prospects and future trends", William Andrew, (Eds.), (2018).
- [216] Pathak Y. V., and Lokhande J. N., "Handbook of metallonutraceuticals", CRC Press, (Eds.), (2014).
- [217] Kulkarni S. K., "Nanotechnology: Principles and Practices", Cham, Switzerland: Springer International Publishing and New Delhi, (2015).
- [218] Semnani D., "Geometrical Characterization of Electrospun Nanofibers", in Electrospun Nanofibers, Woodhead Publishing, pp. 151-180, (2017).
- [219] Lis G. P., Mastalerz, M., Schimmelmann, A., Lewan, M. D., and Stankiewicz, B. A., "FTIR Absorption indices for thermal maturity in Comparison with vitrinite reflectance R<sub>0</sub> in type-II kerogens from Devonian black shales", Organic geochemistry, vol. 36, no. 11, pp. 1533-1552,(2005).
- [220] W. Ahmed and Mark j. Jackson, "Emerging Nanotechnologies for Manufacturing, Micro and Nanotechnology Series", second ed., elsevier, london, (2015).

## References

- [221] Anupama A. V., Rathod V., Jali V. M., and Sahoo B., "Composition Dependent Elastic and Thermal Properties of Li Zn Ferrites", *Journal of Alloys and Compounds*, vol. 728, pp. 1091-1100, (2017).
- [222] Provder T., Urban M. W., and Barth H. G., "Hyphenated Techniques in Polymer Characterization", American Chemical Society, (1994).
- [223] Tauc J., Grigorovici R., and Vancu A., "Optical Properties and Electronic Structure of Amorphous Germanium", *physica status solidi (b)*, vol. 15, no. 2, pp. 627-637, (1966).
- [224] Chiang C. H., "Higher Energy Gap Control of Fluorescence in Conjugated Polymers", (2018).
- [225] Yan M. Rothberg L., Hsieh B. R., and Alfano R. R., "Exciton Formation and Decay Dynamics in Electroluminescent Polymers observed by Sub Picosecond Stimulated Emission", *Physical Review B*, vol. 49, no. 14, pp. 9419, (1994).
- [226] Schulman S. G., "Fluorescence and Phosphorescence Spectroscopy: Physicochemical Principles and Practice", Elsevier, (2017).
- [227] Satrijo A., "Controlling the Architectures and Optical Properties of Conjugated Polymer Aggregates and Films", (Doctoral dissertation, Massachusetts Institute of Technology), (2007).
- [228] Di Bartolo B., and Collins J., "Biophotonics: Spectroscopy, Imaging, Sensing, and Manipulation", Springer, (2010).
- [229] S. A. Hamdan, "Growth of Seed-assisted  $Y_2O_3$ -Doped  $Co_3O_4$  Films for Sensing Applications", PH. D. Thesis, University of Baghdad, Iraq, (2019).
- [230] A. S. Edgar, F. A. Scarlat, and C. S. Juliana, " Nanostructured Polypyrrole Powder: A Structural and Morphological Characterization", *Journal of Nanomaterials*, (2015).

## References

- [231] Lawrence Kumar, Pawan Kumar, Amarendra Narayan and Manoranjan Kar, "Rietveld Analysis of XRD Patterns of different sizes of Nanocrystalline Cobalt Ferrite", *International Nano Letters*, vol. 3, no. 1, pp.1-12, (2013).
- [232] B.B.V.S. Vara Prasad, K.V. Ramesh and A. Srinivas, "Structural and Magnetic studies on Co-Zn Nanoferrite Synthesized Via Sol-Gel and Combustion Methods", *Materials Science-Poland*, vol.37 no.1, pp. 39-54, (2019).
- [233] Mah Rukh Siddiquah, "Effect of Doping of Various Metal Cations on Structural, Electrical and Magnetic Properties of Nano Cobalt Ferrites", Ph. D. Thesis, Quaid-I-Azam University, Pakistan-Islamabad, (2008).
- [234] Fu Y., Su Y. S. and Manthiram A. , "Sulfur-Polypyrrole Composite Cathodes for Lithium-Sulfur Batteries", *Journal of the Electrochemical Society*, vol. 159, no. 9, (2012).
- [235] Tavakkol E., Tavanai H., Abdolmaleki A., and Morshed M., "Production of Conductive Electrospun Polypyrrole/poly (vinyl pyrrolidone) Nanofibers". *Synthetic Metals*, vol. 231, pp. 95-106, (2017).
- [236] Huyen D. N., Tung N. T., Vinh T. D., and Thien N. D. , "Synergistic Effects in the Gas Sensitivity of Polypyrrole/single wall Carbon Nanotube Composites", *Sensors*, vol. 12, no. 6, pp. 7965-7974, (2012).
- [237] Preeti Thakur, Deepika Chahar, Shilpa Taneja, Nikhil Bhalla and Atul Thakur, "A review on MnZn Ferrites: Synthesis, Characterization and Applications", *Ceramics international*, vol.46, no.10, pp.15740-15763, (2020).
- [238] R.D. Waldron, "Infrared Spectra of Ferrites", *Physical Review*, vol.99, no.6, pp. 1727-1735, (1955).
- [239] Mazen S. A., and Abu-Elsaad N. I., "IR spectra, Elastic and Dielectric Properties of Li-Mn Ferrite", *International Scholarly Research Notices*, (2012).

## References

- [240] Nag S., Ghosh A., Das D., Mondal A., and Mukherjee S., "Ni<sub>0.5</sub>Zn<sub>0.5</sub>Fe<sub>2</sub>O<sub>4</sub>/Polypyrrole Nanocomposite: A novel Magnetic Photocatalyst for Degradation of Organic Dyes", *Synthetic Metals*, vol.267, pp. 116459, (2020).
- [241] Gill N., Sharma A. L., Gupta V., Tomar M., Pandey O. P., and Singh D. P., "Enhanced Microwave Absorption and Suppressed Reflection of Polypyrrole-Cobalt Ferrite-Graphene Nanocomposite in X-band", *Journal of Alloys and Compounds*, vol.797, pp. 1190-1197, (2019).
- [242] W. Xiaocong, T. Saide and Z. Chenxi, "Uniform Fe<sub>3</sub>O<sub>4</sub>-PANi/PS Composite Spheres with Conductive and Magnetic Properties and their Hollow Spheres", vol. 11, no. 4, pp. 923-929, (2009).
- [243] Mohammed Ihasan," Synthesis and Characterizations of PPy/Ag- NiO Nanocomposites and Their Physical Applications, Ph. D. Thesis, (2021).
- [244] J. Samuel Smart, "The Neel Theory of Ferrimagnetism", *American Journal of Physics* , vol. 23, no. 6, pp. 356-370, (1955).
- [245] Chen D., Liang Z., Xiao J. K., and Wei F. H., "Synthesis of Co-Substituted Mn-Zn Ferrite Nanoparticles by Mechanochemistry Approach", *Journal of Electroceramics*, vol. 36, no. 1, pp. 158-164, (2016).
- [246] Ramarao K., Babu B. R., Babu B. K., Veeraiiah V., Rajasekhar K., Kumar B. R., and Latha B. S., "Enhancement in Magnetic and Electrical Properties of Ni Substituted Mg Ferrite", *Materials Science-Poland*, vol. 36, no. 4, pp. 644-654, (2018).
- [247] Z. X. Sun, F. W. Su, W. Forsling, and P.-O. Samskog, "Surface Characteristics of Magnetite in Aqueous Suspension", *Journal of Colloid and Interface Science*, vol.197, no. 1, pp. 151-159, (1998).

## References

- [248] Prasad S. R. "Synthesis and Characterization of ZnO and SiO<sub>2</sub> Nanoparticles Doped Polypyrrole for Gas Sensing Application", (Doctoral dissertation, Central Scientific Instruments Organisation), (2016).
- [249] Joshi G. P., Saxena N. S., Mangal R., Mishra A., and Sharma T. P., "Band Gap Determination of Ni-Zn Ferrites", *Bulletin of Materials Science*, vol. 26, no. 4, pp. 387-389, (2003).
- [250] Yuliantika D., Taufiq A., Hidayat A., Hidayat N., and Soontaranon S., "Exploring structural Properties of Cobalt Ferrite Nanoparticles From Natural Sand", In *IOP Conference Series: Materials Science and Engineering*, vol. 515, no. 1, pp. 012047, (2019).
- [251] Abdalsalam A. H., Ati A. A., Abduljabbar A., and Hussein T. A., "Structural, Optical, Electrical and Magnetic Studies of PANI/ferrite Nanocomposites Synthesized by PLD Technique", *Journal of Inorganic and Organometallic Polymers and Materials*, vol. 29, no. 4, pp. 1084-1093, (2019).
- [252] Wen P., Tan C., Zhang J., Meng F., Jiang L., Sun Y., and Chen X., "Chemically Tunable Photoresponse of ultrathin polypyrrole", *Nanoscale*, vol. 9, no. 23, pp.7760-7764, (2017).
- [253] Wang X., Lv L., Li L., Chen Y., Zhang K., Chen H. and Huang H., "High-Performance all-Polymer Photoresponse Devices based on Acceptor-acceptor Conjugated Polymers", *Advanced Functional Materials*, vol. 26, no. 34, pp. 6306-6315, (2016).
- [254] Liu Y., Ma H., Zhang Y., Pang X., Fan D., Wu D., and Wei Q., "Visible light Photoelectrochemical Aptasensor for Adenosine Detection based on CdS/PPy/g-C<sub>3</sub>N<sub>4</sub> Nanocomposites", *Biosensors and Bioelectronics*, vol. 86, pp. 439-445, (2016).
- [255] Singh S. K., and Shukla R. K., "Optical and Photoconductivity Properties of pure Polypyrrole and Titanium Dioxide-doped Polypyrrole

## References

Nanocomposites", *Materials Science in Semiconductor Processing*, vol. 31, pp. 245-250, (2015).

[256] Liu H., Sun Q., Zhang Z., Zheng Z., and Zhao K., "Fast photoresponse of zinc ferrite nanotube arrays fabricated by electrodeposition", *Journal of Physics D: Applied Physics*, vol. 49, no. 9, pp. 095107, (2016).

[257] Tiantian Yang, Jie Wei, Yaxin Guo, Zhibin Lv, Zhuo Xu, and Zhenxiang Cheng, "Manipulation of Oxygen Vacancy for High Photovoltaic Output in Bismuth Ferrite Films", *ACS applied materials & interfaces*, vol. 11, no. 26, pp. 23372-23381, (2019).

[258] Mohua Chakraborty, R. Thangavel, Amrita Biswas and G. Udayabhanub, " Facile Synthesis, and The optical and Electrical Properties of Nanocrystalline  $ZnFe_2O_4$  Thin films", *Cryst. Eng. Comm.*, vol. 18, no. 17, pp. 3095-3103, (2016).

[259] I. M. Ibrahim, A. S. Mohammed, and A. Ramizy, "Responsivity Enhancement of Lutetium Oxide Doped-NiO Thin Films," *Journal of Ovonic Research*, vol. 14, no. 1, pp. 17-25, (2018).

[260] Taewhan Kim, Woosung Choi, Heon Cheol Shin, Jae-Young Choi, Ji Man Kim, Min-Sik Park, and Won-Sub Yoon, "Applications of Voltammetry in Lithium Ion Battery Research", *Journal of Electrochemical Science and Technology*, vol. 11, no. 1, pp. 14-25, (2020).

[261] Aparna M. L., Grace A. N., Sathyanarayanan P., and Sahu N. K., "A comparative Study on the Supercapacitive Behaviour of Solvothermally prepared Metal Ferrite ( $MFe_2O_4$ , M= Fe, Co, Ni, Mn, Cu, Zn) Nanoassemblies", *Journal of Alloys and Compounds*, vol. 745, pp. 385-395,(2018).

[262] Liu T., Finn L., Yu M., Wang H., Zhai T., Lu X., and Li Y., "Polyaniline and Polypyrrole Pseudocapacitor Electrodes with Excellent Cycling Stability", *Nano letters*, vol. 14, no. 5, pp. 2522-2527, (2014).

## References

- [263] Shrikant S. Raut and Babasaheb R. Sankapal, "First report on synthesis of  $\text{ZnFe}_2\text{O}_4$  thin film using Successive ionic Layer Adsorption and Reaction: Approach towards Solid-state Symmetric Supercapacitor Device", *Electrochimica Acta*, vol. 198, no. 20, 2016, pp. 203-211 (2016).
- [264] Ishaq S., Moussa M., Kanwal F., Ehsan M., Saleem M., Van T. N., and Losic D., "Facile Synthesis of Ternary Graphene Nanocomposites with Doped Metal Oxide and Conductive Polymers as Electrode Materials for High Performance Supercapacitors", *Scientific reports*, vol. 9, no.1, pp.1-11, (2019).
- [265] Shanmugavani A., and Selvan R. K., "Synthesis of  $\text{ZnFe}_2\text{O}_4$  Nanoparticles and their Asymmetric Configuration with  $\text{Ni}(\text{OH})_2$  for a Pseudocapacitor", *RSC Advances*, vol. 4, no. 51, pp. 27022-27029, (2014).
- [266] Xu R., Guo F., Cui X., Zhang L., Wang K., and Wei J., "High Performance Carbon Nanotube based Fiber-shaped Supercapacitors using Redox additives of Polypyrrole and Hydroquinone", *Journal of Materials Chemistry A*, vol. 3, no. 44, pp. 22353-22360, (2015).
- [267] S. D. Raut, V. V. Awasarmol, B. G. Ghule, S. F. Shaikh, S. K. Gore, R. P. Sharma, P. P. Pawar and R. S. Mane, "Enhancement in room-temperature Ammonia Sensor Activity of Size-reduced Cobalt Ferrite Nanoparticles on  $\gamma$ -Irradiation", *Materials Research Express*, vol.5, no. 6, pp. 65035, (2018).
- [268] Yang X., and Li L., "Polypyrrole Nanofibers Synthesized Via Reactive Template Approach and their  $\text{NH}_3$  Gas Sensitivity", *Synthetic metals*, vol. 160, no. 11-12, pp. 1365-1367, (2010).
- [269] Wu K., Li J., and Zhang C., "Zinc Ferrite Based Gas Sensors: A review", *Ceramics International*, vol. 45, no. 9, pp. 11143-11157, (2019).
- [270] Yahya K. "Characterization of Pure and Dopant  $\text{TiO}_2$  Thin Films for Gas Sensors Applications," Ph. D., University of Technology Department of Applied Science, pp. 1-147, (2010).

## References

- [271] Saheb L., and Al-Saadi T. M., "Synthesis, Characterization, and NH<sub>3</sub> Sensing Properties of (Zn<sub>0.7</sub>Mn<sub>0.3-x</sub>Ce<sub>x</sub>Fe<sub>2</sub>O<sub>4</sub>) Nano-Ferrite", In Journal of Physics: Conference Series, vol. 2114, no. 1, pp. 12040, (2021).
- [272] Achary L. S. K., Kumar A., Barik B., Nayak P. S., Tripathy N., Kar J. P., and Dash P. , "Reduced Graphene Oxide-CuFe<sub>2</sub>O<sub>4</sub> Nanocomposite: A highly Sensitive Room Temperature NH<sub>3</sub> Gas Sensor", Sensors and Actuators B: Chemical, vol. 272, pp. 100-109, (2018).
- [273] Li Y., Ban H., and Yang M. , "Highly Sensitive NH<sub>3</sub> Gas Sensors Based on Novel Polypyrrole-coated SnO<sub>2</sub> Nanosheet Nanocomposites", Sensors and Actuators B: Chemical, vol. 224, pp. 449-457, (2016).
- [274] Joulazadeh M., and Navarchian A. H., "Ammonia Detection of One-Dimensional Nano-structured Polypyrrole/metal Oxide Nanocomposites Sensors", Synthetic Metals, vol. 210, pp. 404-411, (2015).

## الخلاصة

ركز هذا البحث على تحضير ألياف نانوية لبوليمر البولي بايرونول (PPy-NFs) بتقنية البلمرة الكيميائية وتحضير جسيمات نانوية لـ  $(Co_{0.8-x}Zn_xMn_{0.2}Fe_2O_4)$  بتقنية الترسيب المشترك وبعدها تمت معالجتها حرارياً في مفاعل الاوتوكلاف الحراري المائي، حيث كانت قيم  $(x)$  ضمن المدى  $(0.8-0)$  ومقدار التغير في قيمة  $(x)$  هو  $(0.2)$  في كل تجربة، بعد ذلك تم تطعيم الألياف النانوية لبوليمر البولي بايرونول (PPy-NFs) بالجسيمات النانوية للسلاسل الفيروايتية المختلفة لانتاج مترابكات نانوية (PPy-NFs/Ferrite nanoparticles).

تمت دراسة المواد المحضرة وتشخيصها باستخدام العديد من التقنيات ومنها تقنية حيود الأشعة السينية (XRD) ومطياف الأشعة تحت الحمراء (FTIR) ومجهر مجال الانبعاث الإلكتروني الماسح (FESEM). حيث بينت نتائج (XRD) النسق غير المتبلور للبولي بايرونول والنسق المتبلور ذو الطور الاحادي للجسيمات النانوية الفيروايتية. لقد كان الحجم البلوري  $(D_{311})$  للجسيمات الفيروايتية ضمن المدى  $(14.47-8.54)$  نانومتر. كذلك كشفت صور (FESEM) ان البولي بايرونول قد تبلمر في شكل شبكة ألياف نانوية أحادية البعد  $(1D)$  في حين أن الجسيمات النانوية الفيروايتية كانت كروية الشكل مع تغير طفيف في توزيع الحجم للجسيمات. أظهر التحليل الطيفي (FTIR) للسلاسل الفيروايتية عن وجود حزم امتصاص مميزة تعود لمواقع رباعي السطوح وثمانى السطوح على التوالي وكذلك عن ترابط مميز ما بين بوليمر البولي بايرونول (PPy-NFs) والمواد المشوبة (Ferrite nanoparticles) وهذا يدل على تكون المترابكات النانوية. لقد تم أيضاً دراسة الخصائص البصرية للعينات ولوحظ أن مقدار فجوة الطاقة وسلوك الامتصاصية لها يتغيران بتغير نسب الاضافة ومحتوى الفيروايت المضاف.

أظهرت الفحوصات المغناطيسية التي أجريت في درجة حرارة الغرفة أن للعينات خواص مغناطيسية مميزة، كما لوحظ تباين قيمة مغنطة التشبع من خلال تغير محتوى الكوبالت في التركيبة وبلغت أعلى قيمة لها في المركب  $(Co_{0.8-x}Zn_xMn_{0.2}Fe_2O_4)$  عند  $(x=0)$  ثم تقل مغنطة التشبع تدريجياً مع نقصان محتوى الكوبالت.

تم استخدام المترابكات المحضرة لتحسين حساسية جهاز الكشف الضوئي حيث كانت أعلى تحسسية للبولي بايرونول (PPy-NFs) بحدود  $(43.42\%)$  وللجسيمات النانوية بحدود  $(81.47\%)$  عند  $(x=0.8)$  وللعينات المترابكة  $(PPy-NFs/Zn_{0.8}Mn_{0.2}Fe_2O_4)$  بحدود  $(103.74\%)$  لضوء ذو

قدرة (30) ملي واط وطول موجي (405nm) حيث كان وقت الصعود ووقت الهبوط بحدود  $(5 \times 10^{-1})$  (sec).

تم تحضير المكثفات الفائقة لكل من البولي بايرونول وعينات الفيرايت والعينات المترابطة من أجل الحصول على عينات ذات سعات مميزة ومستقرة دورياً والتي تم تقييم أدائها باستخدام مقياس الجهد الدوري (CV) والتحليل الطيفي للمعاوقة الكهروكيميائية (EIS) وتقنية الشحن والتفريغ الكلفانوستاتيكية (GCD) حيث كانت أعلى سعة تم حسابها للقطب المتراب (PPy-NFs/Zn<sub>0.8</sub>Mn<sub>0.2</sub>Fe<sub>2</sub>O<sub>4</sub>) بمعدل مسح (20 mV/s) تساوي (414.12 F/g).

أخيراً تمت دراسة استجابة العينات المحضرة للكشف عن غاز الأمونيا (NH<sub>3</sub>) ووجد أن استشعار غاز الأمونيا يتغير تدريجياً مع زيادة محتوى الزنك في عينات الفيرايت النقي والعينات المترابطة ولوحظ أن أكبر استجابة لغاز الأمونيا عند درجة حرارة (50<sup>0</sup>C) للجسيمات النانوية عند (x=0.8) تساوي (679.01%) وللعينات المترابطة (PPy-NFs/Zn<sub>0.8</sub>Mn<sub>0.2</sub>Fe<sub>2</sub>O<sub>4</sub>) كانت تساوي (423.11%).



جمهورية العراق  
وزارة التعليم العالي والبحث العلمي  
جامعة ديالى  
كلية العلوم  
قسم الفيزياء



تحضير وتوصيف المترجمات النانوية (بولي بيروول- فيرايت) وتطبيقاتها  
الفيزيائية

اطروحة مقدمة الى  
مجلس كلية العلوم – جامعة ديالى  
وهي جزء من متطلبات نيل درجة الدكتوراه فلسفة  
في علوم الفيزياء  
من قبل

عمر أحمد حسين الجبوري  
بكالوريوس علوم الفيزياء (2006)  
ماجستير علوم الفيزياء (2012)  
باشراف

الأستاذ الدكتور  
عصام محمد ابراهيم  
2022 م

الأستاذ الدكتور  
تحسين حسين مبارك  
1444 هـ

